Universidade de Aveiro
2023

Carolina Teixeira
de Sousa Gouveia

Bio-Radar: Sistema de aquisição de sinais vitais sem contacto

Bio-Radar: Contactless acquisition system for vital signs

Universidade de Aveiro
2023

Carolina Teixeira
de Sousa Gouveia

Bio-Radar: Sistema de aquisição de sinais vitais sem contacto

Bio-Radar: Contactless acquisition system for vital signs

Tese apresentada à Universidade de Aveiro para cumprimento dos requisitos necessários à obtenção do grau de Doutor em Engenharia Eletrotécnica, realizada sob orientação científica do Prof. Dr. José Manuel Neto Vieira, Professor Auxiliar no Departamento de Eletrónica, Telecomunicações e Informática da Universidade de Aveiro, e co-orientada pelo Prof. Dr. Pedro Renato Tavares Pinho, Professor Auxiliar no Departamento de Eletrónica, Telecomunicações e Informática da Universidade de Aveiro e também pelo Prof. Dr. Daniel Filipe Albuquerque, Professor Adjunto da Escola Superior de Tecnologia e Gestão de Viseu do Instituto Politécnico de Viseu.

Esta tese foi realizada com o apoio financeiro da Fundação para a Ciência e Tecnologia (FCT), através do Fundo Social Europeu e do Programa Operacional Regional do Centro, sob a bolsa de doutoramento com a referência SFRH/BD/139847/2018

o júri / the jury

presidente / president

Professor Doutor Vitor Brás de Sequeira Amaral
Professor Catedrático da Universidade de Aveiro

vogais / examiners committee

Professor Doutor Adão Paulo Soares da Silva
Professor Associado da Universidade de Aveiro

Professor Doutor Paulo Alexandre Carapinha Marques
Professor Coordenador do Instituto Superior de Engenharia de Lisboa

Professora Doutora Matilde Pós-De-Mina Pato
Professora Adjunta do Instituto Superior de Engenharia de Lisboa

Professor Doutor Hugo Humberto Plácido da Silva
Professor Auxiliar Convidado do Instituto Superior Técnico - Universidade de Lisboa

Professor Doutor José Manuel Neto Vieira
Professor Auxiliar da Universidade de Aveiro (orientador)

agradecimentos

Começo por dar um agradecimento especial à Fundação para a Ciência e Tecnologia (FCT), uma vez que o meu trabalho foi apoiado por esta através do Fundo Social Europeu (FSE) e do Programa Operacional Regional do Centro, sob a bolsa de PhD com a referência SFRH/BD/139847/2018.

De seguida deixo o meu agradecimento à minha equipa de orientação, ao Prof. José Vieira, ao Prof. Pedro Pinho e ao Prof. Daniel Albuquerque pelo apoio, suporte e conhecimento transmitido, imprescindíveis para ter conseguido conduzir os meus trabalhos no caminho certo.

Estou muito grata pelas parcerias que surgiram neste trajecto, entre elas devo destacar a Prof. Caroline Loss da Universidade da Beira Interior pela ajuda no desenvolvimento de antenas têxteis, e também a Filipa Barros e a Prof. Sandra Soares do Departamento de Educação e Psicologia da Universidade de Aveiro pelo auxílio no estudo das emoções.

Saúdo também todos os meus colegas do Instituto de Telecomunicações pela ajuda e pelas discussões de ideias que de alguma forma contribuíram para ajudar a completar o meu trabalho.

Quero agradecer muito à minha família, em especial aos meus pais e irmãos, pelo apoio incessante nesta etapa. Por fim, quero expressar profunda gratidão ao Rodrigo pelo amor, apoio e a infindável paciência, que me deram confiança para chegar até ao fim.

A todos, muito obrigada!

Palavras-chave

Sinais vitais, Radar Onda Contínua, Efeito Micro-Doppler, Antenas Têxteis, Movimento Corporal Aleatório, Reconhecimento de Emoções

Resumo

O sistema Bio-Radar permite medir sinais vitais com precisão, nomeadamente o sinal respiratório e cardíaco, utilizando ondas electromagnéticas para esse fim. Desta forma, é possível monitorizar sujeitos de forma remota e confortável durante longos períodos de tempo. Este sistema é baseado no efeito de micro-Doppler, que relaciona a variação de fase do sinal recebido com a alteração da distância entre as antenas do radar e a caixa torácica do sujeito, que ocorre durante a função cardiopulmonar. Considerando a variedade de aplicações onde este sistema pode ser utilizado, é necessário avaliar o seu desempenho quando aplicado em contextos reais e assim demonstrar as vantagens que os sistemas bio-radar podem trazer à população geral. Neste trabalho, foi desenvolvido um protótipo do bio-radar com o objectivo de verificar a viabilidade de integrar estes sistemas em aplicações específicas, utilizando soluções robustas e discretas que garantam igualmente o seu bom desempenho, indo simultaneamente de encontro às necessidades do mercado. Considerando estas duas perspectivas em que o sistema pode ser melhorado, foram desenvolvidas soluções de diferentes níveis. Do ponto de vista de hardware, foram desenvolvidas antenas têxteis para serem integradas no estofo de um banco automóvel, alcançando uma solução discreta e fácil de incluir num processo de industrialização. Contextos reais de aplicação implicam períodos de monitorização longos, onde podem ocorrer movimentos corporais involuntários que produzem sinais de elevada amplitude que se sobrepõem aos sinais vitais. Ambientes de monitorização não controlados podem produzir reflexões parasitas variantes no tempo que têm impacto directo no sinal. Adicionalmente, a estrutura física do sujeito e a sua postura durante o período de monitorização podem ter impactos diferentes na qualidade dos sinais. Desta forma, foram desenvolvidos algoritmos de processamento de sinal robustos a sinais de baixa qualidade e a cenários não estáticos. Por outro lado, o potencial do bio-radar pode também ser maximizado se os sinais adquiridos forem pertinentemente utilizados de forma a ajudar a identificar o estado psicofisiológico do sujeito, permitindo mais tarde agir em conformidade. O movimento corporal aleatório que foi até agora visto como uma fonte de ruído, pode no entando também fornecer informação útil sobre o estado do sujeito. Neste sentido, o sinais vitais e outros movimento corporais adquiridos foram utilizados em algoritmos de aprendizagem automática com o objectivo de identificar as emoções do sujeito e assim verificar que sinais vitais adquiridos remotamente podem também conter informação útil.

Keywords Vital Signs, Continuous Wave (CW) Radar, Micro-Doppler Effect, Textile Antennas, Random Body Motion (RBM), Emotion recognition

Abstract The Bio-Radar system is capable to measure vital signs accurately, namely the respiratory and cardiac signal, using electromagnetic waves. In this way, it is possible to monitor subjects remotely and comfortably for long periods of time. This system is based on the micro-Doppler effect, which relates the received signal phase variation with the distance change between the subject chest-wall and the radar antennas, which occurs due to the cardiopulmonary function. Considering the variety of applications where this system can be used, it is required to evaluate its performance when applied to real context scenarios and thus demonstrate the advantages that bio-radar systems can bring to the general population. In this work, a bio-radar prototype was developed in order to verify the viability to be integrated in specific applications, using robust and low profile solutions that equally guarantee the general system performance while addressing the market needs. Considering these two perspectives to be improved, different level solutions were developed. On the hardware side, textile antennas were developed to be embedded in a car seat upholstery, thus reaching a low profile solution and easy to include in the industrialization process. Real context scenarios imply long-term monitoring periods, where involuntary body motion can occur producing high amplitude signals that overshadow the vital signs. Non-controlled monitoring environments might also produce time varying parasitic reflections that have a direct impact in the signal. Additionally, the subject's physical stature and posture during the monitoring period can have a different impact in the signals quality. Therefore, signal processing algorithms were developed to be robust to low quality signals and non-static scenarios. On the other hand, the bio-radar potential can also be maximized if the acquired signals are used pertinently to help identify the subject's psychophysiological state enabling one to act accordingly. The random body motion until now has been seen as a noisy source, however it can also provide useful information regarding subject's state. In this sense, the acquired vital signs as well as other body motions were used in machine learning algorithms with the goal to identify the subject's emotions and thus verify if the remotely acquired vital signs can also provide useful information.

Contents

List of Figures

List of Tables

Acronyms

ANN	Artificial Neural Networks
ARCM	Arc Method
BPC	BIOPAC
BPF	Band-pass filter
BPM	Beats per minute
BRD	Bio-Radar
BRPM	Breaths per minute
CDC	Complex DC
CNN	Convolutional Neural Networks
CS	Cardiac Signal
CV	Cross-Validation
CW	Continuous-Wave
CWS	Chest Wall Simulator
CWT	Continuous Wavelet Transform
DSP	Digital Signal Processing
DWT	Discrete Wavelet Transform
ECG	Electrocardiogram
EMD	Empirical Mode Decomposition
EEMD	Ensembled Empirical Mode Decomposition
ERS	Estimated Radar Signal
FEMDM	Full Ellipse Method with Detectable Motion
FIR	Finite Impulse Response
FL	Full-version

FMCW	Frequency Modulated Continuous-Wave
GM	Global Model
HPBW	Half-Power Beamwidth
HRV	Heart Rate Variability
IBI	Interbeat Interval
ICNIRP	International Committee for Non-Ionizing Radiation Protocol
IM	Individual Model
IMF	Intrinsic Mode Functions
IQ	In-phase and Quadrature
ISM	Industrial, Scientific and Medical
KNN	K-Nearest Neighbour
LHCP	Left-Handed Circularly Polarized
LM	Gauss-Newton method with Levenberg-Marquardt correction
LSF	Least Squares Fitting
MAE	Mean Absolute Error
MS	Maximum of the Spectrum
NN	Neural Networks
OC	Optimized Cost Method
ORS	Original Radar Signal
PCPTF	Pure Copper Polyester Taffeta Fabric
pNN50	Percentage of successive Normal sinus IBI more than 50 ms
PSD	Power Spectral Density
RBM	Random Body Motion
RCS	Radar Cross Section
RF	Radio-Frequency
RFO	Random Forest
RHCP	Right-Handed Circularly Polarized
RMSE	Root-Mean-Squared Error
RMSSD	Root Mean Square of Successive Differences

RS	Respiratory Signal
SAR	Specific Absorption Rate
SDNN	Standard Deviation of Normal-to-Normal intervals
SDR	Software-Defined Radio
SDRR	Square Root of the IBI variance
SIGP	Substrate Integrating the Ground Plane
SINR	Signal-to-Interference plus Noise Ratio
SH	Short-version
SLL	Side-Lobe Level
SMA	SubMiniature version A
SNR	Signal-to-Noise Ratio
SVM	Support-Vector Machines
UWB	Ultra Wideband
WPD	Wavelet Packet Decomposition
ZC	Zero-Crossing

Chapter 1

Introduction

In this chapter, the background and motivation supporting this PhD work are presented. The objectives of the work are defined, considering the raised questions and the identified gaps. Then, the contributions provided to the scientific community are outlined. Finally, the structure of this document is presented.

1.1 Background and motivation

The ability to assess vital signs remotely is a topic that is being highly discussed in the research community. Multiple solutions have been presented, where the most appealing ones use radar systems, allowing wireless vital signs monitoring that can be performed from afar. Radar systems can capture vital signs, such as the respiratory and cardiac signals, through the measurement of the chest wall displacement. Generally based in the micro-Doppler effect, electromagnetic waves are transmitted towards the subject's chest wall, and the reflected echo is received by the radar front-end. The received signal is a phase modulated version of the transmitted one, caused by the chest wall motion according to the cardiopulmonary function [1]. Figure 1.1 presents a simplified scheme that depicts this working principle, while using a Continuous-Wave (CW) radar for instance [1], [2].

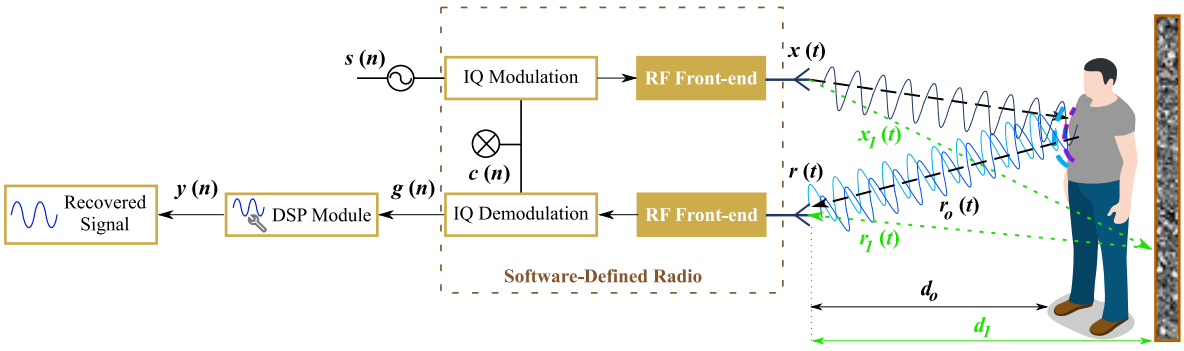

Figure 1.1: Example of a radar operation principle to capture vital signs [1], [2].

These radar-based systems, will be from now on referred as *Bio-Radar* systems. They present multiple applications, not only in the medical field, where the direct interaction with the subject is avoided, but either in other situations of our daily life. Continuous monitoring

can improve the sensing of differences in the vital signs patterns and thus help identify sudden events, such as the drowsiness of a vehicle driver or the apnea of an infant during sleep time [1]. With this technology it is also possible to monitor bedridden patients in critical state or with highly infectious diseases (such as the COVID-19), and possibly help in cardiopulmonary disease diagnosis. Applications in psychology are also feasible, for example the measurement of stress response [3], or even the follow-up of patients with psychological disorders, such as autism, through emotion recognition [4], [5]. In such applications, it is essential to minimize the subject awareness of the measurement to enable authentic reactions [5].

The concept of non-contact extraction of human physiological parameters using radar had been demonstrated by pioneers in the 1970s [6]–[8], where the respiration was measured along with the heartbeat during apnea interspersed periods. Thenceforth, several solutions have been presented using different Radio-Frequency (RF) front-ends, either using combined RF components [9], [10] or using more compact solutions such as the Software-Defined Radio (SDR) [11]. Later on, the technology advancement allowed an accessible implementation of bio-radar systems. Off-the-shelf radars are already available in the market and ready to use, with recommended features dedicated to vital signs monitoring, such as the mmWave radar sensors from Texas Instruments [12], the SensorLogic radars [13] or the NOVELIC radars [14].

From the research perspective, literature has been presenting several solutions oriented towards the improvement of specific modules contained in the system. Therefore, the systems' implementation challenges can be divided in distinctive areas, mainly grouped in hardware and software approaches. On the hardware side, the antenna selection plays an important role, since it is in the front line to determine the physical dimensions and appearance of the overall system, while assuring the received signal quality at a superior level [15]–[17]. Other aspects regarding the overall hardware definition are related with the carrier frequency [18], [19] and the radar operation mode [20]. In turn, the software side solutions are mostly developed to enhance the overall system efficiency and to solve issues that cannot be addressed using hardware solely. Among them, it can be highlighted the phase demodulation to extract vital signs [21], [22], the parasitic reflections compensation [23], [24] or the cardiac signal extraction [25], [26].

Nowadays, the research in this area is increasingly focused on the system's improvement, aiming to reach solutions that guarantee low power, small dimensions, better accuracy, long range detection and a more robust operation. The flexibility to adapt this system to any environment is even more appealing, due to the wide range of bio-radar applications. Thus, considering real context scenarios, there are challenges arising from the monitoring environment of the target application, which are also inherent to the biosignals nature and that need to be overcome. The challenges common among all applications are the following:

- Long-term monitoring periods:
  - The subject body motion can **interfere in the vital signal extraction**, since it produces high amplitude signals that can overshadow the vital ones [27], [28];
  - The subject body motion can result in a **misalignment between the antenna beam and the chest wall area**, leading to signals attenuation [29], [30];
- Multipath environment:
  - Parasitic reflections **add Complex DC (CDC) offsets** to baseband signals, hampering the extraction of vital signs information [23], [24], [31];

  - **Non-static monitoring environments** might produce different parasitic reflections, **changing the CDC offset values** accordingly over time [25];

- Appropriate **antennas design and location** are required, aiming to concurrently guarantee the system low profile and the effectiveness of capturing vital signs of all population, regardless of their body structures;

- Vital signs extraction and inter-individual variability:

  - Cardiac signals are perceived by radar through the measurement of the heart mechanical motion over the chest wall surface. These **motions are tenuous** and **lack in resolution** turning difficult the cardiac signal extraction [32], [33].
  - Respiratory and cardiac signals might be extracted **with different accuracies over the population** under test, depending on the individual differences and body statures [34]–[36];
  - Vital signs might **contain patterns**, which could be used for health condition or **psychological state assessment** [4], [37].

Aiming to address the aforementioned challenges, the selection of the most suitable radar front-end is a topic that does not follow an agreement between the different literature authors. For instance, the multipath effect could be minimized by using front-ends different from the CW, such as Frequency Modulated Continuous-Wave (FMCW) radars or Ultra Wideband (UWB) radars, but with the cost to add more complexity to the hardware implementation, since these approaches require wideband operation [20]. On the other hand, higher carrier frequencies could also be used to ease the detection of the cardiopulmonary motions which are imperceptible. For instance, millimeter-wave frequencies have smaller wavelengths, which allow the detection of micro-signals as the cardiac one. However, this option decreases the detection range [38], [39] and leads to an extreme sensitivity to high amplitude motions from other body parts.

In fact, the Random Body Motion (RBM) is difficult to avoid in long-term applications, as in overnight monitoring, where it is natural for the subject to roll over in bed, or in vehicular applications where the RBM is necessarily present due to the driving action. The elimination of the interference caused by the RBM is a current challenge in this research field. Many solutions to mitigate the effect of RBM have been proposed, either based in hardware solutions through the usage of external modules [28], [40], [41] or beamforming techniques and/or multi-antenna systems [29], [30], [42], either based in software through the implementation of signal processing techniques to attenuate the disruption [27], [43], [44]. However, some forms of body motion can also contribute as an informative element, not only to improve the extraction algorithms, but also to interact in pattern recognition for biometric identification, diseases diagnostic or the evaluation of the subject's psychological state. The RBM can be seen as additional information, since it is an inherent event relatively to what we do in our routine and how we feel in that exact moment.

In sum, bio-radar systems can in fact be seen as an advantageous solution to monitor vital signs remotely. But, in practical terms and considering the challenges identified above, what are the constraints of its operation in a real-context scenario? Is it possible to integrate the bio-radar system in a specific application addressing the market needs and concurrently assuring the system's performance? Which information is contained in the radar signals and

how can one maximize the system potential with it? Can the RBM be used as important information, rather than being fully eliminated?

1.2 Objectives

Considering the raised questions, this PhD work aims to study the bio-radar performance in real applications and further develop valid solutions to address some of the aforementioned challenges. In this framework, two specific case studies are going to be considered. The **first case study** is focused on integrating the bio-radar system in a specific application. For this purpose, vehicular applications were the selected target, therefore it is intended to fully integrate the bio-radar in a car seat, following the automotive market requirements. In this sense, a low profile solution need to be designed in order to accommodate the bio-radar system as a car feature and thus streamline the manufacturing process. The system should not be visible and the subject should not feel it, in order to guarantee a comfortable usage. Concurrently, the system should provide accurate results and be suitable for the maximum number of subjects possible, considering different body structures. All these goals could be accomplished by exploring alternative materials for the antenna manufacturing, such as textiles and thus integrate part of the system (i.e. the antennas) directly in the upholstery. Such solution is effective if an appropriate antenna design is selected and if signal processing algorithms are developed considering extreme cases of low Signal-to-Noise Ratio (SNR).

The **second case study** is focused on the proper extraction of the vital signs information (both respiratory and cardiac signals), regardless of the monitoring conditions, the acquisition duration and the population under test. Furthermore, these signals are also going to be further exploited to perform pattern identification and verify if it is possible to assess the psychological state of a subject. For this purpose, different machine learning algorithms are going to be applied and their performance compared, using the vital signs acquired simultaneously by the bio-radar and by a certified measuring equipment.

In sum, the final goal is to identify potentials and limitations related with the bio-radar integration in specific applications, and develop solutions to address the following aspects:

- Robust operation in non-controlled environments;
- Low profile appearance for a full integration of the system in a specific application;
- Effectiveness in long-term monitoring periods by extracting useful information from weak signals;
- Develop vital signs extraction algorithms robust to any body structure;
- Make use of the extracted vital signs for psychological state assessment.

1.3 Contributions

This PhD document is based on a series of scientific communications and publications in important journals of this field. Among all, it can be highlighted the following contributions:

Patents

1. R. Silva, M. Midão, D. Esteves, A. Leite, P. Peixoto, **C. Gouveia**, P. Pinho, J. Vieira, D. Pires, T. Silveira, C. Loss, and R. Salvado, "Vehicle seat cover with a monitoring system," International Patent Pending WO/2022/070 137, PCT/IB2021/059 011, Apr., 2022.

Journal Papers

1. **C. Gouveia**, D. Albuquerque, F. Barros, S. C. Soares, P. Pinho, J. Vieira "Performance Comparison of Emotion Recognition using Bio-Radar and Contact-Based Methods", *IEEE Transactions on Affective Computing*, submitted for publication in July 2022.

2. **C. Gouveia**, C. Loss, P. Pinho, J. Vieira, D. Albuquerque, "Low Profile Textile Antenna for Bio-Radar Integration into a Car Seat Upholstery", *IEEE Antennas and Propagation Magazine*, submitted for publication in July 2022.

3. **C. Gouveia**, D. Albuquerque, P. Pinho, and J. Vieira, "Bio-Radar Cardiac Signal Model used for HRV Assessment and Evaluation Using Adaptive Filtering," *IEEE Transactions on Instrumentation and Measurement*, vol. 71, pp. 1-10, July 2022

4. **C. Gouveia**, D. Albuquerque, P. Pinho, and J. Vieira, "Evaluation of Heartbeat Signal Extraction Methods using a 5.8 GHz Doppler Radar System in a Real Application Scenario," *IEEE Sensors Journal*, vol. 22, no. 8, pp. 7979–7989, 2022

5. **C. Gouveia**, D. Albuquerque, J. Vieira, and P. Pinho, "Dynamic Digital Signal Processing Algorithm for Vital Signs Extraction in Continuous-Wave Radars", *Remote Sensing*, vol. 13, no. 20, pp. 4079, 2021

6. C. Loss, **C. Gouveia**, R. Salvado, P. Pinho and J. Vieira, "Textile Antenna for Bio-Radar Embedded in a Car Seat", *Materials*, vol. 14, no. 1, p. 213, 2021

7. **C. Gouveia**, A. Tomé, F. Barros, S. C. Soares, J. Vieira, P. Pinho, "Study on the Usage Feasibility of Continuous-Wave Radar for Emotion Recognition", *Biomedical Signal Processing and Control*, vol. 58, January 2020, p. 101835.

8. **C. Gouveia**, C. Loss, P. Pinho and J. Vieira, "Different Antenna Designs for Non-Contact Vital Signs Measurement: A Review", *Electronics*, vol. 8, no. 11, p. 1249, 2019

9. **C. Gouveia**, J. Vieira, and P. Pinho, "A Review on Methods for Random Motion Detection and Compensation in Bio-Radar Systems", *Sensors*, vol. 19, no. 3, p. 604, 2019

International Conferences

1. R. Duarte, **C. Gouveia**, P. Pinho and D. Albuquerque, "Limits of WPT through the human body using Radio Frequency", IEEE 16^{th} European Conference on Antennas and Propagation (EuCAP), pp. 1-5, 2022

2. **C. Gouveia**, C. Loss, Z. Raida, J. Lacik, P. Pinho and J. Vieira, "Textile Antenna Array for Bio-Radar Applications", 23^{rd} International Microwave and Radar Conference (MIKON), Warsaw, Poland, p. 315-319, 2020

3. **C. Gouveia**, P. Pinho, and J. Vieira, "Motion Detection Method for Clutter Rejection in the Bio-Radar Signal Processing", 20^{th} International Conference on Radar Science and Technology, Barcelona, Spain, pp. 518-526, 2018

Other achievements

1. **C. Gouveia**, D. Albuquerque, P. Pinho and J. Vieira, "Potentials and Limitations of Customized Bio-Radar Applications", Research ANACOM-URSI Portugal Award, November, 2021

2. **C. Gouveia**, C. Loss, Z. Raida, J. Lacik, P. Pinho and J. Vieira, "Textile Antenna Array for Bio-Radar Applications", EuMA first prize at MIKON Conference 2020, related with the Young Scientist Contest, October, 2020

3. **C. Gouveia**, J. Vieira, P. Pinho, "Motion Detection Method for Clutter Rejection in the Bio-Radar Signal Processing", Best Paper Award by the Program Committee as per the Conference Awards Scheme, in ICRST 2018: International Conference on Radar Science and Technology, August 2018.

1.4 Document organization

This thesis is focused on the bio-radar integration in specific applications, in order to identify eventual potentials and limitations, and propose solutions accordingly. For this purpose, two case studies are going to be explored. In order to address them evenly, a multidisciplinary work was developed and it was organized in seven chapters, as depicted in Figure 1.2. The state of the art supporting this work is presented in the beginning of each chapter in order to follow the reader through the matter opportunely.

The chapters content is the following:

- **Chapter 1 - Introduction -** presents the background and motivation that led to the development of this PhD work. The main objectives of the work are presented, as well as the contributions that it was possible to provide to the research community considering the obtained results.

- **Chapter 2 - Methodology Selection -** presents the trade-offs considered in the overall system components selection. In this chapter, it is also described the final prototype that was further used in the case studies and its hardware characterization. Some aspects about the procedure conducted for the datasets acquisition are also provided.

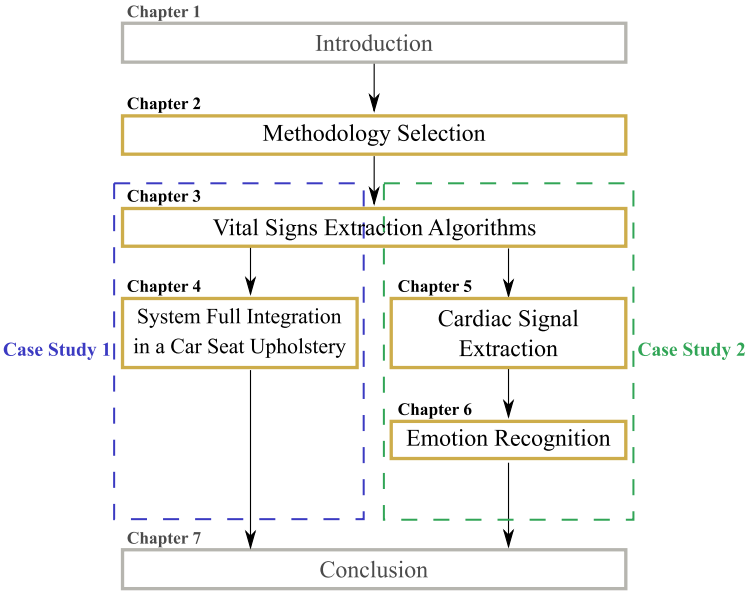

Figure 1.2: Thesis structure schematics.

- **Chapter 3 - Vital Signs Extraction Algorithms -** presents the signal processing algorithms applied to the acquired signals in general. These algorithms are mainly focused on removing the parasitic components received together with the useful signal and then extract the respiratory signal accordingly. Two main versions are presented: the first is a simplified version, where one assumes a static monitoring environment; the second version was developed aiming to solve issues inherent to real applications, namely the non-controlled/non-static environments and the subject's physical variability. The algorithms herein described are the basis for both case studies, so they will be used by the following chapters.

- **Chapter 4 - System Full Integration in a Specific Application -** is fully dedicated to the first case study and presents the considerations that should be kept in mind while integrating the bio-radar system in a customized application. In this sense, the prototype of a car seat upholstery is developed, containing two textile antennas therein integrated, that will be used further as the transmitting and receiving antennas. The potentials and limitations of this integration are discussed and the results of the final prototype validation are also presented.

- **Chapter 5 - Cardiac Signal Extraction -** is dedicated to the second case study and presents the algorithms developed to extract the cardiac signal exclusively. The bio-radar received signal contains both respiratory and cardiac components, being the latter challenging to extract due to the amplitude difference and spectral proximity. Additionally, the ability to retrieve specific cardiac signal parameters, such as the Heart Rate Variability (HRV) is inspected.

- **Chapter 6 - Emotion recognition -** demonstrates the potential of using bio-radar signals to identify events, more specifically by verifying if it is possible to assess the subject's psychological state. For this purpose, the algorithms developed in Chapter 3 and

Chapter 5 are herein applied, pertinent features are extracted from the respiratory and cardiac signals and machine learning algorithms are implemented to recognize subjects' emotions. This is the final step of the second case study.

- **Chapter 7 - Conclusion -** the conclusion presented in this chapter brings forward an overall reflection regarding the bio-radar suitability to be integrated in customized applications and to be used in real context scenarios. Some suggestions of future work are also provided.

Chapter 2

Methodology Selection

This chapter is focused on the description of the methodology considered in this PhD. The radar system architecture is defined after evaluating the trade-offs of all options, specially regarding the radar front-end and the antenna design. A system characterization is also performed and some other aspects are provided regarding the procedure conducted to acquire vital signs and create datasets.

Some of the developments of this chapter resulted in the following contributions:

- C. Gouveia, C. Loss, P. Pinho and J. Vieira, "Different Antenna Designs for Non-Contact Vital Signs Measurement: A Review", *Electronics*, vol. 8, no. 11, p. 1249, 2019
- C. Gouveia, J. Vieira, and P. Pinho, "A Review on Methods for Random Motion Detection and Compensation in Bio-Radar Systems", *Sensors*, vol. 19, no. 3, p. 604, 2019
- R. Duarte, C. Gouveia, P. Pinho and D. Albuquerque, "Limits of WPT Through the Human Body using Radio Frequency", IEEE 16^{th} European Conference on Antennas and Propagation (EuCAP), pp. 1-5, 2022

2.1 Introduction

Bio-radar systems have been highly discussed in the research community, due to its incredible utility but challenging accomplishment. The successful integration and operation of the bio-radar in real applications imply dealing with issues inherent to subject stability and physiology, while assuring the system optimal performance. In this sense, two specific case studies are explored, in order to identify, study and overcome these impairments and thus improve the overall system considering real applications.

In order to step forward on the system optimization taking the market needs into consideration, beyond the system accuracy improvement, its portability and low profile are also important aspects that should be properly studied. Having this in mind, a primary version of a portable bio-radar prototype was developed in [2] and this prototype was further improved in this PhD. Figure 1.1 depicts the block diagram of its implementation and Figure 2.1 shows its composition. The first version of the prototype used an SDR as the selected RF front-end, namely the USRP B210 board from Ettus Research^{TM} [45], two 4×4 antenna arrays [46]

used for transmission and reception and the LabVIEW software for signal processing. The system used the CW operation mode with a single carrier of 5.8 GHz and it could operate in real time, enabling the respiratory signal display during its acquisition time. A validation was performed, where the respiratory signal was acquired using simultaneously the bio-radar prototype and a certified measuring equipment, namely the BIOPAC MP100. The signals were compared afterwards and both acquisitions revealed approximated waveforms and breathing rates [2], [47].

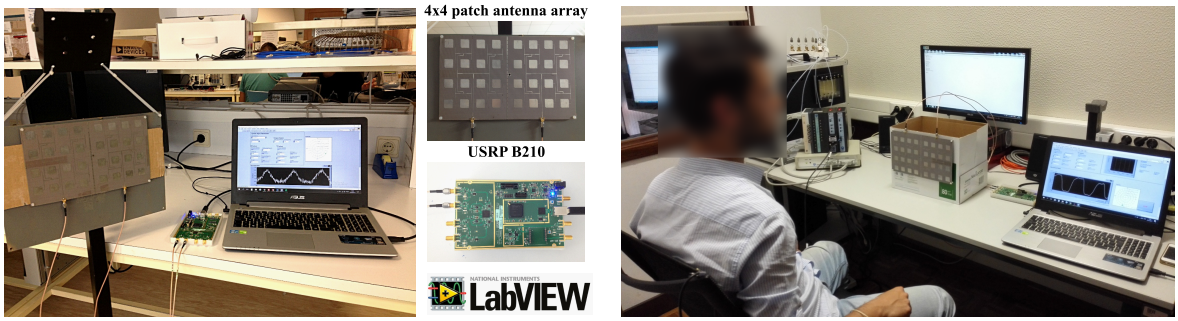

(a) (b)

Figure 2.1: First version of the portable bio-radar prototype developed in [2]: (a) prototype setup, (b) acquisition scenario.

The further developments conducted throughout this PhD used the system proposed in [2] as a starting point, beginning with a performance evaluation considering the specific case studies and improving it accordingly. One of the first steps was to verify the suitability of the selected front-end components.

All the system elements are somehow interconnected with each other, therefore the final system architecture must be defined with care. For instance, the selection of the radar operation mode have influence in the antenna design and in the algorithms implemented for biosignals extraction. The micro-Doppler radar is the basis of different radar operation modes, namely the CW radar, the FMCW radar and the UWB radar, as depicted in Figure 2.2.

The **CW radar** transmits and receives an RF signal continuously towards the target. Usually, the transmitted signal is defined as a single-tone. The system is composed by a signal generator, which uses a local oscillator to generate a signal with a specific carrier frequency for transmission and also to down-convert the received signal to baseband. The target's motion induce a frequency shift on the received signal due to the micro-Doppler effect. This Doppler frequency shift $f_d(t)$, can be represented by equation (2.1) [48]:

$$f_d(t) = \frac{2f_c}{c} v(t) = \frac{2v(t)}{\lambda} \tag{2.1}$$

where f_c is the carrier frequency, c is the speed of light, λ is the wavelength of the transmitted signal and $v(t)$ is the motion velocity. In turn, if the target is moving approximately with a periodic motion and with no net velocity, the Doppler shift can be represented by a time-varying phase modulation [48]. In the bio-radar context, the target at hand is the subject's chest wall, hence the phase modulation corresponds to the chest displacement caused by the cardiopulmonary function.

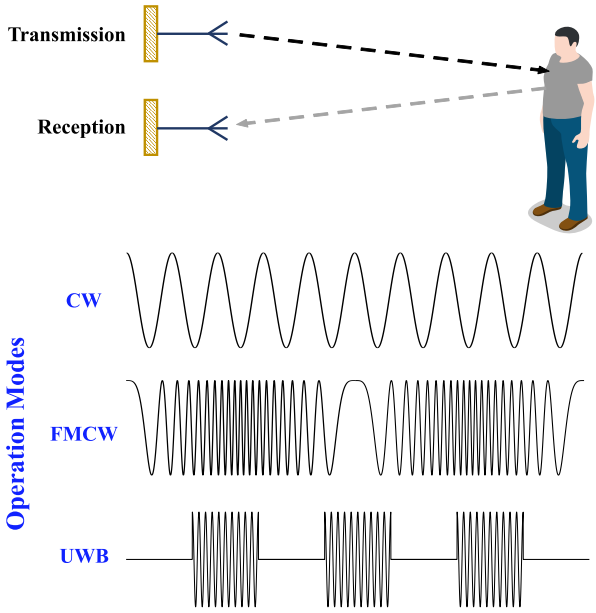

Figure 2.2: Micro-Doppler radar applied to vital-signs acquisition using different operation modes.

The **FMCW radars** allow the computation of the target's velocity and the distance between the target and the radar, once it has more range resolution that does not exist for a single frequency waveform [48]. In this operation mode, frequency modulation can be performed for instance with a linear chirp, by increasing and decreasing the frequency linearly over time. The linear chirp signal previously transmitted is received after being reflected by obstacles. The received signal is a delayed version of the transmitted one, being the delay equal to $T = 2R/c$ seconds, where R is the radar range (distance to the target). The modulated signal bandwidth determines the accuracy of the range measurement, and the modulation rate determines the maximum detectable range without ambiguity. The mix between the transmitted and the received signals results in a frequency difference f_r, that changes according to the target motion and from where the vital signs are extracted.

Finally, the **UWB radar** is a special application of the pulsed radar since very short duration pulses are generated, leading to wide bandwidth signals. The Federal Communications Commission has established that a signal can be categorized as UWB if it has a bandwidth equal to or higher than 500 MHz [49]. UWB radars transmit short pulses and the target reflects a portion of them. The total range ΔR of this radar is given by the equation (2.2) [50]:

$$\Delta R = \frac{\tau c}{2} \tag{2.2}$$

where τ is the bandwidth of the radar pulse in time domain. With this type of radar, it is also possible to compute the distance to target d_T, by applying equation (2.3):

$$d_T = \frac{\Delta t \times c}{2} \tag{2.3}$$

where Δt is the delay between the transmitted and the received signal. The selection of the appropriate operation mode is not consensual along the literature [51], so there is a vast

number of publications using CW radars [27], [33], [42], [52], using FMCW radars [53]–[56] and using UWB [57]–[60].

On the other hand, the antenna design plays also a crucial role in the performance of the bio-radar, since it is a key element to maintain the SNR at a superior level. Several types of antennas have been used in literature, covering a wide range of frequencies, polarization modes, and Half-Power Beamwidth (HPBW), according to the application at hand. However, most of the papers related to the bio-radar system, do not have the antenna information clearly detailed [15]. The majority of the papers do not mention the design of the antennas and its importance in the global behavior of the system, being rather focused on specific challenges that had to be overcome, such as new algorithms to extract the vital signs.

Generally, designing an antenna is a challenging task, since it is based on a group of trade-off decisions. Different antenna parameters should be achieved having in mind specific restrictions and requirements regarding the application at hand. Although the same case is applied for bio-radar applications, there are common characteristics that must be assured, to minimize the influence of parasitic reflections and maximize the SNR. In [15], a preliminary survey on the best antenna characteristics for bio-radar applications was presented. This study encompassed different antenna types, such as microstrip, slot, dipole, helical and array antennas. The authors concluded that regardless on the antenna type, frequency or design, it is crucial to guarantee high gain and directivity.

Within the framework of this PhD, a detailed review was performed aiming to define guidelines that might be followed commonly in every bio-radar implementation, irrespective of the application [61]. The comprehensive research conducted in [61] revealed that the antennas state of the art can be divided according to two main goals that should be addressed: signal quality improvement and system manufacturing streamline. Table 2.1 shows the most relevant references discussed in [61].

Goal		**Reference**
Directivity and gain		[16], [18], [62]–[64]
Antennas for beam-steering		[30], [42], [65]
Frequency diversity		[18], [19], [66]–[71]
Circularly polarized antennas		[17], [63], [66], [72]–[75]
Textile antennas for vital signs monitoring		[76]–[87]
Techniques to reduce the antenna size:	Using a single antenna for TX/RX	[72], [73], [88]–[90]
	Using dual antennas for TX/RX	[64], [91]–[94]

TX - Transmission, RX - Reception

Table 2.1: Summary of the bio-radar antennas state of the art [61].

Additionally, since the system herein developed uses electromagnetic waves to capture vital signs, there is a body exposure to electromagnetic fields within a proximal range. Therefore, the subjects safety must be accounted during the system configuration in terms of radiated power. Depending on the operation frequency and exposure time, the electromagnetic exposure can cause tissue heating, derived from the electromagnetic waves penetration in the body and causing the molecules vibration [95]. According to [95], the worrisome frequency range can be sub-divided in four ranges:

- 100 kHz – 20 MHz → significant absorption occurs in the neck and legs;
- 20 MHz – 300 MHz → high absorption in the whole body;
- 300 MHz – 10 GHz → non-uniform local absorption;
- Above 10 GHz → energy absorption occurs at the body surface.

Basic restrictions were suggested by responsible entities, such as the International Committee for Non-Ionizing Radiation Protocol (ICNIRP), which released in 1998 a set of exposure guidelines [95]. The limit values are expressed in terms of Specific Absorption Rate (SAR) measurement, which relates the absorbed power on biological tissues per unit of mass. Table 2.2 sums up the restrictions suggested by ICNIRP [95], divided by body regions and target population.

Target Population	Whole body	Head and Trunk	Limbs
Occupational	0.4	10	20
General public	0.08	2	4

Table 2.2: Basic localized SAR restrictions for frequencies within the range 10 MHz - 10 GHz [95] [W/kg] .

The *occupational* exposure is referred to the maintenance personnel of base stations for instance, which work nearby the center of the microwave beam where the power densities are extremely high. In these cases, workers are equipped with protective equipment, such as glasses, gloves and garments. Under these situations, higher SAR values are allowed, when compared to the ones permitted for the *general* population, which were set taking into account the different population age and health conditions. For general population, considering the head and trunk areas, the limit is 2 W/kg for any 10 g of tissue, the whole-body exposure limit is 0.08 W/kg and for the limbs is 4 W/kg. Measures are presented for a portion of tissue of 10 g, because it represents the amount of continuous tissue with approximate homogeneous electrical properties [95].

ICNIRP assumes that it is possible to have some difficulties in direct SAR measurements, since the human body does not have the same structure and there are some areas where this average mass cannot be applied, like the wrists [95]. Therefore it is difficult to relate the amount of power that leads to these SAR values. In [96] a study was conducted to verify if it is possible to perform wireless power transfer to inside the human body to efficiently feed implantable medical devices, while simultaneously respecting the SAR limits suggested by ICNIRP [95]. SAR simulations were performed in CST Microwave Studio 2017 to verify the amount of power that leads to the recommended limits. In order to be able to further reproduce those measurements in practice, the limbs were the inspected body part and a simplified skin-to-skin biological model was build containing the following layers: skin - fat - muscle - bone - muscle - fat - skin. Simulations were conducted at 970 MHz with the antenna located in contact with the skin and one could conclude that the recommended SAR limits are achieved with an input power equal to $\approx$ 140 mW which is equivalent to $\approx$ 21.5 dBm [96].

Considering all the bio-radar system components and the possible variations aforementioned, an appropriate selection must be conducted considering the main goal of this PhD. Therefore, the trade-offs related with hardware components, namely the radar operation mode

and the antenna design are evaluated the next sections. Thereafter, a hardware characterization was also performed with the goal to properly configure the front-end and further adapt Digital Signal Processing (DSP) algorithms if necessary, turning them robust to hardware impairments. Moreover, since the targets of interest are subjects, appropriate protocols should be defined and followed to assure the privacy, appropriate ethical conduct and safety.

2.2 Radar operation mode selection

In the literature, there is no agreement on which is the best radar operation mode for vital signs acquisition, since all possibilities present advantages and disadvantages. In [20] a survey is presented regarding these different radar systems and the trade-offs are discussed. For example, in [20] it is stated that the radar resolution of CW radars is only restricted to noise, while detection resolution in FMCW and UWB radars depends on the used frequency bandwidth, which can be an advantage to CW radars. Furthermore, in [97] it is mentioned that the estimation of vital signs using phase measurements can provide high precision results and this is possible with CW and FMCW.

On the other hand, the gathered references in [20] showed that the maximum detectable range for CW radars is limited to a few meters, and UWB radars stands out in being the one that achieves the maximum range. Both UWB and FMCW radars are able to measure the target distance, through the received pulse delay and receive frequency tone, respectively. Since they transmit instantaneous bandwidth, they are able to have range isolation between the target and the clutter [97]. This feature enable FMCW and UWB radars to identify the target in noisy environments, which is not possible for CW radars. The poor isolation of the desired target reflections in CW radars can hamper the ability to detect small motions (as the cardiac signal) in noisy scenarios.

Regarding the hardware complexity, authors in [20] state that UWB radars are simple to implement since they do not require frequency conversions leading to lower power consumption, as it is required in CW and FMCW radars. Besides, CW radars are subjected to CDC offsets and In-phase and Quadrature (IQ) imbalance, which can complicate the final architectures [97]. Nonetheless, there are digitally-based techniques to compensate CDC offsets and IQ imbalance, as we will see further. On the other hand, CW radars can be less complex to implement considering the bandwidth perspective. Narrow bandwidth operation eases the hardware components design (such as the antennas) and assures a coherent operation in terms of performance. The same is difficult to guarantee when large bandwidths are required, since the behaviour of the components can vary with frequency. In [98], a comparison is made between CW radar and pulsed-radar. The authors highlighted the simplicity of CW radar implementation, since it requires a single oscillator for both transmission and reception and the narrow bandwidth avoid interferences, as well as ease the other hardware components requirements.

Safety and regulatory issues were also reviewed in [20], where the authors have concluded that UWB and FMCW performances can be compromised due to the emission masks compliance according to regulatory entities. This is not a problem for CW radars, since they use narrower bandwidth generally within the Industrial, Scientific and Medical (ISM) band.

All in all, the transceiver operation mode can also depend on the target application for the bio-radar. For example, applications that aim to distinguish between different individuals, i.e., where there are multiple subjects to monitor, should use FMCW technology, since the

usage of chirps can help to indicate the subject location. The same can be performed with a simpler CW radar, with a different hardware implementation based in beamforming [30], [42]. Furthermore, rescue applications imply that electromagnetic waves cross obstacles. UWB as well as FMCW front-ends are more indicated for through-wall detection [99]. Finally, if the goal is to monitor bedridden patients in controlled environments, CW is enough and the hardware and signal processing are less complex.

Having in mind the advantages and disadvantages of the aforementioned radar systems, this PhD is focused mostly in the CW radar for the following reasons:

- Simple hardware and easy to find in the market. There are opensource toolkits available with good technical support, such as the SDR which confer more flexibility to the system [45];
- Easy antenna design due to the narrowband requirement;
- High resolution results due to phase demodulation;
- The target applications under study do not require the chirp usage with wide bandwidth;
- Operation within the ISM band;
- It is possible to detect the target within the range without ambiguity.

Nonetheless, since CW radars do not transmit instantaneous bandwidth, it is highly susceptible to parasitic reflections. Therefore, solutions were explored in this work to overcome this issue, and they are discussed further in Chapter 3.

2.2.1 Signal model for a CW bio-radar

After defining the appropriate radar operation mode according to this PhD objectives, a mathematical model of the involved RF signals should be defined to anticipate how and where the scenario impairments might have impact.

The bio-radar signal model (supported by Figure 1.1) starts with a baseband signal generated digitally. The signal is a complex sinusoid[1] with angular frequency ω_0, and it is represented by equation (2.4):

$$s(n) = e^{j\omega_0 n}. \tag{2.4}$$

Signal $s(n)$ is then modulated with using an IQ modulation, with a carrier frequency ω_c, leading to the signal (2.5), which is transmitted towards to the target.

$$x(t) = \cos[(\omega_0 + \omega_c)t]. \tag{2.5}$$

A copy of the $x(t)$ signal is reflected by all targets located in the scenario, being either the subject under monitoring or other objects located nearby. For instance, the signal $x_1(t)$ depicted in Figure 1.1 is a transmitted signal copy arriving at an object located behind the subject. Hence, the received signal described by equation (2.6), encompasses not only the time variant signal $r_0(t)$ correspondent to the chest wall reflection, but also a parasitic component

[1] In this case a sinusoid is used to avoid the local oscillator leakage and the circuitry clutter present on the receiver side [2] (where ω_0 can be further seen as an intermediate frequency).

$r_1(t)$ which represents the sum of the total sources of clutter (more specifically, parasitic reflections occurring in static targets).

$$\begin{aligned} r(t) &= r_0(t) + r_1(t) \\ &= A_0 \cos[(\omega_0 + \omega_c)t + \varphi(t)] + A_1 \cos[(\omega_0 + \omega_c)t + \theta_1], \end{aligned} \tag{2.6}$$

where A_0 and A_1 are the amplitudes of the received components from the subject and clutter, respectively, $\varphi(t)$ is the phase change function containing the respiratory information and θ_1 is the phase change due to clutter. This phase change term can be expressed as $\theta_1 = 4\pi d_1/\lambda$, considering that the clutter source is located at a distance d_1 from the radar and λ is the wavelength. After its reception, signal $r(t)$ is IQ demodulated resulting in (2.7), and it is sampled at the same sampling rate f_s used in the transmission channel.

$$g(n) = g_0(n) + g_1 = A_0 e^{j\varphi(n)} + A_1 e^{j\theta_1} \tag{2.7}$$

The phase change function $\varphi(n)$, results from the chest wall motion, which changes the wave traveled distance and hence modulates the reflected signal. Thus, the phase change function can be described by (2.8):

$$\varphi(n) = \theta_0 + \frac{4\pi v_s(n)}{\lambda}, \tag{2.8}$$

where θ_0 is the phase corresponding to the distance traveled by the wave, expressed as $\theta_0 = (4\pi d_o/\lambda) + \phi$, considering the nominal distance between the radar and the target d_o, and the phase shift at the target's surface ϕ. The respiratory component is described by $4\pi v_s(n)/\lambda$. In [100], [101], simulations showed that the respiratory signal should not be modeled as a simple sinusoid function, so its model should be defined as a half-cycle sinusoid raised to the p_{th} power, as in (2.9)

$$v_s(n) = a_r(1 - \sin^p(\pi f_R n)), \tag{2.9}$$

where a_r is the amplitude of the chest movement and f_R is the breathing rate.

Figure 2.3a depicts the signal $g_0(n)$ in the complex plane, where the phase variation induced by $\varphi(n)$ generates an arc. The variables of the baseband signal $g(n)$ (equation (2.7)) have a different impact on the arc format and position in the complex plane. In an ideal scenario (without the clutter component $g_1(n)$), the arc fits to a perfect circle centered on the origin. The length of the arc is proportional to the amplitude of the respiratory signal a_r, depending on the wavelength of the carrier. Higher carriers lead to higher sensitivity to detect weak motions due to the decreased wavelength, which means that regarding the same motion amplitude a_r, shorter wavelengths create wider arcs rather than longer wavelengths. The radius of the arc is the received signal amplitude A_0. The arc position in the circle varies with the distance between the radar and the target, defined as d_0. In [2] a mathematical simulation of the signal $g(n)$ parameters was performed, in order to understand the aforementioned effects.

In real-world scenarios there are some effects that change the obtained arc and could influence in the accuracy of the signals rate extraction. For instance, the clutter component $g_1(n)$ is perceived as a CDC offset addition to the IQ components, leading to a deviation of the arc center from the complex origin, as depicted in Figure 2.3b.

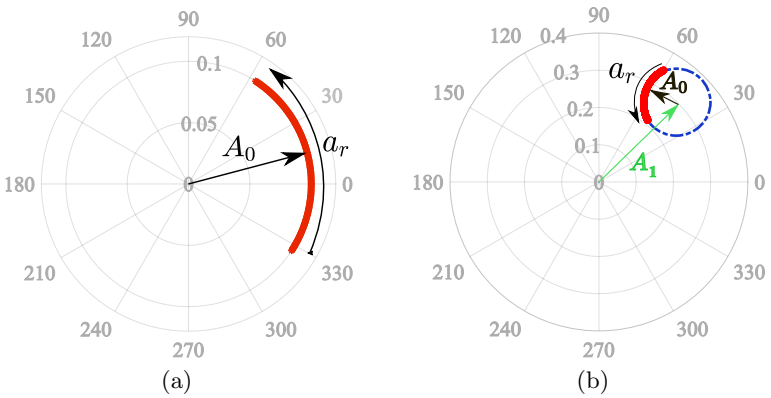

Figure 2.3: Resulting baseband signal in the complex plane using a CW bio-radar [102]: (a) for an ideal scenario, (b) for a scenario with parasitic reflections.

Furthermore, there are hardware impairments which can contribute to increase the CDC offsets value, namely the weak isolation between the transmission and reception chains. Besides, hardware imperfections can also cause an IQ imbalance effect, which occurs when both real and imaginary parts do not have the same amplitude and the phase relationship is not exactly 90° [103]. Hence, the formed arc fits an ellipse instead of a circle.

All these issues hamper the proper phase demodulation and hence compromises the effectiveness in the signals extraction. Therefore, DSP algorithms must be developed to compensate these effects.

2.3 Antenna design

Considering the antenna state of the art summed up in Table 2.1 and the state of the art review presented in [61], the important key features that should be taken into account on the antenna design for bio-radars can be divided in two perspectives: signal quality improvement and system manufacturing streamline. The schematics depicted in Figure 2.4 and Figure 2.5 present an overview of the guideline features that should be considered on each perspective and all the trade-offs are discussed in the following sub-sections.

2.3.1 Key features for antenna design considering the signal quality improvement

The signal quality is directly related with the antenna performance, which can be evaluated through the parameters presented Figure 2.4 [61]. For this case, the most important features are directivity, polarization and isolation. The appropriate directivity would require narrow HPBW and high gain antennas [104]. In [16], the importance of directivity was demonstrated by comparing the performance of different antennas with narrow and wide beams, respectively. Authors concluded that highly directive antennas could provide more accurate results in the signal rate estimation, more self-isolation between the transmitting and receiving antennas (if located at least a wavelength apart) and an increased Signal-to-Interference plus Noise Ratio (SINR). In [18], the authors have studied the relation between the carrier frequency and the antennas beamwidth, and their impact in the vital signs spectral magnitudes. The authors

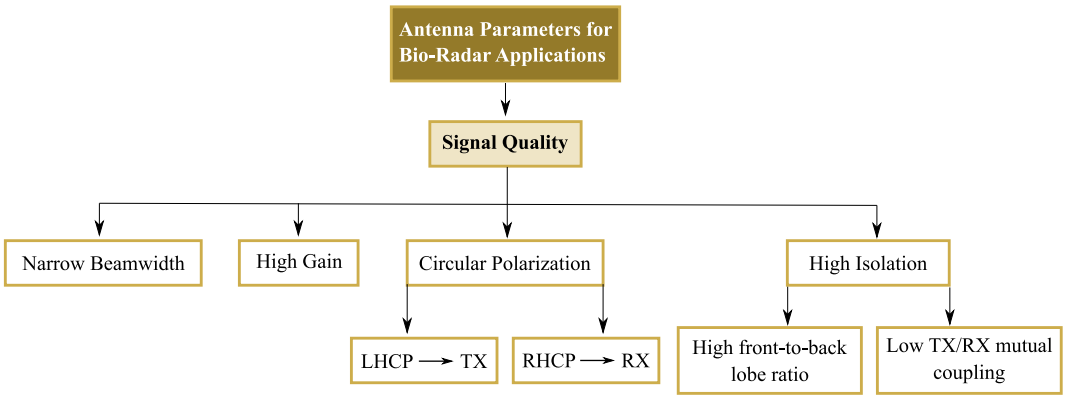

Figure 2.4: Antenna parameters to improve the acquired signal quality, where TX and RX correspond to the transmitting and receiving antennas respectively (adapted from [61]).

simulated a received baseband signal, considering that the amplitude of the chest wall motion related with respiration was equal to 1.2 mm and the amplitude of the heartbeat perceived at the chest wall surface was 0.15 mm. After analyzing the spectrum of the simulated signals, the authors concluded that the cardiac signal magnitude is higher if narrow beamwidths are used. Furthermore, the relation between the cardiac and the respiratory signal magnitudes varies with the frequency if a large beamwidth is used [18]. This evaluation was performed within the frequency range of 0 - 25 GHz. On the other hand, the relation between both signals keeps a stable behavior over frequency if narrow beamwidths are being used.

Helical antennas were proposed in [16], [62], [63] as an antenna type to provide directivity, with $\approx 40^\circ - 50^\circ$ of HPBW and high gain ($\approx 9 - 10$ dBi). However, helical antennas are bulky, therefore patch antenna arrays can be a more low-profile option. Nonetheless, even patch antenna arrays require larger dimensions to confer directive beams. Thus, a trade-off must be defined between the antennas dimension and how narrow the beams should be. Antennas with larger sizes have a larger near-field region [104], where the electromagnetic propagation cannot be modeled linearly. In these cases, there is a wide range where the antenna behavior cannot be foreseen. In parallel, the main lobe beamwidth should not be too narrow, since it hampers the alignment with the subject's chest wall. These also difficult the generalization of the system operation to be suitable for different subjects. If too narrow beams are used, prior calibrations would be required for different subjects, according to their body structures and heights, as one will see further in Chapter 4.

Hereinafter, the gain range for bio-radar applications was proposed in [64], where the authors state that a gain under 5 dBi is not enough, and the typical gain value for antennas applied in non-contact vital signs acquisition is around 9 dBi.

Concerning now with antenna isolation, the mutual coupling effect occurs when one antenna receives part of the energy radiated from a second antenna located nearby. This can happen due to three reasons: the radiation pattern of each antenna is not narrow enough, the separation between both antennas is not enough, and the main lobe orientation of both antennas might be deviated [104]. Mutual coupling can alter the radiation pattern of each radiating element, by for instance shifting the maximum and nulls location or filling the nulls when it was not supposed to [104]. In order to avoid this issue, transmitting and receiving antennas should be separated at least half-wavelength, but the distance between antennas

should be enough to guarantee the monostatic [2] radar function.

The usage of circular polarization can be an alternate solution for this issue. According to [72], if antennas with linear polarization are used, the reflected signal during propagation can rotate θ degrees in total, hence the signal at the receiver input has its power decreased by a factor of $\cos\theta$, and the radar sensitivity is largely reduced. Thus, antennas with circular polarization are generally a good alternative, since they are not affected by polarization mismatch. Furthermore, if the system uses transmitting and receiving antennas with different rotation directions (for instance with Left-Handed Circularly Polarized (LHCP) for transmission and Right-Handed Circularly Polarized (RHCP) for reception), there is no power reduction due to the signal rotation when reflecting at the target's surface, and there is no mutual interference because at the front-end side antennas have crossed polarization [66]. Thus, a system using antennas with circular polarization has low mutual coupling [72], [73].

Additionally, in [74] the authors have pointed out other emerging problems due to the usage of antennas with linear polarization. There is fading Radar Cross Section (RCS) due to the scattering reflection on the target. The human body is composed of different materials, shapes, sizes, and thicknesses. Hence, different surfaces cause electric vector rotation, which lead to a misalignment with the receiver antenna [74]. Moreover, the target at hand is moving and consequently, a time-varying RCS arises [105]. Antennas with circular polarization stabilize the RCS over time and keep the alignment between scatter signals and the receiver [74]. In this sense, it is possible to conclude that circular polarization is the best strategy, as proven in [17], [63], [66], [72], [73], [75], where several experiments were conducted to compare the system performance using antennas with circular polarization and linear polarization.

2.3.2 Key features for antenna design considering the system manufacturing streamline

The characteristics presented in Figure 2.5, are more focused in the physical features of the antenna and its robustness during operation.

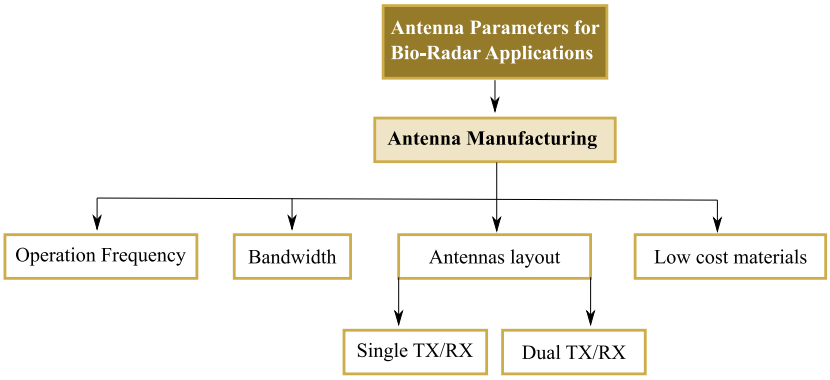

Figure 2.5: Antenna parameters to consider for manufacturing purposes, where TX and RX correspond to the transmitting and receiving antennas respectively (adapted from [61]).

Starting with the carrier frequency, there are some studies that aim to determine the optimal frequency band for bio-radar applications which is a non-consensual topic. In [18], a mathematical model and its simulation are presented to seek for the best operating frequency

[2] Monostatic radars have the transmitter and receiver in the same location [48]

that allows both respiratory and cardiac signals detection. Authors have concluded that the signal strength increases when using frequencies above 5 GHz, and it stabilizes until the lower region of the K-band (18 GHz - 27 GHz). Above 20 GHz, the signal strength decreases slightly. Authors in [18], state as well that nonlinear phase modulation causes harmonic intermodulation, which is more evident for frequencies above 27 GHz than for frequencies around 5 GHz. In addition, a system evaluation was made in [19], with the goal to compare the performance of a system operating at 2.4 GHz (from [90]), with a 10 GHz system (from [70]). For this purpose, the vital signs of a subject were acquired at different distances, starting with 0.3 m until 2.9 m away from the radar, using both systems. The authors have concluded that, despite the advantages of using higher frequencies related with the sensitivity, the system had not shown significant improvement when compared to the 2.4 GHz bio-radar system.

All in all, higher frequencies might detect easily imperceptible motions, as the cardiac signal, however they suffer from high attenuation and they are also more sensitive to higher amplitude motions, as the RBM, which influence could be harder to compensate. On the other hand, sub-GHz antennas allow the electromagnetic waves penetration in the human body, which enables an alternative way to measure vital signs, as it was performed in [59], [71], [106]. Besides, low-profile systems can be accomplished by hiding the radar inside specific objects. Low frequency carriers allow this integration, also due to the electromagnetic waves penetration in dielectric materials. Finally, higher frequencies allow on-chip integration, reducing considerably the system size [66]–[68]. However, the antenna design for high frequencies is more challenging and it results in a much more complex process when compared with the antenna design for lower frequencies.

The bandwidth is an important feature for FMCW and UWB radars, but it is challenging to guarantee the desired antenna performance for a wideband frequency range. The bandwidth is not critical in the framework of this PhD, since CW radar is going to be used. Even though, it is preferable to reserve significant bandwidth (around 100 MHz considering a central frequency of 5.8 GHz), to provide a safe margin for construction errors.

The system size is also a concern, to enable its portability and to facilitate its usage and integration in specific applications. Using a single antenna for both transmission and reception operations could be an immediate solution, as proposed by [72], [73], [88]–[90]. However, proper isolation must be assured, using circulators for instance. Besides, using two antennas enables an increased detection range, as proved in [91], where a test was conducted to compare the system performance using a single antenna and two separate antennas for transmission and reception. The results obtained in [91] showed that a single antenna has good accuracy in vital signs' detection, considering a short-range distance. However, two separated antennas could cover a wider range with the same level of signal quality [91].

Opting by two separate antennas, the usage of different material technology and the development of integrated chips are possible solutions to decrease the system's size, as proposed in [64], [92]–[94].

2.4 Final prototype definition and characterization

Considering the trade-offs presented in Section 2.2 and in Section 2.3 and the objectives defined for this PhD, one continued to use the radar setup firstly proposed in [2], which is composed by a CW radar operating at 5.8 GHz. The advantages of using CW radars in

the scope of this work were already mentioned in the end of Section 2.2. In regard to the carrier frequency, 5.8 GHz represents a good trade-off between sensitivity, detectable range, and simplicity for the antenna design. Besides, this frequency is covered by the RF front-end board [45] and it enables to hide the antennas in specific objects, which reveled being useful during the first case study dedicated to the system integration in a car seat upholstery.

The RF front-end consisted on the USRP B210 board from Ettus Research^{TM} [45]. SDRs are a hardware approach suitable for system integration studies, since they are compact and allow the digital configuration of their input and output (receiver and transmitter), regarding the required carrier frequency and sampling rate of the target application [11]. Furthermore, the USRP B210 board is based on homodyne receivers, which are capable to use the same source in both transmitter and receiver, guaranteeing the range correlation and avoiding issues as the phase noise [107].

Considering the setup base defined in [2], different prototype variations were developed throughout the different stages of this PhD. These variations were mostly related with the antennas design, as shown in Figure 2.6.

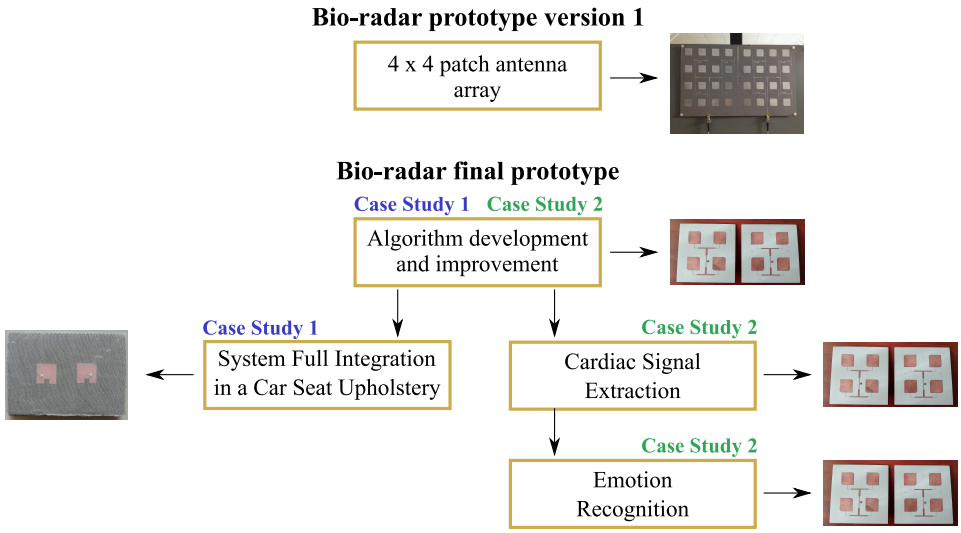

Figure 2.6: Antenna final design selection throughout the different work stages of the PhD.

At the beginning of the PhD, some preliminary studies mostly performed for proof-of-concept purposes (on each case study), used the prototype described in [2], where the transmitting and receiving antennas were 4×4 antenna arrays [46]. Then, the prototype was improved aiming to resolve existent issues, such as antenna mismatch [2] and the increased size of the antenna array. In this sense, 2×2 antenna arrays with crossed circular polarization were developed, since they respect a good trade-off between the antenna size and directivity. This antenna design and the corresponding measured parameters are presented in the next subsection. These antennas were used in the final prototype (in both case studies) for the DSP algorithms development. The 2×2 antenna arrays were further used in the second case study, more specifically to capture signals for the cardiac signal extraction and for the final stage of the emotion recognition.

Since the first case study was dedicated to explore the ability to fully integrate the bio-radar system in the car seat upholstery, textile single patch antennas were developed to confer a low profile to the system. The textile antenna design selection and development are

presented and discussed later in Chapter 4.

Finally, the signals received by the first version of the prototype [2] were acquired with the LabVIEW software and the prototype improved versions used the GNU Radio software for the same purpose. In all cases, signals were acquired using a sampling frequency of 100 kHz. Then, DSP algorithms were developed to process and extract vital signs, and they were all applied offline using MATLAB. The DSP algorithms are explained in detail in Chapter 3.

2.4.1 Final antenna design

Aiming to respect the trade-offs presented in Section 2.3, 2×2 antenna arrays were designed to be further used in the final prototype. These antennas have circular polarization with crossed orientations, so a LHCP antenna was developed to be used as the transmitting one and a RHCP antenna was developed to be used for the reception. The circular polarization was achieved with a squared patch design with truncated corners. LHCP and RHCP antenna arrays were simulated and optimized in CST Microwave Studio 2017, and the final designs are shown in Figure 2.7.

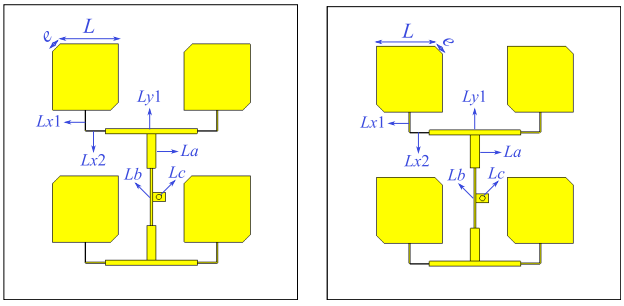

(a) (b)

Figure 2.7: Antenna arrays design: (a) LHCP antenna used for transmission, (b) RHCP antenna used for reception.

Starting with the LHCP antenna case, the array design started with the optimization of a single element by varying L and e parameters, with a view to achieve the antenna matching at 5.8 GHz and simultaneously an axial ratio below 3 dB at the same frequency [108]. The feeding network was developed afterwards, considering the input impedance of the single element, the manufacturing constraints due to the lines width and the number of quarter-wavelength transformers used. This latter aspect should be the minimum as possible, since the quarter-wavelength transformers are highly restrictive in bandwidth [104]. Thus, $Lx1$, $Lx2$, $Ly1$ and La are quarter-wavelength transformers, Lb is a 100 Ω line and Lc is a 50 Ω line, used for the feeding point. At the end, the full array was optimized, where the patch centers were $3\lambda/4$ apart from each other. This distance was the result of a balanced trade-off between optimal antenna parameters, such as gain, HPBW and Side-Lobe Level (SLL), and the overall antenna dimensions. The SubMiniature version A (SMA) connector model was also included in the final stage of the full array simulation. The RHCP antenna used the same feeding network strategy, so only few adjustments were required.

Table 2.3 shows the antennas dimensions, where l and w are the length and width of the feeding network lines, respectively. Both LHCP and RHCP arrays have a final size of 70×70 mm.

Antenna	L	e	Lx1		Lx2		Ly1		La		Lb		Lc	
			l	w	l	w	l	w	l	w	l	w	l	w
LHCP	13.76	2.5	4.74	0.26	4.57	0.26	21.6	1.19	8.10	2.13	13.61	0.57	3	2.10
RHCP	13.76	2.5	4.74	0.26	4.57	0.26	21.6	1.10	7.90	2.18	14.01	0.57	3	2.10

Table 2.3: LHCP and RHCP elements dimensions [mm].

Both antennas were manufactured using ROGERS RO4725JXR substrate, with height equal to $h = 0.78$ mm, $\varepsilon_r = 2.55$ and $\tan\delta = 0.0026$ @ 10 GHz (see the final antennas in Figure 2.8). Then, the antenna parameters were measured. The S_{11} parameter of both antennas is shown in Figure 2.9. The LHCP antenna presented a measured S_{11} of -16.1 dB at 5.8 GHz, while the measured one for the RHCP was equal to -13.8 dB. The radiation pattern was also measured and the result is shown in Figure 2.10.

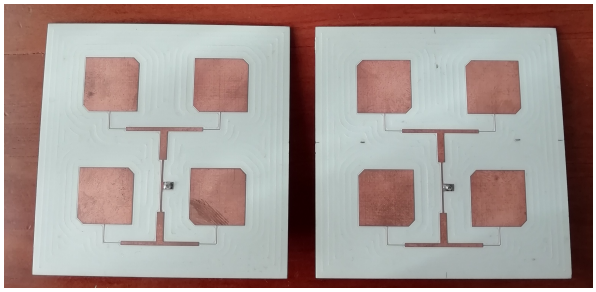

Figure 2.8: Final RHCP and LHCP antenna arrays to use for transmission and reception respectively.

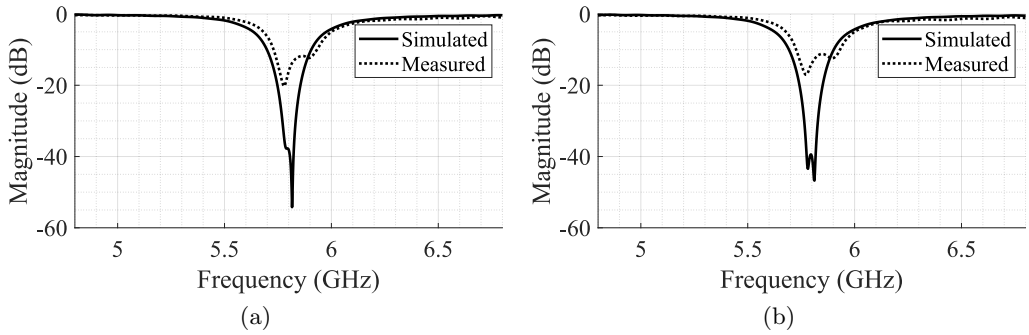

Figure 2.9: Simulated and measured S_{11} for antenna arrays: (a) LHCP antenna, (b) RHCP antenna.

Both antennas present a measured radiation pattern similar to the simulated one. The simulated HPBW of the LHCP antenna was equal to 41.4°, while the measured one was equal to 42°. The LHCP antenna presented also a measured SLL equal to -19.6 dB while the simulated was equal to -19.8 dB. Similarly, the RHCP antenna presented a measured HPBW equal to 41° and the simulated was equal to 40.8°. In regard to the SLL, the simulated one was equal to -19.4 dB and the measured was -17.1 dB. The simulated gain for both antennas

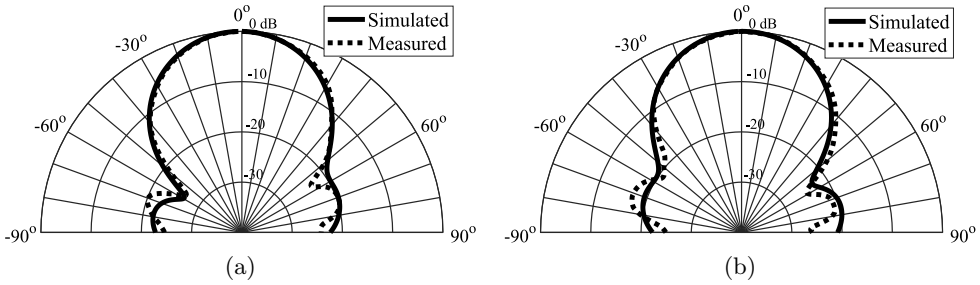

Figure 2.10: Simulated and measured normalized radiation pattern for antenna arrays: (a) LHCP antenna, (b) RHCP antenna.

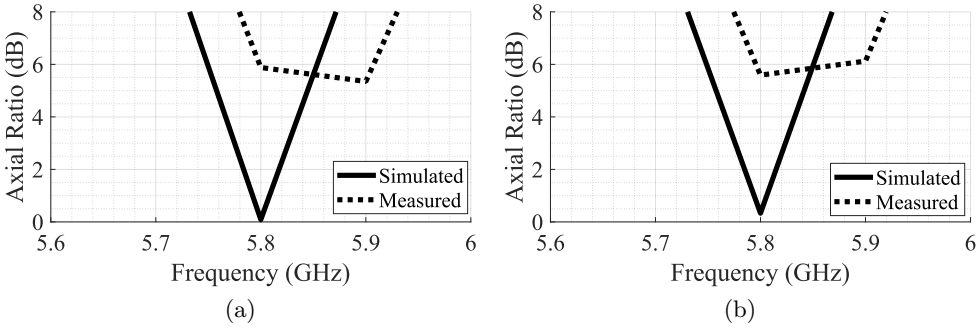

Figure 2.11: Simulated and measured axial ratio for antenna arrays: (a) LHCP antenna, (b) RHCP antenna.

---

was equal to 12.2 dBi, and the measured ones were equal to 11.9 dBi and 11.7 dBi for the LHCP and RHCP, respectively.

Finally, the axial ratio of both antennas was measured and the result is shown in Figure 2.11. The measured axial ratio at 5.8 GHz was equal to 5.9 dB for the LHCP antenna and 5.6 dB for the RHCP one, while the simulated values were equal to 0.09 dB and 0.35 dB, respectively. Overall, the slight deviations observed in the results might be related with eventual deviations due to the manufacturing process, specially due to the $Lx1 - Lx2$ quarter-wavelength transform, since they required a thin line with 0.26 mm width. The impact was more evident in the axial ratio results, being both above 3 dB, leading one to conclude that both antennas present an elliptical polarization, rather than circular [108]. According to the conclusions reached in [17], [63], [66], [72]–[75] regarding the bio-radar performance with linearly polarized antennas, one can assume that the obtained elliptical polarization is sufficient for our case.

2.4.2 RF front-end power characterization

The received signal SNR is directly related with the transmitted and received power. But once again, a balanced trade-off must be defined in order to simultaneously guarantee the signals quality, while the subject under monitoring safety is not jeopardized. Thus, hardware characterization tests were performed to select the adequate transmitted and receiver gains for the USRP B210.

Figure 2.12 shows the setup block diagram for these tests.

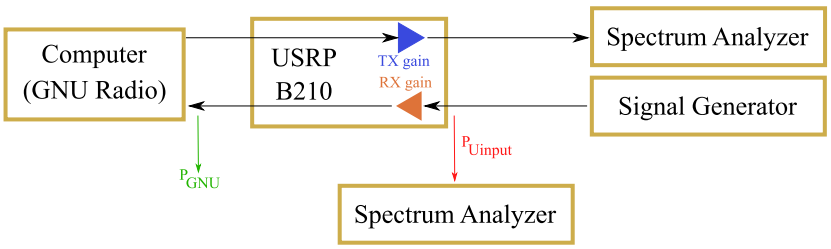

Figure 2.12: Block diagram of the setup used to characterize the transmitted and received power considering the USRP B210 gain variation.

Starting with the transmission chain characterization, the power at the antennas input was measured for different transmitting gains. For this purpose, a sinusoidal signal with frequency equal to 10 kHz was generated and transmitted at 5.8 GHz using the GNU Radio Companion software. The transmitter output was connected to the Rohde & Schwarz FSH13 spectrum analyzer, using a SMA to SMA coaxial cable from Crystek Corporation with 2.54 mm of thickness, stretched to prevent additional bending attenuation. Since this is the cable used in the final setup and one intend to measure the power on the transmitting antenna input, the cable attenuation was not compensated and the stretched position is considered for being the more optimistic one. Table 2.4 and Figure 2.13 show the results of the input power measured in the spectrum analyzer.

One can see that for a transmission gain equal to 90 dB, the USRP achieves its maximum transmitting power, being $\approx$ 10 dBm [45]. The 2 dBm was the selected power (provided by a transmission gain equal to 80 dB), not only to avoid hardware impairments that might occur while operating within the USRP limits, but also to ensure the subjects' safety.

Considering the experiment conducted in [96] as a reference, 2 dBm is far below the power value necessary to reach SAR limits. Furthermore, the amount of power that arrives the subject's body is below 2 dBm considering the antenna efficiency, propagation loss and the distance to the target. Finally, 2 dBm is even below other radiated power sources that we use in order daily lives, such as our cellular phones, Bluetooth transmitters or Wi-Fi routers, which generally use transmitted power between 10 dBm and 30 dBm, settled by to the Federal Communications Commission [109].

In turn, the received signal is severely attenuated not only due to the two-way path

TX gain [dB]	Transmitted Power [dBm]
50	-28.2
60	-18.2
70	-8.2
80	2.0
90	10.1
100	10.1

Table 2.4: Measured transmitted power for different transmission gains.

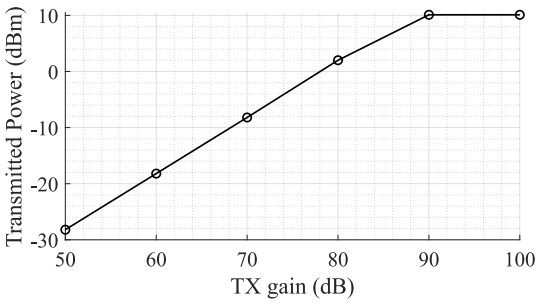

Figure 2.13: Graph of the transmitted power variation with different transmission gains

RX gain [dB]	P_{GNU} [dBm]
0	-18.5
5	-17.8
10	-13
15	-7.9
20	-2.9
25	2.1
30	7.5
35	12
40	16.8
45	21.8
50	26.7

Table 2.5: Measured received power for different reception gains.

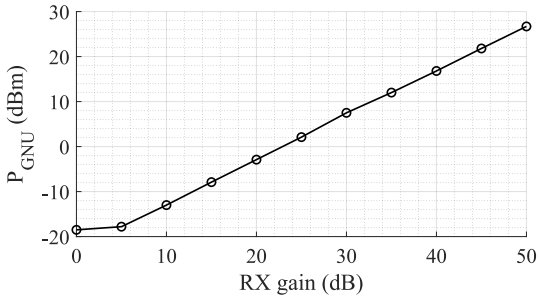

Figure 2.14: Graph of the received power variation with different reception gains

propagation loss, but also due to some signal absorption occurring in the subject's body [95]. Thus, the receiver gain should be adjusted to concurrently aid the signal quality and avoid the device receiver saturation. For this reason, the receiver chain was also characterized.

The power at the USRP input was firstly measured and a lookup table was then created with the receiver gains and the corresponding power measurements. Here, the coaxial cable used was the same that had been utilized for the transmission chain characterization. Then a signal was generated using the Signal Generator SMR40 from Rhode&Schwarz, with a carrier frequency equal to 5.8 GHz and with an output power of -26.4 dBm. The USRP input power (P_{Uinput} in Figure 2.12) was confirmed with the Spectrum Analyzer, being -30 dBm (accounting with the cable attenuation). Table 2.5 and Figure 2.14 were afterwards created by computing the received signal power (through equation (2.10)) in the GNU Radio Companion (P_{GNU} in Figure 2.12) for different reception gains.

$$P_{GNU}[dBm] = 10\log_{10}\left(\frac{\frac{1}{N}\sum_{n=1}^{N}|x(n)|^2}{1\times 10^{-3}}\right) \tag{2.10}$$

where, $x(n)$ is the baseband complex signal and N denotes the signal length. During the experiment it was observed a signal saturation for the 50 dB gain value. Therefore, a reception gain equal to 20 dB was the selected to configure the USRP reception gain.

2.4.3 IQ imbalance measurement

As one will see further in Chapter 3, in the work presented in [2] which served as basis to this PhD work, a DSP algorithm is proposed to extract vital signs. Beside the CDC offsets compensation, the developed algorithm takes also into consideration a hardware impairment, namely the IQ imbalance. The IQ imbalance behavior is divided in phase imbalance that occurs when signal in-phase and quadrature components are not exactly 90° out of phase, and in gain imbalance which occurs when these signals do not have the same amplitude [103]. This issue has impact in the phase demodulation by creating an undesired linear transformation on the IQ signals, affecting the orthonormal properties important in quadrature systems.

Thus, the baseband signal include both phase ψ_E and amplitude A_E error terms, where ψ_E is the angular difference between the phases of the IQ signals minus 90°, and A_E is the ratio between the amplitudes from IQ signals. Under these circumstances, the baseband signal (2.7) should be defined as (2.11):

$$\begin{aligned} g_I(n) &= A_r \cos\left(\theta_0 + \frac{4\pi v_s(n)}{\lambda}\right) \\ g_Q(n) &= A_r A_E \sin\left(\theta_0 + \frac{4\pi v_s(n)}{\lambda} + \psi_E\right) \end{aligned} \tag{2.11}$$

Consequently, the extracted phase will have a phase error, that can be expressed as the equation (2.12):

$$\varphi_E(n) = \arctan\left(\frac{A_E \sin(\zeta(n) + \psi_E)}{\cos(\zeta(n))}\right) \tag{2.12}$$

where $\zeta(n) = \theta_0 + \frac{4\pi v_s(n)}{\lambda}$ for a simpler notation [98].

In [2], the ψ_E and A_E parameters were measured being $\psi_E = 18°$ and $A_E = 1.0788$, and they were then compensated using the the Gram-Schmidt orthonormalization method, expressed as equation (2.13) [103]:

$$\begin{bmatrix} g_{I,O}(n) \\ g_{Q,O}(n) \end{bmatrix} = \begin{bmatrix} 1 & 0 \\ -\tan(\psi_E) & \frac{1}{A_E \cos(\psi_E)} \end{bmatrix} \begin{bmatrix} g_I(n) \\ g_Q(n) \end{bmatrix} \tag{2.13}$$

However, the procedure used in [2] to measure them is not highly robust. More specifically, a signal was transmitted towards a metallic target and ψ_E and A_E were computed over the received reflection, namely using the in-phase and quadrature components superimposed in time-domain. In this case, the signal is most likely affected by a two-path way attenuation and contains CDC offsets traces.

In this sense, an extended IQ imbalance characterization was performed to fully validate if they can be indeed neglected throughout this PhD work. The considered setup consisted in connecting directly the transmission port to the reception one, using a 10 dB attenuator for precaution, and a sinusoidal signal with frequency equal to 10 kHz was transmitted. The original received signal in the complex plane is shown in Figure 2.15. Once again, the superimposed in-phase and quadrature components were analyzed in time-domain (Figure 2.15b).

Throughout the signal, the ψ_E and A_E were computed between in-phase and quadrature consecutive peaks. For the amplitude error, values did not vary much more than the same order of magnitude, so it was considered the averaged value being $A_E = 1.0042$. As for the phase error, different values were observed throughout the signal, being 4.4554°, 0.8911°, −2.6733° and −6.2376°. Although all error values were below the ones measured in [2], they might encompass additional measurement errors. Figure 2.16 show the resultant signals if these phase errors would be compensated using the Gram-Schmidt orthonormalization method [103].

From the obtained results, one can conclude that the IQ imbalance in this front-end can be neglected, otherwise its compensation might even increase the phase error due to eventual inaccuracies on its measurement, as it can be observed in Figure 2.16d.

2.5 Datasets description

Throughout the PhD, several datasets were collected using different volunteers, not only to validate the setup performance during the different work stages, but also to develop robust

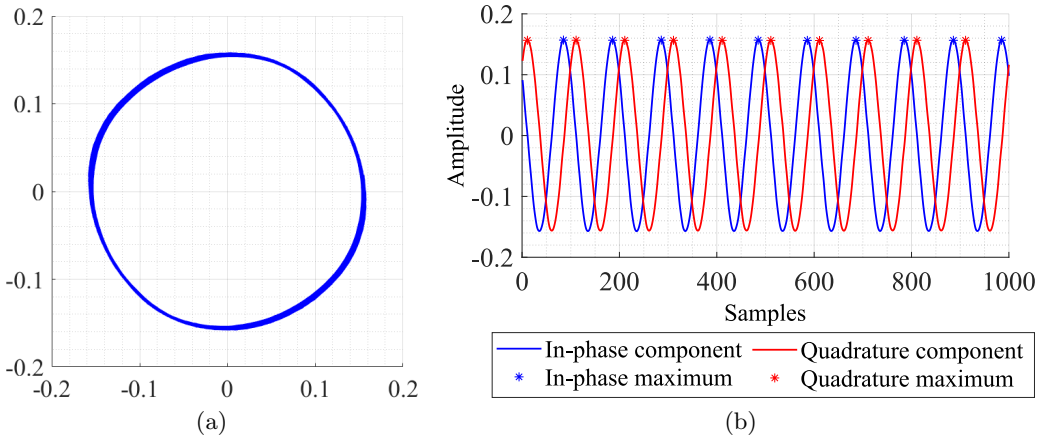

Figure 2.15: Received signal for IQ imbalance characterization: (a) in the complex plane, (b) superimposed in-phase and quadrature components in time-domain.

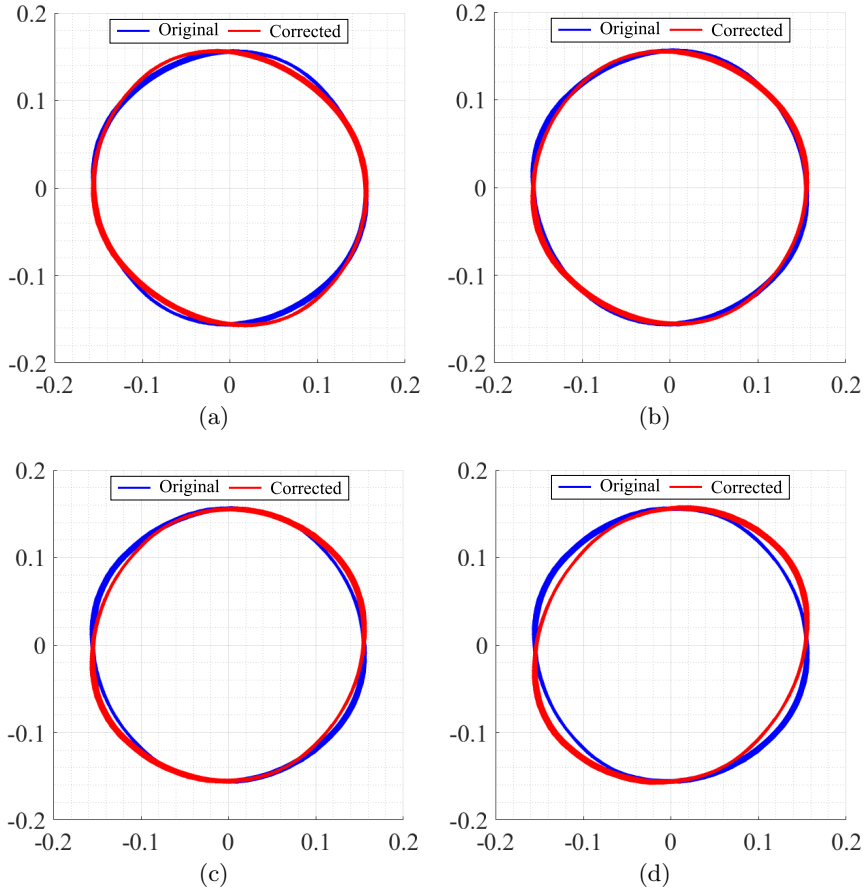

Figure 2.16: Signal after the IQ imbalance compensation using the Gram-Schmidt orthonormalization method, considering $A_E = 1.0042$ and : (a) $\psi_E = 4.4554°$, (b) $\psi_E = 0.8911°$, (c) $\psi_E = -2.6733°$, (d) $\psi_E = -6.2376°$.

algorithms embracing the different case studies. For this purpose, approval of all ethical, experimental procedures and conducted protocols was granted by the Ethics and Deontology Committee of University of Aveiro, Portugal, under the Application No. 29-CED/2021, and all the conducted procedures were performed in line with the Declaration of Helsinki. Additionally, an informed consent was obtained from all the subjects before initializing the experiments.

The datasets can be divided in two groups, where each group belongs to a specific case study. The reasons why these protocols were used will be opportunely exposed during the different chapters. The protocols followed for each case study were the following:

- Datasets group from **case study 1** - *Car Seat Protocol* - The subject was comfortably seated in a car seat and was asked to breathe normally during the full test. The subject's arms were placed on a table located in front of the car seat to simulate the driver's posture. In this case, the antennas were located in the car seat upholstery. Signals have a general duration of 1 minute maximum;

- Datasets group from **case study 2** - *Emotional Protocol* - The subject was seated and the vital signs were measured while he/she was watching a set of videos. The experiment was conducted in three different days, spaced by at least two days. Each session was composed by a baseline lasting 5 minutes and an emotion inducing period lasting between 25-30 minutes, using different thematic videos. The thematic videos were used to induce emotions. More specifically, happiness was induced via comedy videos, whereas fear was induced using scary videos and documentaries were used on the baseline and also to induce the neutral condition. The antennas were located in front of the subject at a distance of half a meter.

2.6 Final considerations

In this chapter, considerations regarding the bio-radar setup used during this PhD are presented. First of all, the prototype used in [2] served as a working basis and all system elements were re-evaluated to verify the suitability considering the PhD objectives, namely the radar operation mode, carrier frequency, the RF front-end and the antenna design.

In this sense, the final prototype consists on a CW radar operating at 5.8 GHz. The prototype uses an SDR as RF front-end, namely the USRP B210 board from Ettus Research^{TM}, with two coaxial cables from Crystek Corporation with 2.54 mm of thickness. Different antennas were used throughout the different work stages. More specifically, 2×2 antenna arrays were developed and they were used to capture vital signs to further develop DSP algorithms. These antennas were also used on the second case study. On the other hand, in the first case study it was necessary to develop a low profile solution. Therefore, textile antennas with different designs were studied, being the single patch antenna the selected option, as one will see further in Chapter 4.

The setup was characterized in terms of power and hardware impairments, in order to correctly configure the front-end and develop appropriate algorithms. Finally, the protocols followed during the datasets acquisition were briefly described.

Chapter 3

Vital Signs Extraction Algorithms

This chapter is focused on the development of algorithms to remove the influence of parasitic reflections in the received signals and extract the vital signs through phase demodulation. Furthermore, the accuracy to estimate the respiratory frequency was evaluated and validated, by comparing with a certified measuring equipment.

The developments of this chapter resulted in the following publications:

- C. Gouveia, P. Pinho, and J. Vieira, "Motion Detection Method for Clutter Rejection in the Bio-Radar Signal Processing", 20^{th} International Conference on Radar Science and Technology, Barcelona, Spain, pp. 518-526, 2018

- C. Gouveia, D. Albuquerque, J. Vieira, and P. Pinho, "Dynamic Digital Signal Processing Algorithm for Vital Signs Extraction in Continuous-Wave Radars", *Remote Sensing*, vol. 13, no. 20, pp. 4079, 2021

3.1 Introduction

The advantages of using CW radar front-ends were highlighted in Chapter 2. In sum, CW radars require a reduced bandwidth, are simple and enable the vital signs estimation through phase measurements, which provides high precision results [97]. However, the selection of this front-end comes with inherent challenges that should be overcomed, in order to extract the vital signs accurately.

As presented in Chapter 2, RF front-ends with quadrature receivers process the baseband signals as complex signals. Considering an ideal monitoring scenario without any parasitic reflections, vital signs are perceived as an arc in the complex plane, as previously depicted in Figure 2.3a. Since CW radars are not able to measure the distance between the subject and the radar [20], the reflection from the chest cannot be isolated. Therefore, the received signal is a vector addition, corresponding to the desired signal and other parasitic reflections that occur in stationary objects located within the monitoring scenario and even other body parts, as depicted in Figure 2.3b.

Parasitic reflections can be referred as CDC offsets due to two main reasons: they increase the spectral component magnitude of 0 Hz and they cause a misalignment of the phase signal (the arc) in relation to the complex plane origin, as depicted in Figure 2.3b, where A_1 corresponds to the parasitic component amplitude.

One can anticipate the influence of the CDC offsets in the extracted signal, if they are not compensated, through a mathematical simulation. The baseband signal represented by equation (2.7) was simulated in MATLAB with the following parameters:

- Carrier frequency - $f_c = 5.8$ GHz;
- Sampling frequency - $f_s = 1000$ Hz;
- Amplitude of the signal $g_0(n)$ - $A_0 = 0.003$;
- Initial phase shift - $\phi = \pi/12$ rad;
- Breathing frequency - $f_R = 0.3$ Hz;
- Distance to a static object - $d_1 = 1.2$ m;
- Amplitude of the clutter signal $g_1(n)$ - $A_1 = 0.5$.

The assigned values to A_0 and A_1, were selected considering the worse case scenario where the parasitic reflections come from metallic objects and hence producing a reflection with high amplitude. Figure 3.1 shows the arc obtained considering that the main target is located at two different distances: $d_0 = 0.79$ m and $d_0 = 0.775$ m. For each simulation the extracted signal was obtained through the arctangent computation [21]. Figure 3.1 demonstrates that if the arc center is shifted, depending on its position in relation to the origin, the arc can be wrongly projected in the axis, resulting in a signal distortion and/or an amplitude decrease.

Thus, the CDC offsets must be removed to guarantee a proper phase demodulation for vital signs extraction. Several solutions have been reported in literature being performed through either software or hardware approaches. On the hardware side, antennas with high directivity can be advantageous, since they enable a focused steering on the desired area, enhancing the SNR and reducing the parasitic reflections acquisition [16], [75], [92], [110]. Nonetheless, increase directivity implies implementation drawbacks and also might not be sufficient, as previously discussed in Section 2.3.

Thus, the CDC offsets compensation performed through signal processing could be more suitable due to its flexibility. The most direct solution would be the usage of a high-pass filter [107], [111]. Although it would be a straightforward approach, filtering reduces the amplitude of the vital signs [107], or could even cause distortion. Moreover, filters remove the CDC information related to the target's position, which is necessary for the phase demodulation [23]. Some authors suggested a prior calibration, by measuring the CDC offsets of the environment without the target present in the room [21]. This solution is not practical, since it requires a calibration every time the system is used, and is not effective if the monitoring scenario changes. Besides, other body parts can also be seen as static targets, and hence produce more parasitic reflections. Due to this fact, Park et al. [23] proposed a solution based on the arc center estimation and subsequent subtraction from the original signal. As result, the arc position is reestablished around the complex origin and the arctangent method [21] can be applied to recover the vital signs waveform. Currently, the arc center estimation approach is widely used in literature [23], [25], [101], [112], [113], where circle or ellipse fitting methods are the most common.

Despite the proved effectiveness of the Park et al. [23] method, it has a strong dependence with the arc shape. This means that the estimation of the arc center can be compromised when signals have a low amplitude [113], [114].

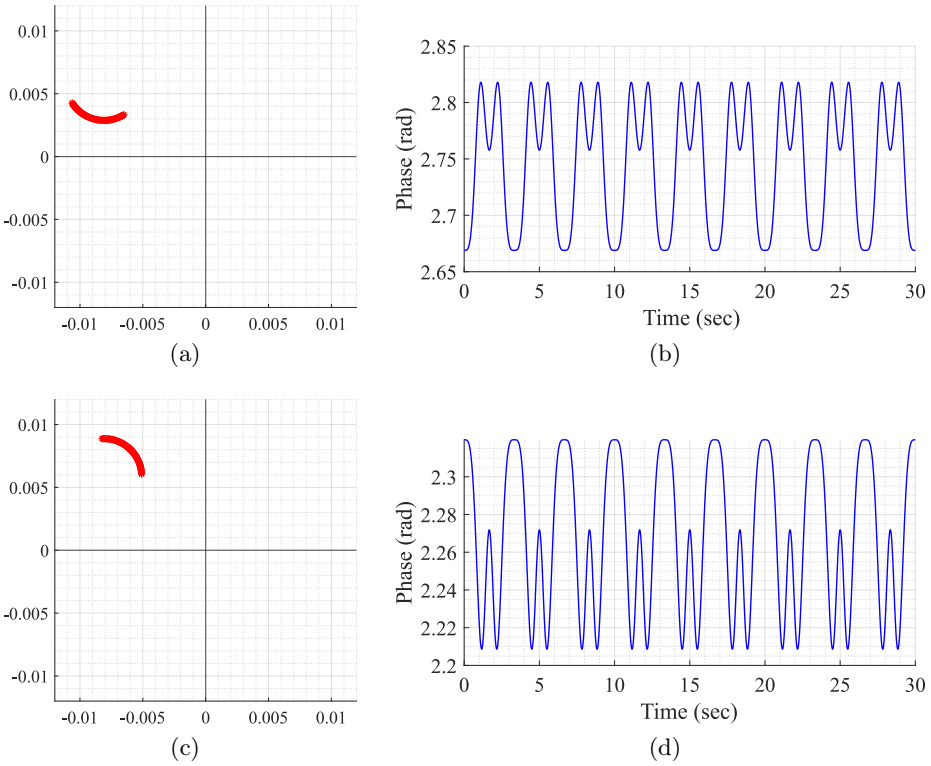

Figure 3.1: Simulation of the impact that CDC offsets can have in the extracted time domain signal for different d_0: (a) Polar diagram for $d_0 = 0.79$ m, (b) Extracted time domain signal for $d_0 = 0.79$ m, (c) Polar diagram for $d_0 = 0.775$ m, (d) Extracted time domain signal for $d_0 = 0.775$ m.

In fact, low amplitude signals could be recurring in real application scenarios, due to several reasons, namely:

1. Multipath signal degradation;
2. When the vital signs acquisition is performed in an alternate position like the chest wall sideways (as it will be presented further in Chapter 4);
3. When the subject's physical characteristics lead to a lower chest wall displacement.

The latter example, is supported by a study presented in [36], where the authors present a correlation between the anatomical differences relative to gender and the induced chest wall displacement. The authors in [36] have concluded that the men's lungs are bigger in absolute volume, which produces wider volume variations. Men's rib cage have a higher antero-posterior diameter and a larger cross-sectional area and volume. On the other hand, women have a smaller rib cage comparing with men, and hence a lower cross-sectional area. This could mean that men might produce high amplitude signals and women lower amplitude ones (hence leading to shorter arc lengths).

Figure 3.2 shows two examples of the possible signal arcs, acquired in a real context. More specifically, Figure 3.2a presents a well defined arc, corresponding to a received signal with high amplitude A_0 and Figure 3.2c presents a case where A_0 is severely decreased, as well

as its arc length a_r. This consists on a weak signal case, since it has either low amplitude and the overall signal consists on several arcs dispersed rather than being concentrated in a defined area. In order to demonstrate the impact of the signal quality in the circle fitting performance, Figure 3.2 shows also the CDC offsets estimation using circle fitting (with the Kasa method [115]) and subtraction results. In Figure 3.2a, the center estimation can be easily inferred and it can be seen as a pair of IQ coordinates (VI_{iq}, VQ_{iq}). On the other hand, in Figure 3.2c due to its lack of resolution, circle fitting algorithms consider that the overall samples cluster fit a circle, where its center is in between the radar samples, neglecting the supposed arc shape. Hence, the desired fitting is compromised and the center estimation is misleading. The case depicted in Figure 3.2c presents the result of a circle fitting with radius r close to 0, which in practice force the arc to oscillate in the complex origin after the CDC offsets removal (Figure 3.2d), leading later to incorrect arctangent results. Thus, for the CDC offsets removal, the radar samples fitting must be performed correctly, by leaving a standard space between the arc and its estimated center, i.e. the arc radius r must be $r >> 0$.

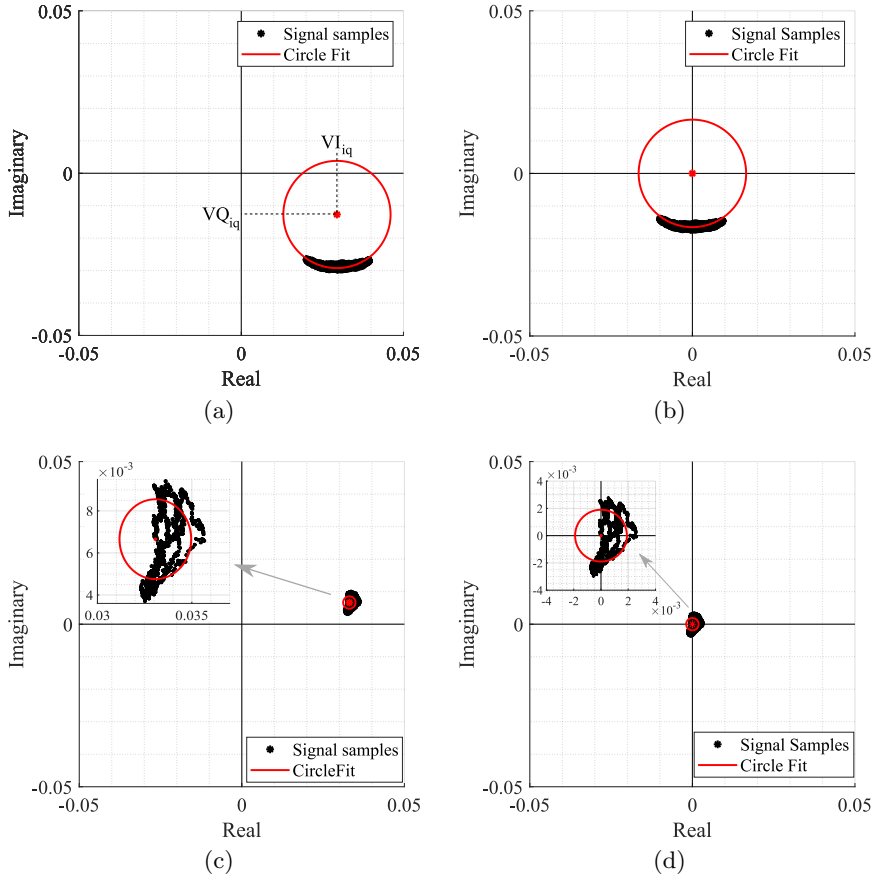

Figure 3.2: Example of how A_0 and a_r influence the fitting methods accuracy to estimate the arcs center (adapted from [102]): (a) Circle fitting result for **high** values of A_0 and a_r, (b) Arc disposition after removing the CDC offsets for **high** values of A_0 and a_r, (c) Circle fitting result for **low** values of A_0 and a_r, (d) Arc disposition after removing the CDC offsets for **low** values of A_0 and a_r.

In cases similar or worse to the one presented in Figure 3.2c, the formed arcs are not sufficient to estimate the corresponding fitting circle. Exploratory techniques can be implemented to search for more information in order to enhance the CDC offsets estimation. For instance, in [113], [114] the authors presented approaches where multiarcs are induced to gather more CDC information. In [113] the target's distance in relation to the radar was changed purposely, before starting the vital signs acquisition and in [114] the local oscillators were tunned with different angles during the down conversion of the received signal. However, the solutions presented in [113], [114] were developed assuming that the scenario is fully static or that the signal characteristics, as its amplitude, do not change over time.

In fact, in real case scenarios, more specifically in long term monitoring applications, slight motions from the subject could occur often, once it is highly difficult to remain totally still during longer acquisition periods. Even if these motions are not significant in the recovered signal, they can still uncover new objects located in the monitoring scenario, producing different CDC offset values. This situation can be worse when the monitoring scenario is not fully static. For instance, if other subjects move around in the same room, the parasitic reflections behavior changes accordingly, as figuratively depicted in Figure 3.3.

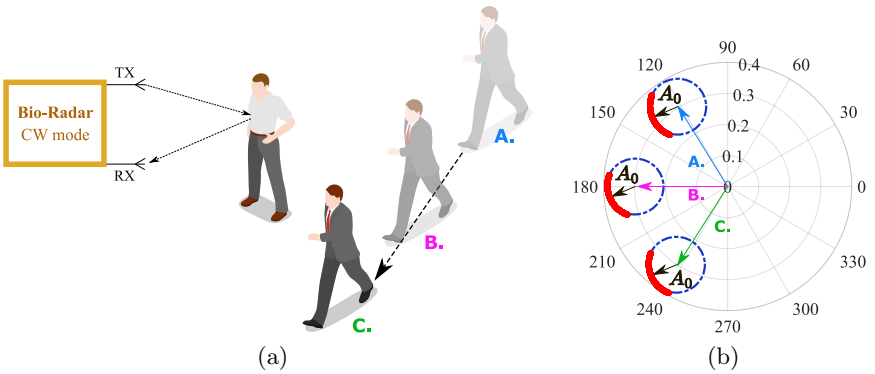

(a) (b)

Figure 3.3: Illustration of the effect of a non-static scenario in the complex plane [102]: (a) Reflections schematic on the monitoring environment, (b) Equivalent projection of the received signal on the complex plane.

In order to address this issue, in [25] a dynamic CDC offset cancellation was implemented with the goal to account such environment changes. Nonetheless, the authors only presented signals from short acquisitions, with 5-minutes duration maximum. Moreover, the authors do not provide information regarding the algorithm effectiveness with low amplitude signals.

In this chapter, DSP algorithms for vital signs extraction are described. During the workflow followed in this PhD, two versions of the algorithms were used. The first version, from now on referred as *Simplified DSP*, is presented in Section 3.2 and it was assumed that the parasitic reflections are static, hence leading to the same CDC offsets over time. The algorithm is an adaption of the one developed in [2]. It is based in the Park et al. [23] solution, which uses the circle fitting approach to determine the CDC offsets values and subsequently subtract them from the full signal. Later, a solution for the Park et al. [23] arc length dependency was developed and it is explained in sub-section 3.2.1. The algorithm is based on the same principle of [113], [114], but instead of impose a slightly change on the target's distance to generate consecutive arcs or re-tuning the radar multiple times, the developed solution takes advantage of the body motion that might occur in long-term signals.

Later, the second version of the DSP algorithm was developed, from now on referred as *Dynamic DSP* and it is described in Section 3.3. This algorithm is robust in non-static monitoring scenarios and is suitable for any SNR. At the end, the accuracy of this latter algorithm was evaluated and validated by estimating the respiratory frequency of a group of 20 subjects and comparing it with the one obtained by a certified measuring equipment.

3.2 *Simplified DSP* algorithm

The workflow of the first version of the DSP algorithm is presented in Figure 3.4.

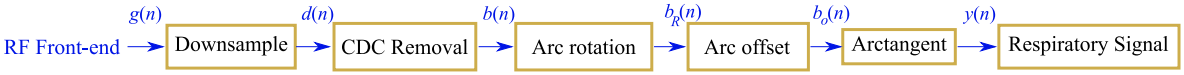

Figure 3.4: Block diagram of the *Simplified* DSP algorithm.

The algorithm works as the following: usually RF signals are acquired by quadrature receivers in CW radars, with a high sampling rate due to front-end restrictions [45]. In this case, the front-end output consists of a complex baseband signal $g(n)$, which was acquired with a sampling rate equal to 100 kHz. This signal is downsampled, since vital signs are low frequency signals, so the decimated signal $d(n)$ presents a sampling rate equal to 100 Hz, embracing both respiratory and cardiac signal characteristics. Afterwards, the CDC offsets are estimated using the Kasa method [115], considering the full signal. The CDC offsets (VI_{iq}, VQ_{iq}) are then subtracted from the complex signal $d(n)$ leading to signal $b(n)$.

After the CDC removal, the arcs can be located in any position in the complex plane. In order to prevent the oscillation around the π value, which generate the wraps occurrence, the full signal is rotated accordingly to oscillate around the 0° value, resulting in signal $b_R(n)$. This is performed by applying the following equation:

$$b_R(n) = b(n) \times e^{-j\theta_R}, \tag{3.1a}$$

$$\theta_R = \arg\left(\sum b(n)\right) \tag{3.1b}$$

where θ_R is the necessary angle to rotate the full signal $b(n)$.

One should note the advantages of this rotation step. Aside from avoiding wraps occurrence, the specific rotation for the 0° angle allows an automatic implementation and can ease the vital signs rate computation through spectral analysis. Since $y(n)$ is a phase signal, the location of the arc in other quadrants would increase the magnitude of the spectral component at 0 Hz, which might overlap with the spectral peak correspondent to the respiratory component.

Depending on the signal quality, the CDC offsets estimation might be misleading. An example of this situation is shown in Figure 3.2d, in which the arc ends up located in the origin after the CDC offsets subtraction. In order to guarantee the proper signal recovery, an offset can be added to the real component of the $b_r(n)$ signal (as depicted in Figure 3.5), resulting in $b_o(n)$ signal. At this stage, the value of such offset was selected by visual inspection, knowing that high values can affect the signal amplitude. Finally, the vital signs can be recovered after computing the arctangent [21] and resulting in the $y(n)$ signal.

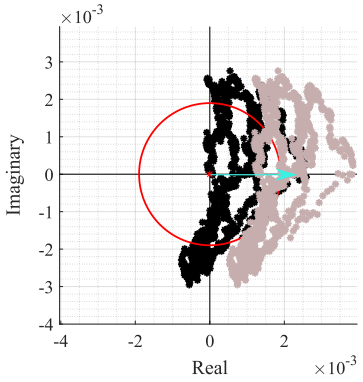

Figure 3.5: Offset addition to the real component of $b_r(n)$ signal in case it is located in the complex origin.

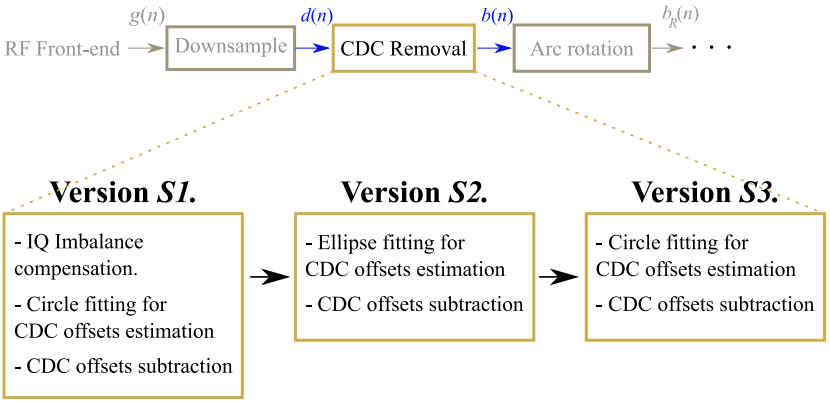

Figure 3.6: Evolution of all versions of the *Simplified* DSP algorithm.

This algorithm is the result of a series of work iterations and Figure 3.6 shows the sum of all algorithm versions. The differences among the versions are mainly related with the implementation of the CDC offsets estimation. The first developed algorithm (**Version *S1***) was presented in [2]. The conducted approach applies the Gram-Schmidt orthonormalization method [103] to correct the IQ imbalance prior to estimate the CDC offsets values, which is performed afterwards through circle fitting. Later, it was observed that the impact of the IQ imbalance was not significant on the extracted signal, therefore in **Version *S2*** the Gram-Schmidt step was skipped and an ellipse fitting was applied to estimate the CDC offsets. Finally, an extended imbalance characterization was performed and it was already described in Chapter 2 (sub-section 2.4.3). It was concluded that the existent IQ is not substantial, so it can be indeed neglected, leading to the current version - the **Version *S3***.

3.2.1 Exploitation of body motion for CDC offsets removal

As demonstrated previously in Figure 3.2c, arcs from real acquisitions do not always have a perfect shape due to low amplitude signals and this hampers the effectiveness of the CDC coordinates estimation and subsequent removal.

During long term monitoring periods, it is impossible to avoid the subjects' RBM. These motions are detected by the radar, together with the respiratory signal and they stand out

once their amplitude is higher than the amplitude from vital signals. Instead of arcs, the RBM produces full circles in the complex plane, if the target is moving towards or backwards the radar. Assuming that the CDC offsets are the same over time, in a signal containing this type of RBM it is easier to estimate their values (VI_{dc}, VQ_{dc}).

Thus, herein one aim to demonstrate that the body motion that naturally occur in long term acquisitions can be used as additional information to estimate the CDC offsets. This new method is from now on referred as the Full Ellipse Method with Detectable Motion (FEMDM) [116] and for comparison purposes, the single arc fitting method is going to be referred as the Arc Method (ARCM). In this PhD work stage the **Version *S2*** of the *Simplified DSP* algorithm was the current version being used[1], where the estimation of the CDC offsets was performed using an ellipse fitting algorithm [117].

Figure 3.7 depicts the block diagram of one possible DSP algorithm which could benefit from the motion samples to improve the CDC removal effectiveness. The CDC offsets could be

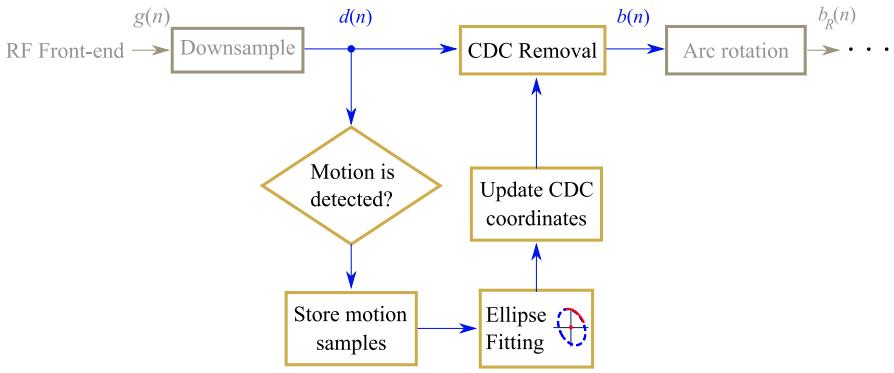

Figure 3.7: Example of a motion based algorithm for proper CDC offsets estimation and removal (adapted from [116]).

estimated and compensated over time and at an appropriate rate. After the signal reception and downsampling, a raw estimation of the CDC offsets value could be performed as a preliminary estimation, through ARCM over the first received samples of signal $d(n)$. In parallel a motion detector is applied and everytime a random motion is detected, the breathing rate measurement is suspended, the motion samples are stored and the ellipse fitting is applied over them. Then, the CDC offsets are updated and the remain steps towards the vital signs extraction could be the same as the ones used in the *Simplified DSP* algorithm (Figure 3.4).

FEMDM validation

In order to evaluate if FEMDM could be applied, an experiment was carried out. The conducted experiment used the Chest Wall Simulator (CWS) (Figure 3.8a) to simulate the chest wall motion due to respiration [2]. The CWS consists on a metal plate assembled in a mechanical platform that is pushed and pulled horizontally with a motion rate equal to 0.4 Hz. Tests were conducted using the CWS rather than a subject, aiming to guarantee the same acquisition conditions, since the CWS motion keeps the same amplitude and frequency over time.

[1] **Version *S3*** of the *Simplified DSP* algorithm was not yet developed at this time.

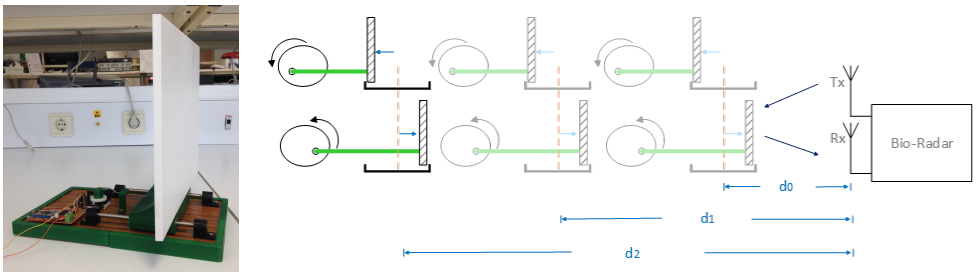

(a) (b)

Figure 3.8: Schematics of the conducted experiment for FEMDM validation [116] (a) Chest wall simulator, (b) Chest wall simulator displacement.

The practical procedure is depicted in Figure 3.8b. It started with the CWS signal acquisition during 15 seconds and at a distance of half a meter, and then its position was changed several times by 5 cm. For a preliminary inspection, the arctangent of the raw signals was computed and the extracted phase signal is shown in Figure 3.9.

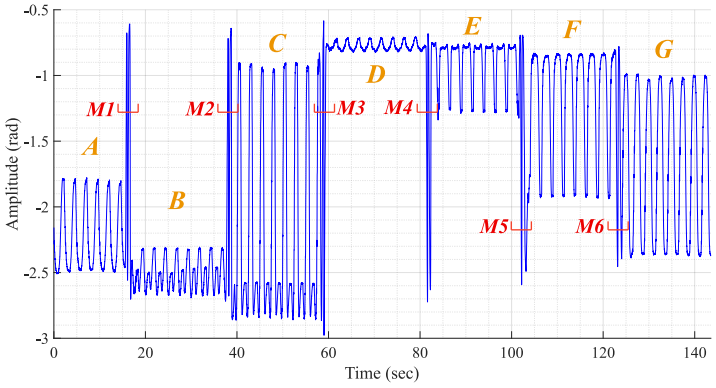

Figure 3.9: Extracted CWS motion from the arctangent (adapted from [116]).

The obtained signal present two interleaved behaviors: sinusoidal signals marked with the letters *A* - *G*, which are the result of the breathing motion emulated by the CWS and high frequency signals with higher amplitude marked with *M1* - *M6*, corresponding to the motion caused while the CWS is displaced to a new position (for instance moving backward, from d_0 to d_1).

Furthermore, the influence of the CDC offsets in the extracted signals can be observed. The signal can be affected differently, depending on the arc position in the complex plane. For example, in slots *B* and *C* a second peak is present with smaller amplitude, in slots *E* and *F* the sinusoidal waveform is inverted and all slots *A* to *G* have different amplitudes, where slot *D* is the one with the lowest amplitude.

The signal was divided in segments, where *A* - *G* are respiratory segments and *M1* - *M6* are the motion segments. The CDC offsets were estimated for each segment using the ARCM and the FEMDM, respectively and the absolute value of the coordinates (VI_{dc}, VQ_{dc}) was computed. The results are presented in Table 3.1. In particular, the C_{iq} point corresponds to the CDC offsets estimation and it is represented by the complex number $C_{iq} = VI_{dc} + jVQ_{dc}$, and the $|C_{iq}|$ is the absolute value of the C_{iq} point.

	ARCM			FEMDM	
	C_{iq}	$\lvert C_{iq}\rvert$		C_{iq}	$\lvert C_{iq}\rvert$
A	$-2.3 - j6.4$	6.9	**M1**	$0.0 - j6.3$	6.3
B	$2.0 - j9.3$	9.5	**M2**	$-0.3 - j6.2$	6.2
C	$5.7 - j28.4$	28.9	**M3**	$-0.4 - j6.4$	6.4
D	$4.1 - j3.9$	5.7	**M4**	$-0.3 - j6.6$	6.6
E	$1.6 - j3.3$	3.7	**M5**	$0.2 - j6.5$	6.5
F	$0.8 - j2.7$	2.8	**M6**	$-0.2 - j6.1$	6.1
G	$0.1 - j9.0i$	9.0			

All the results are multiplied by ($\times 10^{-3}$)

Table 3.1: CDC offsets estimation using ARCM applied to single arcs and FEMDM applied to motion segments [116].

Concerning these results, some conclusions can be made. First, from the result of $|C_{iq}|$ of FEMDM, it is possible to observe that the CDC component did not change significantly during the change of the CWS position, at least in the considered monitoring scenario. This means that the CDC offsets update can be done sporadically. Moreover, the results correspondent to ARCM vary among segments and the ones obtained from the FEMDM are more stable around the same value, which proves that the full ellipse could be used to estimate the CDC offsets, as it gives more accurate results.

The optimal performance of FEMDM in comparison with ARCM can be observed in Figure 3.10 and Figure 3.11. Figure 3.10a-3.10c represent the ARCM implementation using slot A, slot C and slot E respectively. It can be noticed that each arc has a different format, which leads to different CDC offsets estimations. In contrast, Figure 3.10d shows the exploitation of motion to do the ellipse fitting. For all *M1-M6* slots, the center remains approximately the same.

Figure 3.11 shows the vectorial diagram of the complex signal, with and without CDC offsets, using FEMDM and ARCM for comparison purposes. More specifically, Figure 3.11a shows the complex signal with CDC offsets, where C_{iq} is the CDC component with coordinates (VI_{dc}, VQ_{dc}). Vector $r_1(t)$ represents the distance between the origin and C_{iq}, and the vector $r_0(t)$ represents the distance between C_{iq} and the arcs. After CDC offsets removal, the $|r_0(t)|$ value should prevail approximately the same for all arcs.

Figures 3.11b and 3.11c show the complex signal after the ARCM and FEMDM application and it can be seen that both methods were able to recenter the arcs back to the origin. In the case of FEMDM, the arcs are uniformly distributed around the origin, keeping the same $|r_0(t)|$ value for all slots as expected. On the other hand, the ARCM presents different $|r_0(t)|$ values for the different slots, which proves that this method cannot guarantee the accuracy of the CDC removal. Hence, the extracted signal can be affected as shown in Figure 3.12. More specifically, Figure 3.12a shows the arctangent result after using ARCM and the amplitudes of slots B, C and G are smaller since their correspondent arcs are too far away from the origin as shown in Figure 3.11c. On the other hand, all the slots from Figure 3.12b have approximately the same amplitude.

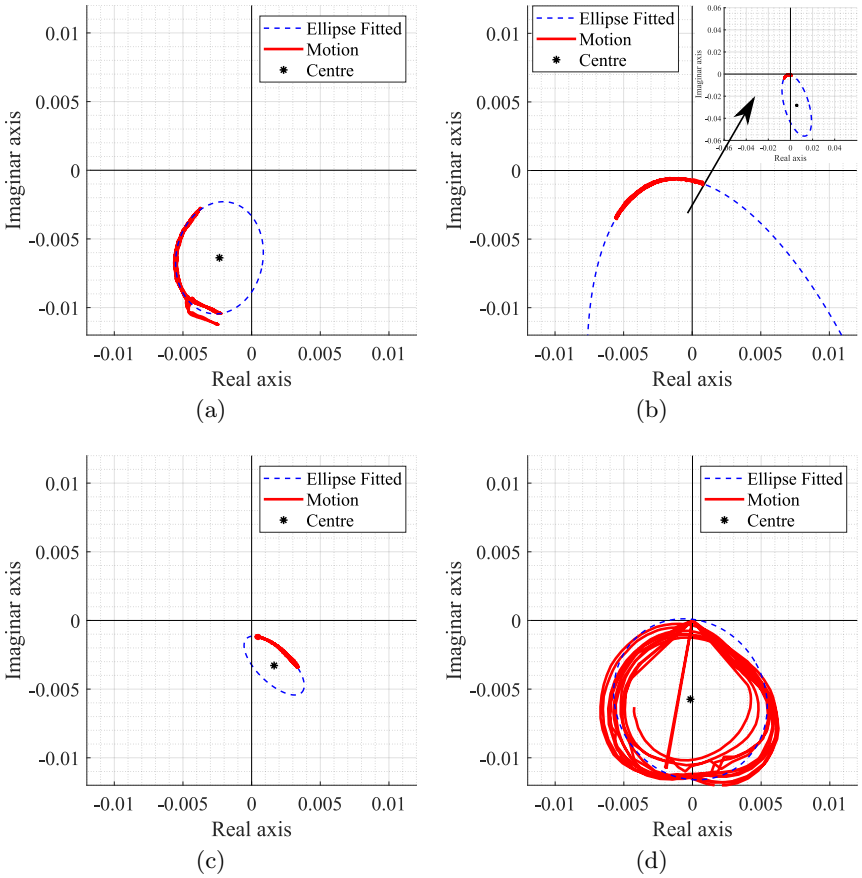

Figure 3.10: Ellipse fitting using ARCM and FEMDM (adapted from [116]): (a) ARCM for slot *A* (b) ARCM for slot *C*, (c) ARCM for slot *E*, (d) FEMDM for all slots *M1-M6*

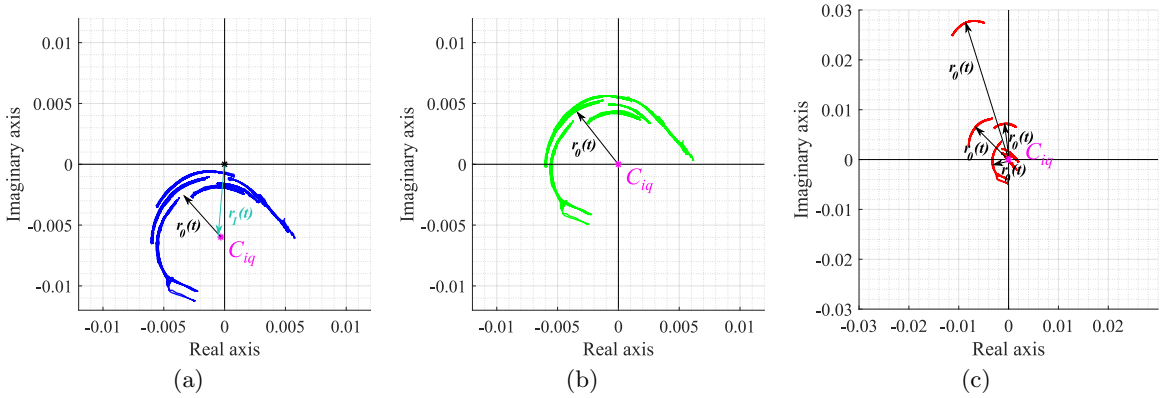

Figure 3.11: Performance evaluation of FEMDM regarding the vectorial diagram [116]: (a) Original signal with CDC component (b) Signal after CDC removal using FEMDM, (c) Signal after CDC removal using ARCM.

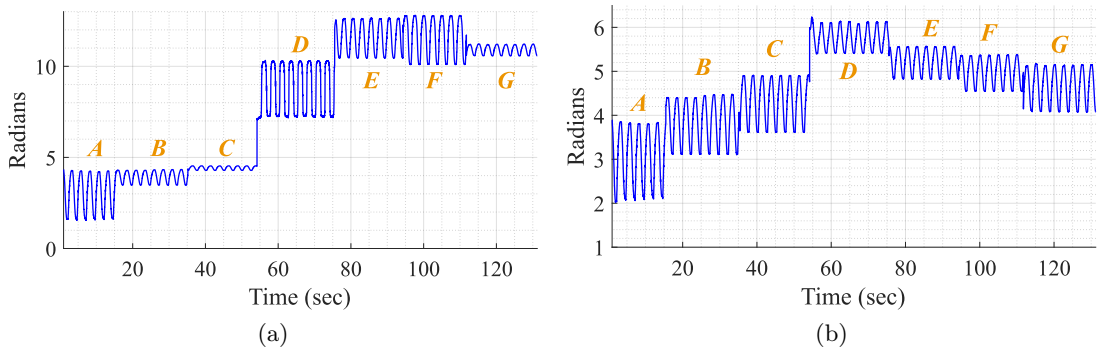

Figure 3.12: Final angle computation for both methods [116]: (a) ARCM, (b) FEMDM.

3.3 *Dynamic DSP* algorithm

The algorithm proposed in Section 3.2, can be used if one assume that the monitoring scenario is static, leading to an exclusive pair of CDC offsets coordinates. Nonetheless, Figure 3.2d demonstrated a case where that algorithm fails, leading the arc to be located in the complex origin. Aiming to prevent failure in the CDC offsets compensation, a solution was proposed in sub-section 3.2.1, where the RBM was used as information to improve the accuracy of CDC offsets estimation, which can be updated every time a new RBM is detected. However, the occurrence of body motion is unpredictable, it might generate different signal patterns (rather than full circles) and signal fading might occur meanwhile.

In this sense, a new solution was developed and it contains two specific features:

1. The CDC offsets are estimated using a novel arc fitting algorithm, which forces the search to be outside the radar samples, turning the algorithm effective to low amplitude signals;

2. The novel arc fitting method is implemented dynamically through a windowing approach, in order to track and account the CDC changes over time.

3.3.1 Novel arc fitting algorithm

The CDC offsets removal is usually performed in the literature using fitting algorithms that aim to search for a circle that fits the radar complex samples, finding its radius and center coordinates, which are used afterwards to remove the CDC offsets. Least Squares Fitting (LSF) is a common example of this approach [118]. In cases where the data is well distributed, the literature suggests that the Gauss-Newton method with Levenberg-Marquardt correction (LM) is a LSF robust solver, which is quite stable, reliable and fast converging [101], [118]. It uses a cost function and identifies the possible solutions by finding the parameters that lead to the cost function minimization [101]. In [25], the authors apply also a circle fitting method based on a cost function minimization, to compensate the CDC offsets. For their case, the center coordinates are identified when the radius variance is minimized.

Nonetheless, both LM and the method presented in [25] require an optimization stage, which consumes an unpredictable processing time to achieve the desired solutions. Additionally, algorithms based in LSF are sensitive to outliers [119], hence might not be effective in

cases where the data is noisy or lacks in resolution, which is a common case in the bio-radar context, as demonstrated previously in Figure 3.2c.

Other impairment of the circle fitting methods relies on the dependence of the circle radius as an optimization parameter (as in the [25] case). Badly formed arcs with low lengths and wide thickness can drive the algorithm to provide center solutions within the radar signal samples, as demonstrated in Figure 3.2c. The algorithm is forced to search for a circle that fits all points, assigning the radius that enables this fitting. In these situations, the cost function minimum zone is located within the radar data points, which corresponds to the center of such circle.

In order to better understand this effect, Figure 3.13 presents an example of a weak signal arc in the complex plane, acquired in a real context scenario. A cost function based in circle

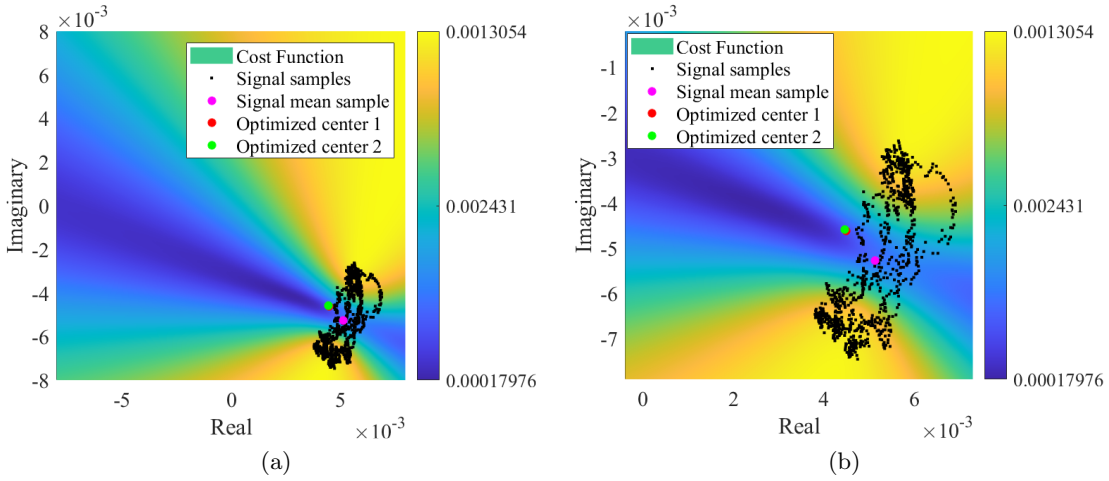

Figure 3.13: Color map of the cost function result using the signal mean value as optimization starting point [102]: (a) Representation of the optimized solution, (b) Zoomed visualization of the optimized solution.

fitting was defined to be further optimized, aiming to find the arc center. The cost function considered for this example is given by equation (3.2):

$$S_j = \sum_{n=1}^{N} \left(|C_j - d(n)| - r \right)^2 , \tag{3.2}$$

where C_j is the center of the arc, $d(n)$ is the radar signal, N is the length of signal $d(n)$ and r is the radius of the arc, given by equation (3.3):

$$r = \text{med}(|C_j - d(n)|). \tag{3.3}$$

where med(.) denotes the median value.

Figure 3.13 presents also the color map of the cost function S_j solutions for each C_j value. An optimization was then performed to find the proper arc center. For this purpose, it was used a multidimensional unconstrained nonlinear minimization, namely the Nelder-Mead method [120], with 100 iterations and a termination tolerance equal to 1×10^{-4}. As starting point it was considered the radar signal mean value, which was already located in a

cost function minimum zone. As shown Figure 3.13b, the optimized solution was found near the data samples (marked as a red dot). Therefore, a second optimization stage was carried out by increasing the number of iterations to 10000 and decreasing the termination tolerance to 1×10^{-16}. Even if the number of iterations is increased or the boundary conditions are wider, the optimized solution remains the approximately the same (marked as a green dot in Figure 3.13b).

As it can be observed in Figure 3.13, the cost function minimum zone extends forward the arc. Thus, by taking as prior knowledge that the radar samples are disposed according to an arc rather than a circle (which is the case for low carrier radars), it is possible to set the searching zone already outside the signal samples. In this sense, the novel arc fitting method, from now on referred as Optimized Cost Method (OC), aims to determine the most appropriate arc center using a cost function minimization, but the searching area is limited to the arc sideways zones, avoiding the center solutions within the radar samples. For this purpose, a set of C_k points circularly distributed around the arc were defined as possible arc center points, as depicted in Figure 3.14a.

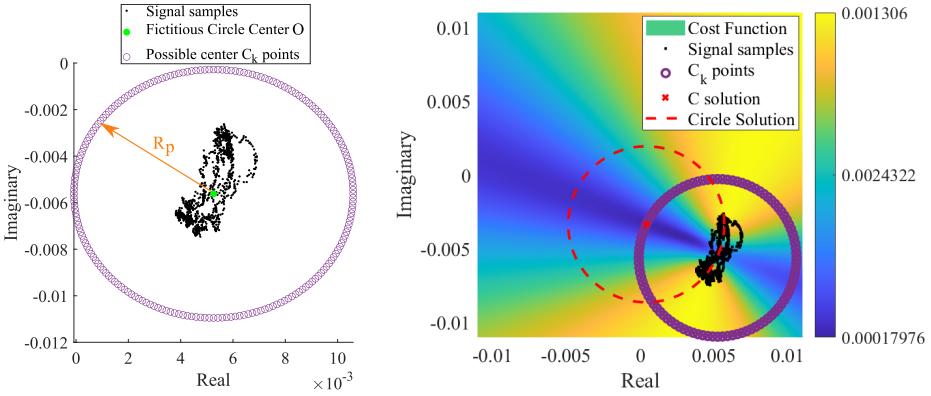

Figure 3.14: Illustration of the novel arc fitting method [102]: (a) definition of the possible C_k solutions, (b) cost function result with the selected C solution.

Those C_k points form a fictitious circle with radius R_p, selected to push the estimation away from the radar samples. The radius R_p is expressed by equation (3.4):

$$R_p = A_W \times \text{med}(|d(n) - O|), \tag{3.4}$$

where A_W is an arbitrary scale factor, $d(n)$ are the radar samples and O is the center of such fictitious circle, given by equation (3.5):

$$O = \text{med}(\text{Re}(d(n))) + j\,\text{med}(\text{Im}(d(n))), \tag{3.5}$$

The scaling factor A_W dictates how much large should be the searching area, considering the arc length. In order to guarantee that the selected center C is not within the arc samples, the scaling factor should be $A_W > 1$. In the context of this work, the $A_W = 3.5$ value was selected empirically.

The arc center solution C is obtained through the cost function (3.2) minimization, calculated with each C_k (note that $C_j = C_k$). The median operation was used in equations (3.3),

(3.4) and (3.5) as it is a robust estimator in the presence of outliers [119].

After obtaining the C_j points and evaluating the S_j function for each, the final C solution is the C_j that allows S_j to be minimum. Therefore, C can be written as (3.6):

$$C = \underset{C_j}{\operatorname{argmin}}\, S_j. \tag{3.6}$$

Since the searching area is already forced to be outside the radar samples, the solution is direct and do not require any optimization stage. This procedure is depicted Figure 3.14b, where the most suitable arc center is marked with a red cross.

Limitations of the OC

One should note that the OC presents three limitations [102]. First of all, the S_j minimum zones can occur in both arc sides, i.e. inside and outside its concavity, as it can be observed in Figure 3.14b with the location of the dark blue zones. In the next sub-section, the dynamic implementation of this algorithm is explained, so it is able to accommodate CDC changes over time. For such implementation it is required to perform the CDC estimation in overlapped windows (w_i), in order to provide a progressive and coherent CDC estimation over time. When signals are considerably weak, successive windows might present center solutions (C_i) in opposite sides of the arc, as depicted in Figure 3.15, adding an undesired variability degree to the overall center estimation.

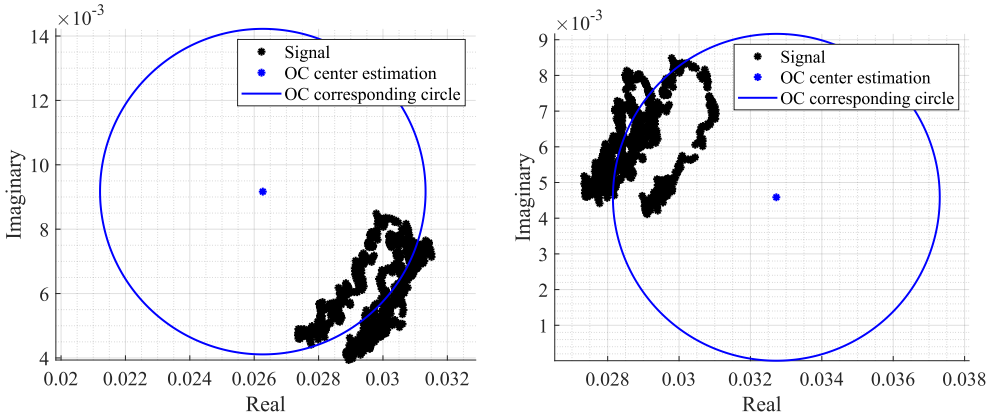

Figure 3.15: Center estimations in opposite arc sides in consecutive windows, using as an example [102]: (a) the window nº 74, (b) the window nº 75.

In order to avoid this issue, the distance between the current window center C_j and the last *acceptable* window center C_a, was included as a new cost in the cost function. Therefore, equation (3.2) should be re-written as equation (3.7):

$$S_j = \sum_{n=1}^{N} \left(|C_j - d(n)| - r\right)^2 + \alpha |C_j - C_a|^2, \tag{3.7}$$

where α represents a weight and C_a is the last *acceptable* center estimation. For this case, one defined *acceptable* center C_a as a solution located far from the radar samples. Thus, the value

C_a is updated if such condition is verified, otherwise the previous value is preserved. This new term reduce estimate transitions in successive windows, by giving to α a fair value, having in mind that lower α values allow more transitions and higher α values prevents transitions, even the ones that are indeed necessary when the arc orientation changes. In this work, the α term was set to 1.

The second limitation is regarding the vital signs amplitude, after performing the arctangent method. The searching area is set outside the radar sample points, by giving a considerable value to the A_W scale factor. This value must be selected having in mind that it should always provide estimations outside the radar data samples. However, a special care should be accounted, since larger A_W values push the arc away from the complex plane origin, reducing the angle variation range. Therefore, higher amplitude vital signs are obtained if the arc is located close to the origin, but its amplitude can slightly decreased if they are too distant. This also means that the final signal amplitude might not be the original one. The amplitude variation over the original signal can indicate changes in the subject psychophysiological state. Therefore, one should use the same A_W for all signal windows, in order to try to preserve eventual signal amplitude variations as the maximum possible.

Finally, as mentioned previously, in order to implement this algorithm, the radar samples must be disposed according to an arc, which is only valid when low frequency carriers are being used. Note that higher carriers induce full circles instead of arcs, and in these cases the traditional circle fitting algorithms are indeed more appropriated.

3.3.2 Dynamic arc position adjustment

The CDC offsets can be estimated and removed over time, by performing the arc fitting with a windowing approach, enabling an implementation for both offline signal processing (which is the case of this work) or in a real-time application (with the proper adjustments to maximize the algorithms performance).

The implementation of the *Dynamic DSP* algorithm is similar to the *Simplified DSP* algorithm presented in Section 3.2 and uses the same block diagram as the one presented in Figure 3.4. The main differences are the following:

- The CDC offsets estimation is performed with the OC rather than using the Kasa method;
- The CDC offsets estimation is performed dynamically over time through a windowing approach;
- The arc rotation is also performed dynamically using the windowing approach.

The implementation of the dynamic CDC offsets estimation and rotation are depicted in Figure 3.16. Starting with the CDC offsets estimation (Figure 3.16a), the $d(n)$ signal is divided in windows with 1000 samples length and with 50% overlap while moving forward. This window length was selected considering the used sampling frequency (equal to 100 Hz after downsampling) and the possible respiratory rates across the population. Healthy subjects generally breathe at a rate around 0.2 Hz (12 breaths/min) [121], but it is also possible to reach lower values such as 0.1 Hz (6 breaths/min) [122]. Under these circumstances, 10 seconds are required to obtain a full arc, leading to a minimum of 1000 samples and thus guaranteeing always that a complete arc is obtained. The same approach was used in [25].

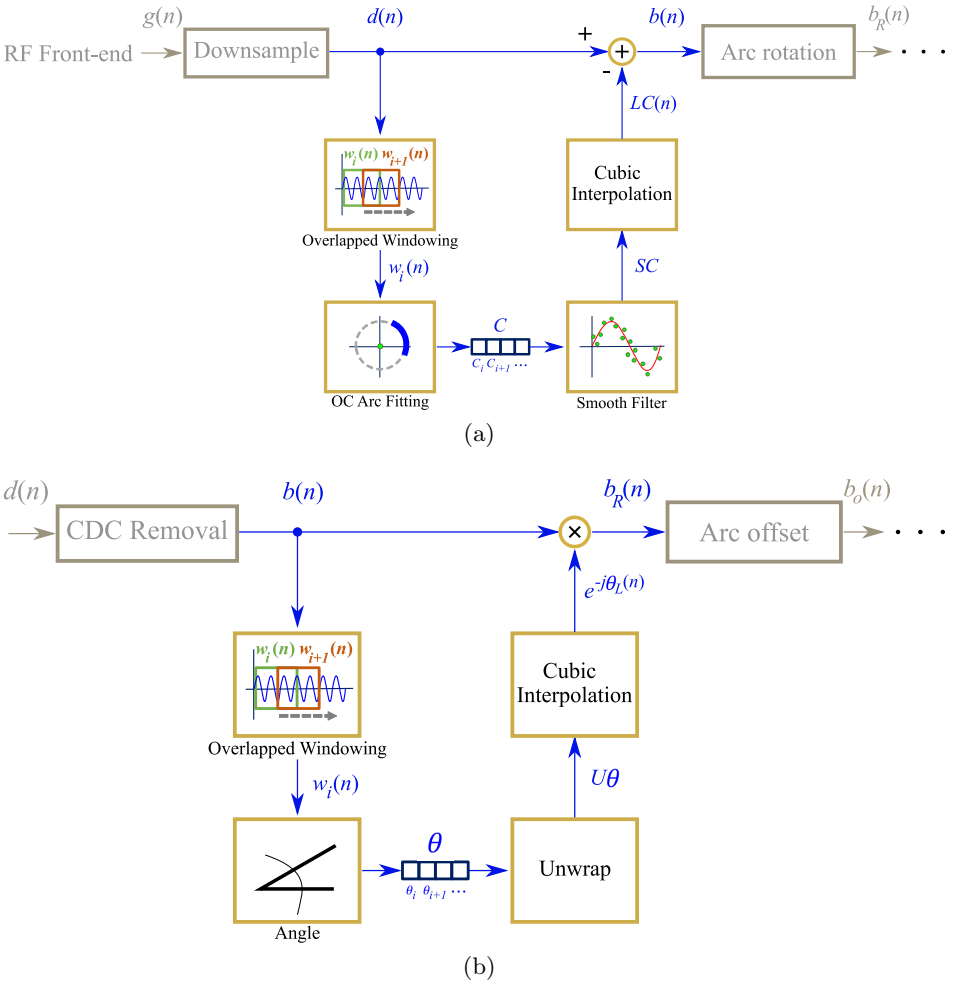

Figure 3.16: DSP dynamical implementation (adapted from [102]): (a) Dynamic CDC removal, (b) Dynamic arc rotation.

The arc fitting method is applied to each window w_i and the center C_i coordinates correspondent to the window i are stored the vector C. Note that C is a complex number, therefore the real and imaginary parts are stored separately. A smooth filter was applied to the each vector in order to prevent outliers. The selected smooth filter was a 1^{st} order Savitzky-Golay filter with a frame length equal to 31, resulting in the smoothed vector SC. Then, the vectors are interpolated in order to assign a CDC offset coordinates for each signal sample, resulting in $LC(n)$. For this purpose, it was used the shape-preserving piecewise cubic interpolation, since it provides a smooth result and it has a good approximation behavior on the vector extremes [123]. Finally, the interpolated vector is subtracted from the decimated signal $d(n)$, resulting in signal $b(n)$.

After removing the CDC component, the arc position in relation to the complex plane is adjusted to avoid wraps. The CDC change over time affects also the arc orientation in relation to the origin. Therefore, this rotation step must be also implemented dynamically over time, by dividing the signal in windows again. This procedure is depicted in Figure 3.16b. The goal is to rotate all window arcs until they oscillate around the 0° angle. This is per-

formed by computing for each window, the necessary angle required to rotate the arc. This is accomplished using equation (3.8) (adapted from equation (3.1b)):

$$\theta_i = \arg\left(\sum w_i(n)\right). \tag{3.8}$$

where θ_i is the necessary angle to rotate the arc $w_i(n)$ from window i. Similarly to the CDC offsets window estimations, an angle vector θ is created with all θ_i values. The θ vector is unwrapped and interpolated using the same type of interpolation used for the CDC offsets. Then, the full signal is evenly rotated by applying equation (3.9), resulting in signal $b_r(n)$:

$$b_r(n) = b(n) \times e^{-j\theta_L(n)}, \tag{3.9}$$

where $b(n)$ is the full signal without CDC offsets and $\theta_L(n)$ is the angle vector, unwrapped and interpolated.

The implementation of equation (3.7) in the arc fitting stage decreases the number of CDC offset estimation transitions in successive windows, but do not solve them all. When there are transitions in successive windows, that signal portion is affected after the CDC offsets removal due to the effect of the smooth filter. More specifically, the mean of consecutive C_i is considered, leaning towards zero and pushing that arc portion to the origin. In these cases, it is necessary to add again the small offset, resulting in signal $b_o(n)$. In the *Simplified DSP* algorithm, the offset value was selected by visual inspection of the signal, but this time it was computed automatically, as depicted in Figure 3.17. When the final arc is centered in the

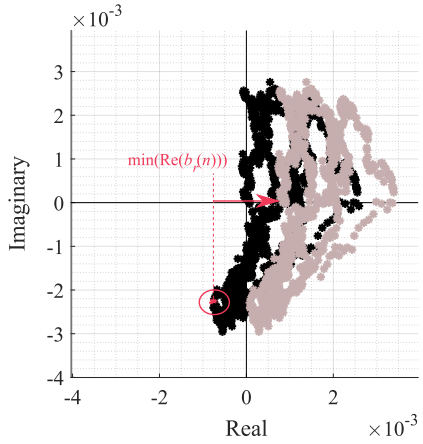

Figure 3.17: Automatic offset addition to the real component of $b_r(n)$ signal.

origin there are samples with a negative values on the real component. Therefore, the signal with offset can be obtained by applying equation (3.10):

$$b_o(n) = b_r(n) + \min(\mathrm{Re}(b_r(n))). \tag{3.10}$$

where $\min(\mathrm{Re}(b_r(n)))$ denotes the minimal value of the real component of $b_r(n)$ signal.

3.3.3 Algorithm testing using a real application scenario

After developing the *Dynamic DSP* algorithm, its limitations were verified and its performance was tested considering real application scenarios. For this purpose, the vital signs of

three different subjects were acquired during 25 minutes approximately, following the *Emotional Protocol* to gather individual variability, leading to more robust results. Each subject represents a different test case with specific acquisition conditions, embracing both problems herein mentioned: the CDC offsets changing over time and the lack of arc resolution which hampers the arc center estimation. Vital signs were acquired in two scenarios and using subjects with different gender, in order to provide unequal chest wall displacement amplitudes according to [36]. The considered test cases are described in Table 3.2, and the corresponding baseband signals can be observed in Figure 3.18.

Case Nº - M/F	**Monitoring Scenario**	**Chest wall amplitude**	**Height [m]**	**CWP [cm]**	**BMI [kg/m^2]**
Case 1 - M	Static	High	1.75	90	22.20
Case 2 - M	Non-static	High	1.76	96.5	27.44
Case 3 - F	Non-static	Low	1.56	82	25.07

M - Male, F - Female, CWP - chest wall perimeter, BMI - Body mass index

Table 3.2: Description of the test cases considered for the *Dynamic DSP* algorithm evaluation [102].

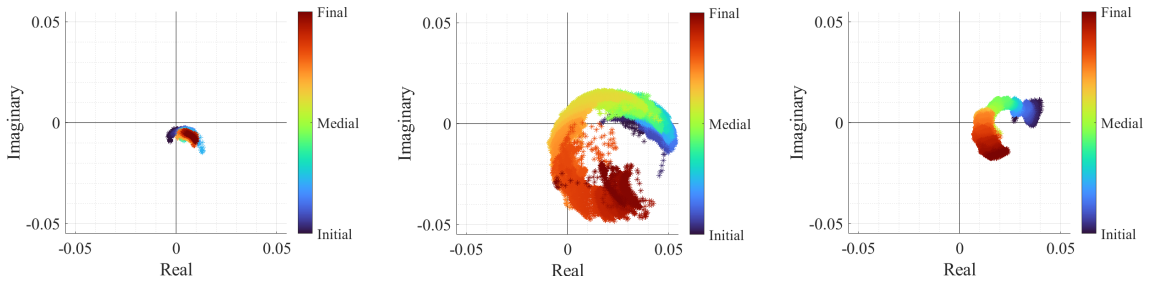

Figure 3.18: Real/Imaginary plots of the considered test cases baseband signals [102]: (a) Case 1, (b) Case 2, (c) Case 3.

The signal of Case 1 shown in Figure 3.18a, represents a reference case study, with a high amplitude displacement and acquired in a static environment. In Figure 3.18a it can be seen that the arc center rarely moved. Nonetheless, a slight displacement might be justified with eventual motions that the subject did, since it is difficult to remain completely still for such period of time. In Case 2 (Figure 3.18b), the CDC offsets variation challenge is introduced. In this case, it is possible to observe that the arcs are changing their position over time. Finally, the last test case in Figure 3.18c represents the worst case scenario, where beside the CDC variation, the signal presents a lower amplitude derived from a lower chest wall motion.

The scenario schematics used on these experiments is depicted in Figure 3.19. In order to induce the non-static scenario for Cases 2 and 3, the vital signs were acquired in a room with other moving subjects inside. The static scenario (Case 1) used the same layout as the one shown in Figure 3.19, but without the additional moving subjects.

For all cases, the algorithm presented in Figure 3.16 was equally applied, using a window length of 1000 samples and a sampling rate of 100 Hz. More than 420 windows were analyzed

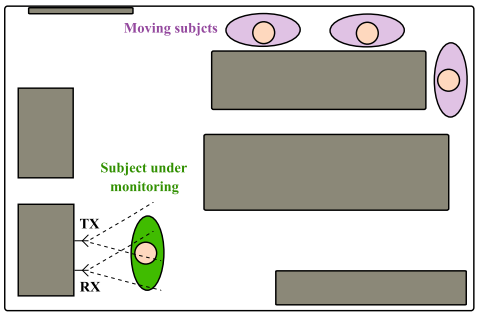

Figure 3.19: Schematics of the monitoring scenario [102].

per test case. The results presented in this stage are mainly focused on the arc fitting performance, which was performed using either the OC and other state of the art circle fitting algorithms, namely the LM algorithm [118], [124], the Kasa (KA) algorithm [115], [124] and the Taubin (TAU) algorithm [124], [125]. The LM algorithm required an initial guess for the arc center coordinates C_i to start the optimization, so for a fair comparison it was used the estimation provided by OC, as starting point.

The fitting results encompassed the location of C_i in relation to radar samples. For instance, it is considered a failure case when the C_i estimation is within the arc data samples, as previously presented in Figure 3.2c. In order to identify a failure case, the distance between C_i and all signal samples was computed for all windows, as showed in Figure 3.20a.

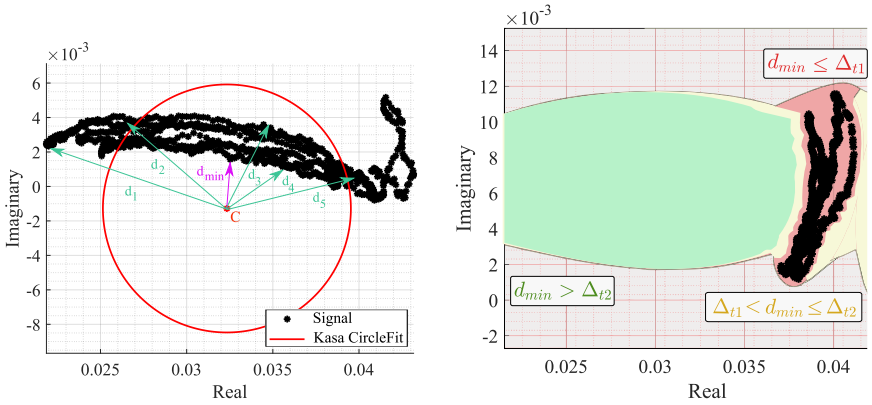

Figure 3.20: Identification of a failure case using a windowed signal [102]: (a) Illustration of the distances computation and d_{min} identification, (b) Color map of the defined thresholds - red zone is defined when $d_{min} \leq \Delta_{t1}$, yellow zone is defined when $\Delta_{t1} < d_{min} \leq \Delta_{t2}$ and the green zone is defined when $d_{min} > \Delta_{t2}$.

Then, the minimum distances d_{min} of all windows were analyzed and two thresholds were defined: $\Delta_{t1} = 4 \times 10^{-4}$ and $\Delta_{t2} = 8 \times 10^{-4}$, as depicted in Figure 3.20b. When $d_{min} \leq \Delta_{t1}$, it means that C_i is located in the red zone, within the arc data samples and this is a clear failure case. On the other hand, if $\Delta_{t1} < d_{min} \leq \Delta_{t2}$, it means that C_i is out of the arc samples but yet too close, being in the yellow zone. The cases above Δ_{t2} threshold are in the green zone and they can be considered admissible, since it already allows the correct angle

estimation and further arc rotation.

When the fitting is applied dynamically, the CDC offsets estimate cannot vary largely to guarantee a successful interpolation and smooth CDC removal in the overall signal. Therefore, it is also crucial that the selected fitting algorithm provides stable estimates among the different signal windows.

In sum, the considered metrics to evaluate the arc fitting performance are [102]:

- The behavior of estimations over time, obtained through the first difference of consecutive C_i estimations: $\Delta_C = C_i - C_{i-1}$;
- The standard deviation of consecutive C_i estimations ($\sigma(\Delta_C)$), where Δ_C is computed in the complex form;
- The percentage of failure cases ($d_{min} \leq \Delta_{t1}$) for each case study;
- The percentage of cases that can be critical to the algorithms performance ($\Delta_{t1} < d_{min} \leq \Delta_{t2}$) for each case study;
- The average run time ($\overline{RT}$) that each algorithm takes to provide a windowed estimation.

Although the OC does not require an optimization stage, the number of points used in the fictitious circle (from now on referred as N_{PTS}) have impact on the computational time. For starters, the fictitious circle have a total of 200 C_k points, which respects a balanced trade-off between resolution and time consumption. Results are also presented with a lower number of points, in order to verify the impact in computational time and in the algorithm performance.

Additionally, and since the algorithm herein presented applies a smooth filter on the vector containing the CDC estimations (before interpolating it), the smoothed vector version is the one used for the CDC offsets removal rather than the original estimation provided directly by the OC algorithm. As mentioned previously, this means that the method can actually fail and the arc can reach the complex origin, which is the undesired. Therefore, the performance evaluation includes also the number of failure cases after removing the CDC offsets using the OC method. For this purpose, the $b(n)$ signal was again divided in windows and the same metrics are used, where d_{min} is now related to the minimal distance between the arc samples and the complex origin, $\sigma(\Delta_C)$ is referred to the estimation variation after applying the smooth filter and the run time is now regarding to the CDC estimation and removal using the OC method. This evaluation was only performed for 200 C_k points, which represents the most optimistic case.

At the end, the final aspect of each case study signal after the DSP algorithm implementation is also shown.

3.3.4 Results discussion

In general, different estimations of the C_i coordinates were obtained by the different algorithms. The Case 1 was the one that provided more similar results and the Case 3 represented a limit case, where all algorithms presented the worse performance.

Since the Case 2 includes a wide variation of the CDC offsets over time, but yet with a high chest wall motion amplitude, it was possible to observe the most common estimation behaviors for all the tested algorithms. Figure 3.21 shows some examples of the estimation

results along the signal, disposed by crescent order of window number. The first aspect that should be noticed is the arc position over the complex plane and its orientation. If signals were obtained in static conditions and with the subject stable, the arc would barely move and would kept the same orientation over time. In this case, the contrary was observed as expected. This arc position variation, along the windows, indicates the urge to perform both arc fitting and arc rotation dynamically.

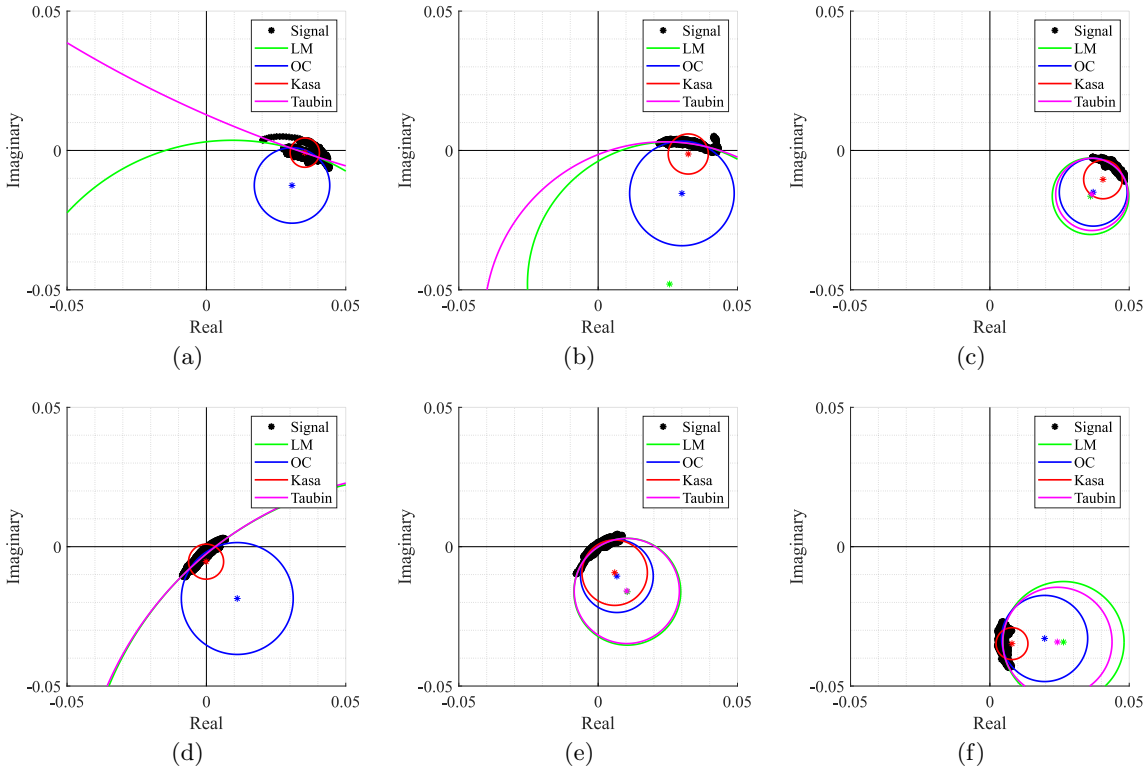

Figure 3.21: Circle fitting result over time for Case 2 [102]: (a) Window 2, (b) Window 4, (c) Window 35, (d) Window 318, (e) Window 327, (f) Window 413.

Secondly, Figure 3.21 also shows how some algorithms provided discrepant estimates for C_i coordinates. For instance, in Figure 3.21a, 3.21b and 3.21d, the LM and TAU algorithms provided estimations out of the arc range, which were seen as outliers. This fact also contributed to a variability increase on the provided solutions over time. Moreover, in Figure 3.21a, 3.21d and 3.21f the KA algorithm failed, since its estimation lied within the arc samples. On the other hand, Figure 3.21c and 3.21e, presented some cases where all algorithms provided approximate estimations, without any failure. It is also important to notice that the OC algorithm presented a stable estimation for all the aforementioned examples, without any failure case.

Figure 3.22 shows the behavior of consecutive estimations Δ_C over time, for each test case. Considering that a perfect case would be the one that presents more values near 0, which means that the consecutive estimations are the same, Case 1 presented the lowest variation among all test cases as expected. Even though, while KA and OC presented a stable estimation over time, LM and TAU algorithms provided few outlier estimations. Case 2

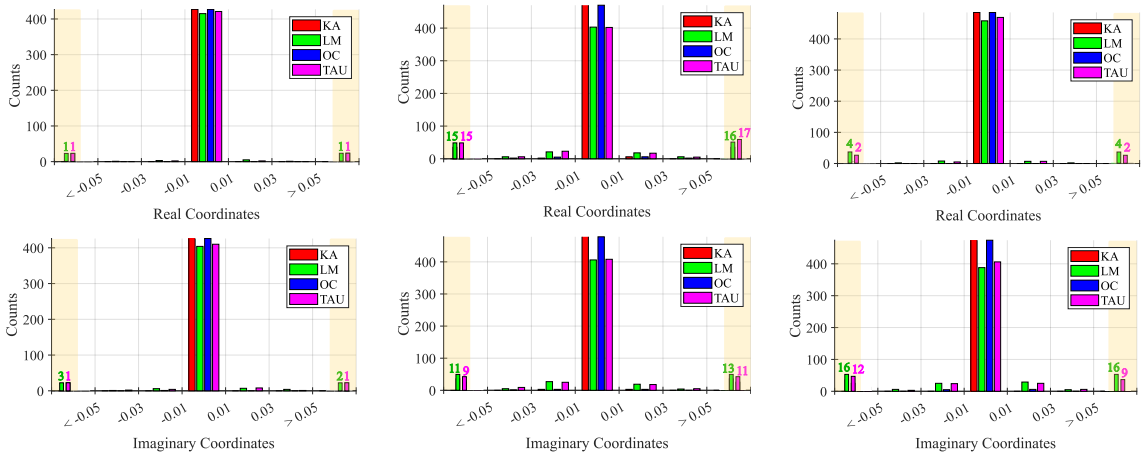

Figure 3.22: Histogram of the behavior of consecutive estimations Δ_C over time [102]: (a) Case 1, (b) Case 2, (c) Case 3.

and Case 3 presented an increased variability, justified with the observed CDC change over time. In these cases, the estimations must track the CDC change, which justifies the overall variability. Once again KA and OC were the more stable algorithms, when comparing with LM and TAU, which behavior got worse, showing a higher number of outliers greater than 0.05 and less than -0.05, respectively.

The overall fitting algorithms performance results are presented in Table 3.3, 3.4, 3.5, for each test case respectively. These tables contain the results relative to the estimations of the CDC offsets for all methods.

Method	N_{PTS}	$\overline{RT}$ (ms)	$\sigma(\Delta_C)$	$d_{min} \leq \Delta_{t1}$ (%)	$\Delta_{t1} < d_{min} \leq \Delta_{t2}$ (%)
KA	-	0.052	0.001	4.2	1.9
LM	-	4.8	0.077	0	0.2
TAU	-	0.18	0.047	0.7	0.47
OC	200	4.4	0.001	0	0
	20	0.64	0.001	0	0
OC (no CDC)	200	1900	0.00007	0	0

N_{PTS} - number of points used in the fictitious circle (OC method)

$\sigma(\Delta_C)$ - standard deviation of consecutive C estimations, $\overline{RT}$ - Average run time

$d_{min} \leq \Delta_{t1}$ - number of failure cases, $\Delta_{t1} < d_{min} \leq \Delta_{t2}$ - number of critical cases

Table 3.3: Arc fitting results for Case 1 [102].

For Case 1, all algorithms present a low percentage of failure cases as expected. Even though, the KA method presents the worst performance, with 4.2% of failure cases. On the other hand, the LM and TAU methods presented a higher estimation variation, with the highest value of $\sigma(\Delta_C)$. The OC algorithm is the one with the best performance, not only because do not present any failure or any case within the critical limit, but also because provided more stable results among all the signal windows. Regarding the run time, the

Method	N_{PTS}	$\overline{RT}$ (ms)	$\sigma(\Delta_C)$	$d_{min} \leq \Delta_{t1}$ (%)	$\Delta_{t1} < d_{min} \leq \Delta_{t2}$ (%)
KA	-	0.057	0.004	4.7	3.12
LM	-	4.9	4.1×10^4	0	0.41
TAU	-	0.18	0.075	0.2	0.83
OC	200	4.4	0.007	0	0
	20	0.63	0.007	0	0.2
OC (no CDC)	200	2150	0.0003	0	0

N_{PTS} - number of points used in the fictitious circle (OC method)

$\sigma(\Delta_C)$ - standard deviation of consecutive C estimations, $\overline{RT}$ - Average run time

$d_{min} \leq \Delta_{t1}$ - number of failure cases, $\Delta_{t1} < d_{min} \leq \Delta_{t2}$ - number of critical cases

Table 3.4: Arc Fitting results for Case 2 [102].

Method	N_{PTS}	$\overline{RT}$ (ms)	$\sigma(\Delta_C)$	$d_{min} \leq \Delta_{t1}$ (%)	$\Delta_{t1} < d_{min} \leq \Delta_{t2}$ (%)
KA	-	0.050	0.001	64.6	9.3
LM	-	5.2	2.3×10^3	16.5	4.7
TAU	-	0.18	0.055	26.1	5.4
OC	200	4.5	0.003	0	0.2
	20	0.63	0.003	0	0.2
OC (no CDC)	200	2170	0.0002	5.76	6.17

N_{PTS} - number of points used in the fictitious circle (OC method)

$\sigma(\Delta_C)$ - standard deviation of consecutive C estimations, $\overline{RT}$ - Average run time

$d_{min} \leq \Delta_{t1}$ - number of failure cases, $\Delta_{t1} < d_{min} \leq \Delta_{t2}$ - number of critical cases

Table 3.5: Arc Fitting results for Case 3 [102].

KA and TAU are quicker, and this can be justified by the fact that they do not require any optimization stage (as the LM case), neither use a high number of points to search the solution (as the OC method), using in contrast algebraic computations for that purpose [115], [125]. Nonetheless, if a lower number of fictitious circle points N_{PTS} is used in the OC method, the run time decreases considerably, and the algorithm performance is barely affected, as it can be seen by the estimation variation $\sigma(\Delta_C)$ and the same number of failure cases obtained.

On the Case 2, it is possible to infer that the overall CDC offsets varied, since all $\sigma(\Delta_C)$ values increased. One should note the sudden increase of $\sigma(\Delta_C)$ for the LM method. This happened due to some outliers provided by the method, causing this high variation. The number of failure and critical cases barely changed for all methods, which might be related with the arc length of this signal. Once again the OC method stands out with the best performance, however the number of critical cases increased slightly, if few circle points N_{PTS} are considered.

Finally, the Case 3 served as a limit test. In general, a higher percentage of failure cases was observed for all methods due to the severe decrease on the arc length, excepting the OC method. The OC method kept a high performance, since we are imposing to search outside the data points. Thus, the KA presented the worst performance with 64.6% of failure cases and 9.3% of critical cases. The remain algorithms, presented failure percentages above 16%.

The OC algorithm presented the same performance observed for the Case 2, with 0 failure cases and only 0.2% of critical cases, regardless the number of circle points used.

The OC results presented in Tables 3.3, 3.4 and 3.5, showed that the number of circle points do not have a significant impact in the algorithm performance, since $\sigma(\Delta_C)$ parameter barely moved. Figure 3.23 shows the OC algorithm performance if points are even lower, by evaluating the run time and the $\sigma(\Delta_C)$, respectively. The run time decreases if the number of

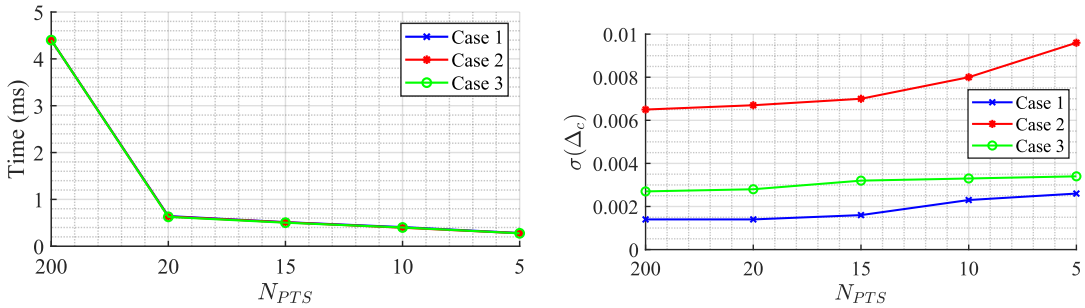

Figure 3.23: OC algorithm performance for few C_k points [102]: (a) Run time, (b) Estimation variability $\sigma(\Delta_C)$.

points are reduced, achieving a minimum value of 0.28 ms for a total of 5 C_k points. However, this value is still above the TAU and KA algorithms and it comes with a cost of increasing estimation variability. Therefore, the selection of 20 C_k points, seems to respect a balanced trade-off between estimation stabilization over time and a decreased run time as possible.

Considering now the performance of the overall CDC offset removal using the OC method, only the Case 3 presented arcs near the origin, with 5.76% of failed cases and 6.17% of critical cases. Cases 1 and 2 remained with a high rate of success, presenting no failed cases after the CDC removal. On the other hand, the smooth filter application decreases highly the estimation variability, as it can be seen on the $\sigma(\Delta_C)$ parameter for all cases. Finally, the implementation of the full algorithm herein proposed takes approximately 2 seconds (for 25 minute signals), regardless on the case study.

After removing the CDC offsets with the OC method and adjusting the arc position dynamically, all case studies should present equally the optimal conditions to perform the arctangent demodulation, as it can be seen in Figure 3.24. This figure shows the aspect of signal $b_o(n)$ of the block diagram presented in Figure 3.4, after applying the *Dynamic DSP* algorithm.

3.3.5 Impact of the body motion in the algorithm performance

As mentioned previously the OC method is more suitable for the acquired signals perceived as arcs in the complex plane. However, real case scenarios might contain signal portions with wide arcs or even full circles, if the subject under monitoring moves the body during the monitoring period. In order to verify the performance of the algorithm herein proposed under conditions of RBM, an additional test case was considered. The vital signs of a subject were acquired during 6 minutes, while he/she was performing specific motions in three moments: raising the arm and touch the head, raising the arm and touch the chest and move forward and backward in relation to the radar. Figure 3.25 shows the resulting signal in both time domain

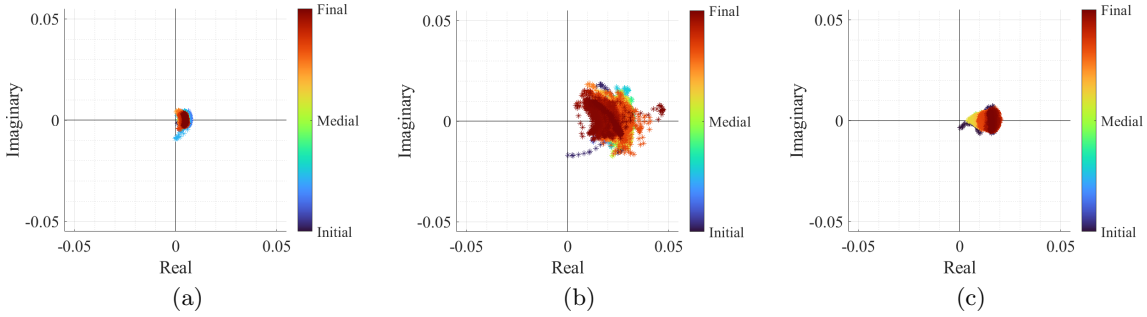

Figure 3.24: Real/Imaginary plots of the considered test case signals after implementing the *Dynamic DSP* algorithm [102]: (a) Case 1, (b) Case 2, (c) Case 3.

---

and the equivalent projection in the complex plane, before and after the implementation of the proposed algorithm.

By comparing Figures 3.25b and 3.25c it is possible to verify that the algorithm is robust to sudden and sporadic motions, even if they present full circles in the complex plane. The algorithm was able to remove the CDC offsets successfully, regardless the presence of high amplitude motion and this fact can be justified by three algorithm features. Firstly, the usage of overlapped windows enables one to address the motions smoothly by separating the motion in different windows. Secondly, the additional cost applied in the OC method (referred in equation (3.7)) used to prevent estimation transitions, was also useful when motions occur, because the estimated CDC offsets stay in the same zone. Finally, the smooth filter usage over the windows estimations before the interpolation, helped also the attenuation of eventual outlier estimations.

Figure 3.26 shows the corresponding arc shapes when the motions occurred and how all the tested algorithms behave under these circumstances. The first aspect that can be highlighted is the fact that not all types of motion generate full circles in the complex plane. For instance, raising the arm in front of the radar (see Figure 3.26a) generated a cluster of dispersed samples around what was supposed to be the arc. In this case, the OC method searches for a solution out of those samples, which is often close to the one obtained in the previous window. On the other hand, moving towards and backwards the radar (see Figure 3.26b) generates complete circles, since the motion amplitude is equivalent to more than one wavelength, and the OC method kept the same behavior.

The algorithm effectiveness was once again compared with state of the art algorithms. The LM was the most stable in both motion cases and the KA failed in the arm motion due to the wide cluster shape. As expected, both KA and LM algorithms seemed to provide accurate estimations of the exact values of CDC offsets, when applied to full circles. Thus, the potential of the algorithm herein proposed might be enhanced if combined with the usage of traditional circle fitting methods, when this type of motion is detected.

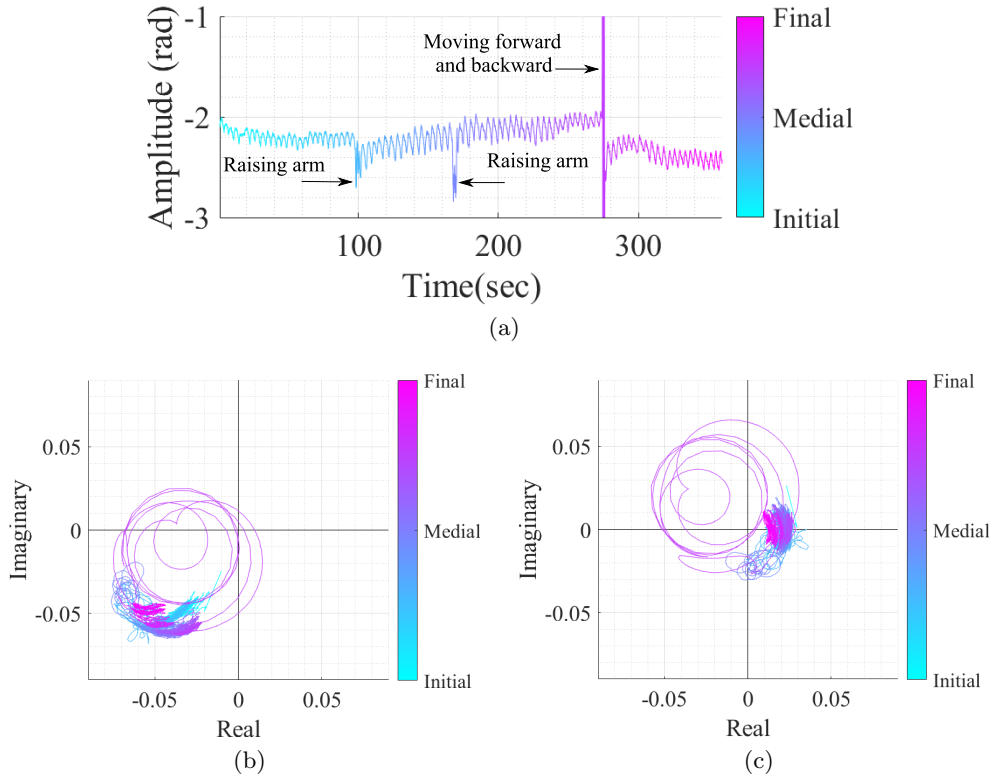

Figure 3.25: Case 4 containing vital signs with body motion [102]: (a) Time domain signal with CDC offsets, (b) Real/Imaginary plots with CDC offsets, (c) Real/Imaginary plots after applying the *Dynamic DSP* algorithm.

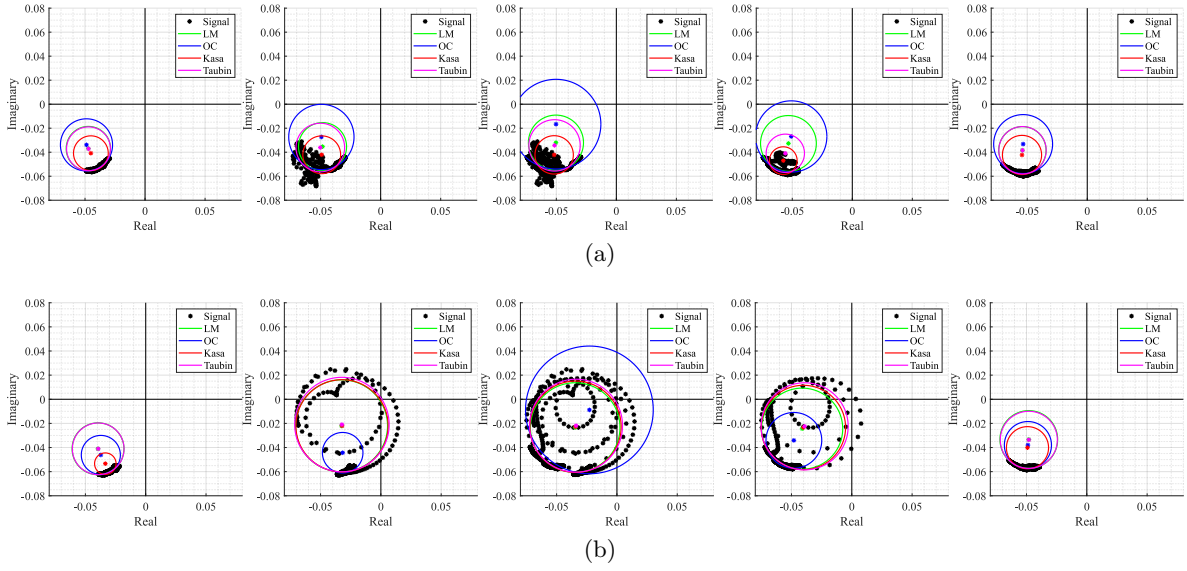

Figure 3.26: Circle fitting result over time for Case 4 [102]: (a) Windows 18 to 22 containing the motion of an arm raising up to the head, (b) Windows 53 to 57 containing the motion of the body moving forward and backward with respect to the radar.

3.4 Respiratory signal accuracy with improved *Dynamic DSP* algorithm

The *Dynamic DSP* algorithm presented in Section 3.3 was developed and evaluated in a primary stage using signals of three subjects. The dataset was further increased and the algorithm was again tested in 20 new subjects, being 10 males and 10 females with different physical characteristics and within the age range of 20-30 years old. Their physical statures are described in Table 3.6. The vital signs were again acquired following the *Emotional Protocol*.

Subject ID	Gender	Height [m]	CWP [cm]	**Subject ID**	Gender	Height [m]	CWP [cm]
ID01	F	1.62	80	ID11	M	1.88	94
ID02	M	1.78	114	ID12	M	1.86	84
ID03	F	1.73	109	ID13	F	1.64	80
ID04	M	1.88	87	ID14	F	1.75	80.5
ID05	F	1.61	73	ID15	F	1.71	80
ID06	F	1.68	77	ID16	M	1.74	81
ID07	M	1.75	87	ID17	M	1.62	91
ID08	M	1.81	98.5	ID18	M	1.77	94
ID09	F	1.54	71	ID19	M	1.78	108
ID10	F	1.61	72	ID20	F	1.57	73

F - Female, M - Male, CWP - chest wall perimeter

Table 3.6: Description of the physical stature of the 20-subject dataset.

The dataset has a total duration of 1626 minutes ($\approx$ 27 hours, 1 hour and 30 minutes per subject). The respiratory signal was acquired concurrently using the bio-radar prototype and the certified measuring equipment to serve as reference, namely the BIOPAC MP160 Data Acquisition System with Acknowledgment 5 Software (from BIOPAC Systems, Inc.). The BIOPAC (BPC) system is connected to an acquisition board, which have several modules for different types of signal acquisition, such as the Electrocardiogram (ECG), breathing or blood pressure. In this case, the respiratory signal was measured with the module RSP100C, which uses a transducer chest band placed around the chest cavity of the subject at test. This transducer measures the respiratory effort by analysing the instantaneous thoracic perimeter.

In order to synchronize both signals, the subjects were asked to perform a breathing pattern composed by three deep breaths, an apnea period around 10 seconds and a slow exhale as depicted in Figure 3.27. The final algorithm validation was performed by estimating the respiratory rate of all 20 subjects and by determining the error in Breaths per minute (BRPM) in relation to the result obtained with the BPC.

As mentioned in Section 3.3, the *Dynamic DSP* algorithm presents some limitations and one of them stand out negatively during this testing stage. The arc center estimations can occur in opposite sides of the arc as depicted in Figure 3.15 and hence successive windows might present opposite solutions, adding an undesired variability degree to the overall center estimation over time. In order to attenuate the general variability of the center estimations, a Savitzky-Golay filter was applied to the coordinates vectors before interpolation. However, in situations as Figure 3.15, the Savitzky-Golay filter provides intermediate values between consecutive windows and this affects the final aspect of the signal because the arc is pushed

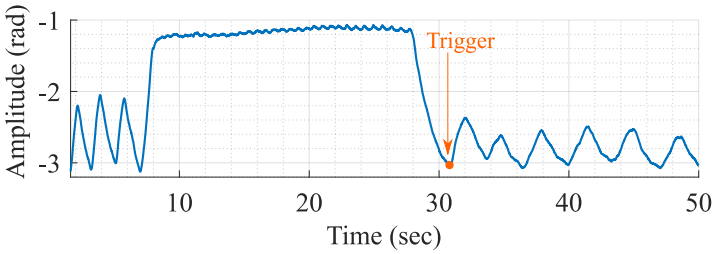

Figure 3.27: Breathing pattern and trigger definition for BRD and BPC signals synchronization.

---

to the complex origin. An additional cost was added to the cost function (see equation (3.7)), but this demonstrated not to be enough.

In order to solve this problem and others that arose subsequently, different versions of the *Dynamic DSP* algorithm were developed and they are summarized in Figure 3.28. In sum,

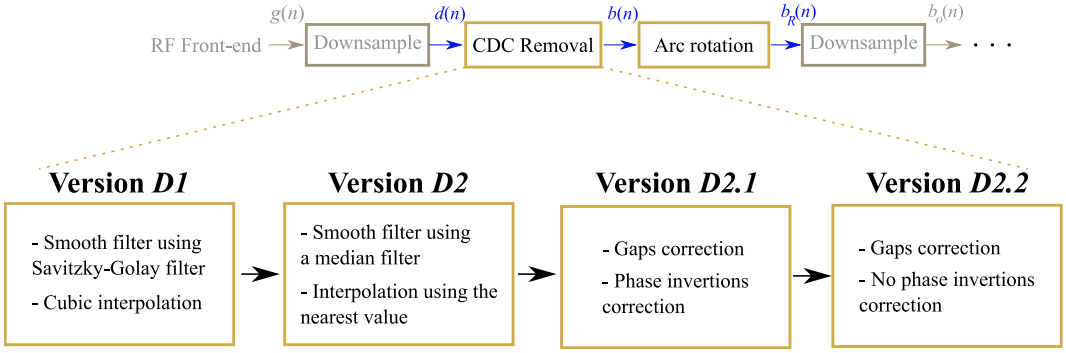

Figure 3.28: Evolution of all versions of the *Dynamic DSP* algorithm.

Version *D1* consists on the algorithm presented in Section 3.3, which uses the Savitzky-Golay filter to smooth the center estimations vector and uses the cubic interpolation to assign a CDC coordinates pair to each signal sample. In **Version *D2***, this filter was replaced by a median filter and the interpolation uses the nearest value instead of being a cubic interpolation. This update revealed being more effective since it was possible to remove the CDC offsets without altering the original signal. On the other hand, it led to two additional problems. The median filter kept the estimations located on the opposite side of the arc concavity, leading to phase inversions in the time-domain signal. Furthermore, the nearest value interpolation introduces discontinuity to the signal. The discontinuity problem was solved by correcting the phase everytime a gap occurred leading to **Version *D2.1***. Nonetheless, the phase inversion problem was more challenging to solve automatically, therefore a dedicated study was carried out.

3.4.1 Phase inversion impact

In order to understand if the phase inversions have impact in the signal rate accuracy, the signals of the 20-subjects dataset were processed using the different variants of **Version *D2*** of the *Dynamic DSP* algorithm, and the respiratory rate was computed for the different situations:

- Case i) is the **Version *D2.1*** test, where the phase inversions were corrected manually;
- Case ii) is the **Version *D2.2*** test, where the phase inversions were not corrected at all;
- Case iii) is the **Improved Version *D2.2*** test, where the phase inversions were not corrected and signals were pre-processed to improve the rate results.

For this purpose, Bio-Radar (BRD) and BPC signals were divided in one-minute segments and the respiratory rate was computed using the Zero-Crossing (ZC) method depicted in Figure 3.29. Firstly the zero-crossing intervals were identified (marked with a green cross) and the maximum of each interval was determined, corresponding to a peak (red dots). The time between peaks, also known by Interbeat Interval (IBI), was computed for each one-minute segment and a time threshold was applied afterwards to remove outliers. The threshold was computed using half of the mean IBI over the full segment. The number of BRPM was determined by the inverse of the median of the IBI. The same method is used later in Chapter 5 for the heart rate computation.

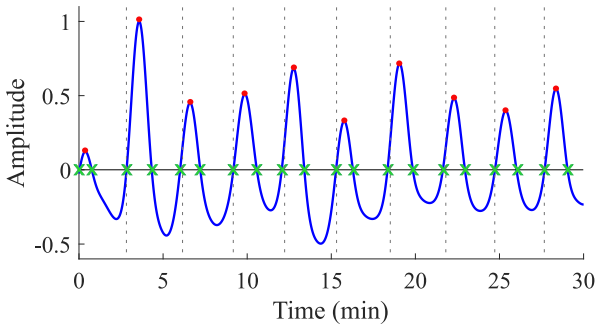

Figure 3.29: Representation of the ZC method for the signal rate estimation.

For each version test, the Mean Absolute Error (MAE) and the Root-Mean-Squared Error (RMSE) were computed and the results are presented in Table 3.7. One can verify that the results for Case i) and Case ii) are not substantially different, therefore it can be concluded that the phase inversions can be neglected.

Thereafter, an additional step was implemented to reduce the error in the respiratory rate accuracy, consisting on the Case iii). Before applying the ZC method, both BRD and BPC signals were filtered to remove noise, using a 200-order low pass Finite Impulse Response (FIR) filter with cut frequency equal to 0.5 Hz. This filter order was selected because it provides a 20 dB attenuation for frequencies above 1 Hz, turning signals more smooth. The mean value of the filtered signals was removed using a moving mean approach with a window length equal to 1000 samples. This window length was selected assuming that the signal mean does not change highly in a 10 seconds period. Finally, signals were normalized according to their maximum amplitude and the ZC was applied. In general, the MAE and RMSE decreased slightly in the Case iii) as it can be observed in Table 3.7. The average MAE of all subjects was equal to 0.33 BRPM and since both BRD and BPC signals were processed through the same approach, it is possible to conclude that the BRD signals have an accuracy identical to the BPC.

Since the *Dynamic DSP* algorithm is somehow complex, the respiratory rate was computed using the *Simplified DSP* algorithm for comparison purposes. The error results are shown in the last two columns of Table 3.7. In general, the respiratory rate errors increase if BRD

Subject ID	*Dynamic DSP*						*Simplified DSP*	
	Case i)		Case ii)		Case iii)			
	MAE	RMSE	MAE	RMSE	MAE	RMSE	MAE	RMSE
ID01*	0.21	0.28	0.20	0.27	0.17	0.25	0.13	0.19
ID02	0.22	0.36	0.22	0.36	0.17	0.31	0.64	1.35
ID03*	0.47	1.29	0.51	1.33	0.42	0.99	1.42	3.59
ID04*	0.91	2.84	0.92	2.89	0.84	2.63	0.90	2.14
ID05*	0.41	0.69	0.50	0.95	0.40	0.63	0.71	1.32
ID06*	0.18	0.27	0.18	0.26	0.14	0.20	0.15	0.20
ID07	0.21	0.38	0.21	0.38	0.20	0.37	0.25	0.44
ID08*	0.81	1.55	0.82	1.53	1.09	2.13	1.03	2.05
ID09*	0.28	0.58	0.28	0.55	0.31	0.63	0.76	1.64
ID10	0.29	0.43	0.29	0.45	0.35	0.97	0.74	2.05
ID11*	0.45	1.68	0.40	1.10	0.25	0.34	0.28	0.43
ID12	0.29	0.61	0.29	0.61	0.22	0.33	0.26	0.38
ID13	0.33	0.89	0.33	0.89	0.32	0.51	0.45	1.16
ID14	0.18	0.22	0.18	0.22	0.14	0.17	0.22	0.41
ID15*	0.15	0.29	0.16	0.23	0.16	0.30	0.22	0.32
ID16*	0.39	0.83	0.42	1.17	0.29	0.81	0.55	1.84
ID17	0.47	0.82	0.47	0.82	0.42	0.67	0.66	1.50
ID18*	0.55	1.28	0.48	1.07	0.26	0.48	0.66	1.70
ID19*	0.17	0.22	0.18	0.23	0.16	0.20	0.48	0.99
ID20*	0.18	0.28	0.21	0.31	0.24	0.51	0.38	1.02
Average	0.36	0.79	0.36	0.76	0.33	0.67	0.55	1.24

IDXX* - signals with phase inversions, Case i) test of **Version *D2.1***,
Case ii) test of **Version *D2.2***, Case iii) - test of **Version *D2.2*** with improved results

Table 3.7: Error of the respiratory rate in BRPM.

signals are processed with the *Simplified DSP* algorithm, but different results were presented among subjects. For instance, ID01, ID04 or ID06 kept the same error values, indicating that for these specific subjects both algorithms could be used. Nonetheless, the same is not applied for subjects ID03, ID05 or ID16, since the errors increased, specially the RMSE. The RMSE increase indicates the presence of outliers, i.e. signal segments with an increased discrepancy in relation to the BPC. The reason why the signals of some subjects can be equally processed with both algorithms but others do not, might be related with the individual variability, which is related not only with the cardiopulmonary function [34], but also with the RBM occurring during the experiment. The RBM is unpredictable, so in general the usage of the *Dynamic DSP* algorithm is indeed more indicated, at least in longer monitoring periods.

3.5 Final considerations

In this chapter, different DSP algorithms were proposed to remove the CDC offsets caused by parasitic reflections and to recover the vital signs from a baseband bio-radar signal. Throughout the different stages of this PhD work, different versions were used and they can be mainly divided in two main algorithms: the *Simplified DSP* algorithm and *Dynamic DSP* algorithm. Respectively, the final versions are the **Version *S3*** for the *Simplified DSP* algorithm and the **Version *D2.2*** for the *Dynamic DSP* algorithm. Both simplified and dynamic versions are based in fitting algorithms applied to the arc perceived in the complex plane, in order to estimate its center coordinates and remove them accordingly. After removing the CDC offsets, the arc position in relation to the complex plane is adjusted to be oscillating around the 0° phase value and the arctangent is computed to extract the vital signals.

It was concluded that the effectiveness of the CDC offsets removal is directly related with the offset values estimation. Low amplitude signals do not contain enough information to perform this task successfully. One possible solution for this problem was developed, and it consisted of taking advantage of the forward and backward RBM, since it provokes complete circles rather than arcs in the complex plane. The solution was indeed effective, however it is restricted to one type of body motion, that might not occur often in real context scenarios. Besides, the CDC offset values might change over time due to non-static monitoring conditions, either due to the environment itself or related to the subjects instability.

In this sense, the *Dynamic DSP* algorithm was developed as an improved version of the *Simplified DSP* one. This algorithm is robust enough to encompass the CDC offsets change over time and to the lack of arc resolution due to low amplitude chest wall motion. For this purpose, an arc fitting algorithm was developed and applied dynamically through a windowing approach. This method is based on a cost function minimization that only depends on the arc center estimation regardless on its radius. In contrast, circle fitting algorithms based on LSF optimization, such as the LM or KA methods, are is highly sensitive to outliers leading to center estimations within the signal samples. The developed arc fitting method is forced to start searching for a suitable solution outside the data points and it demonstrated to be robust in signals with low resolution.

For comparison and validation purposes, different fitting algorithms including the proposed one, were tested using three monitoring scenarios. The CDC component from a total of 1400 windows was analyzed using all fitting methods, and the proposed method did not presented any failure case among all windows and presented only 0.2% of cases in a critical situation. These results could be achieved using a lower number of searching points, which enables the run time reduction. Additionally, it provides stable estimations over the full signal, as demonstrated by the standard deviation of the estimated CDC offsets. The remain methods presented higher variability and a higher number of failure cases.

The CDC offsets estimation is performed dynamically over time through windowing, as well as the arc rotation to force the arcs to oscillate around the 0°. This arc rotation presented several advantages, since thus it is possible to avoid the wraps occurrence. Although, the *Dynamic DSP* algorithm was implemented and tested using offline signals, its flow allows a real time implementation, taking a run time of 2 seconds to process full 25-minute signals.

The effectiveness of the *Dynamic DSP* algorithm in conditions of body motion was also tested, and it was successful in case of sudden and sporadic motions. However, a more detailed study is required to understand the algorithm limits in terms of body motion duration and

body motion types.

Furthermore, the *Dynamic DSP* algorithm presents other limitations. The CDC offsets estimation might occur in opposite sides of the arc concavity. If this effect is smoothed, intermediate values are provided for consecutive windows, which forces the final arc to oscillate over the complex origin during that instances, causing a disruption of the final signal. An alternate version was developed to improve this aspect, which in practice neglects the window transitions leading to phase inversions in the time domain signal. After inspection, it was concluded that such phase inversions do not affect the signal rate computation.

Due to these issues and also due to the increased complexity of the *Dynamic DSP* algorithm in comparison to the *Simpified DSP* version, a final validation was carried out by comparing the respiratory signal error if signals are extracted with both algorithms. The results demonstrated that the *Dynamic DSP* algorithm outperforms the *Simplified DSP* version, since the RMSE increases from 0.67 BRPM to 1.24 BRPM if the simplified version is used.

Chapter 4

System Full Integration in a Car Seat Upholstery

The work presented in this chapter was developed in collaboration with the FibEnTech Research Unit from Universidade da Beira Interior. This work stage was dedicated to evaluate which were the constraints of integrating the bio-radar system in a customized application, addressing the market needs. In this context a car seat upholstery prototype was developed, integrating textile antennas to further monitor the respiratory signal of the driver.

Part of the work herein presented was performed within the scope of the project TexBoost - less Commodities, more Specialities[1], more specifically the PPS4: Development of iETextiles, smart solutions for sensing and monitoring in vehicular mobility. The goal of this project was to develop a smart seat cover, containing a sensor network to monitor the driver comfort. All sensors were integrated in the upholstery textile, including the bio-radar antennas, a temperature sensor, a humidity sensor and a pressure sensor.

The developments of this chapter resulted in the following contributions:

- C. Gouveia, C. Loss, Z. Raida, J. Lacik, P. Pinho and J. Vieira, "Textile Antenna Array for Bio-Radar Applications", 23^{rd} International Microwave and Radar Conference (MIKON), Warsaw, Poland, p. 315-319, 2020

- C. Loss, C. Gouveia, R. Salvado, P. Pinho and J. Vieira, "Textile Antenna for Bio-Radar Embedded in a Car Seat", *Materials*, vol. 14, no. 1, p. 213, 2021

- C. Gouveia, C. Loss, P. Pinho, J. Vieira, D. Albuquerque, "Low Profile Textile Antenna for Bio-Radar Integration into a Car Seat Upholstery",*IEEE Antennas and Propagation Magazine*, submitted for publication in July 2022.

- R. Silva, M. Midão, D. Esteves, A. Leite, P. Peixoto, C. Gouveia, P. Pinho, J. Vieira, D. Pires, T. Silveira, C. Loss, and R. Salvado, "Vehicle seat cover with a monitoring system," International Patent Pending WO/2022/070 137, PCT/IB2021/059 011, Apr., 2022.

[1]This work was funded by European Regional Development Fund (FEDER), through the Competitiveness and Internationalization Operational Program (COMPETE 2020) of the PT2020 framework [Project TexBoost with Nr. 024523 (POCI-01-0247-FEDER-024523)], in paternship with Instituto de Telecomunicações, Universidade da Beira Interior, CeNTI - Centro de Nanotecnologia e Materiais Técnicos, Funcionais e Inteligentes and Borgstena Textile Portugal, Unipessoal Lda.

4.1 Introduction

One possible solution to fully integrate the bio-radar setup in customized objects, is the antenna design and the manufacture process using non-conventional substrates. Antennas are the system element which stipulates the line-of-sight between the radar and the target. Therefore, their full integration in the application-objects is a possible solution to enable the system camouflage. Textiles might be used for this purpose, however the bio-radar performance cannot be compromised and the quality of the signals should be kept accordingly.

Textile materials are thin, lightweight, low profile, and easy to adapt to any surface [76]. Planar antennas (as for the microstrip antenna case) are suitable for textile implementation, which can be accomplished by assembling textile layers, using conductive materials for the radiating element and the ground plane, interleaved with a dielectric material for the substrate [79], [126]. The performance of these antennas depends on the material selection. There is a vast diversity of materials that can be used as a substrate (woven, non-woven, knits, etc.), depending on the desired application. Also, there is a large range of commercially available electro-textiles, incorporating fibres, filaments, or coatings of metals, with high conductivity, enabling the development of antennas with acceptable performance [79], [126].

Nonetheless, textile antennas must be developed with care. Textile materials are porous, and their electromagnetic properties depend on the density of the fibres, air volume and the size of the pores [127]. Moreover, they are also flexible and compressible, which might cause changes in thickness and density during the manufacturing process. Thus, these impairments should be taken into account in the antenna design [128]. For instance, it might be required to adjust the relative permittivity value (ϵ_r), through the Microstrip Resonator Patch Method proposed by [77]. This method consists on designing a patch antenna using an estimated ϵ_r, manufacture it and measure its S_{11}. The real ϵ_r value is determined through the eventual shift observed in the measured S_{11} [77]. As for the substrate thickness, it is typically measured using compressional tests [129]. Considering that some manufacturing techniques apply compression over the antenna [78], or the antenna integration in the final application might be conducted within a tight area, the substrate height used in simulations should not be the measured one with the fabric at rest, but rather the average value measured under the compressional process [130]. The manufacturing process is an important aspect as well. Beyond the different techniques proposed in literature, it can be highlighted the laminating process [78], [79], screen-printing [80], [81] and embroidered [82], [83]. The laminating technique is the most common technique to manufacture textile antennas and it consists on assembling the antenna components with thermal adhesive sheet through ironing.

Literature had already presented radar solutions using textile antennas. For example, in [84] a radar system is fully integrated in a rescue worker garment, to perform a through-wall target detection. For this purpose, a four-element antenna array was developed to scan the surroundings, and the echo signals are received using an active wearable antenna. In [85] a textile waveguide antenna is developed to perform beamforming from 7° to 20°. In the biomedical context, on-body solutions were proposed in [86], [87] to measure vital signs. In [86] it is demonstrated the ability to detect the respiratory signal using multi-material fiber antennas. The respiratory signal was extracted through the detection of the antenna physical deformation due to the chest wall motion, and also through the change of the dielectric properties from the lungs during inhale and exhale functions. Additionally, in [87] a textile coupler is proposed for vital signs monitoring, through the evaluation of the S_{21} parameter phase variation.

Considering the vehicular case study, the bio-radar system can be used to monitor the vital signs of the driver, reducing the probability of accidents due to sudden disease or to the fatigue state. Solutions embracing the bio-radar application in vehicles have already been proposed in literature [59], [106], [131]–[133]. For instance, in [131], [133] an UWB pulsed radar was used to capture the vital signs of the car occupants, with the radar located in the area of the rear-view mirror. In the same context, [132] used a CW radar operating at 24 GHz to detect forgotten children on the rear bench of a vehicle. The developed sensor is mounted in the ceiling, allowing the full coverage of the area occupied by the child. All [131]–[133] works have used commercial radars, simply placed in the car.

Object-integrated solutions were presented in [59], [106], as a discrete alternative to capture the driver's vital signs. In these studies, the cardiac and respiratory signals were acquired from the back of the subject under test. The vital signs were captured through active near-field coherent sensing, wherein a significant part of the RF energy couples into the human body. In this case, the motion of the body organs alters their dielectric properties accordingly, affecting the near-field coupling between the transmitting and receiving antennas. Nonetheless, some drawbacks of body coupling technique were identified in [59]. For instance, the direct contact with the body can cause the antenna near-field to be loaded by the dielectric behavior of the biological tissues, so it is necessary to keep a certain distance. Body coupling methods also restrict the range of possible upholstery materials since leather induces high attenuation to signals, according to [59]. Furthermore, the direct contact with the subject's body can affect the results since the body motion can cause friction over the antennas, leading to their damage in a long term perspective. Thus, the exact location of the antennas should be selected with care.

Aiming to develop of a fully operational prototype, concurrently discrete and comfortable for the user, in this work, a trilaminate upholstery fabric was designed and manufactured, integrating two textile antennas to be used for transmission and reception in a bio-radar system. The upholstery is then applied to a car seat to monitor the respiratory signal of the subject. An example of the proposed prototype is depicted in Figure 4.1.

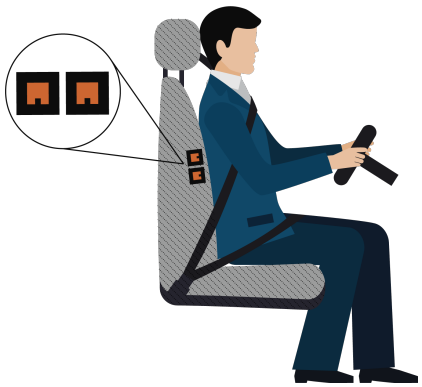

Figure 4.1: Illustration of the proposed upholstery prototype.

In order to reach the solution depicted in Figure 4.1, first of all it was necessary to select the appropriate location for the antennas in the car seat. Then, different prototype versions were developed aiming to identify the most suitable antenna design for this application. Figure 4.2 summarize the different prototype versions developed for each work stage.

First of all, **Version *P1*** used textile single patch antennas and their performance to

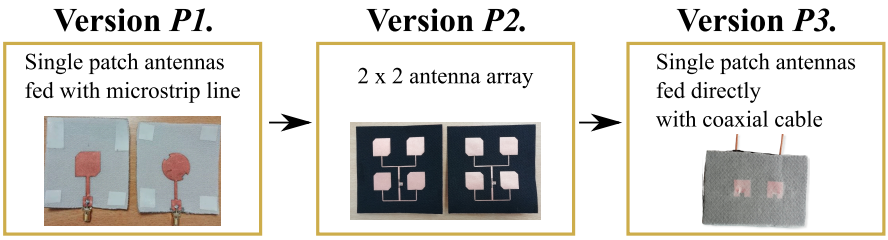

Figure 4.2: Evolution of the different upholstery prototype versions developed for this case study.

---

capture vital signs was compared with conventional-substrate ones. After validating the textile antennas usage, the **Version *P2*** was developed in order to identify which is the most appropriate antenna directivity for this specific case study. Finally, **Version *P3*** consisted on the upholstery final prototype, developed with the antennas embedded. A final validation was carried out by measuring the vital signs of different subjects with the final prototype and compare them with a certified measuring equipment.

4.2 Selection of the antennas location in the car seat

Typically, bio-radar systems are operated in front of the subject, where the chest wall displacement amplitude is maximum [39], [134]. This specific case study requires the bio-radar operation in an alternate location, therefore a series of preliminary tests were conducted aiming to select the most appropriate position.

For this purpose, conventional-substrate antennas were placed in different locations of the car seat. The used antennas are shown in Figure 4.3 and they were previously developed in [135]. They consist on LHCP microstrip patch antennas operating at 5.8 GHz. They are a circular and a square patch and their substrate is the Rogers RO4360G2™ (Rogers Corporation, USA), with $\varepsilon_r = 2.55$, $\tan \delta = 0.0038$ @ 10 GHz and 0.78 mm of height. These antennas have circular polarization, which is an important feature for the bio-radar applications, as previously highlighted in Section 2.3.

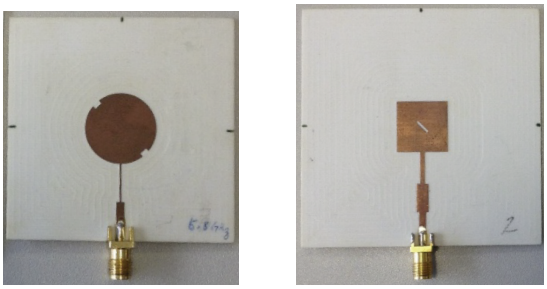

(a) (b)

Figure 4.3: LHCP antennas using conventional-substrate for 5.8 GHz from [135]: (a) circular patch antenna and (b) squared patch antenna.

Figure 4.4 presents the tested locations, which are the following:

- **Test 1** - Exterior part of the side lumbar support (Figure 4.4a). The center between the transmitting and receiving antennas was aligned with the chest wall of the subject;
- **Test 2** - Interior part of the side lumbar support (Figure 4.4b). This test aimed to verify the impact of the extracted signal if the antennas are closer to the human body;
- **Test 3** - Exterior part of the back lumbar support (Figure 4.4c);
- **Test 4** - Interior part of the seat pad. In this case the antennas were slightly tilted towards the subject (Figure 4.4d).

(a) (b) (c) (d)

Figure 4.4: Tested positions for the antenna location selection: (a) Test 1 - side lumbar support (exterior), (b) Test 2 - side lumbar support (interior), (c) Test 3 - back lumbar support, (d) Test 4 - seat pad.

The respiratory signal of a subject was measured on each test, following the *Car Seat Protocol* as represented in Figure 4.4a. Signals were acquired during 20 seconds and then processed using the *Simplified DSP* algorithm (see Section 3.2). After extracting the respiratory signal, their mean value was removed and the signals were normalized according to their maximum amplitude. The obtained time-domain signals are shown in Figure 4.5.

The signals in Figure 4.5 demonstrate that it is possible to measure the respiratory signal from all the tested locations. As it was discussed in Chapter 3, it is difficult to drive conclusions regarding the signal amplitude and SNR looking only to the time domain signals, since the extraction algorithms and the arc position in the complex plane have a direct impact in the signal amplitude. Therefore, more conclusions can be driven from the raw complex signals, presented in the polar diagram of Figure 4.6. First of all, the signal containing the lowest CDC offsets and an arc with high amplitude was the signal from **Test 4**, which was somehow expected since the antennas are in line-of-sight with the chest wall front. **Test 1** and **Test 2** presented slightly higher CDC offsets and the measured sideways chest wall displacement produced arcs with a decreased amplitude when compared to the other tests. The increased CDC offsets can be justified by the reduced radar cross-section area. Finally, **Test 3** was the one presenting the highest CDC offsets, which were probably due to the metallic structure of the car seat.

Although **Test 1** was the one presenting the lowest arc amplitude, the exterior part of the side lumbar support was still the selected location for the following reasons: when located in the exterior part of the car seat, a relative distance is kept between the antennas and

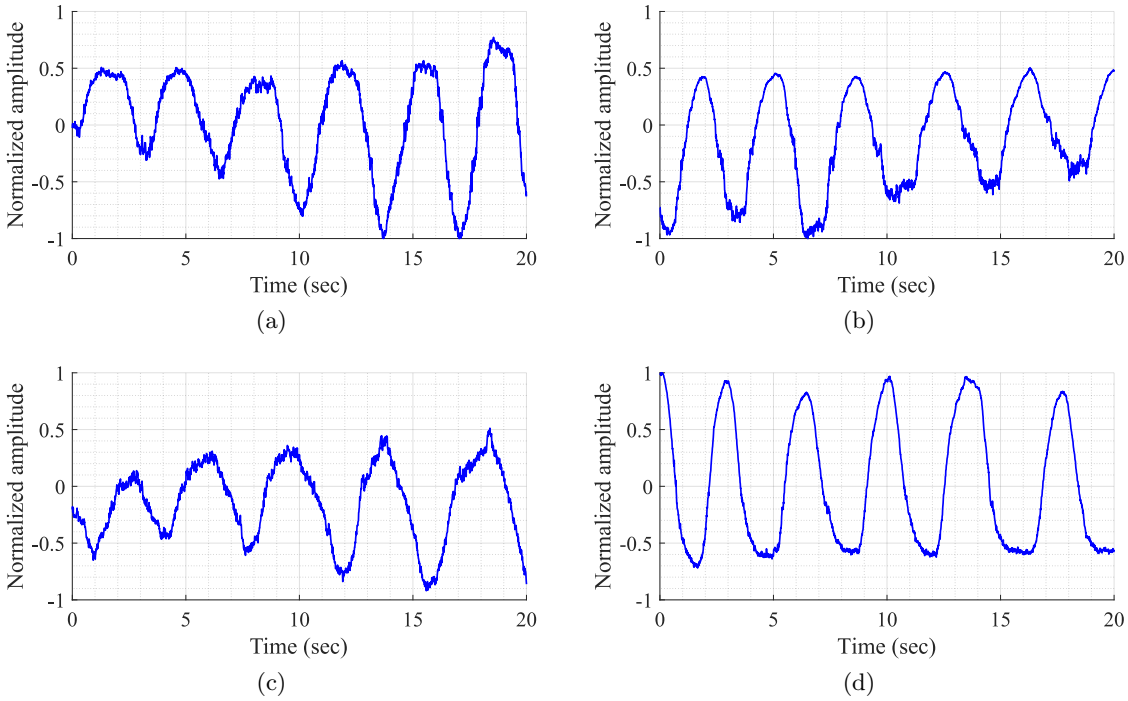

Figure 4.5: Extracted respiratory signals for each position test: (a) Test 1, (b) Test 2, (c) Test 3, (d) Test 4.

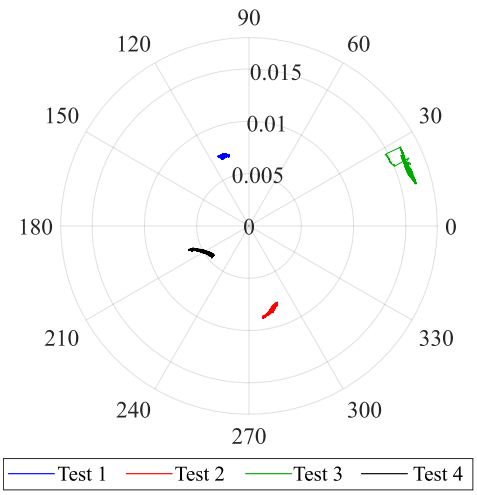

Figure 4.6: Polar diagram of the raw signals from all the conducted position tests.

---

the subject, assuring the extraction of vital signs based in the micro-Doppler effect and also the far-field operation, if the final antennas are small enough. Furthermore, if the antennas would be located in the interior part of the side lumbar support as in **Test 2**, the body friction could generate additional noise and in long term the antennas could be more damaged. In contrast with the **Test 4**, the selected location assures the comfort of the subject, since for the **Test 4** case the subject should keep the legs straddled, which could be uncomfortable for

long periods of time. Finally, in the **Test 3** the antennas were located behind the metallic structure of the car seat, which could generate an unpredictable multipath environment that could have a destructive behavior on the received signal. But since the goal is to integrate them in the upholstery, over the car seat structure, another impairment arises because the antennas would need to be too close the subject's body as well.

4.3 Textile antenna validation for vital signs acquisition

4.3.1 Textile single patch antennas design

After selecting the appropriate location for the antennas in the car seat, the usage of textile antennas in this case study was validated. For this purpose, a comparison was performed between conventional-substrate antennas (namely the antennas presented in Figure 4.3 [135]) and textile-substrate antennas (prototype **Version *P1***).

The textile antennas were manufactured using a Substrate Integrating the Ground Plane (SIGP), based on the 3D weft-knitted spacer fabric. This textile integrates the dielectric substrate and the conductive ground plane in a single sheet, as showed in Figure 4.7. The relative permittivity of the SIGP were re-evaluated for 5.8 GHz using the Microstrip Resonator Patch Method [77] and a more detailed information can be found in [136].

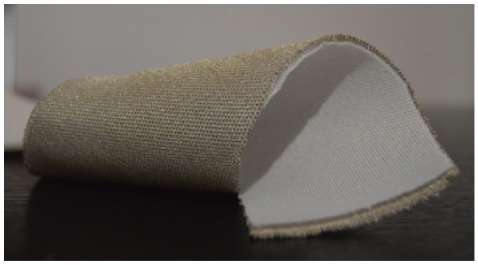

Figure 4.7: SIGP textile for the antenna substrate composed by a dielectric part in white, which is a 3D weft knitted spacer fabric and the integrated conductive layer in gold color [136], [137].

Its characteristics are the following: it has a substrate height equal to $h = 1.957$ mm, with a relative permittivity $\varepsilon_r = 1.3$ and $\tan\delta = 0.006$ @ 2.25 GHz [127]. The integrated ground plane presents a thickness equal to $t = 0.043$ mm and a conductivity equal to $\sigma = 54$ kS/m. The patch was manufactured using a Pure Copper Polyester Taffeta Fabric (PCPTF) (Less EMF Inc., USA), with a thickness equal to $t = 0.08$ mm and conductivity equal to $\sigma = 62.5$ kS/m.

For a fair comparison, the antennas design of Figure 4.3 [135] was replicated for the textile antennas, which were subsequently simulated and optimized in the CST Microwave Studio 2017, namely using a circularly-shaped patch with slots (Figure 4.8a), and a square patch with truncated corners, (Figure 4.8b), both with LHCP.

Figure 4.8 shows both circular and squared designs. These antennas were fed through a feeding line, which is composed by a quarter wavelength transformer identified by line L and a 50 Ω line identified by T. The final stage of the simulation was performed using a SMA connector model designed in CST software. Both textile antennas were 70×70 mm and their final dimensions are presented in Table 4.1.

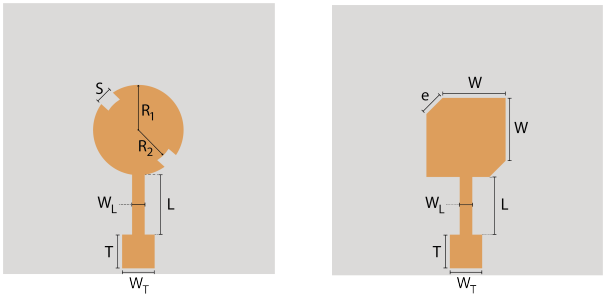

(a) (b)

Figure 4.8: Textile LHCP antennas using SIGP [136]: (a) circular patch antenna and (b) squared patch antenna.

Circular Patch Antenna							Squared Patch Antenna					
R1	R2	S	L	T	W_L	W_T	e	W	L	T	W_L	W_T
11.60	9.35	4.10	14.00	8.85	3.00	8.30	5.50	20.40	14.50	8.50	3.65	8.30

Table 4.1: Final dimensions of both optimized textile antennas [mm] [136].

After their optimization in the simulation environment, both textile antennas were manufactured using the laminating technique [78] in the FibEnTech Research Unit from Universidade da Beira Interior. Thermal adhesive sheet was used to assemble all the antenna components, using an industrial ironing press under 10 bar at 200°C, and during 6 seconds without steam [128]. All parts of the antenna were cut by a laser cutting machine to ensure geometrical accuracy [128]. To feed the antennas, a SMA connector was used.

4.3.2 Textile single patch antennas performance evaluation

After manufacturing both antennas their performance was evaluated. Starting with the S_{11} parameters, they were measured using a Vector Analyzer Network, namely the Keysight PNA-X N5242A and they are shown in Figure 4.9 and Figure 4.10, for the circle and square patch respectively. It is possible to observe that the measured results are slightly shifted in frequency, in relation to the simulated ones. Nonetheless, acceptable S_{11} values were obtained for 5.8 GHz, namely -12.43 dB for the circle patch and -15.15 dB for the square patch. Beside the S_{11}, the radiation pattern was also measured and it is presented in Figure 4.11.

It is possible to observe that once again the achieved results are in agreement with the simulated ones. Circular patch presented a measured HPBW equal to 81° while the simulated was equal to 79.9°. The measured HPBW for the squared patch was equal to 69°, while the simulated was equal to 68.7°. The gain was also measured and both antennas presented results similar to the simulated ones. The simulated gain corresponding to the circular patch antenna was equal to 6.6 dBi, while the measured one was equal to 6.2 dBi. The squared patch antenna presented a simulated gain equal to 7.2 dBi and the measured one was equal to 8.2 dBi. Finally, since these antennas have circular polarization the axial ratio was measured and the results are shown in Figure 4.12. The minimum measured axial ratio of the circular patch antenna was centered in 5.8 GHz as it was simulated, having a measured magnitude equal to 4.12 dB, while the simulated was 0.44 dB. On the other hand, the same was not

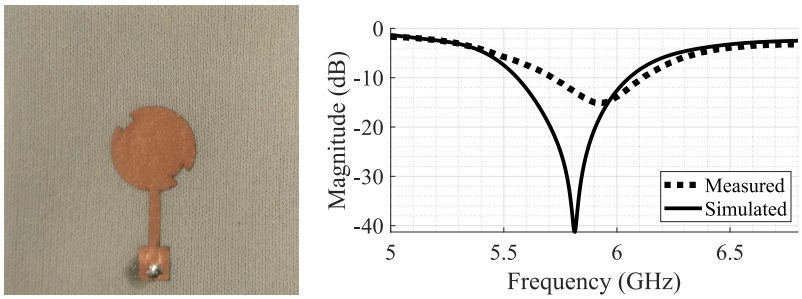

(a) (b)

Figure 4.9: Circular patch textile antenna [136]: (a) manufactured antenna and (b) S_{11} results.

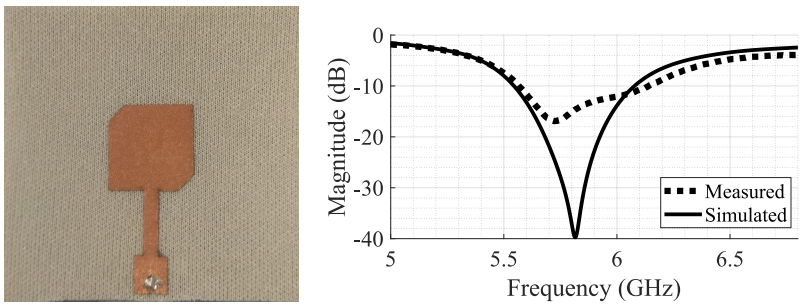

(a) (b)

Figure 4.10: Squared patch textile antenna [136]: (a) manufactured antenna and (b) S_{11} results.

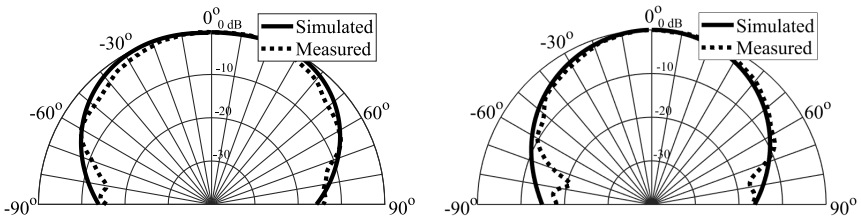

(a) (b)

Figure 4.11: Simulated and measured normalized radiation pattern [136]: (a) circular patch antenna and (b) squared patch antenna.

---

observed for the squared patch case. The measured axial ratio minimum was centered at 5.9 GHz and the magnitude at 5.8 GHz was equal to 4.53 dB, while the simulated one was equal to 0.93 dB. Thus, in practice the antennas present an elliptical polarization [108].

Overall the measured antenna parameters were close to the simulated ones. The eventual deviations were mostly observed in the S_{11} parameter and in axial ratio, and they can be due to several factors. Textile antennas are heterogeneous and highly porous, and according to [128] the superficial roughness generates air gaps between the dielectric substrate and the patch, leading to inaccuracies in the results. Furthermore, in [77] it is also pointed out that errors can be introduced by the SMA connector soldering, as well as the the manual

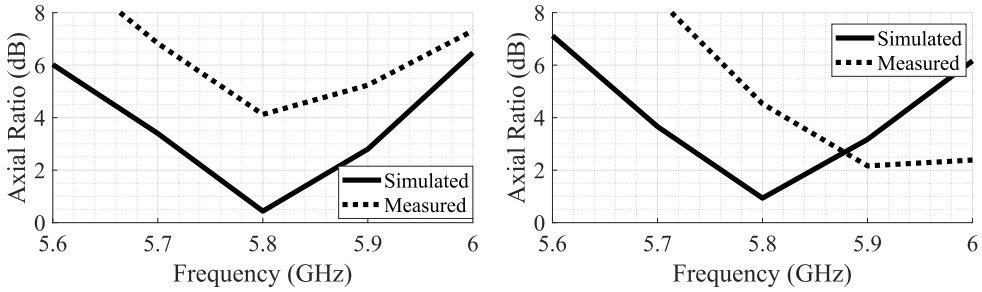

Figure 4.12: Simulated and measured axial ratio [136]: (a) circular patch antenna and (b) squared patch antenna.

procedure of the manufacture. Hence, more inaccuracies in the measured results are expected when compared with the conventional-substrate antennas. As for the results obtained in the axial ratio, they could be worsened by the design used to induce circular polarization, since single-feed techniques were used and they have as drawback the narrowband axial ratio performance [108].

4.3.3 Respiratory signal acquisition using textile antennas

Thereafter, the usage of textile antennas in the bio-radar framework was validated by acquiring the respiratory signal of one subject following the *Car Seat Protocol* as depicted in Figure 4.4a. The same measurement was performed using the textile and conventional substrate antennas, where in both cases the antennas were placed in the exterior part of the side lumbar support and approximately in the same location, as showed in Figure 4.13.

Figure 4.13: Position of the transmitting and receiving antennas in the car seat, to acquire the respiratory signals using [136]: (a) conventional-substrate antennas and (b) textile-substrate antennas.

Signals were once again processed with the *Simplified DSP* algorithm, and the obtained breathing signal is shown in Figure 4.14. One can observe that textile antennas have the same capability to detect the respiratory signal as the conventional-substrate antennas. Eventual differences on both signals amplitudes were expected, once the respiratory signals were not acquired at the same time. During the testing antennas switch, the same location was approximately kept but the exact illumination area was impossible to ensure.

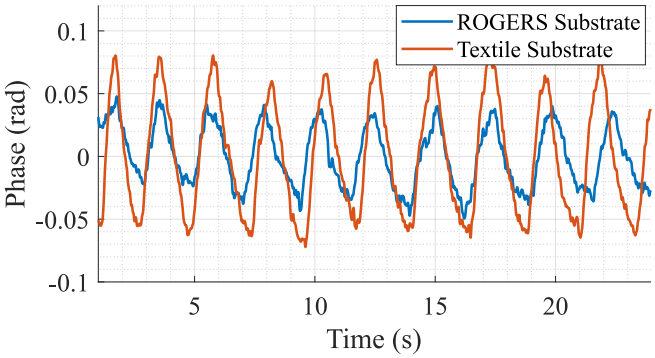

Figure 4.14: Comparison of the respiratory signals acquired using conventional and textile substrate antennas [136].

The amplitude differences observed in Figure 4.14 raised other important aspect respecting to the integration of the bio-radar in a specific application. It is necessary to have a considerable level of flexibility to equally capture the subject's vital signs regardless his/her physiognomy. More specifically, it is important to align the antennas beam with the subject's chest wall, however in a real context it is not feasible to calibrate the antennas position every time the subject changes. In this sense, this first test served also to determine which might be the most appropriate location of the antennas in the side lumbar support, by identifying where is the best detection point common to the majority of the population at hand. Then, an additional validation step was performed by acquiring the respiratory signal of six different subjects, with different physical statures, without adjusting the antennas position. Table 4.2 describes the subjects physical characteristics, which beside the chest wall perimeter and height, it was also considered a Distance D corresponding to the distance between the diaphragm and the midpoint between the transmitting and receiving antennas. The Distance D is an important parameter since it can vary largely regardless of the subject's height. Furthermore, this measure shows the expansion that the radar is evaluating, which can vary between the belly or the chest wall motions. For people with larger chest cavities, the radar could also measure the back motion, rather than the chest wall leading the signals with a decreased amplitude.

The obtained respiratory signals of each subject can be observed in Figure 4.15. With this experiment, it was possible to detect the respiratory signals of all subjects regardless of their physical structure, which means that the signal can be acquired even if the detection point is not optimal for all subjects. Considering the same signal duration (30 seconds), it is possible to distinguish diverse characteristics among the detected signals. For instance, different respiratory rates were obtained, where the subject 2 presented a lower respiratory rate, and subject 4 presented a higher breathing rate. Other breathing patterns can also be identified, for example, subject 5 had laughed after 15 seconds of the experiment, which caused a sudden slope on the waveform. As the positioning of the antennas was not changed

Subject No.	Gender	Chest wall perimeter [cm]	Height [m]	Distance D [cm]
1	Female	70	1.50	7
2	Male	94.1	1.69	16
3	Male	84.5	1.73	16.5
4	Female	74.5	1.65	11.5
5	Female	75.5	1.56	12
6	Male	82	1.60	13

Table 4.2: Physical description of the subjects under test to validate the best antennas location in the side lumbar support [136].

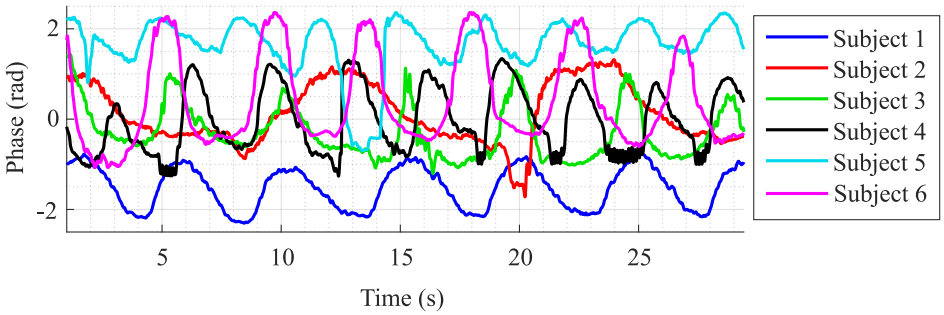

Figure 4.15: Respiratory signals of six subjects captured without changing the textile antennas position (adapted from [136]).

between subjects, signals showed different peak-to-peak amplitudes, different mean values, and different SNR levels as expected, when compared with the signal in Figure 4.14.

The ability to equally acquire the vital signs of different subjects is mainly related with the antennas HPBW. In this case, single patches were used which presented a wider beamwidth. On the other hand, and as seen in Chapter 2, directive antennas might provide a better SNR, at least during a traditional bio-radar operation (when the antennas are located in front of the subject). Considering now this specific application, in the next Section it is verified if the usage of directive antennas can be equally advantageous.

4.4 Selection of the antenna directivity for customized bio-radar applications

4.4.1 Textile antenna arrays design

Higher directivity can be obtained with a patch antenna array. A directive beam allows the energy to be focused on the subject's chest wall, decreasing the reception of parasitic reflections that occur within the monitoring environment. Nonetheless, narrow beams imply antennas with larger dimensions, which can be an impairment for the bio-radar integration in a specific application. For instance, the side lumbar support have a restricted area where the antennas can be located, in order to guarantee the proper alignment with the majority of the population. Thus, 2×2 textile antenna arrays was the selected design, since it respects a balanced trade-off between directivity and antennas dimensions.

Two textile antenna arrays were designed, manufactured and tested (prototype **Version *P2***). The developed antennas are circularly polarized, where one is LHCP and the other is

RHCP, respecting the conclusions reached in Chapter 2. The SIGP textile material used in the previous section for the development of single patches presented a slightly higher height. In this sense, a new textile was also tested in this stage. The array was simulated on CST Microwave Studio software using as dielectric substrate the PDE Black (Borgstena Textile Portugal, Portugal), which is a 100% polyester warp knitting, with h =0.98 mm, $\varepsilon_r = 1.385$ and tan$\delta = 0.0068$ @ 5.8 GHz. For the conductive parts, the PCPTF was also used.

Figure 4.16 shows the arrays designs. To reach the depicted solution the same approach presented in Section 2.4 was conducted. A single element was firstly optimized using the truncated square design. The feeding network was developed afterwards, considering the input impedance of the single element. In both antenna cases, it was equal to 100 Ω, therefore the feeding lines of the patches could be simple 100 Ω lines (identified as *L1* and *L2* in Figure 4.16). The upper part of the array was connected with the lower part by a quarter wavelength transformer, identified as *L3* line, and a 100 Ω line (*L4*). Finally, to introduce the SMA connector, a 50 Ω line identified as *L5*, was introduced in the middle of *L4* line. The feeding network was designed considering that the lines should be as narrow as possible to avoid parasitic effects, but they should also be wide enough to enable a successful manufacturing. At the end, the full array was optimized, where the patch centers were $3\lambda/4$ apart from each other. This distance was the result of a balanced trade-off between optimal antenna parameters, such as gain, HPBW and SLL, and the overall antenna dimensions. The SMA connector model was also included in the final stage of the full array simulation.

Figure 4.16 shows the final designs of the LHCP and RHCP antennas and Table 4.3 shows their dimensions, where l and w are the length and width of the feeding network lines, respectively.

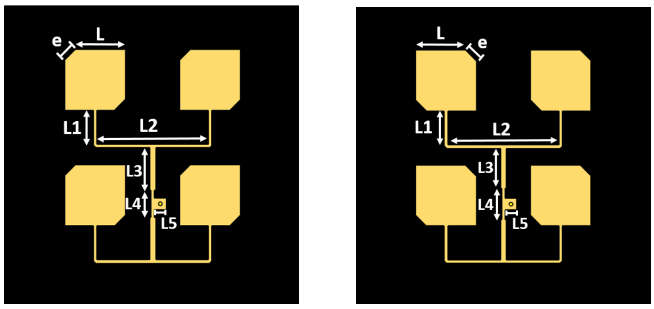

(a) (b)

Figure 4.16: Textile array antenna design [138]: (a) LHCP antenna, (b) RHCP antenna.

Antenna	L	e	L1		L2		L3		L4		L5	
			l	*w*	*l*	*w*	*l*	*w*	*l*	*w*	*l*	*w*
LHCP	20.5	5.2	11.5	1.15	37.643	1.15	14.2	2.05	9.243	1.15	4	3.9
RHCP	20.5	5.2	11.5	1.15	37.643	1.15	13.5	1.96	10.643	1.15	4	3.9

Table 4.3: LHCP and RHCP textile antenna arrays dimensions [mm] [138].

After the antenna array optimization, the antennas were manufactured using the laminating technique previously described and they can be seen in Figure 4.17.

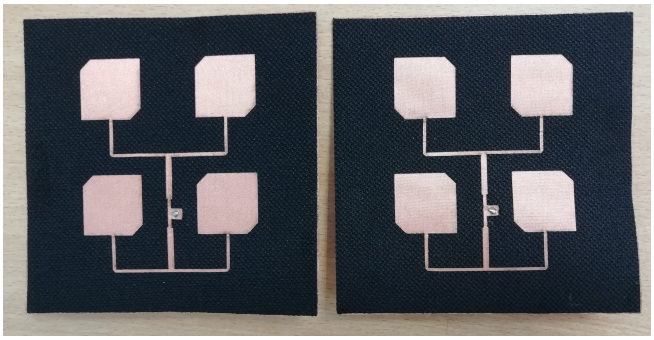

Figure 4.17: Manufactured LHCP and RHCP textile antenna arrays [138].

4.4.2 Textile antenna arrays performance evaluation

Several antennas parameters were measured in order to evaluate their performance in comparison with the simulated ones. The S_{11} presented in Figure 4.18 shows that the resonance frequency is centered on 5.8 GHz for both antennas, with an acceptable magnitude. The S_{11} is bellow -10 dB as desired, more specifically equal to -11.41 dB for the LHCP antenna and equal to -15.81 dB for the RHCP antenna.

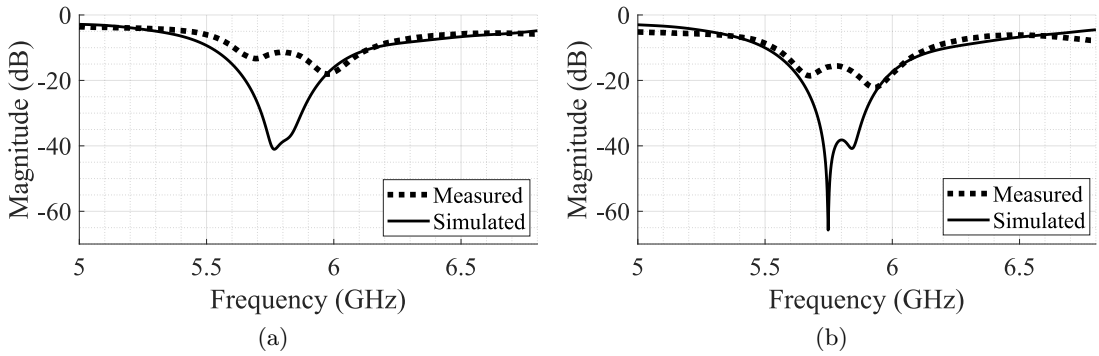

Figure 4.18: Simulated and measured S_{11} parameters for the textile antenna arrays [138]: (a) LHCP antenna, (b) RHCP antenna.

Figure 4.19 shows the measured normalized radiation pattern. Both LHCP and RHCP antennas presented similar patterns in comparison to the simulated ones. Furthermore, the HPBW and the SLL parameters were computed from the practical measures, to support the accordance between the obtained results and simulations. Starting with the LHCP antenna, the simulated HPBW was equal to 33.5°, while the measured one was equal to 34°. The simulated SLL was -15.2 dB, and the measured was -14.24 dB. For the RHCP antenna, the simulated HPBW was equal to 32.5° and the measured one was equal to 35°. The simulated and measured SLL were -13.6 dB and -14.40 dB, respectively.

On the other hand, this time both antenna gains were considerably below the expected. The simulated gain of both antennas was equal to 10.4 dBi, but the measured for the LHCP antenna was equal to 4.7 dBi and for the RHCP antenna was equal to 7.9 dBi. The axial ratio of the antennas was also measured and the results are presented in Figure 4.20. Both antennas presented axial ratios centered at 5.8 GHz. The measured magnitude for the LHCP

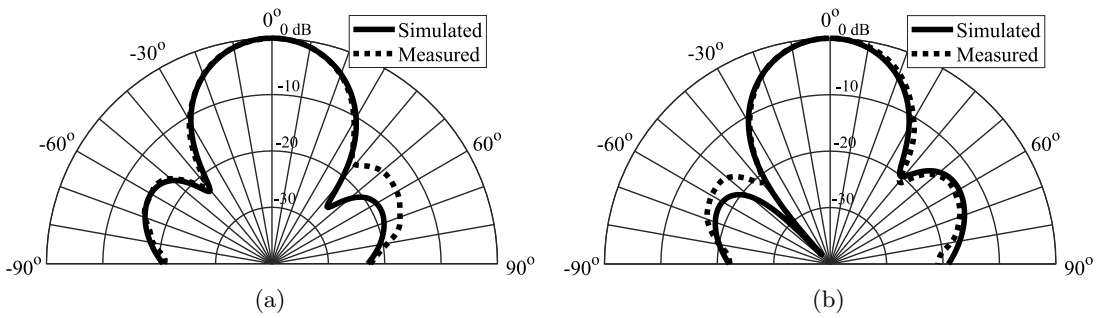

Figure 4.19: Simulated and measured normalized radiation pattern for the textile antenna arrays [138]: (a) LHCP antenna, (b) RHCP antenna.

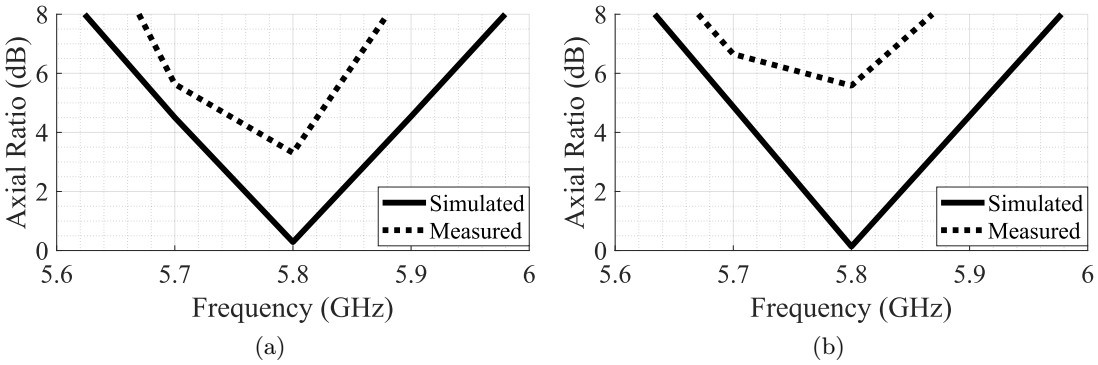

Figure 4.20: Simulated and measured axial ratio for the textile antenna arrays [138]: (a) LHCP antenna, (b) RHCP antenna.

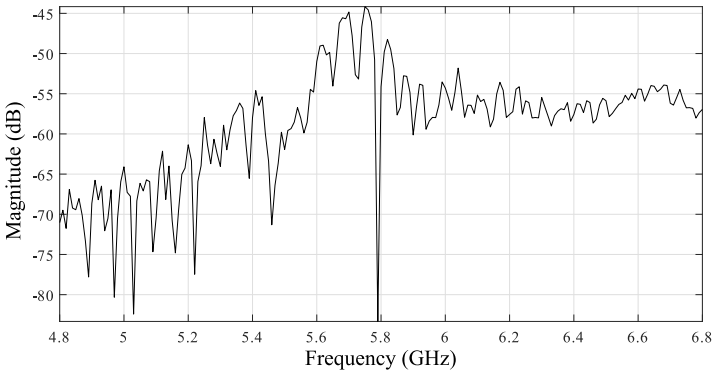

Figure 4.21: S_{21} parameter between LHCP and RHCP textile antennas arrays [138].

antenna was equal to 3.3 dB, while the simulated was 0.3 dB. As for the RHCP antenna, the measured magnitude was equal to 5.6 dB and the simulated was 0.14 dB.

Finally, since both transmitting and receiving antennas are located side by side and relatively close together to guarantee a monostatic radar operation, the cross-talk was evaluated by analyzing the S_{21} parameter, which is shown in Figure 4.21. This parameter was measured with both antennas located in the monitoring position (see Figure 4.22). By analyzing the

S_{21} parameter graph it is possible to conclude that transmitting and receiving antennas are not affected with cross-talk, being the S_{21} equal to -54.14 dB at 5.8 GHz.

Similarly to what was observed in the single patch antennas manufactured with the SIGP textile, the axial ratio was the parameter that deviate the most from the simulated one. Besides the axial ratio narrowband issue pointed out previously [108], these antenna arrays were more complex to fabricate since some of the feed network lines were too thin. Eventual differences in the line width or their bent disposition could have influence on the axial ratio result. Furthermore, the antennas gain was also severely affected and this could be related not only with the manufacturing process, but also with the textile roughness, which is more evident than the one present in the SIGP textile.

4.4.3 Respiratory signal acquisition using textile antenna arrays

The developed antenna arrays were then used to acquire the respiratory signals of four different subjects in the same conditions as the ones from the SIGP single patch antennas: first of all an optimal detection point was identified commonly for all subjects and the vital signs were acquired while each subject was seated (see Figure 4.22). The description of the physical characteristics of the subjects considered for this test are presented in Table 4.4.

Signals were processed in MATLAB with the *Simplified DSP* algorithm. Figure 4.23 shows the obtained signals during 20 seconds, where the antennas position was not changed between subjects. Once again, it was possible to acquire vital signs of different subjects and notice different rates considering the same time period. Nonetheless, in contrast with the single patch antennas, the identification of the optimal detection point was harder to find due to the increased antenna size and directivity. In this sense, antennas with high directivity are not advantageous for this specific context, since the vital signs acquisition performed sideways is restricted to a very limited detectable area.

Subject No.	**Gender**	**chest wall perimeter [cm]**	**Height [m]**	**Distance D [cm]**
1	Female	74.5	1.65	11.5
2	Female	70	1.50	7
3	Male	82	1.60	13
4	Female	75.5	1.56	12

Table 4.4: Physical description of the subjects considered to test the textile antenna arrays.

4.5 Development of a car seat upholstery with embedded bio-radar antennas

From the preliminary results obtained in Section 4.3 and in Section 4.4, one had concluded that single patch antennas are the most appropriate option for this case study, rather than antenna arrays. Larger beamwidths enable an easier identification of the optimal detection point common to the majority of population. Two different textiles were used, being one the SIGP and the substrate PDE Black, respectively. The performance of the antennas manufactured with both textiles was similar, but the PDE Black ones stand out with worse results in the antenna gain.

Considering the conclusions driven in the latter sections, a fully operational upholstery prototype is now proposed (prototype **Version P3**), which is concurrently discrete and com-

Figure 4.22: Position of the LHCP and RHCP antenna arrays in the car seat to acquire respiratory signals.

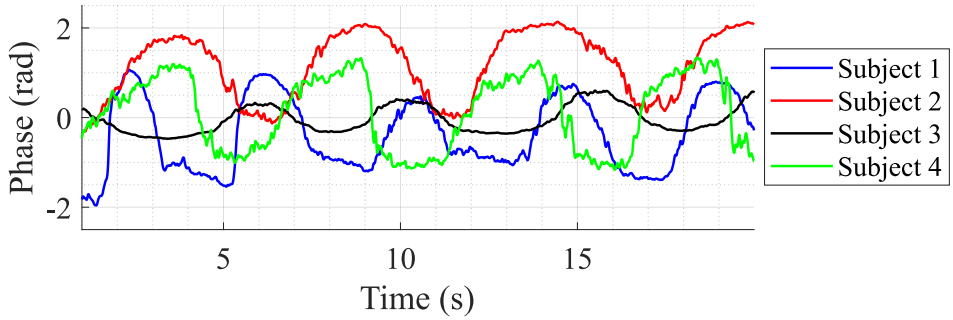

Figure 4.23: Respiratory signals of four subjects without changing the textile antenna arrays position.

---

fortable for the user. For this purpose, a trilaminate upholstery fabric was designed and manufactured integrating the transmitting and receiving textile antennas. Smaller single patch antennas were designed using a 3D spacer knit textile. The manufacturing process of the proposed prototype was optimized and a discrete feeding solution was explored to avoid the usage of bulky connectors, namely the usage of a coaxial cable welded directly to the antenna.

At the end, the performance of the prototype was evaluated in two stages:

1. Two versions of the same prototype were characterized through practical measurements, aiming to compare the performance of the feeding technique, where Prototype 1 used antennas fed with a conventional SMA connector and Prototype 2 used the coaxial cable welded directly to the antennas;

2. The respiratory signal of six different subjects was measured simultaneously with the bio-radar and a certified measuring equipment, while they were seating in a car seat containing the final prototype (Prototype 2).

4.5.1 Upholstery trilaminate composition and antenna design

Aiming the use of the bio-radar for vehicular applications, the textile patch antennas were fully integrated into the trilaminate upholstery material that composes the car seat cover. Synthetic textile materials were used, due to the low interaction with environmental humidity [139].

Figure 4.24a depicts a conventional laminated car seat upholstery material, which is composed by three different materials: top-layer (exterior fabric), foam layer, and scrim back-layer (lining). In the proposed prototype, the developed antennas were integrated between the foam and scrim back layers, as demonstrated in Figure 4.24b. Additionally, for a practical and realistic implementation, a textile microwave absorbing material was added behind the ground plane of the antenna, to insulate the signals coming exclusively from the monitored subject's body. The preliminary tests conducted to validate the effectiveness of this procedure are reported further in Section 4.5.3.

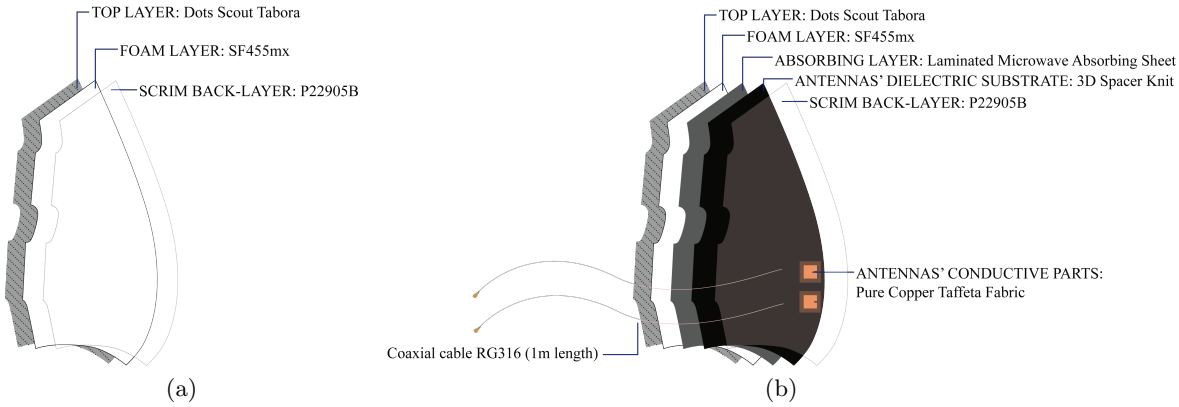

Figure 4.24: Laminated layers that composes the upholstery material: (a) Conventional laminated material design, (b) New developed laminated material.

The materials used to built proposed upholstery solution (Figure 4.24b), are the following:

1. **Top-layer**: 100% polyester weft-knit, named Dots Scout Tabora (Borgstena Textile Portugal), with 0.92 mm of thickness, $\varepsilon_r = 1.10$ and $\tan\delta = 0.005$ @ 5.8 GHz;
2. **Foam layer**: 100% polyurethane foam, SF455mx (Borgstena Textile Portugal), with 3.91mm of thickness, $\varepsilon_r = 1.35$, and $\tan\delta = 0.010$ @ 5.8 GHz;
3. **Absorbing layer**: 100% carbon fibers non-woven material, named Laminated Microwave Absorbing Sheet (Less EMF, USA), with 0.445 mm of thickness and conductivity equals to 740 S/m;
4. **Antenna's dielectric substrate**: 3D spacer knit (LMA, Portugal) with 2.65 mm of thickness, $\varepsilon_r = 1.15$ and $\tan\delta = 0.007$ @ 5.8 GHz;
5. **Antennas conductive parts**: Pure Copper Taffeta Fabric (Less EMF, USA) with 0.08 mm of thickness and conductivity equals to 62600 S/m [79];
6. **Scrim back-layer**: 100% polyester circular knit, P22905B (Borgstena Textile Portugal), with 0.09 mm of thickness, $\varepsilon_r = 1.08$, and $\tan\delta = 0.015$ @ 5.8 GHz.

In regard to the antenna design, a squared patch with a rectangular slot at the bottom was the selected approach aiming to reduce the overall antenna size. Antennas were fed directly in the patch rather than using microstrip lines. Similarly to what has been performed so far, the transmitting and receiving antennas had crossed circular polarization, where the RHCP is induced by feeding on the right side (in relation to the slot) and LHCP is induced by feeding on the left side.

The antenna design process was divided into three stages, as illustrated in Figure 4.25:

- **Stage 1**: A single patch was tuned using only the 3D spacer fabric as dielectric substrate and the PCPTF for the conductive parts. In this stage, the RHCP and LHCP antennas were optimized separately;
- **Stage 2**: The remaining upholstery layers were added afterwards. The absorptive layer was simulated as a lossy metal and it affected the antenna resonance slightly. Hence both RHCP and LHCP antennas were re-optimized accordingly;
- **Stage 3**: Both RHCP and LHCP antennas were gathered to share the same substrate, as shown in Figure 4.25b and 4.25c. Each antenna had its exclusive ground plane, and at this stage, a model of an SMA connector was included to robustly simulate the antenna feeding.

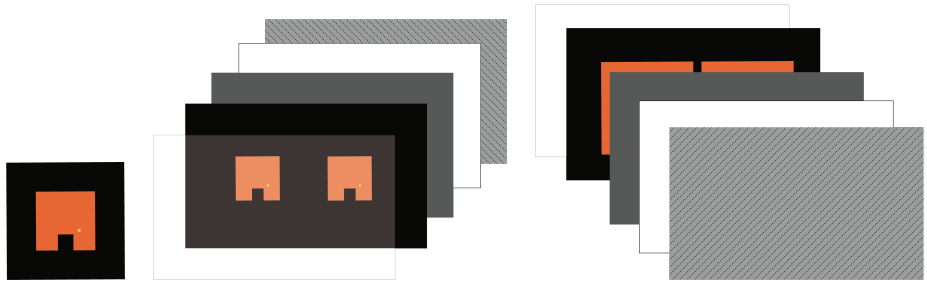

Figure 4.25: Final textile antenna model considered in the simulations: (a) Stage 1, (b) Stage 2 and 3: Front side, (c) Stage 2 and 3: Back side.

The final dimensions of the optimized prototype are presented in Figure 4.26 and in Table 4.5. The distance P is equivalent to $3\lambda/4$, and it was selected having in mind a balance between the antennas' mutual coupling and the space that they would occupy in the car seat side lumbar support. Following the same conclusion regarding directive antennas, the transmitting and receiving antennas should be as close as possible to guarantee the illumination of the best sideways chest wall detection point.

After the optimizing the Stage 3 antennas, the prototypes were manufacture using the laminating technique. All laminating steps were made using a industrial ironing press, under 5 bar, at 110°C. To ensure the geometric stability of the conductive parts, the patch and the ground plane were cut by a laser cutting machine. Two equal prototypes were manufactured to further evaluate the effect of the feeding type on the antenna's performance. The Prototype 1 was fed using a conventional SMA connector and the Prototype 2 was fed using a coaxial cable welded directly to the patch antenna. The manufacturing process of

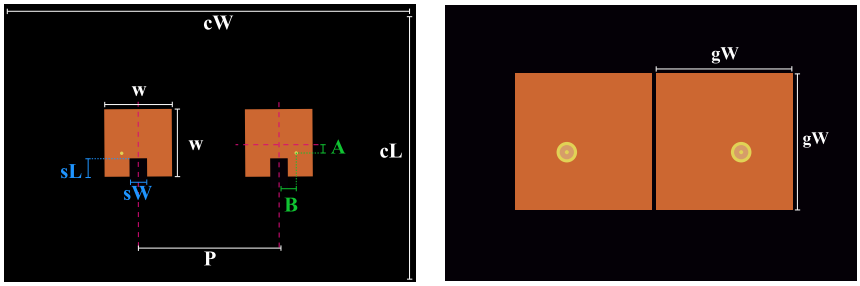

(a) Front (b) Back

Figure 4.26: Layout of the simulated prototype containing the final textile antennas.

Patch dimensions	**w**	**sW**	**sL**	**A**	**B**
	19.58	4.59	4.41	2.72	4.80
Prototype dimensions	**cW**	**cL**	**P**	**gW**	
	117.48	78.32	39.97	39.16	

Table 4.5: Dimensions of the prototype containing the final textile antennas (in [mm]).

Prototype 2 was thorough, with a view to guarantee the mechanical robustness of the feeding point and simultaneously provide a low profile appearance to the prototype. The coaxial cables were prepared, stripping their layers and then the following steps were implemented (see Figure 4.27):

1. The ground planes were laminated to the substrate;
2. The metallic shield of the cables was welded to the ground planes;
3. The cables' dielectric insulators were cut, adjusting their height to the substrate's face. Subsequently, the patches were laminated to the substrate;
4. The center conductors of the coaxial cable were cut and welded on the patch;
5. The absorbing material and the foam layer were laminated to the ground plane;
6. To accommodate the coaxial cables, a small cut on the foam was performed, and the cables were folded;
7. The other textile layers were laminated to the antenna, according to the scheme presented in Figure 4.24.

The manufactured prototypes are shown in Figure 4.28.

4.5.2 Upholstery embedded antennas performance evaluation

The antenna parameters of the two prototypes were measured. The S_{11} and S_{21} parameters were firstly measured to verify the resonant frequency tuning and the mutual coupling

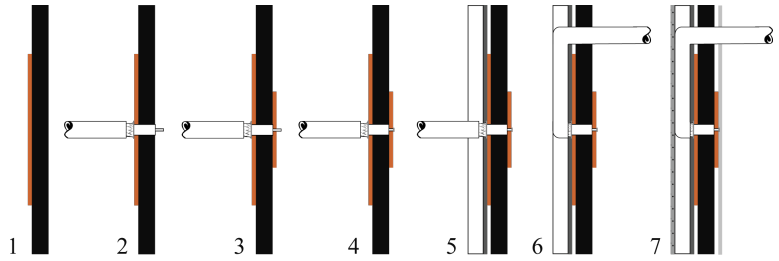

Figure 4.27: Illustration of the steps conducted for the Prototype 2 manufacture.

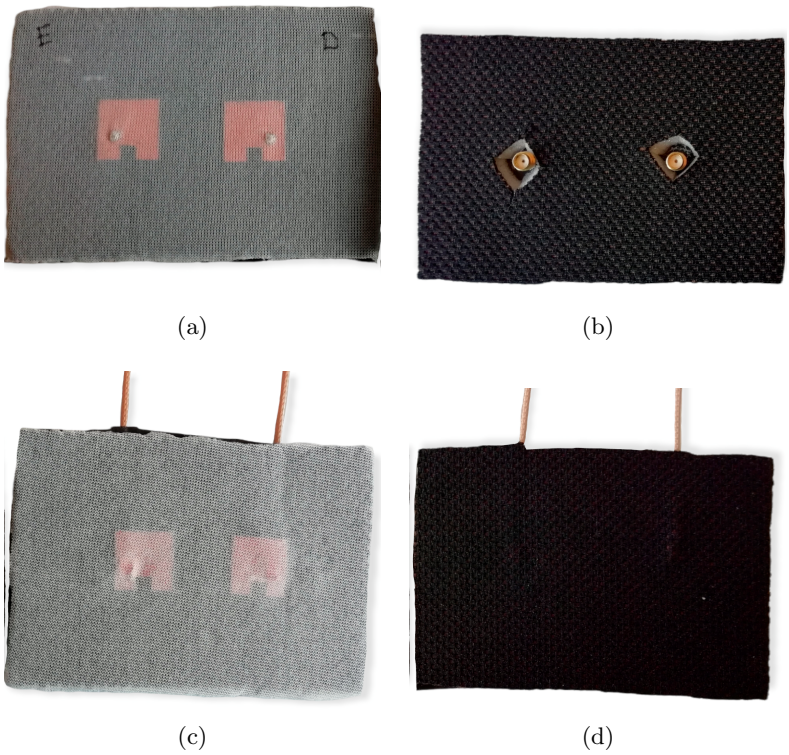

(a) (b)

(c) (d)

Figure 4.28: Manufactured prototypes containing the final textile antennas: (a) Prototype 1 front view, (b) Prototype 1 back view, (c) Prototype 2 front view, (b) Prototype 2 back view.

---

between the RHCP and LHCP antennas. For the Prototype 2, the VNA was calibrated using a coaxial cable exactly equal to the one welded to the antenna.

The results for S_{11} and S_{21} are shown in Figure 4.29. Starting with the S_{11} parameters, the Prototype 1 presented -12.17 dB for the RHCP antenna and -13.93 dB for the LHCP antenna at 5.8 GHz. The S_{11} values obtained for the Prototype 2 were -20.56 dB for the RHCP antenna and -14.05 dB for the LHCP antenna. The differences observed between both prototypes might be due to a slight deformation in the feeding point zone in Prototype 2 caused by the pressure of the coaxial cable in that zone. In this specific case, the patch deformation provided a contributing effect in the S_{11} magnitude. The results presented in Figure 4.29b show that neither prototypes have mutual coupling. While the simulated S_{21}

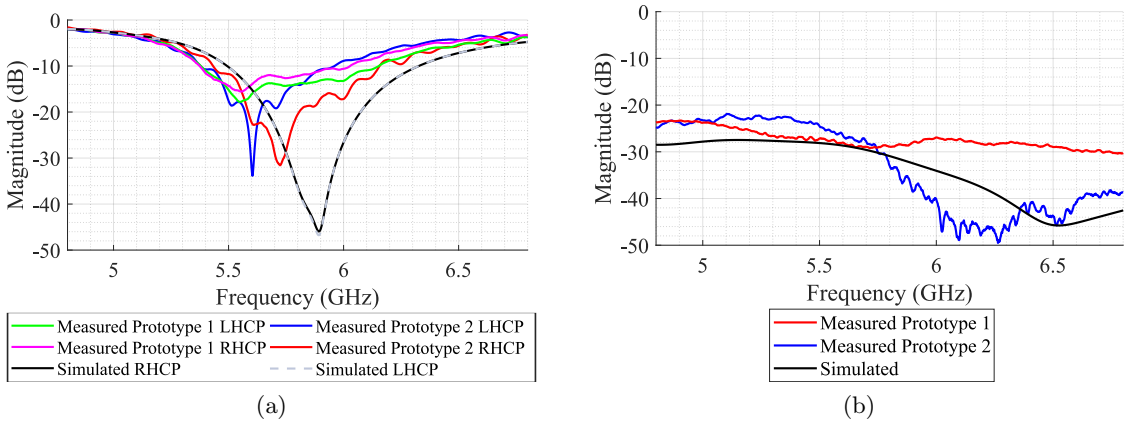

Figure 4.29: Simulated and measured S-parameters for Prototype 1 and Prototype 2: (a) S_{11} parameter, (b) S_{21} parameter.

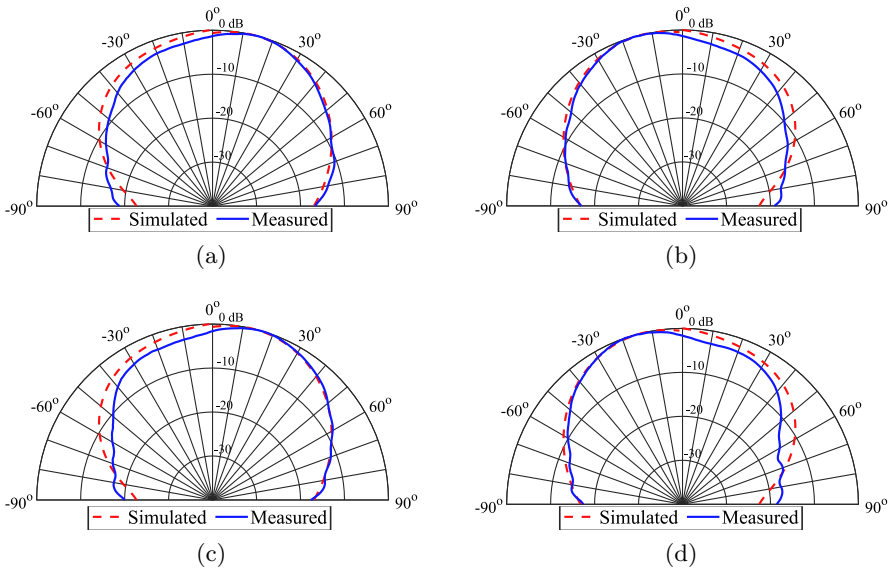

Figure 4.30: Simulated and measured normalized radiation pattern for Phi = 0°: (a) Prototype 1 RHCP, (b) Prototype 1 LHCP, (c) Prototype 2 RHCP, (d) Prototype 2 LHCP

---

was equal to -30.9 dB, the Prototype 1 and Prototype 2 presented a S_{21} equal to -32.9 dB and -28.9 dB measured at 5.8 GHz, respectively.

Figure 4.30 shows the measured normalized radiation pattern in comparison with the simulated one. Both prototypes were measured and it is possible to observe that neither feeding approaches have a notorious impact in the radiation pattern. All measures are close to the simulated one, where the Prototype 1 antennas are the most identical to each other. On the other hand, more differences can be perceived in the Prototype 2, but they are not predominant. The simulated gain was equal to 8 dBi for both LHCP and RHCP antennas. The measured gain for the Prototype 1 was equal to 7.16 dBi and 7.50 dBi for the LHCP and RHCP antennas, respectively. In regard to Prototype 2, the measured gain was equal to

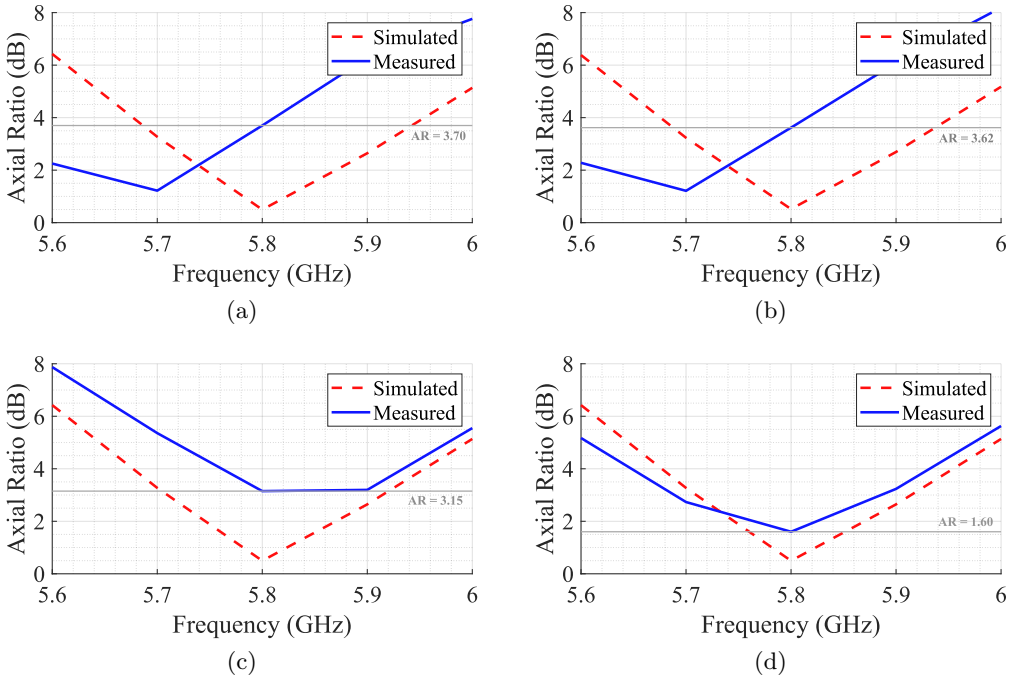

Figure 4.31: Simulated and measured axial ratio: (a) Prototype 1 LHCP, (b) Prototype 1 RHCP, (c) Prototype 2 LHCP, (d) Prototype 2 RHCP.

4.36 dBi and 5.99 dBi for the LHCP and RHCP antennas, respectively.

Finally, Figure 4.31 presents the axial ratio results for all the antennas. In this case, Prototype 1 and Prototype 2 presented different behaviors. First of all, the Prototype 2 was the one presenting the lowest axial ratio values, being 3.15 dB and 1.60 dB for the LHCP and RHCP antennas, respectively. The RHCP antenna presented its minimum axial ratio value centered in 5.8 GHz, while in the LHCP antenna the frequency presenting the minimum value is shifted to approximately 5.85 GHz. Once again, these differences might be related with the cable position and the pressure made in the feeding point. On the other hand, the Prototype 1 antennas presented more similar results between each other. The LHCP and RHCP antennas presented an axial ratio equal to 3.70 dB and 3.62 dB respectively, and both antennas presented its minimum axial ratio value at 5.7 GHz.

The antenna parameters shown in Figure 4.29-4.31 demonstrated that the differences observed in both prototypes are not significant. The only effect that the cable feeding approach has in the antennas performance is the gain decrease, which is still lying within acceptable values. Therefore, the coaxial cable directly welded to the antenna (Prototype 2) can be used as a low profile feeding method.

4.5.3 Insulation tests

In Section 4.2 the side lumbar support was the selected location for the textile antennas. The antennas can be either located on the right side of the car seat, nearby the side passenger, or on the left side near the door. This latter location has the disadvantage of being near an airbag. Hence in case of an accident, the airbag impact could damage the system. Therefore,

to preserve the bio-radar functioning in case of a car accident, the right side was the selected one. However, an issue arises from the selected location. Since antennas also have back side lobes, any motion from the side passenger is also received along with the vital signs acquired by the frontal lobe. This can cause additional noise to the received signal and might compromise the results. Therefore, proper insulation should be performed, to extract signs with superior quality.

To evaluate this issue, a series of practical experiments were conducted in a laboratory environment to verify the effectiveness of the signals insulation. The respiratory signal of one subject (Subject 1) was acquired while seating in the car seat to simulate the driver position. Meanwhile, another subject (Subject 2) located next to Subject 1, simulating the passenger, moves randomly and on purpose. The experiment setup is depicted in Figure 4.32.

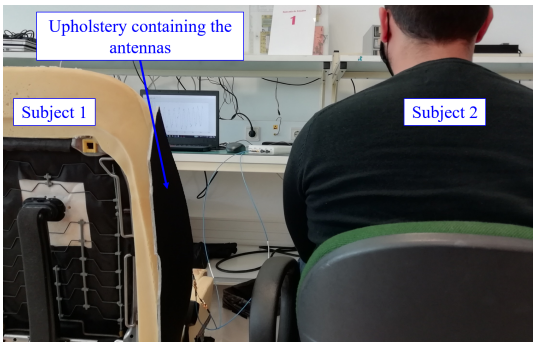

Figure 4.32: Setup used to test the effectiveness of the antenna insulation.

These insulation tests were conducted in two stages:

1. The same test was performed with and without a microwave absorbing material between the antennas' ground plane and Subject 2 (side passenger), which moved in a specific moment for both cases;

2. The effectiveness of the final prototype was tested after being manufactured. The stage 1. was repeated, but this time with and without the Subject 2 moving.

The first stage of the insulation tests served as a proof of concept, so an open-cell polyurethane foam (typically installed on the inner walls of the anechoic chambers) was used as microwave absorbing material. On the other hand, the absorbing material used in the second stage is already included in the prototype, as explained in Section 4.5.1.

In the first stage, each experiment lasted 35 seconds and Subject 2 has moved between the 20^{th} and the 30^{th} second. The resultant signals are presented in Figure 4.33. The exact moment containing the Subject's 2 motion is highlighted in orange. Figure 4.33a, shows that if the antenna is insulated using only its ground plane, the eventual motions performed by the side passenger are perceived as noise in the extracted signal. On the other hand, as shown in Figure 4.33b, if a microwave absorbing material is incorporated behind the ground plane, the antenna insulation is reinforced and those movements are no longer detected.

The same conclusion was verified after conducting the second stage of the insulation tests. In this case, the absorbing material was always attached between the ground plane and the foam layer of the upholstery. The respiratory signals were acquired firstly without any purpose movements from the Subject 2, and then with the movements. These tests were

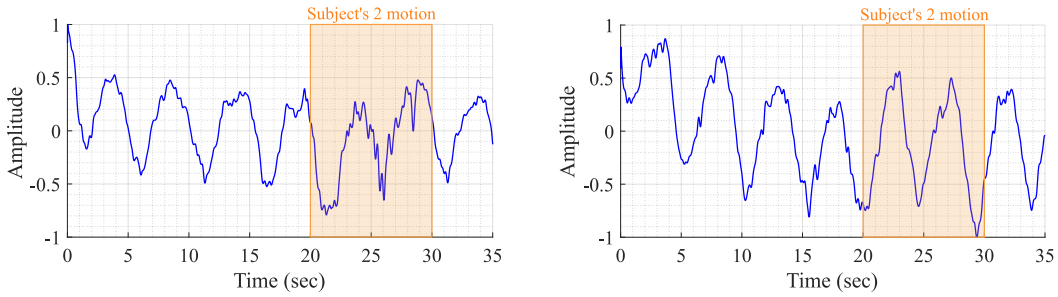

Figure 4.33: Respiratory signal demonstrating the effectiveness of the absorbing material between the antennas' ground plane and the side passenger: (a) acquired with a simple textile antenna, (b) acquired with a textile antenna and an absorbing material behind the ground plane.

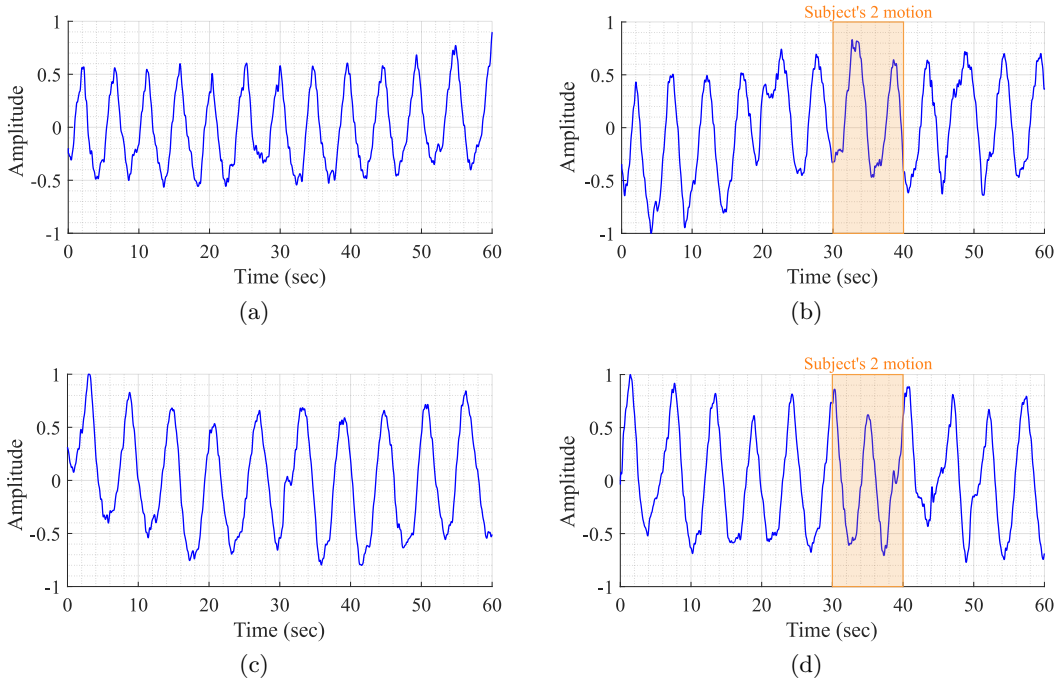

Figure 4.34: Respiratory signal using the developed upholstery prototype. Test 1: (a) Without motion (b) With motion. Test 2: (c) Without motion (d) With motion.

---

performed twice to validate the results. The obtained results are presented in Figure 4.34, where Figure 4.34a and Figure 4.34c are stand-alone respiratory signals without the Subject 2 motion, and Figure 4.34b and Figure 4.34d are respiratory signals acquired under a motion condition. The motion occurred between the 30^{th} and the 40^{th} seconds (also highlighted in orange). Since the prototype is fully covered with an absorbing material integrated as one upholstery layer, it is expected to not detect the motion from Subject 2 and this was indeed accomplished successfully.

4.5.4 Respiratory signal acquisition using upholstery prototype

In order to fully validate the effectiveness of the final prototype (**Version *P3*** - Prototype 2), the respiratory signals of six subjects were acquired. Table 4.6 presents the subjects' physical dimensions and the setup used in the experiment is depicted in Figure 4.35. The setup is composed by the radar front-end, a car seat prototype [140] and the BPC system used for comparison purposes.

Subject ID	Gender	Height [m]	Thoracic Perimeter [cm]	Breathing Rate [BRPM]	MAE [BRPM]
1	Male	1.75	87	16.95	0.14
2	Male	1.76	96.5	11.95	0.02
3	Female	1.56	75	14.91	0.02
4	Female	1.56	66	14.23	0.00
5	Male	1.75	90	11.81	0.00
6	Female	1.50	82	12.11	0.16

Table 4.6: Description of the physical stature of the subjects considered to test the final upholstery prototype.

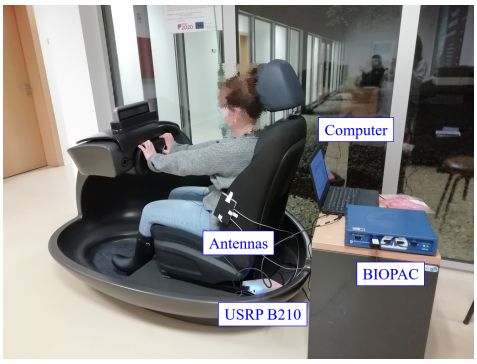

Figure 4.35: Setup used in the vital signs acquisition for the final upholstery prototype validation.

The Prototype 2 containing the transmitting and receiving antennas was attached to the car seat, namely in the side lumbar support, as shown in Figure 4.35. The vital signs were acquired afterwards, following the *Car Seat Protocol*. The respiratory signal was acquired simultaneously using the BRD and the BPC to verify the accuracy of the prototype.

BRD and BPC signals were processed using MATLAB. For the BRD case, the *Dynamic DSP* algorithm was used to remove the CDC offsets and extract the respiratory signal. Then, both BRD and BPC signals were denoised, their mean value was removed and they were normalized according to their maximum amplitude, to better compare the waveforms. Figure 4.36 shows the final BRD and BPC signals for each subject.

For all subjects, it was possible to obtain identical waveforms. The eventual observed differences might be related with the working principles of both systems. While the BPC measures the full chest wall expansion, the BRD measures only the lateral chest wall motion, perceived in a specific zone. Besides, the BPC system is not sensitive to other random body motions, while the BRD can be highly affected.

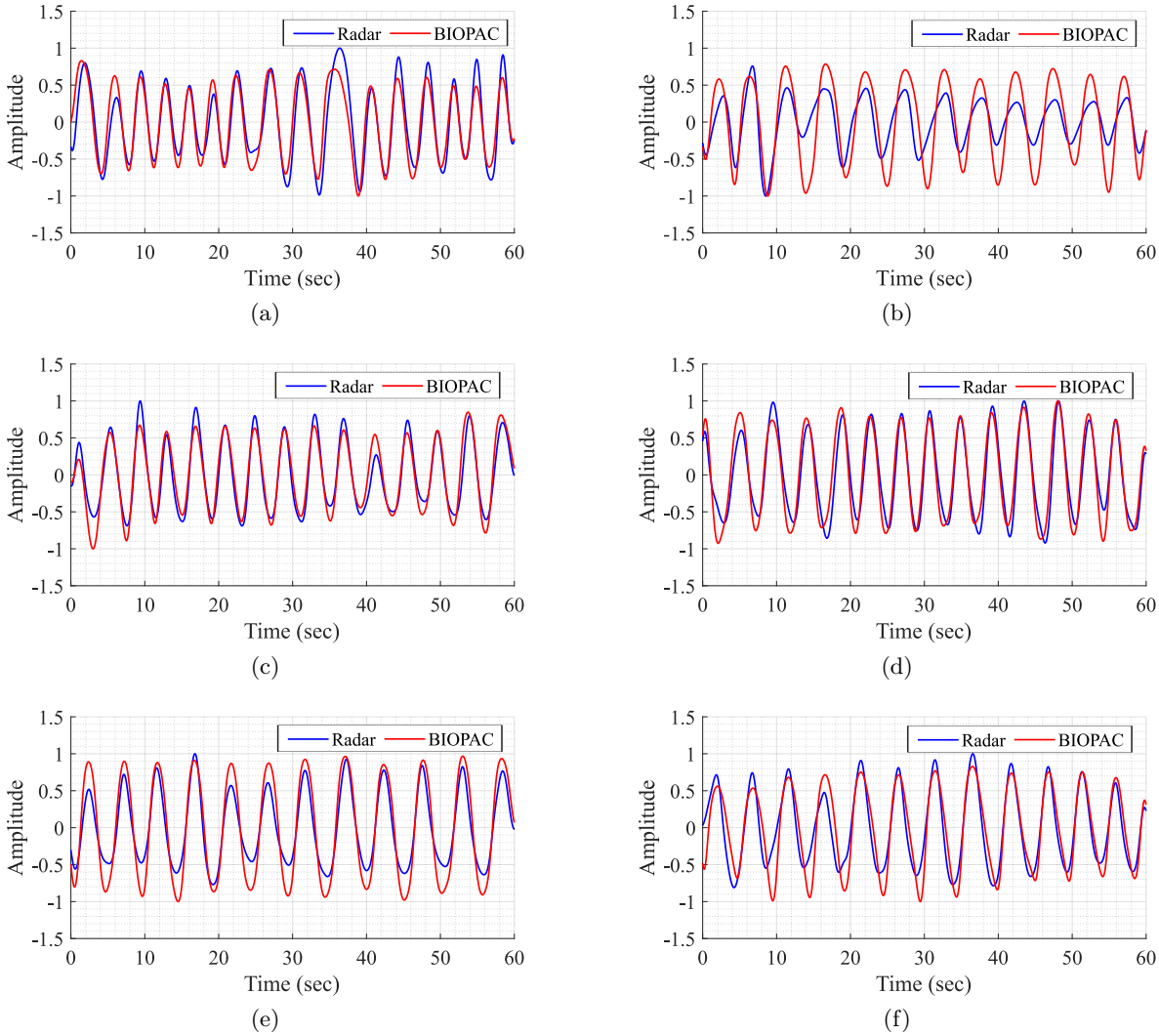

Figure 4.36: Comparison of the subjects' vital signs using BRD and BPC: (a) ID1, (b) ID2, (c) ID3, (d) ID4, (e) ID5, (f) ID6.

The breathing rates for each subject were computed through the ZC method described in Chapter 3. For this purpose, signals were firstly filtered with a 200-order FIR low-pass filter, with a cut-off frequency equal to 0.5 Hz, in order to remove noise and turn the respiratory peaks more prominent. Table 4.6 also presents the average respiratory rate obtained by the BRD signal and the MAE in relation with the BPC signal. The BRD signal keeps track of the BPC one, presenting a low MAE varying between $0 - 0.16$ BRPM.

With these results and waveform similarities, one can assume that the BRD system presents an equivalent capability to monitor the respiratory signal, when compared to certified measuring equipment, even from sideways and using the developed prototype.

4.6 Final considerations

The results presented in this chapter demonstrated that it is indeed possible to fully integrate the bio-radar system in a customized application, without compromising its general appearance and simultaneously guaranteeing the vital signs accuracy.

With the present case study, one could verify that the appropriate antenna design is directly related with the requirements of the target application. For example, herein the vital signs were acquired from sideways, and the obtained results indicated that single patch antennas are the most appropriate option for this situation. In contrast to the most common BRD operation (in front the subject's chest wall), directive antennas do not bring any advantage to this specific case study, because they are larger and hence more difficult to place in such limited area, as well as aligning to an optimal detection point.

Textiles were the selected materials, not only for providing a low profile appearance, but also to streamline the manufacturing process of the target application. In this sense, the viability to embed antennas directly in the car seat upholstery was inspected. The developed antennas allowed the acquisition of vital signs captured on the chest wall side with a similar performance as conventional substrate antennas and as a certified measuring equipment which evaluates the overall chest wall displacement. However, it is important to highlight that the antennas design and manufacturing process can be challenging. Textile materials are porous, and their electromagnetic properties depend on the density of the fibres, air volume and the size of the pores [127]. Due to the variability of textures and fibres composition, the same textile batch can change its dielectric characteristics. Moreover, they are also flexible and compressible, which might cause changes in thickness and can also lead to deformations during the manufacturing process. These problems can have impact in the antennas parameters, therefore one can expect slight differences between the simulated and the measured values.

Additionally, during the final prototype development the application appearance was took into account by adapting the antennas feeding method. Conventional antennas are often fed through SMA connectors, which are bulky. Thus, the proposed prototype was fed with a coaxial cable directly welded to the patch antenna. The impact that this method has on the antenna performance was evaluated, by measuring the antennas parameters and comparing them with equal antennas fed through a conventional SMA connector. In general, all results were close to the simulated ones for both prototypes (using SMA connector and with coaxial cable, respectively). However, the coaxial cable fed prototype presented a lower measurement reproducibility, which might be justified with the cable position and pressure in the patch feeding zone, while the SMA prototype presented more similarities between transmitting and receiving antennas, indicating the robustness of the manufacturing process. Even though, it is worth mentioning that the antennas were manufactured manually, where it is not easy to fully control the process. Thus, as future work, these results can be improved and stabilized in reproducibility tests with a highly calibrated and industrialized manufacturing process.

Chapter 5

Cardiac Signal Extraction

This chapter was mainly dedicated to the development of signal processing algorithms for the cardiac signal extraction. Furthermore, the accuracy to estimate the cardiac frequency was evaluated and improved. Additionally, the ability to assess to HRV parameters was verified and methods were developed aiming to also take advantage of the information that those parameters may provide.

The developments of this chapter resulted in the publication of the following journal papers:

- C. Gouveia, D. Albuquerque, P. Pinho, and J. Vieira, "Evaluation of heartbeat signal extraction methods using a 5.8 GHz Doppler radar system in a real application scenario," *IEEE Sensors Journal*, vol. 22, no. 8, pp. 7979–7989, April 2022
- C. Gouveia, D. Albuquerque, P. Pinho, and J. Vieira, "Bio-Radar Cardiac Signal Model used for HRV Assessment and Evaluation Using Adaptive Filtering," *IEEE Transactions on Instrumentation and Measurement*, vol. 71, pp. 1-10, July 2022

5.1 Introduction

The bio-radar signal contains both respiratory and cardiac signals, wherein the extraction of the cardiac component is a demanding task. This fact is related not only with radar operation limitations, but also due to the own nature of the cardiopulmonary function captured by the radar. Typically, the Respiratory Signal (RS) stands out as the dominating signal, with an amplitude varying between 4 to 12 mm [141], while the maximum displacement due to Cardiac Signal (CS) consists on 0.5 mm [142]. The authors in [142] used laser speckle interferometry to measure the corresponding chest wall motion to each ECG wave and they observed that the highest motion is related with the QRS complex and it is focused in one specific location, namely the apex of the heart. Hu et al. [25] also pointed out that the identification of that area is increasingly hampered if the subject is not at rest or if the radar antenna is not properly aligned with the maximal displacement zone. This latter fact can be worsened if directional antennas are being used, since narrow beamwidths require a precise alignment, and as discussed in Chapter 2, directive antennas are in fact the most recommended for the majority of bio-radar applications.

In addition, the chest wall motion amplitude and the cardiac signals quality are also related with the subjects' physiognomy and gender [25], [32], [36], [143]. The radar follows the same

operating principle as the mechanocardiography, which measures the heart mechanical motion perceived at the chest surface [143]. According to [32], mechanocardiography signals tend to have interpersonal variations carried by the differences on body mass index, age, sex, among other health-related factors, resulting in different beat morphologies, hence implying in the accuracy on determining the heart rate or other cardiac parameters.

Regarding the radar CS extraction, several methods have been proposed in the literature. Band-pass or high-pass filtering could be used as straightforward and direct approach to remove the respiratory component and isolate the CS [111], [144]. For instance, in [144] a filter bank is used with different center frequencies with the goal to extract the CS directly from the radar raw signal, and in [111] the CS is obtained by filtering the respiratory component, through a high-pass filter with a cut-off frequency of 0.5 Hz. However, filtering is not the most suitable technique, since the recovered CS might be distorted and loses resolution [145]. Furthermore, the filter performance is most likely compromised due to the RS nature. The RS cannot be seen as a monotone sinusoid, being rather an harmonic signal, with frequency components overlapping the CS. Hence, a standalone filter is not able to fully isolate the CS [145]. In this sense, other methods might be more suitable and efficient, where it can be highlighted the signal decomposition [44], [146], or the multi-resolution analysis using wavelets [25], [26], [33], [56], [147], [148].

5.1.1 Wavelet transform

In [25], [26], [33], [56], [147]–[149], the wavelet transform was explored as an approach to extract the CS, since it can provide a multi-resolution perspective. In other words, long-time windows are applied to retrieve low frequency components and short-time windows are used for high frequency components.

Wavelets are functions with specific mathematical requirements, that can decompose the original signal into a set of signals [150]. For this purpose, a mother wavelet should be firstly selected, scaled (by stretching or shrinking it) and then compared with the input signal while shifting it over time. This procedure is depicted in Figure 5.1.

The signal decomposition using wavelets can be performed using different analysis [151], such as the Continuous Wavelet Transform (CWT), the Discrete Wavelet Transform (DWT) or the Wavelet Packet Decomposition (WPD). For instance, CWT is widely used in time-frequency analysis and DWT is often used for denoise purposes [151]. The main difference between both is the scaling stage, since CWT provides a finer decomposition and DWT performs a dyadic scaling leading to a sparse decomposition.

Regarding DWT and WPD, both methods are similar to multi-rate filter banks (which provide the dyadic scaling) and this decomposition process is depicted in Figure 5.2. In DWT the original signal is decomposed in a certain number of scale levels [152]. On each scale level, the signal is simultaneously low-pass and high-pass filtered, being hereinafter downsampled by a factor of 2. The output of the high-pass chain consists on the detail coefficients $D_k(n), k = 1, 2, 3...$ and the low-pass chain provides the approximation coefficients $A_k(n), k = 1, 2, 3....$ The decomposition through levels is then performed, using $A_k(n)$ as the new input signal [152]. WPD is an extension of the DWT [152], where the $D_k(n)$ coefficients are also decomposed. In this way, WPD provides a better resolution in terms of frequency, as suggested by [152].

In the general literature, CWT is the most used method to recover the CS. More specifically, in [147] authors studied which is the most appropriated scale factor to determine the

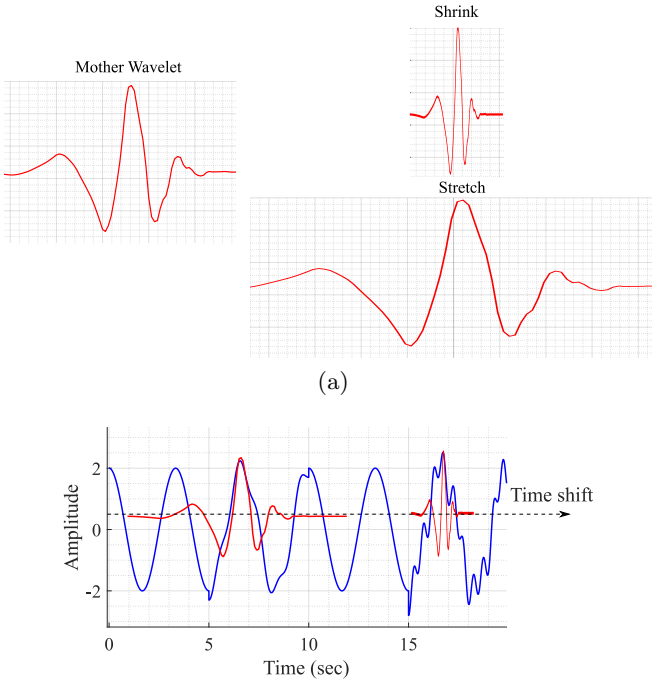

Figure 5.1: Illustration of a wavelet transform: (a) Example of a Daubechies mother wavelet with 4 vanishing moments with its scaled forms (shrank and stretched versions), (b) The scaled mother wavelet is time shifted and compared with the original signal.

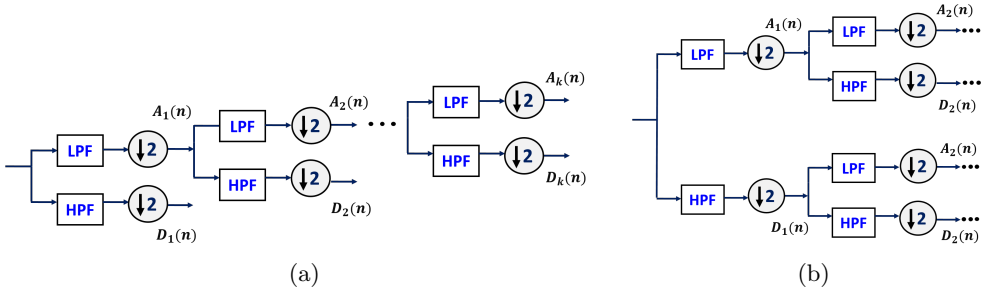

Figure 5.2: Representation of a wavelet transform through dyadic scaling: (a) DWT, (b) WPD.

IBI accurately. In [26], [56] the CWT was used to improve the accuracy on the heart rate computation. More specifically, [26] was focused on short-time applications. The authors compared the performance of their method with a conventional Fourier transform, achieving an average error reduction from 26.7% to 3.5%. In [56] CWT was used to adapt the extraction properties to be suitable for different subjects in different monitoring scenarios. The authors obtained a RMSE varying between 0.1 and 4 Beats per minute (BPM) within the testing scenarios.

On the other hand, DWT is mostly used to denoise the CS, and not necessarily as a mean to isolate it from the RS. In [33] the authors studied which are the best DWT features

to denoise the CS acquired by a 5.8 GHz radar. They analyzed the SNR of 115 potential functions, containing 6 wavelet families and 10 decomposition levels. They concluded that for the denoising purpose, Daubechies and Symlet wavelets with 9 vanishing moments are the most appropriated selection, considering 7 decomposition levels.

Finally, [149] was the only work found using WPD to separate the CS from the radar RS. The authors took advantage of the improved frequency resolution and perform a 6-level decomposition. Respiratory and cardiac signals were recovered through the combination of nodes containing the desired frequency band. CWT was used afterwards to obtain the heart rate, achieving an average absolute error varying between 1.69 and 3.22 BPM.

5.1.2 Empirical mode decomposition

The Empirical Mode Decomposition (EMD) technique consists on separating the input signal into a finite number of components [153], the so-called Intrinsic Mode Functions (IMF). IMF are obtained through a sifting process, which consists in the following procedure [154]: firstly the lower and upper signal envelopes are obtained through cubic spline interpolations on local minima and maxima of the signal. Then, the mean value of both envelopes is subtracted from the input signal, and the same process is repeated until the IMF conditions are verified [153], [154], being:

1. The number of extrema must be equal to the number of zero-crossings, or must differ at most by one;

2. The mean value between the envelop created by the local maxima and by the local minima, must be zero.

The signal decomposition in IMF is performed iteratively, i.e. after finding the first IMF, this component is subtracted from the original signal and the resulting one is submitted to the sifting process all over again. At the end, the original signal can be obtained through the sum of all IMF plus a residual function. Figure 5.3 shows the result of the decomposition process of a radar RS into six IMF plus a residual signal.

EMD techniques are widely used in literature to extract the CS in the bio-radar context. For instance, in [44] the author used EMD to extract the CS even in situations where the subject is randomly moving other body parts. In this case, the respiratory component is mitigated using a high-pass filter and the EMD was applied afterwards. The authors tested the effectiveness of their method considering different amplitudes of body motion and obtained an RMSE between 0.6 to 1 BPM. On the other hand, it was demonstrated in [146] that it is possible to recover both biosignals (RS and CS) concurrently using EMD. Herein the authors gave an implementation example, where the CS was obtained through the first IMF isolation and the RS was reconstructed through the sum of the IMF with more energy in the desired spectral band. The maximum error that the authors obtained in [146] was equal to 4.4 BPM.

More recently, the improved version of EMD, namely the Ensembled Empirical Mode Decomposition (EEMD) was used in [148]. EEMD aims to solve inherent EMD issues, such as the mode mixing [155], which makes the physical meaning of an individual IMF unclear. For this purpose, the EEMD simulates successive observations of the same input signal, by adding white noise to it. Thus, each observation corresponds to the same signal plus noise with different characteristics. Adding noise will provide a relatively uniform reference scale distribution, which improves the EMD performance [155].

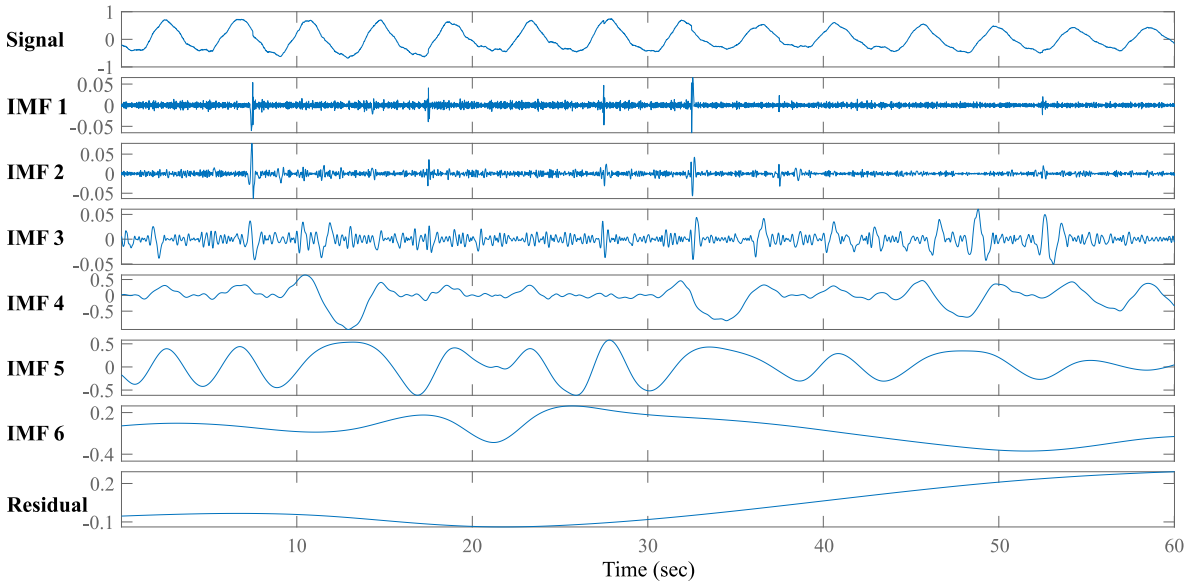

Figure 5.3: Result of the empirical mode decomposition of a radar RS.

Some authors also reported interesting results, combining **signal decomposition methods** with **multi-resolution analysis**. The method proposed in [148] combines the DWT with EEMD. In this case, wavelets threshold were used to denoise IMF. Then, vital signs were accurately extracted by selecting the most appropriate IMF. In this case, the authors considered that the selected IMF for signal reconstruction should contain spectral components within the vital signs bandwidth, being 0.2-0.6 Hz for the RS and 0.9-1.5 Hz for the CS. Then the CS was recovered with an error equal to 0.014 BPM. The same method combination is proposed in [25] to separate the biosignals. Herein the authors state that the combination of both methods can provide results accurate enough to estimate the HRV. Since CS are tenuous in comparison with RS, in [25] wavelets were used due to their optimal resolution in time-domain for high-rate signals, and the EEMD was applied to help in signal reconstruction. Herein, the RMSE varied between 2.53 and 4.83%.

Considering the advantages highlighted in [25], [148], the multi-resolution analysis and the signal decomposition were selected to be explored in this work. The results reported in literature are often related to short datasets that comprehend signals of no more than 10 subjects and with short duration (varying between $1 - 5$ minutes) [25], [26], [33], [44], [56], [146]–[149].

Therefore, in order to step forward in the bio-radar research and contribute for the state of the art, it is required to evaluate these methods efficiency considering the application of bio-radar in real scenarios, where it might imply the radar operation in non-controlled environments and during long periods of time. The system operation in real scenarios also implies its suitability to a wide population, encompassing an inter-individual physical variability, which have a direct impact in the signals quality, as seen in Chapter 3.

5.1.3 Heart rate variability

The bio-radar potential can be maximized if the acquired biosignals are used to infer certain subject conditions such as the emotional state, drowsiness or to help identifying possible

cardiopulmonary diseases. This might be accomplished if the cardiac waveform is recovered correctly and by therein compute parameters such as the heart rate and the HRV.

The nervous system is mainly divided in sympathetic and parasympathetic systems. The sympathetic system is activated in stress situations and prepares the body to run or fight reactions. It is generally noticed with the increase of the heart rate and arterial pressure. On the other hand, the parasympathetic system enables body actions towards calm and rest, by decreasing the heart rate and blood pressure accordingly [156]. The main nerve of the parasympathetic system is the vagus nerve [156], therefore this nervous system activity is also referred as the vagal tone [156]. In practice, the HRV provides an index of the vagal tone, by representing the change in the time interval between successive cardiac peaks, or in other words the IBI variability [156].

The HRV can be divided in *time-domain* and *frequency-domain* parameters. The time-domain parameters quantify the amount of IBI variability and encompass for example the Standard Deviation of Normal-to-Normal intervals (SDNN), the Square Root of the IBI variance (SDRR), the Root Mean Square of Successive Differences (RMSSD) and the Percentage of successive Normal sinus IBI more than 50 ms (pNN50) [157]. The frequency-domain ones estimate the distribution of the IBI power into four frequency bands [157]: the Ultra-Low Frequency (ULF) (≤ 0.003 Hz), the Very-Low Frequency (VLF) ($0.0033 - 0.04$ Hz), the Low Frequency (LF) ($0.04 - 0.15$ Hz) and the High Frequency (HF) ($0.15 - 0.4$ Hz) [158]. Usually, the ULF and VLF bands are indicators of different body parameters, such as the body temperature, metabolism and long-term regulation mechanisms, hence they can only be assessed through 24-hour recordings [156]. On the other hand, LF and HF bands can be assessed in short-term monitoring periods, but no less than 5-minutes [158]. The LF band reflects the contributions of both sympathetic nervous system and the vagal tone [156], and the HF reflects the vagal tone, however it is highly influenced by breathing. Likewise, the time-domain parameters RMSSD and pNN50 are strong indicators of the vagal tone and they are free of the respiratory influence [156].

In order to obtain such delicate parameters, a CS with high resolution is required to correctly identify cardiac peaks location. However, the radar CS lacks in resolution for being measured at the chest surface as the mechanocardiography [32]. Besides, the operating carrier frequency can be an aggravating factor, since it has a direct impact in the system sensitivity. In [18], the authors evaluated the relation between the cardiac SNR and the carrier frequency, concluding that frequencies between 5 GHz and the lower region of K-band provide signals with better SNR.

The works presented in literature so far have been showing interesting results regarding the HRV assessment using radar systems operating with different carriers. Authors using the 2.45 GHz ISM band revealed that HRV parameters cannot be inferred accurately due to intrinsic characteristics of the radar sensor [111], [159]. In [160] this lack of signal resolution is also reported for a radar operating with the same frequency, but an autocorrelation-based algorithm is developed to rectify the missed peaks. On the other hand, accurate HRV results were reported mostly using 24 GHz radars in [144], [161]–[163], and as far as one could know, [25] is the only work reporting HRV results using a 5.8 GHz radar. Despite the outstanding results presented for 24 GHz radars, in Chapter 2 it was established the importance of also performing studies with lower carriers. In sum, the increased sensitivity turn signals prone to be highly affected by RBM during the monitoring period. Furthermore, high carrier signals also suffer from high attenuation, hence the possible range is restricted.

The study presented in this chapter is fully dedicated to the CS extraction and exploita-

tion. It starts with the implementation and comparison of methods based in signal decomposition and multi-resolution analysis to extract the CS. The methods performance is verified using a dataset acquired within certain conditions to emulate a real application scenario, which implies that:

- The monitoring environment cannot be controlled;
- The population under monitoring can encompass subjects with different body statures;
- The signal amplitude might change during long term acquisitions, because it is impossible for the subject to remain completely still and keep the same body position.

The effects aforementioned have impact in the received signal quality and hence they might compromise the effectiveness in the CS extraction.

This work started with a method performance comparison, using a dataset composed by vital signs of four subjects with different physiognomies and with a six-hour duration. Subsequently, the best extraction method was selected and tested in a bigger dataset (the 20-subjects with a total duration of ≈ 30 hours). The individual variability is going to be verified through the estimation of the heart rate and solutions were developed to decrease the rate error. Finally, the ability to assess the HRV parameters was inspected. Since these parameters contain useful information to assess the subject's psychophysiological state, a solution was developed to minimize the estimation error, enabling their usage later as features in machine learning algorithms.

5.2 Methods comparison for the cardiac signal extraction

5.2.1 Data collection and signal processing

In order to emulate a real case scenario, the signals of four subjects were acquired inside a conventional room (outside the laboratory environment). More specifically, the signals acquired in Chapter 3 were used (see Table 3.2), but this time an additional female subject was included to balance the dataset. Table 5.1 presents the updated physical characteristics of all subjects.

Subject No.	**Gender**	**Height [m]**	**CWP [cm]**	**BMI [kg/m^2]**
Subject 1	M	1.75	90	22.20
Subject 2	M	1.76	96.5	27.44
Subject 3	F	1.56	82	25.07
Subject 4	F	1.50	75	18.70

M - Male, F - Female, CWP - chest wall perimeter, BMI - Body mass index

Table 5.1: Description of the physical stature of the subjects considered for the method comparison for the cardiac signal extraction.

The vital signs were acquired following the *Emotional Protocol*, which in this case was used to take advantage of a wider variability in the heart rate caused by the emotions felt and also to account with the individual differences. The collected dataset has a total duration of 367 minutes (around 6 hours). Figure 5.4 shows an example of the number of BPM over

time for Subject 1 and for Subject 2. It varied from 65 to 95 BPM along with the different emotional conditions. Besides, each subject had a different reaction for each set of videos, and these events allowed the attainment of unbiased and more robust results.

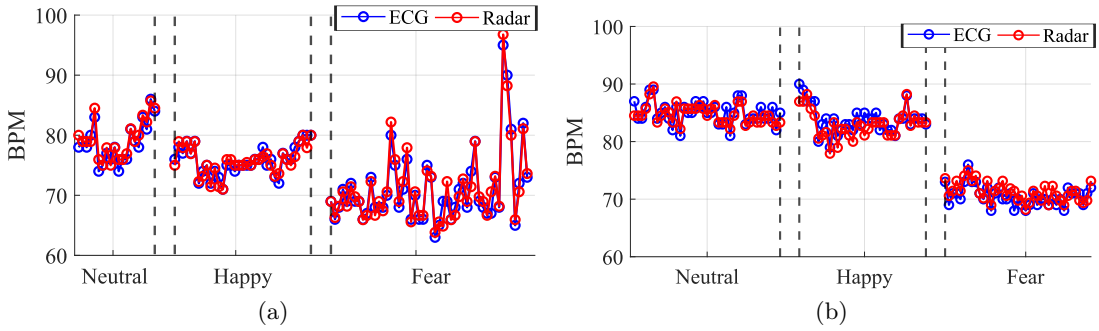

Figure 5.4: BPM variation over time for different emotional conditions [164]: (a) Subject 1, (b) Subject 2.

The vital signs were acquired simultaneously, using theBRD prototype and the BITalino (r)evolution BT board [165], to use the ECG signal as a reference. In order to synchronize both signals, the subjects were asked to perform the breathing pattern depicted in Figure 3.27, where immediately before the next inhale, the subject pushed a trigger button to start the ECG acquisition.

The subjects were seated in front of the antennas at a distance of half meter and they were asked to remain still as much as possible during the experiment. Nonetheless, it was expected for they to move according to their reaction to the videos or even to adjust their position, seeking for a comfortable posture. All these conditions could generate a time varying environment that eventually changes the complex CDC offsets accordingly. The body motion could also cause a misalignment between the antenna beam and the chest wall location that produces the maximum displacement, leading to low amplitude signals.

Furthermore, as previously discussed in Section 3.3 low amplitude signals can also be related with the subjects' body statures, where even the subject's gender may have a role [36]. The impact of the body stature was indeed perceived in the vital signs acquired in the scope of this study, and it is shown in Figure 5.5. More specifically, Figure 5.5a shows the received signal projection in the complex plan. On the left, it is possible to observe the full raw signal obtained during the 30 minute acquisition, from Subject 2 in red and from Subject 3 in black. Both subjects moved during the experiment which caused a change in the CDC offsets. Two distinct groups of arcs can be perceived in Subject 2, marked as A1 and A2. The CDC offsets change is even more pronounced in the Subject's 3 case, respectively marked as B1 and B2. The raw signals samples of Figure 5.5a, also show a difference on the arcs length that might be related with the size of the reflecting areas of both subjects. For a better visualization of the arc length effect, the right side of Figure 5.5a presents the arcs corresponding to one-minute segments of all subjects. Subject 1 and Subject 2 produced an arc larger than Subject 3 and Subject 4. Finally, the same effect is perceived in the extracted respiratory waveform present in Figure 5.5b, after the DSP algorithm, i.e. without the CDC offsets and after the phase demodulation. Herein different amplitude signals were obtained, accordingly *Dynamic DSP*.

Bio-radar signals were acquired using the GNU Radio Companion software, with a sam-

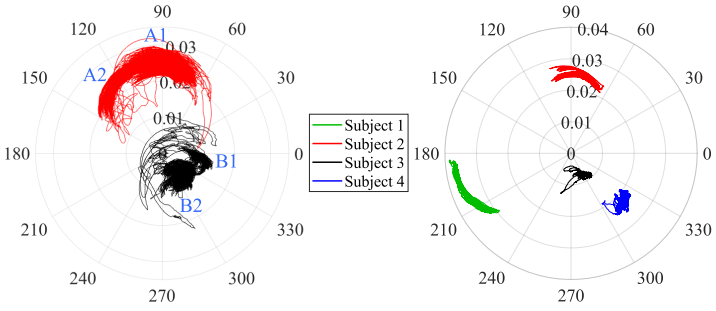

(a)

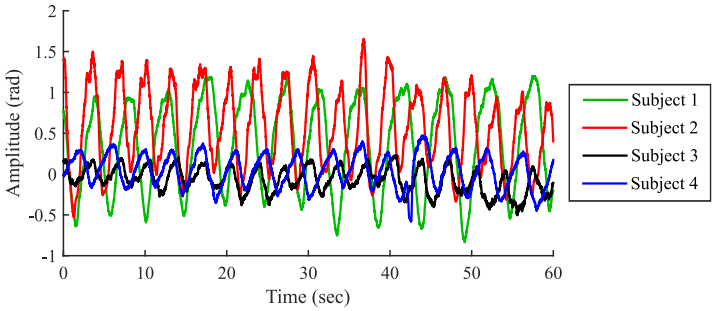

(b)

Figure 5.5: Received signal in a non-controlled environment [164]: (a) Full signal from subjects 2 and 3 (on the left), one-minute segments of each subject (on the right), (b) Extracted one-minute respiratory signals.

---

pling frequency equal to 100 kHz. After receiving the signal, it was processed using MATLAB. First of all, the signal was downsampled to a new sampling rate of 100 Hz and then the CDC offsets were removed to further recover the vital signs correctly. Taking into account the effects observed in Figure 5.5, the *Dynamic DSP* algorithm presented in Section 3.3 was applied for this purpose. At this stage, only the RS can be perceived, so the methods to recover the CS are implemented over this signal. Concurrently, on the ECG side, a 15^{th} order band-pass FIR filter with pass-band equal to 6-20 Hz, was applied to highlight the R-peak detection and remove noise [166], providing a better comparison tool.

5.2.2 Methods implementation

Considering the state of the art previously presented, a total of six methods (M1 to M6) were tested, compared and discussed [164]:

- **M1)** Single Band-pass filter (BPF);
- **M2)** DWT followed by EEMD (DWT+EEMD);
- **M3)** Standalone DWT;
- **M4)** Standalone WPD;
- **M5)** WPD followed by EEMD (WPD+EEMD);
- **M6)** Standalone CWT.

Despite the presented disadvantages of BPF [145], it is still widely used in literature. Therefore it was included as a standalone method and its performance was evaluated as well. Additionally, in preliminary tests it was verified that applying a BPF prior to any other method, attenuates the respiratory component and improves in general the algorithms performance. For this reason, the remain methods (M2 to M6) are applied after a band-pass filtering stage. Each method was implemented using the following specifications:

BPF: This method consists only on a 100^{th} order band-pass FIR filter, with a pass band between 0.7 and 2 Hz. This filter order was selected because it provides a 10 dB attenuation over the respiratory frequency band.

DWT: In this work, DWT is implemented to directly retrieve the cardiac waveform, rather than denoising it. The wavelet coefficients are obtained using the maximal overlap discrete wavelet transform, implemented with *modwt* function from MATLAB, considering 7 decomposition levels, as recommended by [33]. For this purpose, a Daubechies with 4 vanishing moments was selected as mother wavelet by trial. Then, the resultant signal can be recovered from the wavelet coefficients using the *modwtmra* function from MATLAB. The output of this function consists on a set of signals with different frequency components. Since our signals are analyzed with a sampling rate equal to 100 Hz, the cardiac component is mainly present in the 5^{th} and 6^{th} decomposition levels. Therefore, only the signals of these two levels are considered.

WPD: This method is similar to DWT. A decomposition tree can be obtained using the *wpdec* function of MATLAB, with the same mother wavelet used in DWT. In order to avoid redundancy and save computational resources, only the 8^{th} decomposition level was selected to inspect the nodes. This level was chosen by trial, since it was the one providing enough frequency discretization on the cardiac band. The CS was reconstructed using the coefficients of the nodes which had the desired frequency, and this was performed using the *wprcoef* function.

EEMD: In order to implement the EEMD, the guidelines suggested in [155] were followed. White noise was added to the input signal, with an amplitude equal to $A_W = 0.4 \times \sigma(x(n))$, where $\sigma(x(n))$ denotes the standard deviation of input signal $x(n)$. The noisy signal was decomposed in IMF afterwards and these steps were repeated a total of 100 times, using different noisy samples. At the end, it was obtained the ensemble of means from all IMF. Once again, their frequency content is evaluated to select the ones with the desired spectral component and then sum them to reconstruct the CS.

CWT: The CWT was performed using the Morlet wavelet with *cwt* MATLAB function, which is the option suggested by [147] and [26]. In this case, Daubechies was not used since orthogonal wavelets are designed for dyadic scales (which are more spaced comparing with the ones used in CWT, to reduce redundancy) [151]. The CS was recovered using the *icwt* function, which once again selects the coefficients correspondent to the desired frequency band.

All the decomposition methods reconstructed the CS by summing the sub-signals with a spectral content between 0.8 and 2.5 Hz.

5.2.3 Considered metrics for methods evaluation

During the data processing stage, one could observe that different body statures produced signals with different amplitudes. In particular, the male subjects produced signals with higher amplitude and better SNR, comparing with the signals generated by the female subjects. Hence, there was a necessity to divide the dataset in a Short-version (SH) and Full-version (FL), in order to perform a more controlled analysis. Thus, the SH dataset had 217 minutes and included signals from Subject 1 and Subject 2. This dataset was analyzed primarily to define which is the best method to extract the CS properly. Conversely, the FL included signals of all subjects (367 minutes) and it was analyzed afterwards, to understand the impact that lower amplitude signals have in the algorithms performance (produced by the females considered in this study). Each dataset was divided in one-minute segments.

The methods performance was evaluated in two metric levels, respectively. The first metric level was focused on the heart rate accuracy (in BPM). The heart rate was computed using a ZC approach depicted in Figure 3.29. The **first metric level** encompassed [164]:

- The correlation coefficient between the radar CS and the ECG signal;
- The Bland&Altman (B&A) analysis [167];
- The coefficient of variation (CFV), which relates the variation between the radar and ECG measures with their mean values [168];
- The absolute error between the number of BPM of the ECG and the number of BPM of the radar signal ($\epsilon = |BPM_{ECG} - BPM_R|$), evaluated afterwards using the empirical cumulative function distribution;
- The RMSE also in BPM;
- The computational speed to process all one-minute signals in seconds;
- The results coherency in consecutive runs.

The second metric level is related with the study of the peaks position in relation to the ECG signal. HRV parameters could be successfully computed in radar signals, if the peaks position and hence the IBI do not differ largely from the ECG. Thus, ECG and radar signals were superimposed and the peaks position was compared, as depicted in Figure 5.6. Since the radar and ECG signals were synchronized manually, a small delay between them is expected. The most important aspect is to guarantee that this delay remains approximately constant over the segment. Furthermore, one should note that the eventual delay between the radar and ECG signals may not last more than some milliseconds, therefore the delay does not have impact in the total number of BPM because the delay duration is much less than the mean IBI. The **second metric level** comprised [164]:

- The average IBI of radar and ECG signals ($\overline{\text{IBI}}$);
- The standard deviation of $\overline{\text{IBI}}$ for both radar and ECG ($\sigma_{\overline{\text{IBI}}}$);
- The average value of the time difference between the radar and the closest ECG peak ($\overline{\Delta_{\text{t}}}$);
- The standard deviation of such time difference ($\sigma_{\overline{\Delta_{\text{t}}}}$).

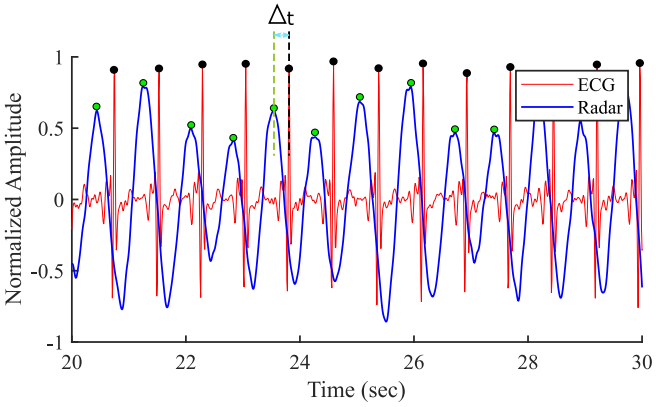

Figure 5.6: ECG and radar signals superposition for peaks location evaluation, with the illustration of two peaks difference Δ_t [164].

The ECG results suggest a slight variability on the $\sigma_{\overline{\text{IBI}}}$, due to the subject's psychophysiological behavior. This is the variation that induce the HRV parameters. The radar signals should vary in the same scale, to equally produce reliable results. Thus, the $\sigma_{\overline{\text{IBI}}}$ for radar is the first indicator of the peaks location consistency. Then, the remain metrics may justify such variation.

For the time difference $\overline{\Delta_t}$, the algorithm seeks for the closest ECG peak in relation to the radar peak under evaluation. The most important metric is the $\sigma_{\overline{\Delta_t}}$, which indicates the variation level of the peaks position in relation to the corresponding ECG peaks, and it should be the lowest as possible.

5.2.4 Results discussion

Starting with the SH dataset evaluation, Figure 5.7 depicts the Correlation and the B&A graphs for all the six methods. Additionally, Figure 5.8 shows the error behavior. The results of both figures are summarized in Table 5.2, which also contains other performance metrics, such as the computational speed and the RMSE. This table presents the results for FL dataset as well, but it will be analyzed afterwards.

Method	Bland & Altman										ϵ (BPM)		Rt (sec)		RMSE	
	r^2		Bias (BPM)		LLoA (BPM)		ULoA (BPM)		CFV (%)							
	SH	FL	SH	FL	SH	FL	SH	FL	SH	FL	SH	FL	SH	FL	SH	FL
M1	0.56	0.30	-4.70	-6.10	-20.0	-26.0	10.0	14.0	10.0	14.0	16.80	28.10	0.68	1.04	8.90	11.80
M2	0.99	0.88	0.49	1.80	-2.0	-3.90	3.0	7.50	1.70	3.70	2.60	7.96	242.14	379.34	1.33	3.38
M3	0.99	0.92	0.19	0.80	-2.10	-3.90	2.50	5.50	1.50	3.20	2.46	5.54	10.80	22.78	1.20	2.55
M4	0.97	0.88	-0.47	-0.24	-4.20	-5.90	3.30	5.40	2.50	3.80	4.31	6.28	233.30	400.70	1.95	2.88
M5	0.98	0.89	0.20	1.10	-2.90	-4.40	3.30	6.60	2.0	3.60	3.10	7.58	458.20	758.08	1.57	4.52
M6	0.98	0.90	-0.21	-0.04	-3.10	-5.30	2.60	5.20	1.90	3.50	2.73	6.16	19.40	35.50	1.47	2.66

SH - short-version dataset, FL - full-version dataset, r^2 - Correlation coefficient, Bias - mean difference between ECG and radar BPM, LLoA - Lower limit of agreement, ULoA - Upper limit of agreement, CFV - Coefficient of variation, ϵ - Error in BPM reached for 95% of the dataset, Rt - run time in seconds, RMSE - Root mean square error

Table 5.2: Heart rate accuracy evaluation metrics for all methods and for both SH and FL datasets [164].

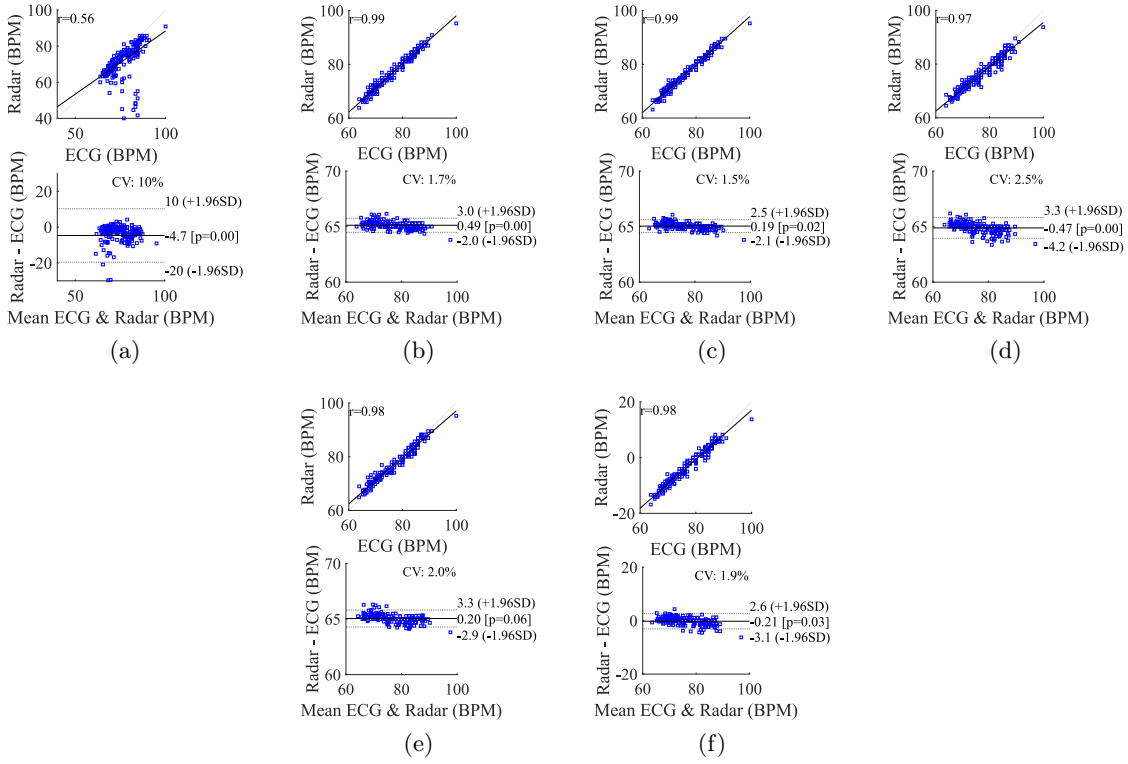

Figure 5.7: Correlation and B&A graphs for tested methods using the SH dataset [164]: (a) BPF (M1), (b) DWT+EEMD (M2), (c) DWT (M3), (d) WPD (M4), (e) WPD+EEMD (M5), (f) CWT (M6).

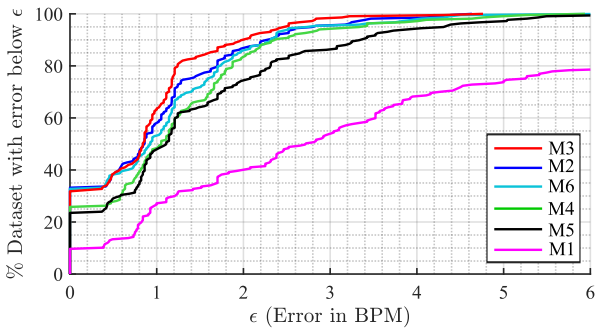

Figure 5.8: Empirical cumulative distribution function of the BPM error for all methods using SH dataset [164].

All methods present a similar BPM accuracy, excepting the M1 method. For instance, it presented a correlation coefficient equal to $r^2 = 0.56$, which clearly indicates a lack of relation between ECG and radar measures. On the other hand, M2 and M3 were the ones standing out with the best performance, having the highest correlation coefficient $r^2 = 0.99$, the lowest coefficients of variation ($CFV = 1.7\%$ and $CFV = 1.5\%$) and the lowest B&A limits of agreement. Between both, it should be highlighted the M3 performance in other metrics. For instance, 95% of the dataset presented an error ϵ that did not exceed 2.46 BPM as shown

in Figure 5.8, and the lowest RMSE being equal to 1.2 BPM. In [18] the authors obtained a similar accuracy using the same carrier frequency and transmitted power. Aside from M1 and M3, M6 is the one that requires less computational resources. However, M6 presents a performance slightly lower than M2 and M3.

Methods that combined wavelets with EEMD (M2 and M5) were specially time consuming, since for each IMF it is required to perform a certain number of repeated observations. Furthermore, EEMD methods presented slightly different results in consecutive runs, probably due to the different characteristics of the noise added on each observation. This could induce an additional error and compromise the results reliability.

The M4 method (using WPD) presented also less satisfactory results, either implemented alone or combined with EEMD. Besides, this method presented a higher execution time, which is related to the nodes decomposition.

Observing now the obtained results for FL dataset (see Table 5.2), the methods with the best performance were M3 and M6, which were the fastest either (neglecting the M1 case). In the FL case, it is possible to verify the results impact due to the smaller reflecting areas and lower amplitude motions of Subject 3 and Subject 4. As expected, the absolute error ϵ in BPM increased in general, namely between 6 and 8 BPM, excepting for the BPF case, where an abrupt increase was verified. The correlation coefficient got also worst, as well as the B&A parameters. Even though, the M3 method stands out for being the best method, having the highest correlation coefficient $r^2 = 0.92$, the lowest CFV, the lowest run time and the lowest RMSE equal to 2.55 BPM.

Regarding the second metrics level, the radar peaks position was evaluated in relation to ECG peaks, through the Δ_t parameter. Starting with the SH dataset, Figure 5.9 shows an histogram that indicates the peaks location distribution in relation to the ECG peak. For instance, if the Δ_t is equal to $\overline{\text{IBI}}/2$, all bars would be around 0.5. On the other hand, if radar peaks were exactly synchronized with ECG peaks, the histogram bars would only fall around the 0.1 value, and this would be the most preferable situation. Assuming that a constant

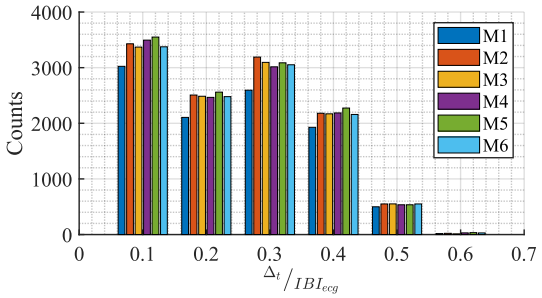

Figure 5.9: Histogram with the distribution of Δ_t over ECG $\overline{\text{IBI}}$ using SH dataset [164].

delay would be acceptable, the bars should lie around any other value, but exclusively that one. In fact, the histogram from Figure 5.9 shows a wider distribution for every value, which indicates a certain level of variability for all methods.

Table 5.3 shows the results of the IBI computation for the radar and the Δ_t variation among all methods. From Table 5.3 and similarly from Figure 5.9, it can be inferred that all methods have a similar behavior and no one stands out in particular. For comparison purposes, the $\overline{\text{IBI}}$ for ECG was equal to 785.72 ms and its $\sigma_{\overline{\text{IBI}}}$ was equal to 37.48 ms. In contrast, the $\overline{\text{IBI}}$ of radar for each method presents a somewhat difference in relation to the

Method	$\overline{\text{IBI}}$ (ms)		$\sigma_{\overline{\text{IBI}}}$ (ms)		$\overline{\Delta_t}$ (ms)		$\sigma_{\overline{\Delta_t}}$ (ms)	
	SH	FL	SH	FL	SH	FL	SH	FL
M1	950.2	977.9	316.0	356.0	177.4	181.2	74.3	88.8
M2	783.9	780.6	94.4	118.5	173.7	179.3	69.4	85.2
M3	792.8	799.2	103.3	131.3	173.2	178.9	67.4	83.7
M4	801.6	809.9	126.8	152.7	174.3	180.0	73.1	87.8
M5	784.1	784.3	109.4	135.1	175.3	180.7	74.6	88.9
M6	800.3	813.1	116.5	147.6	173.8	179.6	70.4	85.9

SH - short-version dataset, FL - full-version dataset, $\overline{\text{IBI}}$ - average IBI, $\sigma_{\overline{\text{IBI}}}$ - average standard deviation of $\overline{\text{IBI}}$, $\overline{\Delta_t}$ - average time difference between radar and the closest ECG peak, $\sigma_{\overline{\Delta_t}}$ - standard deviation of $\overline{\Delta_t}$

Table 5.3: Evaluation metrics for peak location consistency for all methods [164].

ECG $\overline{\text{IBI}}$, which is more notorious for the M1 method. However, wider differences can be noticed in all $\sigma_{\overline{\text{IBI}}}$, which represents a IBI variability higher than expected for the radar side.

These results may be explained with the peak location variation, as suggested by $\overline{\Delta_t}$ results. There is indeed a considerable delay on the radar peak position, and in fact, this delay can be seen as worrisome considering its standard deviation, which varies between 67 and 75 ms. This variation might be translated in an additional error on the IBI determination.

For the FL dataset, the $\overline{\text{IBI}}$ ECG was equal to 789.4 ms and its $\sigma_{\overline{\text{IBI}}}$ was equal to 50.3 ms. The radar $\overline{\text{IBI}}$ results did not altered much, but they became slightly worse for $\sigma_{\overline{\text{IBI}}}$. Likewise, the $\overline{\Delta_t}$ and its $\sigma_{\overline{\Delta_t}}$ increased around 10 ms. Almost all results were affected after adding signals from Subject 3 and Subject 4. In this sense, it is possible to conclude that low amplitude motions hamper even more the methods sensitivity to precisely determine the radar peaks location, which can also compromise the heart rate accuracy.

In sum, although DWT revealed being the best method for heart rate estimation, it might not be suitable for HRV estimation and all methods presented similar results regarding the peak position consistency. Therefore, the direct computation of HRV parameters might not be possible as it is, and other approaches should be explored. This conclusion is in line with Kim et al. in [111], where a different radar with a lower carrier frequency was used.

5.3 Heart rate computation

In the previous section, several methods for the CS extraction were implemented, combined and compared, considering real application scenarios. One could conclude that the standalone DWT is the best method to extract the CS, but these conclusions were derived using signals of only four subjects.

The goal of the current section is to test the selected algorithm in a wider dataset and evaluate the error on determining the heart rate. This time the 20-subject dataset was used (see Table 3.6). The vital signs were acquired following the *Emotional Protocol*, concurrently using the BRD prototype and the BPC to serve as reference.

After extracting the CS using wavelets, the heart rate of all subjects was estimated using two conventional methods: 1) the ZC method from Figure 3.29 and 2) the Maximum of the

Spectrum (MS) method. The MS was computed using the Welch method with the Hamming window and 50% of overlap.

The MAE and RMSE were computed for each method considering the ECG signal rate as reference. Both errors provide different contributions. For instance RMSE is more sensitive to outliers, therefore if its value is closed to the MAE, it means that the subject presents somehow a stable behaviour. On the other hand, if the the RMSE is higher than the MAE, it means that there are outliers, that might be caused due other disruptive sources, such as the RBM. Table 5.4 shows the error results for each subject considering all emotional conditions gathered, the total average error and the average error per emotion. The number of minutes per emotion was balanced for a fair analysis.

Subject ID	ZC		MS	
	MAE [BPM]	RMSE [BPM]	MAE [BPM]	RMSE [BPM]
ID01	4.01	4.64	0.94	1.67
ID02	1.24	1.66	2.29	3.87
ID03	2.04	2.94	3.19	5.96
ID04	14.33	18.06	4.57	8.69
ID05	8.66	10.34	16.73	21.92
ID06	0.85	1.18	0.89	1.21
ID07	1.81	2.83	1.10	1.58
ID08	2.05	2.66	5.37	8.69
ID09	6.78	8.54	7.00	9.78
ID10	6.44	8.41	3.78	6.12
ID11	14.37	15.37	5.90	9.87
ID12	1.11	1.59	2.60	4.43
ID13	5.80	7.76	13.80	19.32
ID14	6.89	8.70	3.71	7.31
ID15	4.73	7.18	7.91	15.56
ID16	0.59	0.98	0.67	0.92
ID17	3.58	4.61	4.62	7.10
ID18	1.93	2.52	2.05	4.04
ID19	2.13	2.82	3.89	7.75
ID20	2.95	3.66	2.88	5.55
Total average	4.61	5.82	4.69	7.57
Average Happiness	5.57	6.61	5.23	7.58
Average Fear	4.27	4.99	4.14	6.21
Average Neutral	4.00	4.70	4.71	6.93

Table 5.4: Comparison of the heart rate error in BPM for both ZC and MS methods using the 20-subject dataset.

Two conclusions can be directly driven from the error results. Considering the MAE, more than half of the subjects presented an error inferior to 4 BPM on both ZC and MS methods, where at least two cases were below 1 BPM, and thus proving the effectiveness of the DWT method used to extract the radar CS. Secondly, the individual variability reported in [32] and previously discussed in Section 5.2, is indeed observed since the other half of subjects presented an MAE superior than 4 BPM and even exceeding 10 BPM at least in two subjects.

The ZC and MS methods present similar results, but the ZC stands out with the lower MAE and RMSE averages. Moreover, the ZC is also the most stable one, since the MAE and RMSE are close most of the times. Even though, one can note that sometimes these methods complement each other. For instance, subjects ID04, ID10, ID11 or ID14 present a high heart rate error if computed using the ZC method, rather than using the MS one, but most of the

times is the other way around.

Figure 5.10 shows the spectrum of some subjects, that may justify the lack of consistency of the heart rate results among the different subjects and between methods. All spectrums are relative to $y(n)$ signal (see Figure 3.4), containing both respiratory and cardiac components. It was selected the 10^{th} minute of the neutral condition, hence assuming the same psychophysiological condition for everybody and assuring the subjects' stability and rest, since it is a moment exactly in the middle of the experiment. Signals were normalized according to their maximum amplitude and their mean value was removed. Each figure shows also a vertical red line with the ECG rate corresponding to that minute.

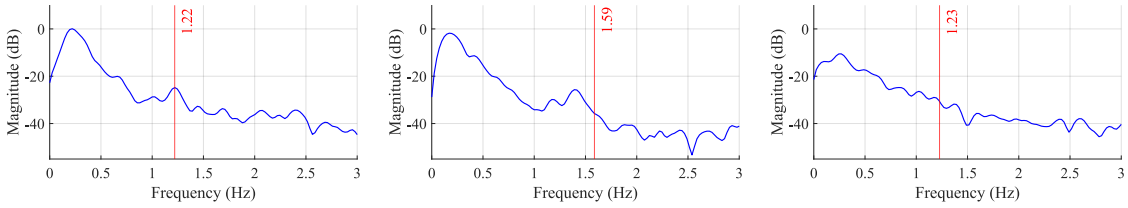

(a) ID1 (b) ID5 (c) ID8

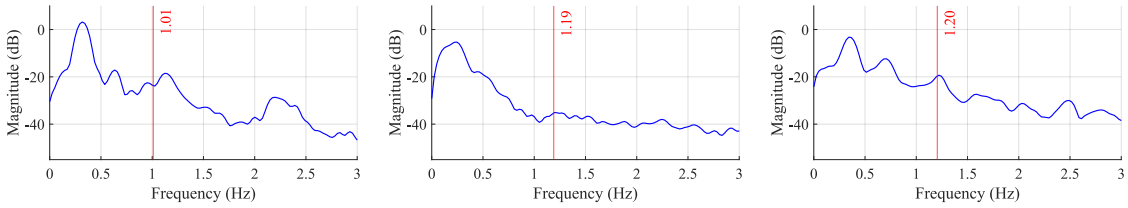

(d) ID7 (e) ID17 (f) ID18

Figure 5.10: Spectrum of the 10^{th} minute of the neutral condition.

The first aspect that one can observe, is that each subject has its exclusive spectral trace. The spectrum can be influenced by the subject's posture, the breathing periodicity or the eventual occurrence of body motions. Periodicity variations might lead to the appearance of harmonics that might superimpose with the cardiac component. An example of this effect can be observed in the spectrum of subject ID07. As for subjects ID01 and ID18, the radar cardiac peak seems to match exactly with the expected ECG frequency. Finally, subjects ID08 and ID17, in that specific moment, seem not having any trace of cardiac component in the spectrum.

Additionally to the individual variability observed even in a neutral scenario, where the subject is mainly at rest, one can also conclude that the psychological condition of the subject can also compromise the heart rate assessment. Considering only the ZC results, for being in general better and more stable, a low error is obtained if the subject is in a neutral condition. On the other hand, if the subject is somehow aroused, the body reaction lead to certain reactions and a change of posture, which might influence the effectiveness of the CS extraction algorithms. This was more clear in the happiness condition, where the error increased in average more than 1 BPM in relation to the neutral condition.

5.4 ANN models for the heart rate accuracy improvement

The heart rate is directly related with the vagal tone, which is mostly activated when subjects are at rest leading to an average of 75 BPM [157]. If the rest condition alters, it will be reflected in the heart rate accordingly. As it will be explained later, the vagal tone is a clear indicator of the subjects' physchophysiological condition. Therefore, in order to fully exploit the bio-radar potential, the vagal tone assessment would be extremely beneficial. In this sense and in order to avoid biased results, it is important to determine the heart rate accurately.

The usage of machine learning algorithms dedicated to the CS extraction or its rate estimation, have been reported in [169]–[172]. These works explored Neural Networks (NN) as machine learning algorithms, using short signals with 300-seconds duration in maximum (≈ 5 minutes) directly in the NN input (instead of computing specific features over the signals). The most used algorithms were the Artificial Neural Networks (ANN) and the Convolutional Neural Networks (CNN). The ANN are nonlinear models following the same principle as the human neural system. The ANN schematics is depicted in Figure 5.11. The algorithm is composed by a input layers containing the features computed over the data, one or more hidden layers and an output layer [173]. Each layer contains nodes weightily connected to the ones of the adjacent layers. The nodes weights W_n are changing during the training phase, providing more importance to the meaningful links. Each node is regulated through an active function, which introduces non-linearity to the model [173]. The final goal of the model is to fit the input data to the output.

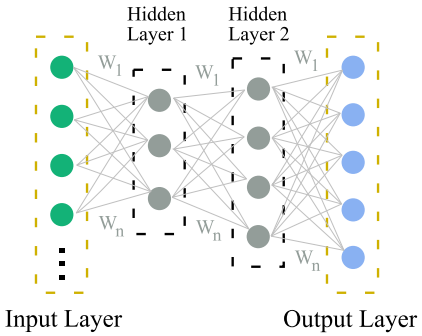

Figure 5.11: Representative ANN schematic (adapted from [173]).

The CNN process data through a grid topology, therefore their are typically used for image processing and recognition. In contrast to ANN, the CNN dismiss features selection to provide on the input layer, since it extracts its own features from the input data through convolutional operations [174]. Its architecture (see Figure 5.12) is similar to the ANN one, since it is also composed by input layers, hidden layers and an output layer. The input data is arranged in a matricial form and decomposed in shorter blocks through filtering (in the convolution layer). Subsequently, such blocks are non-linearly combined aiming to learn and extract pertinent features in the activation layer, creating a feature map. The pooling layer reduces the network complexity by decreasing the size of the feature map and the resulting consists on the input for the next layer. The procedure is conducted progressively over the different layers.

CNN were used in [169]–[171], to reconstruct the corresponding ECG signal from a radar

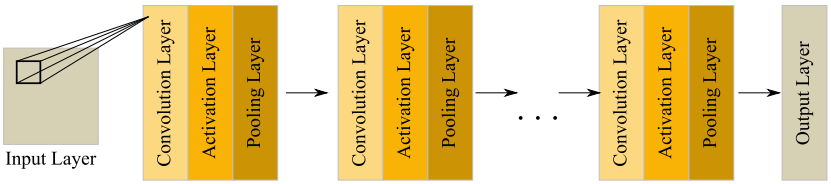

Figure 5.12: Representative CNN schematic (adapted from [174]).

one [169], for person identification [170] and for heart rate estimation [170], [171]. In [169] a hold-out strategy was used to train the model, namely using 70% of the dataset relative to six subjects for training and the remaining for validation and test. The authors were able to reconstruct the ECG signal, even adding artificial noise to the input signal. In [170], individual models were trained using vital signs with 5-minutes duration of each subject individually. These individual models served not only as a biometric personal identifier, but also to determine the heart rate through the IBI estimation, with a maximum error of 48.5 ms. In [171] the performance in the heart rate estimation using different NN is compared, namely with the ANN, the CNN and the combination of CNN with recurrent neural networks. The authors concluded that the latter option achieved the highest performance, presenting 99% of accuracy, but using a single subject exclusively.

On the other hand, ANN were used in [172] for a cardiac peak detection and further instantaneous heart rate estimation. While [169]–[171] developed the models considering 10 subjects in maximum, [172] used an increased dataset of 21 subjects. To train the model, a three-fold cross validation strategy was used. The group of 21 subjects was divided in three groups of 7 subjects, where two groups were used to train the model and the remain one to test. The training and testing process where repeated for different combinations of the groups. At the end, the proposed algorithm was capable to determine the heart rate with an average error of ≈ 3 BPM. Nonetheless, the authors in [172] highlighted that the eventual occurrence of body motion might have impact in the results, and also the error could increase if the population under test increases. CNN are efficient with increased datasets and do not require prior knowledge about the data.

In the previous section, one verified that the accuracy in the heart rate computation can be compromised due to a subject-related variability. Since interesting results for this same purpose were reported in [169]–[172], where NN were implemented using the radar signal as input, the same approach was followed aiming to reduce the heart rate error and standardize the accuracy for all subjects, so this information could be further used to assess for instance the subjects' psychophysiological condition. It was observed that ZC and MS methods seem to complement each other, therefore both methods might contribute with different information. In this sense, instead of using the radar signal as the NN input, as it was done in [169]–[172], pertinent features were computed over the radar signal, where the ZC and MS methods were included for example. Once the dataset at hand is size reduced and the input is a set of known features, ANN were selected to be implemented.

Two approaches were followed in parallel regarding the dataset handling. All the dataset was included to develop a person-independent model, similarly to the work developed in [172], and individual models were also developed to conduct a person-dependent analysis. At the end, the error in heart rate was compared using the ZC, MS, Global Model (GM) and Individual Model (IM) methods.

5.4.1 Global model

For the GM implementation using ANN, an observation matrix was extracted using one-minute signals. Considering the complementary information retrieved from the ZC and MS methods, 12 features were selected manually and they are detailed in Table 5.5. More details

	Feature N^{o}	Description
Signal Harmonics	F1	Heart rate using ZC
	F2	Heart rate using MS
	F3	Respiratory rate
	F4	The energy ratio between respiratory and cardiac components
	F5	Harmonic indicator for ZC
	F6	Harmonics indicator for MS
Windowed Spectral Content	F7	Number of peaks within the window
	F8-F9	Magnitude and frequency of the peak located in the minimum frequency of such window
	F10	Magnitude of the peak located in F2 frequency
	F11-F12	Magnitude and frequency of the peak located in the maximum frequency of such window

Table 5.5: Features considered for the ANN implementation to improve heart rate results.

are now provided over these features computation:

- F1-F2 are the heart rate value provided in Hz;
- F3 is the respiratory rate computed using the ZC and it is also in Hz;
- F4 is obtained by dividing the signal energies before and after applying the BPF (applied before the DWT);
- F5-F6 are obtained by evaluating the remainder after F1/F3 division and after F2/F3 division, respectively;
- F7-F12 are dedicated to the spectral content within a window 10 dB below the magnitude of the maximum peak (F2).

Since features have different natures and their range of values are different from each other, a standardization is required. In this case, the *z-score standardization* was applied to all features, as described by (5.1):

$$\tilde{x}_i = \frac{x_i - m_i}{\sigma_i} \tag{5.1}$$

where, $\tilde{x}_i$ is the standardized feature, x_i is the feature to be standardized, m_i is its mean value and σ_i is its standard deviation.

After selecting the appropriate features and computing them over the data (and thus creating an observation matrix), the ANN hyperparameters must be selected. Considering Figure 5.11, the hyperparameters include the number of hidden layers, the number of nodes inside each hidden layer, the activation function (to be used inside the nodes) and the regularization parameter Λ. Regularization is a technique used to simplify the model and to prevent it to overfit [173]. In [172], the authors selected a set of hyperparameters by testing manually different combinations. Thereafter, the authors evaluated the performance of the model with a three-fold Cross-Validation (CV). They divided the 21-subjects dataset in three groups of

7 subjects, and use two groups for training and one for testing and repeated the process three times.

In our case, the hyperparameters optimization was performed during the training phase in MATLAB. Therefore, the dataset division for training and testing was fixed to keep the coherency and guarantee the results reproduction. The dataset division is represented in Figure 5.13.

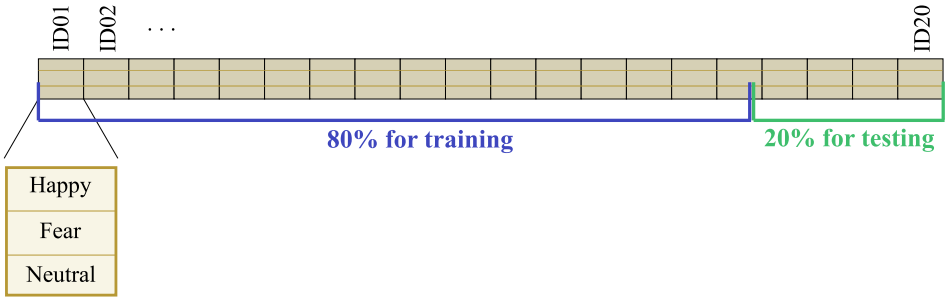

Figure 5.13: Dataset division for training and testing the GM used to improve heart rate results.

For the training, 80% of the dataset was used (considering the total number of observations), whereas the remain 20% was used to test the model. The ANN output was the heart rate result obtained by the ECG. The hyperparameters optimization was performed within a 200 iteration process using the Random Search and within the following ranges:

- Activation function - Rectified linear unit (ReLU) function, Hyperbolic tangent (tanh) function or the Sigmoid function;
- Number of hidden layers - between 1 to 3;
- Number of nodes inside each hidden layer - between 6 and 30;
- Regularization parameter Λ - between 1×10^{-5} and 10;

The final ANN used the following hyperparameters: two hidden layers with 22 nodes each, the hyperbolic tangent as activation function and the regularization term $\Lambda = 8.9371 \times 10^{-4}$. After testing in the remain 20% of the data, an MAE of 4.01 BPM was obtained. Finally, the developed model was applied to each subject individually to verify if the MAE had decreased. The results are presented in Table 5.7 and they are going to be discussed after the Person-dependent model description.

5.4.2 Individual model

For the IM implementation using ANN, the same features set used to generate the GM was computed over one-minute signals and the results were standardized using the *z-score standardization* accordingly. Similarly to the procedure conducted above, the network hyperparameters were optimized during the training process. The data division for training and testing is schematized in Figure 5.14. Since this time an individual model is aimed to be developed, the dataset at hand is severely decreased. Therefore, the dataset partition in 80:20 was performed per emotion rather than being over the subjects' signals as a whole, in

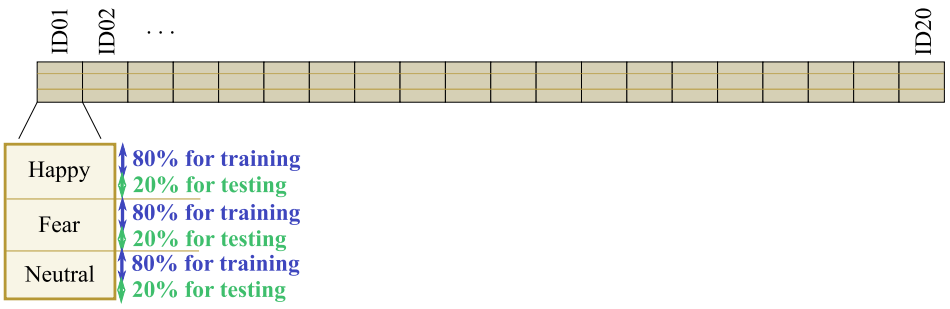

Figure 5.14: Dataset division for training and testing the IM used to improve heart rate results.

order to account the individual variability over the felt emotions. In other words, 80% of each emotion signals was used for training and the remaining to test and this is performed for each subject separately.

The hyperparameters optimization was performed in two stages. First of all, a wider range was considered and their were optimized for each subject separately. The considered ranges for this case were the following:

- Activation function - Rectified linear unit (ReLU) function, Hyperbolic tangent (tanh) function or the Sigmoid function;
- Number of hidden layers - between 1 to 2;
- Number of nodes inside each hidden layer - between 6 and 60;
- Regularization parameter Λ - between 1×10^{-4} and 5;

Table 5.6 shows the set of hyperparameters suitable for each individual network and the corresponding average MAE for each subject.

Thereafter, the hyperparameters presented in Table 5.6 were analyzed and combined in order to verify if there is a specific set that is equally capable to reduce the heart rate error for all subjects. Thus, an individual model was trained with the data of each subject, considering the following common hyperparameters: two hidden layers with 26 and 22 nodes respectively, the Relu activation function and a regularization term equal to 0.0029. The obtained MAE results are presented in Table 5.7.

5.4.3 Final comparison and discussion

Table 5.7 sums up the heart rate MAE obtained for all the methods explored in this section. Between the conventional methods ZC and MS and the implementation of ANN, the first aspect that can be highlighted is that in fact and as expected the error had decreased. Using a GM trained with the signals of all subjects had improved in general the heart rate accuracy, which is specially noticeable in some subjects namely subject ID04, ID05, ID11 or ID13 since they presented errors superior to 10 BPM and they decreased at least 4 BPM. In average, while the ZC and MS errors were 4.61 and 4.69 BPM respectively, with the GM it decreased to 3.39 BPM. On the other hand, if an IM is trained and applied to each subject the results improve substantially, leading to an MAE of around 1 BPM. Although training an individual model for each subject implies a certain degree of implementation complexity, the

Subject ID	Activation function	N^{o} hidden layers	N^{o} nodes	Λ	MAE [BPM]
ID01	tanh	1	[6]	8.4120×10^{-4}	0.62
ID02	ReLU	2	[25 24]	6.2000×10^{-3}	0.96
ID03	Sigmoid	2	[55 16]	1.1813×10^{-4}	1.03
ID04	tanh	2	[52 13]	6.2304×10^{-4}	1.07
ID05	Sigmoid	2	[29 10]	8.5716×10^{-4}	2.25
ID06	Sigmoid	1	[33]	1.2000×10^{-3}	0.61
ID07	ReLU	2	[29 9]	1.4000×10^{-3}	0.55
ID08	ReLU	2	[6 54]	5.6000×10^{-3}	1.24
ID09	ReLU	1	[7]	3.0000×10^{-3}	1.91
ID10	tanh	2	[8 15]	1.0700×10^{-2}	2.38
ID11	Sigmoid	1	[28]	5.2000×10^{-3}	1.51
ID12	ReLU	2	[13 32]	4.6000×10^{-3}	0.94
ID13	Sigmoid	1	[14]	1.7000×10^{-3}	2.14
ID14	ReLU	2	[16 16]	3.4000×10^{-3}	1.03
ID15	Sigmoid	2	[36 18]	1.2310×10^{-4}	1.22
ID16	tanh	2	[25 9]	4.4415×10^{-4}	0.47
ID17	ReLU	2	[6 54]	5.6000×10^{-3}	1.85
ID18	Sigmoid	1	[28]	5.2000×10^{-3}	1.03
ID19	Sigmoid	1	[7]	5.6379×10^{-4}	1.19
ID20	Sigmoid	2	[36 18]	1.2310×10^{-4}	0.97

Table 5.6: Optimized hyperparameters for each individual network.

Subject ID	ZC	MS	GM	IM	Subject ID	ZC	MS	GM	IM
ID01	4.01	0.94	1.40	0.69	ID11	14.37	5.90	6.37	1.10
ID02	1.24	2.29	1.89	0.76	ID12	1.11	2.60	2.37	0.85
ID03	2.04	3.19	2.38	1.05	ID13	5.80	13.80	5.01	1.44
ID04	14.33	4.57	4.21	1.21	ID14	6.89	3.71	3.66	0.98
ID05	8.66	16.73	3.85	1.14	ID15	4.73	7.91	4.57	1.04
ID06	0.85	0.89	0.98	0.57	ID16	0.59	0.67	1.48	0.46
ID07	1.81	1.10	1.30	0.65	ID17	3.58	4.62	4.86	1.56
ID08	2.05	5.37	4.04	0.99	ID18	1.93	2.05	2.10	0.86
ID09	6.78	7.00	4.33	1.71	ID19	2.13	3.89	5.55	0.83
ID10	6.44	3.78	3.74	1.55	ID20	2.95	2.88	3.69	0.81

Table 5.7: MAE of heart rate in BPM for all tested methods.

accuracy provided might compensate, as demonstrated by Figure 5.15. This figure shows the progression of the heart rate error over time and per emotion for all the applied methods. The selected examples include two cases where the error rate is small in general, namely the ID06 and ID16 cases, where the latter only shows an increased error if the heart rate is estimated through GM. On the remain examples, the ZC and MS methods lead to higher errors when compared to the NN methods. Finally, between the NN methods, the IM follows generally the ECG rate, while the GM still deviates considerably.

Thus, in Chapter 6 the heart rate computed with an IM will be used as a feature to assess the psychophysiological state of the subject, since IM is the method that provides an inferior error and hence ensuring unbiased results, despite its complex implementation.

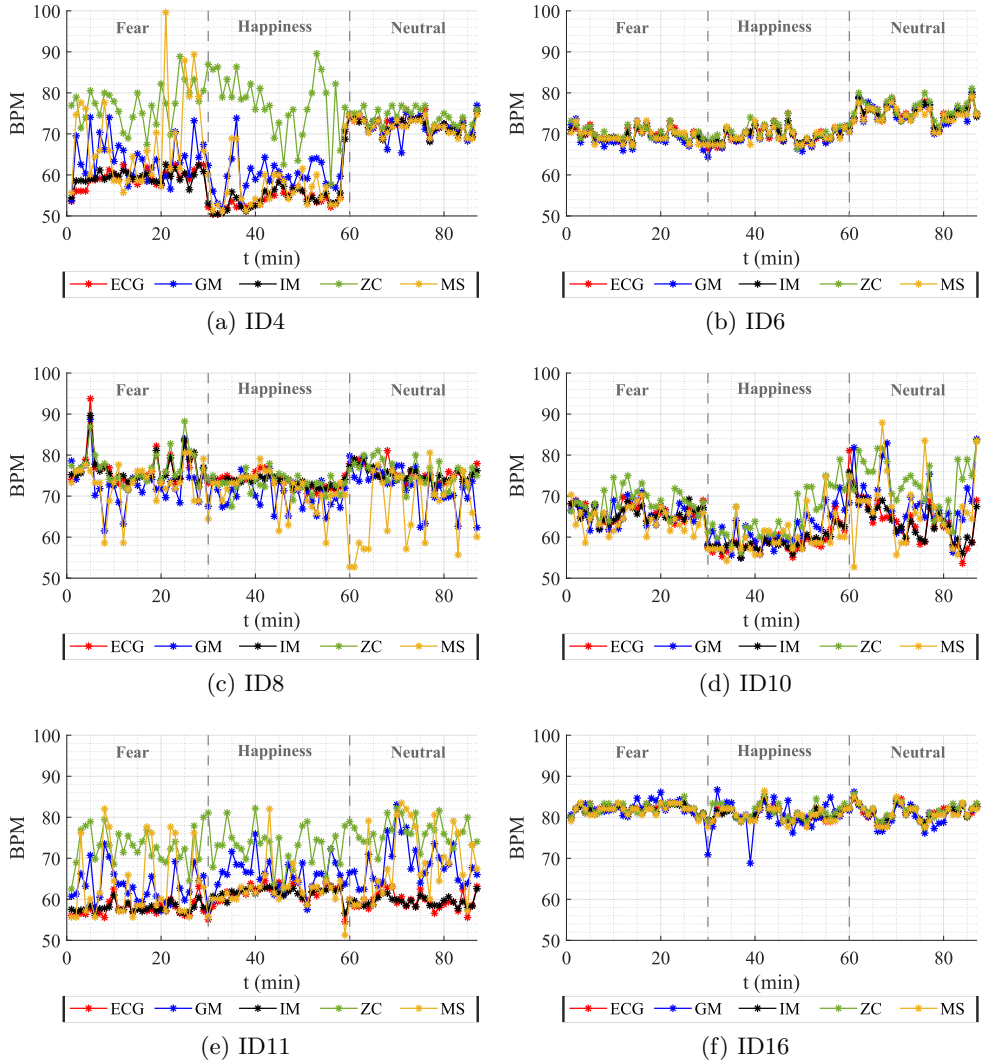

(a) ID4 (b) ID6

(c) ID8 (d) ID10

(e) ID11 (f) ID16

Figure 5.15: Variation of the heart rate in BPM over time and over the different emotions for all methods: (a) ID4, (b) ID6, (c) ID8, (d) ID10, (e) ID11, (f) ID16.

5.5 Heart rate variability assessment evaluation

In Section 5.2, several methods to extract the CS were implemented, combined and compared. Besides the suitable method selection, a preliminary study was carried out to inspect if it would be possible to compute HRV parameters and it was concluded that there is a wide variability regarding the radar peaks position, therefore the HRV assessment might not be possible with the used radar setup. However, this conclusions were derived using a dataset collected considering a real case scenario, where the monitoring environment might not be fully static, the population under monitoring provided signals with different SNR and the signals were acquired during long-term periods, so it was not possible to fully guarantee the subjects stability. It also known that the radar signal quality can be compromised due to different causes, such as:

- The own system sensitivity (also related with the carrier used);
- The alignment between the subject's chest wall and the maximum lobe of the antenna;
- The noise interference acquired within the same frequency band.

The work presented in this section aims to simulate the signals acquisition in an ideal scenario, which are not influenced by those external disruptive sources, and verify if under these ideal circumstances it is possible to compute the HRV parameters using a CW radar operating at 5.8 GHz. For this purpose, an exclusive tool was used, which is fully dedicated to the authentic and unbiased CS. This tool consists on a radar CS model, extracted directly from an ECG signal, using an adaptive filter, namely the Wiener filter [175]. In this way the radar signal model do not encompass any RBM or any other issues presented above and can be further used to computed unbiased HRV parameters. In order to obtain the CS model, an ECG signal was used as the Wiener filter input and a radar CS acquired at the exact same time was used as its output. Since the signal estimation robustness must be guaranteed, a study was performed regarding the correlation between the Estimated Radar Signal (ERS) (CS model) and the corresponding Original Radar Signal (ORS). The correlation variability over time was verified, for different heart rates from the same subject and in-between different subjects and the HRV parameters were computed over the ERS and compared with the ORS and the ECG.

5.5.1 Data collection and signal processing

This study was conducted using the vital signs collected in Section 5.2, namely the signs of Subject 1 and Subject 2 (from the SH dataset). More specifically, it was used the signals acquired from *Fear* and *Neutral* condition sessions. From each session both baseline and emotional condition parts were considered, in order to gather time and rate variation for the same subject. These emotions in turn induce different HRV parameters [156], which will be determined later for both ERS, ORS and ECG, in order to evaluate if it is feasible to use this radar setup for this purpose. Considering the emotions induction and the individual behavior in different days, three different moments are going to be evaluated, being:

- BL1 - Baseline (neutral condition) acquired on the first day;
- F1 - fear condition induced on the first day;
- N2 - neutral condition induced on the second day.

One should remember that the vital signs were acquired simultaneously, using the BRD prototype and the BITalino (r)evolution BT board, and the breathing pattern showed in Figure 3.27 was used to synchronize both signals. In the exact context of this work, where adaptive filtering is being used, it is imperative to assure the system causality. Therefore, the radar signal was considered to start 100 ms before its trigger, to guarantee that in case of synchronization doubt, it is delayed in relation to the ECG signal.

After their acquisition, both ECG and radar signals were processed before being used as input and output, respectively, of the Wiener filter. Figure 5.16, shows the block diagram of the implemented DSP algorithm. Both BRD and ECG signals ($g(n)$ and $g_E(n)$) were processed using MATLAB and the first step was to downsample them to a new sampling rate of 100 Hz, resulting in $d(n)$ and $d_E(n)$ signals. In order to make the R-peak more prominent,

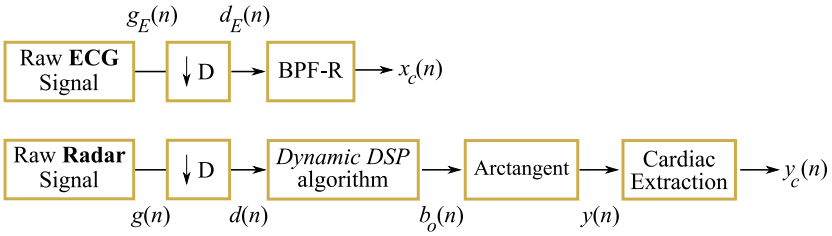

Figure 5.16: Signal processing algorithm for the Wiener coefficients estimation [176].

a 15^{th} order band-pass FIR filter (BPF-R) was applied to $d_E(n)$, between 6 and 20 Hz, as recommended by [166]. In this stage, the resulting ECG signal is the one used as the Wiener filter input $x_c(n)$. On the radar side, the CDC offsets were removed and the arc position was adjusted using the *Dynamic DSP* algorithm presented in Section 3.3. Finally, the vital signs information is extracted through a phase demodulation by applying the arctangent demodulation [21]. Thus, the signal $y(n)$ contains both respiratory and cardiac signals, which are then separated in the *Cardiac Extraction* block, leading to the radar CS $y_c(n)$. Herein, it is used the BPF combined with DWT, which was method selected in Section 5.2.

5.5.2 Wiener coefficients estimation using a short-time signal

The ECG signal can be seen as a sum of waves, correspondent to the different heartbeat phases: the P-wave, QRS complex, T-wave and U-wave [177]. On the other hand, the cardiac radar signal is obtained from the measurement of the mechanical motion of the heart, and thus its rate can be comparable with the fundamental component of the ECG signal.

This fact can be verified in Figure 5.17, which shows an example of a radar and an ECG signals spectrum, normalized according to their maximum magnitudes to ease the analysis. These signals were acquired at the exact same time and for the same subject. The figure presents the radar signal spectrum in two different stages of the algorithm previously presented in Figure 5.16. The dashed-black line shows the spectrum of the $y(n)$ signal, after phase demodulation and yet containing the respiratory component. The blue line shows the spectrum of the cardiac radar signal $y_c(n)$.

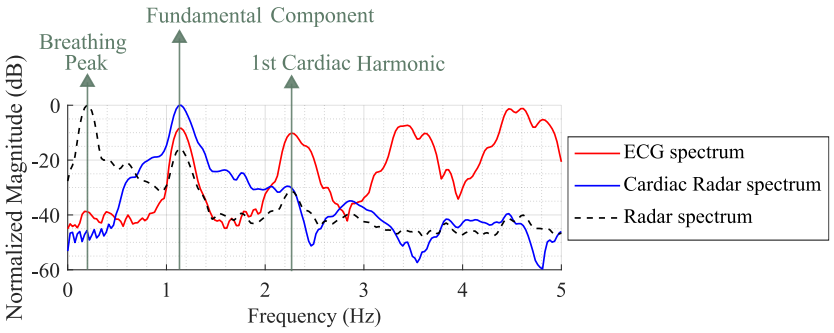

Figure 5.17: Normalized ECG and radar signals spectrum for different stages of the radar DSP [176].

Starting with the radar spectrum ($y(n)$ signal), in Figure 5.17 it is possible to identify the respiratory and cardiac spectral components. Both components are aligned in frequency with

the ECG spectrum. For instance, the respiratory peaks stand in the 0.244 Hz (equivalent to 14.6 breaths per minute) and the fundamental cardiac component stands in 1.123 Hz (equivalent to 67.4 beats per minute) for both radar and ECG signals. The radar signal presents a higher magnitude in the respiratory spectral component, since this signal have an amplitude ten times higher than the cardiac one. More specifically, the radar cardiac component is attenuated almost 20 dB in comparison with the respiratory one. Conversely, the ECG spectrum consists on a set of well-defined harmonics, with high magnitude, inherent to the aforementioned signal nature. The overall radar spectrum matches with the ECG one in the fundamental component and in the first harmonic. The same behavior is observed for the $y_c(n)$ radar signal, where the respiratory component is fully mitigated.

The first stage of this work is to find the filter coefficients $w(n)$ that can relate an ECG signal with the cardiac radar signal acquired at the exact same time. The Wiener filter was selected for being a FIR filter and for presenting a stable behavior. Based on a least squared error approach, the wiener coefficients are computed to minimize the average squared distance between the filter output and input [175], and thus determine the impulse response $h(n)$ that relates both signals. In practice, the impulse response $h(n)$ represents the channel model between the ECG signal and the ORS. The implementation of the Wiener filter to determine $w(n)$ is depicted in Figure 5.18.

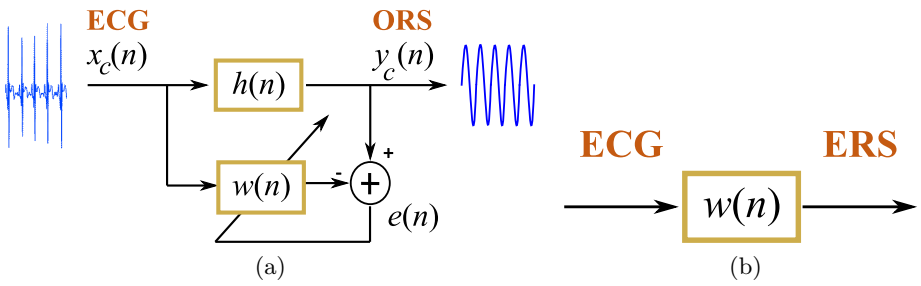

Figure 5.18: Illustration of the procedure to obtain the ERS [176]: (a) Wiener filter implementation to determine $w(n)$ coefficients, (b) Application of the band-pass filter to obtain the ERS.

According to [175], the Wiener theory assumes that signals are stationary. Therefore, $w(n)$ are determined using short time signals, namely with one minute duration to always guarantee a good approximation. The radar signal for a single subject can vary largely over time, specially in a long-term acquisitions due to RBM that the subject might perform for discomfort reasons. Therefore, the selection of such one-minute segment should provide an ERS highly correlated with the ORS, as much as possible. Two different approaches for each subject were conducted to select such one-minute signal:

- A1) A single one-minute segment was selected to compute the $w(n)$ once, and the same filter was applied over time. For this case, the BL1 was analyzed seeking for a moment free of RBM;
- A2) All signals were divided into five-minute segments and the one-minute segment that provided the best correlation for its five-minute slot was selected. In this way, $w(n)$ are updated every 5 minutes leading to a different filter for each instance. This periodicity was selected since signals with a minimum duration of 5 minutes are required for the HRV parameters computation [157].

The selected number of coefficients was the result of a series of trials, that encompass low and higher order approaches. Almost all trials presented similar correlation results as demonstrated by Table 5.8. Thus, it was selected a total number of 1024 coefficients, for being an exponent of power 2 and having in mind an optimal resolution in frequency, but yet a reasonable order to further compensate the caused delay. Moreover, the same number of points was used in the Welch method to obtain the signals spectrum.

Radar Signal	**Subject 1**						**Subject 2**					
	BL1		F1		N2		BL1		F1		N2	
	A1	A2	A1	A2	A1	A2	A1	A2	A1	A2	A1	A2
O = 512	0.85	0.87	0.72	0.74	0.79	0.81	0.74	0.74	0.70	0.71	0.59	0.70
O = 1024	0.84	0.86	0.71	0.73	0.77	0.80	0.72	0.74	0.68	0.71	0.59	0.71
O = 2048	0.83	0.85	0.70	0.72	0.58	0.79	0.69	0.72	0.66	0.72	0.58	0.71
O = 4096	0.80	0.82	0.67	0.74	0.61	0.77	0.68	0.72	0.59	0.71	0.54	0.78

BL1 - baseline day 1, F1 - fear day 1, N2 - Neutral condition day 2, O - filter order

A1 - fully static system, A2 - five-minutes updated static system

Table 5.8: Mean correlation results between ERS and ORS for different filter orders [176].

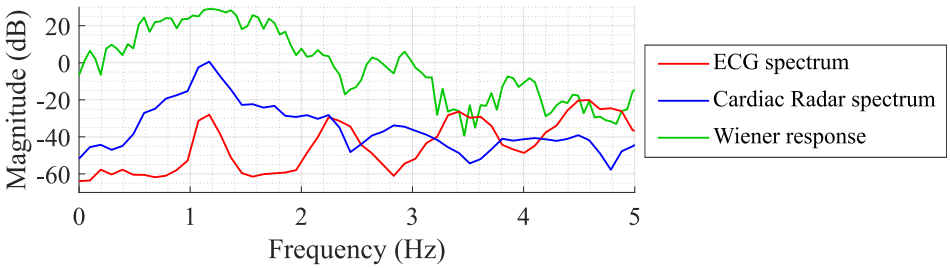

Figure 5.19: Wiener coefficients behavior in frequency domain along with the corresponding ECG and ORS spectrum [176].

As an example, Figure 5.19 shows the frequency response of the resulting $w(n)$ using the A1 approach. In order to approximate the ECG signal to the radar one, $w(n)$ presents a magnitude equal to 30 dB around the fundamental cardiac component, since the ECG fundamental is attenuated that same amount in relation to the radar. On the other hand, the $w(n)$ attenuates the first harmonic around 20 dB and the remain ECG spectral harmonics are attenuated more than 30 dB. After determining $w(n)$, the ERS can be obtained and compared with the ORS, by applying a BPF on the ECG signal using $w(n)$ (Figure 5.18b). Then, the filter delay was compensated and for the subsequently comparison purposes, both ECG and ORS were also compensated assuming the same delay.

Figure 5.20 shows the result, where Figure 5.20a shows the obtained normalized spectrum of ERS, ORS and ECG, and Figure 5.20b presents the corresponding superimposed time domain signals. It is possible to verify that the ERS is highly correlated with the ORS in that signal portion. The correlation can be indeed verified, by computing the cross-correlation between ORS and ERS, which is equal to 0.95 in this case.

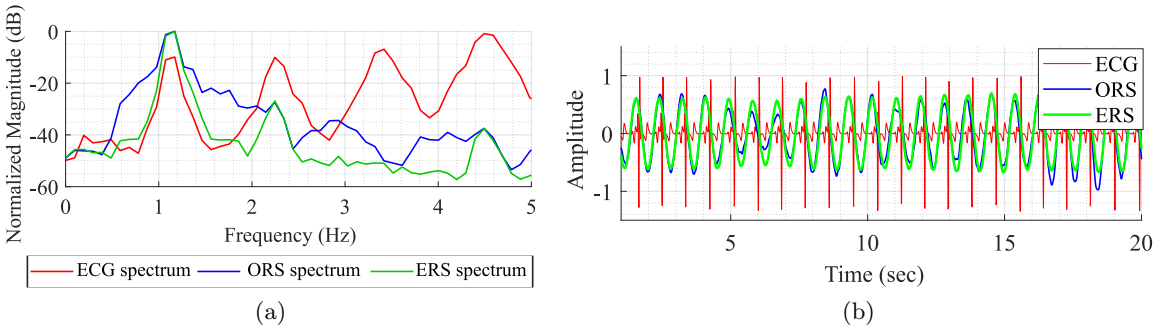

Figure 5.20: Evaluation of the obtained estimated radar signal [176]: (a) Normalized spectrum of ERS, ORS and ECG signals, (b) Time domain signals.

5.5.3 Estimated radar signal analysis

Before computing the HRV parameters associated to ERS, it is required to evaluate the correlation between the ERS and ORS over time, for the different subjects in all moments. High correlation demonstrate the similarity of both signals, allowing a reliable analysis. Nonetheless, it is worth to highlight that the purpose of this study is to evaluate the effectiveness of obtaining HRV parameters considering a static system. For these reason, the results of both approaches used for the $w(n)$ extraction were analyzed simultaneously, where A1 represents a full static system and A2 represents a system that it is only static during 5 minutes.

Figure 5.21 shows the cross-correlation between the ERS and the ORS and the corresponding residual error on the $w(n)$ estimation for different moments: Figure 5.21a corresponds to BL1; Figure 5.21b corresponds to F1; and Figure 5.21c corresponds to N2. The residual error was estimated through the ratio between the energy of the error ($ORS–ERS$) and the energy of the ORS. Furthermore, Figure 5.22 shows the spectral coherence between ERS and ORS, computed at the ORS fundamental frequency.

Starting with the time correlation for subject 1 for the A1 approach, on the BL1 case the cross-correlation is kept above 0.8 most of the time, presenting a mean value of 0.84. Worst correlation results were obtained for the F1 case, where the cardiac rate is changing probably due to frights and the occurrence of more RBM is also expected. Even though, some of the correlation results were above 0.8, presenting a mean value of 0.71. The neutral condition on a different day (N2 case), presented also correlation close to 0.8, where the mean value decreased slightly to 0.77. With this results, it is possible to state that ERS and ORS are identical, excepting some differences inherent to heartbeat changes or sporadic involuntary motions, that were not accounted by $w(n)$. For the A2 approach the results were slightly better, where a correlation of 0.86, 0.73, 0.80 was obtained for the BL1, F1 and N2 cases respectively. One can also see that the residual error keeps the correlation pace, increasing when lower correlations were observed and vice-versa.

More differences between A1 and A2 approaches were observed in the spectral coherence analysis in Figure 5.22, where A1 stand out with the worst results, specially on the F1 case. The A1 represents a fully static system, so the eventual physiological changes due to the fear feeling might be hided. Thus, A1 might not represent fully the actual CS that subject 1 presented that day. On the other hand, A2 keeps track of the cardiac changes that occurred during the experiment, leading to a better match with the ORS signal frequency.

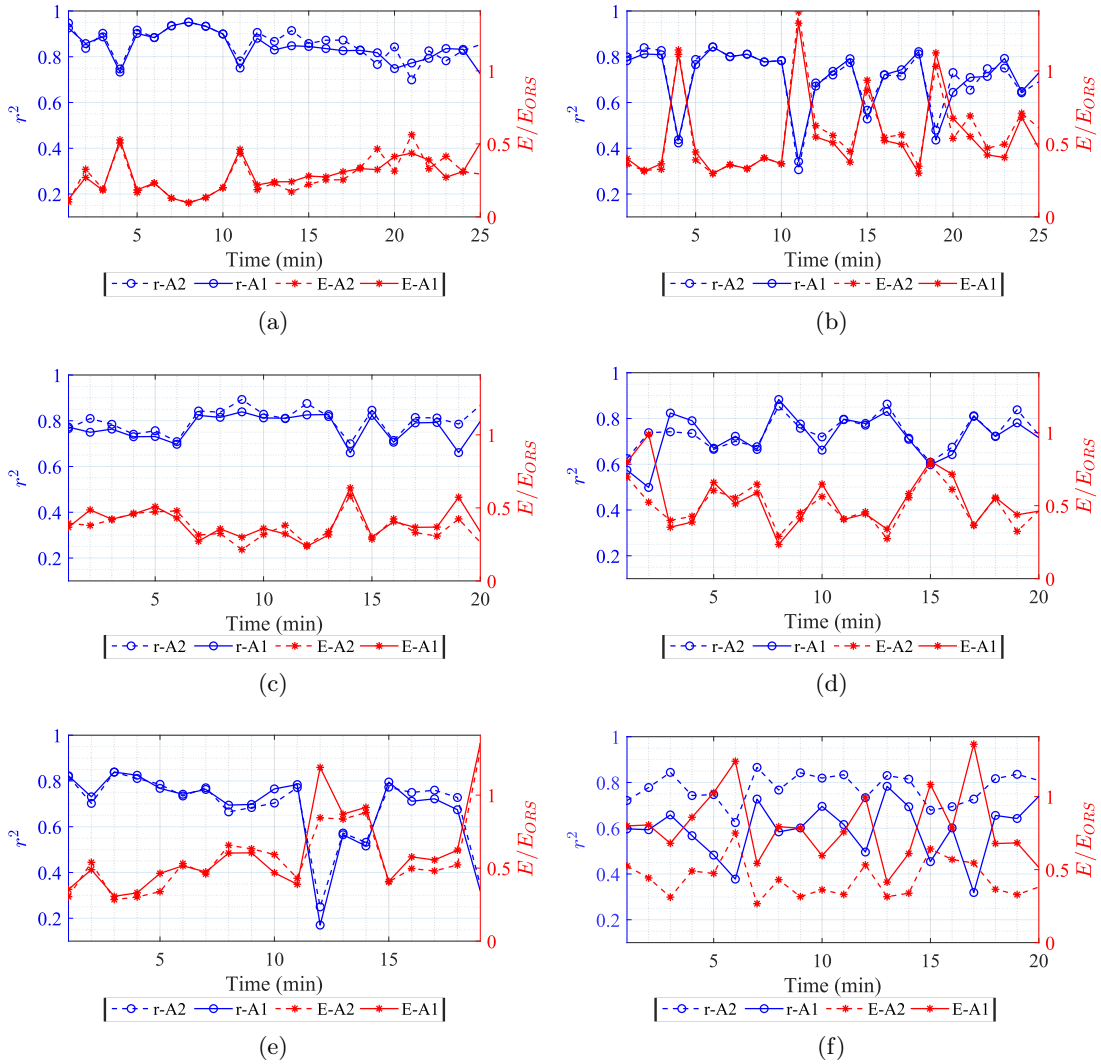

Figure 5.21: Cross-correlation between ERS and ORS over time and the corresponding residual error on the $w(n)$ estimation [176]: (a) subject 1 BL1, (b) subject 1 F1, (c) subject 1 N2, (d) subject 2 BL1,(e) subject 2 for F1, (f) subject 2 for N2.

Figure 5.21d, Figure 5.21e and Figure 5.21f show the time correlation results and the corresponding residual errors for subject 2. In this case, the correlation results were worse for both A1 and A2 approaches. Starting with the A1 approach, the BL1 case presented several cases above 0.8, but a higher number of cases around 0.7, leading to a mean value of 0.72. The cases related to the fear condition and the neutral condition on a different day, embraced higher variations leading to a mean correlation of 0.68 and 0.59, respectively. On the other hand, A2 stand out with a better correlation, presenting 0.74 for the BL1 and 0.71 for F1 and N2 cases.

The low correlation results of subject 2 for the A1 approach, suggest that a reliable analysis requires the estimation of new $w(n)$ coefficients over time, using in this way a block-adaptive approach where Wiener theory can be equally applied, as indicated in [175]. This

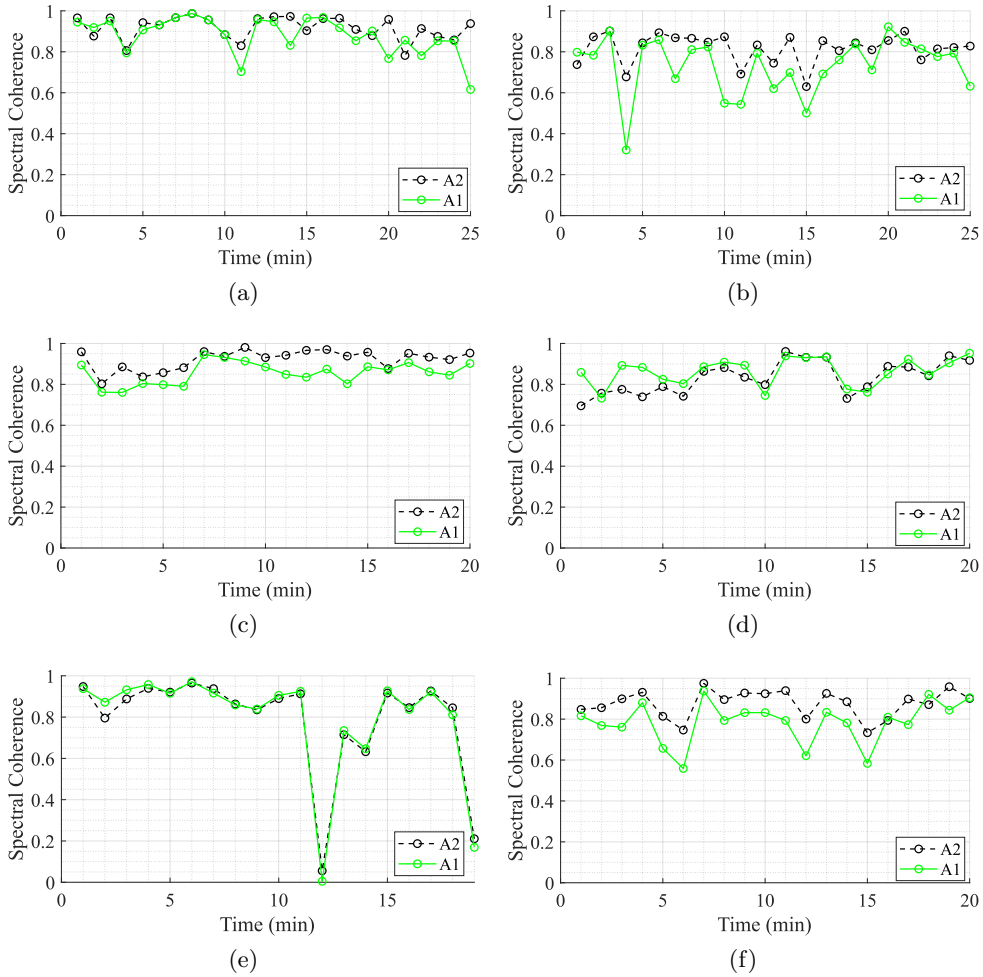

Figure 5.22: Spectral coherence between ERS and ORS over time [176]: (a) subject 1 BL1, (b) subject 1 F1, (c) subject 1 N2, (d) subject 2 BL1,(e) subject 2 for F1, (f) subject 2 for N2..

---

was somehow accomplished with the A2 approach, by updating the $w(n)$ on every 5 minutes. Thus, despite the lower correlation obtained in some one-minute segments, one can assume that the obtained correlation is in general enough to evaluate the heartbeat parameters of the ERS, specially having in mind that the ERS does not contain subject motions and keeps that same signal quality over time.

5.5.4 Feasibility of heart rate variability assessment

In order to validate the usage of radar systems for HRV computation, the number of BPM was firstly computed over time, as well as its error in relation with ECG. All signals rate were obtained through the ZC method, where the ECG peaks were identified using an amplitude threshold.

Figure 5.23 shows the comparison of the BPM between ECG, ORS and ERS, in the different moments for subject 1 and subject 2. The error behavior of both ORS and ERS

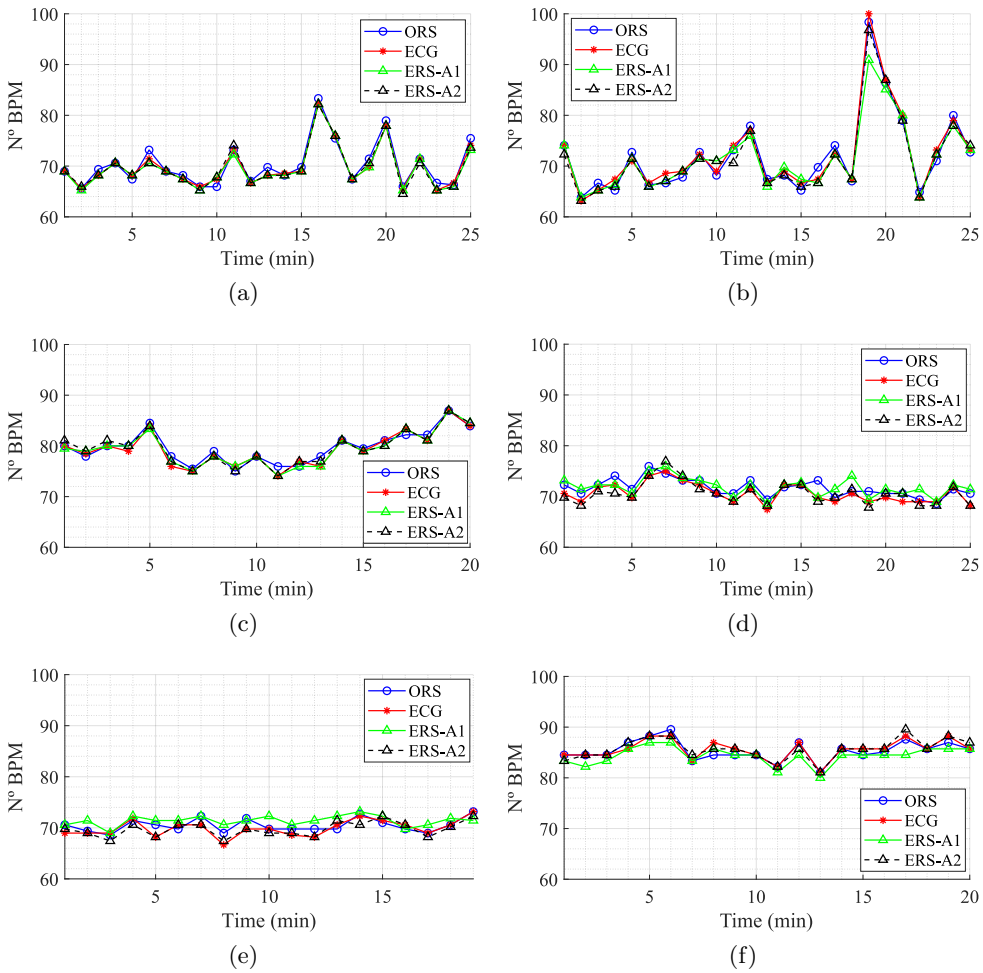

Figure 5.23: BPM between ERS, ORS and ECG over time [176]: (a) subject 1 BL1, (b) subject 1 F1, (c) subject 1 N2, (d) subject 2 BL1,(e) subject 2 for F1, (f) subject 2 for N2..

---

was evaluated through its empirical cumulative distribution function, depicted in Figure 5.24. Table 5.9 presents the error values in BPM taken by 95% of the dataset.

More similarity between the three signals can be observed for subject 1. On the other hand, the ERS presented an increased error for subject 2 for the A1 approach. Overall, the ORS presented an error varying between 1.63 and 2.3 BPM. For the subject 1 case, ERS-A1 presented a lower error varying between 0.87 and 2.0 BPM and the error varied between 0.89 and 2.9 for ERS-A2. A higher error was obtained for subject 2 using the A1 approach which exceeded 3 BPM. This increased error might be related with the lack of correlation observed previously.

The HRV evaluation was focused on the time-domain parameters, since they enable a vagal tone assessment without being influenced by the respiratory cycles [156]. The considered time-domain parameters were the SDNN and the RMSSD, which were computed using equations

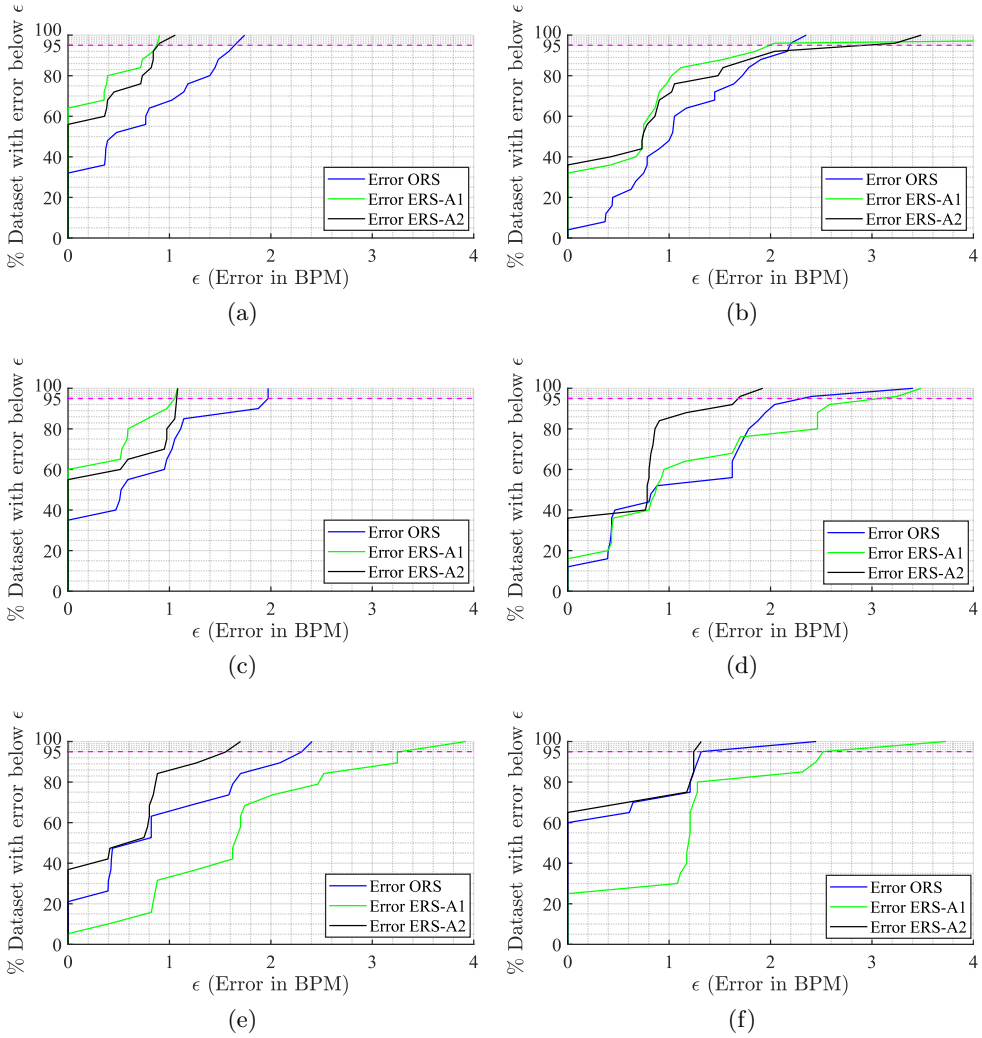

Figure 5.24: Empirical cumulative distribution function of the error in BPM [176]: (a) subject 1 BL1, (b) subject 1 F1, (c) subject 1 N2, (d) subject 2 BL1,(e) subject 2 for F1, (f) subject 2 for N2.

Radar Signal	**Subject 1**			**Subject 2**		
	BL1	F1	N2	BL1	F1	N2
ERS-A1	0.87	2.00	1.04	3.08	3.28	2.52
ERS-A2	0.89	2.92	1.07	1.68	1.56	1.24
ORS	1.63	2.19	1.97	2.32	2.30	1.32

BL1 - baseline day 1, F1 - fear day 1, N2 - Neutral condition day 2

Table 5.9: BPM error of ERS and ORS for each subject on the different conditions [176].

(5.2) and (5.3), respectively [156]:

$$SDNN = \sqrt{\frac{1}{N_{IBI}-1}\sum_{i=1}^{N_{IBI}}\left|\Delta_t[i]-\overline{\Delta_t}\right|^2} \tag{5.2}$$

$$RMSSD = \sqrt{\frac{1}{N_{IBI}} \sum_{i=1}^{N_{IBI}} \left(\Delta_t[i] - \Delta_t[i-1]\right)^2} \tag{5.3}$$

where N_{IBI} is the total of IBIs on the signal segment, $\Delta_t[i]$ corresponds to the IBI value on the i^{th} position, $\Delta_t[i-1]$ is the value on the previous position and $\overline{\Delta_t}$ is the mean value of all IBIs on the signal segment.

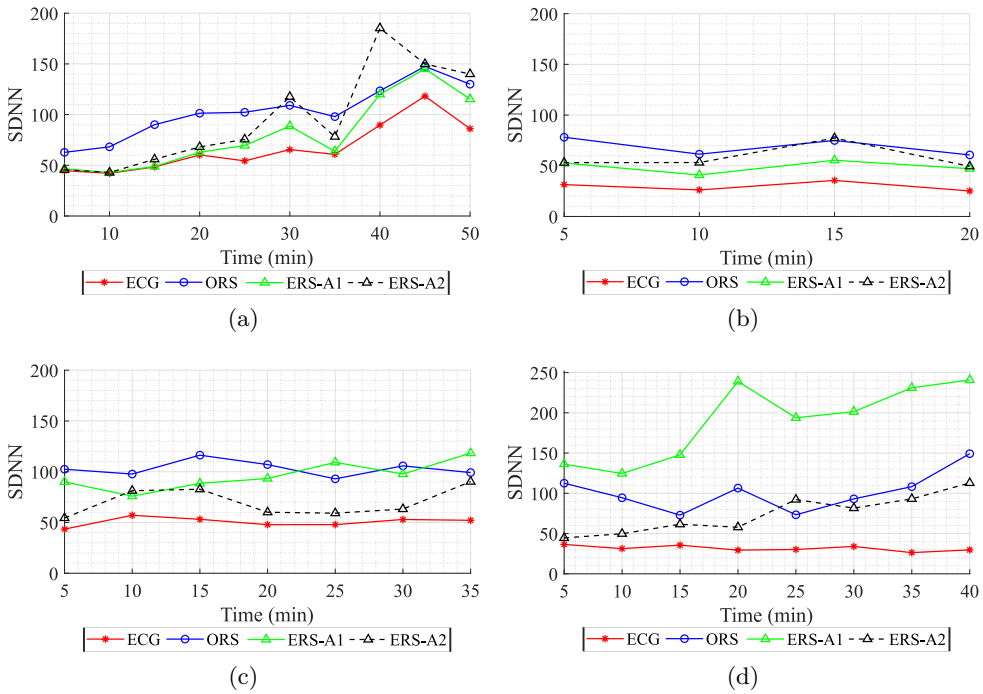

Figure 5.25: SDNN [176]: (a) using a fear condition of subject 1, (b) Using a neutral condition of subject 1, (c) using a fear condition of subject 2, (d) Using a neutral condition of subject 2.

The HRV parameters were computed in the full signals, that included baseline and emotional condition, but divided in 5-minute segments according to the guidelines defined in [156]. The obtained results are shown in Figure 5.25 and in Figure 5.26. Overall, the HRV parameters computed for the ORS present results largely different from the ones provided by the ECG signal, and the same effect is observed for the ERS signal for both A1 and A2 approaches.

The lack of correlation observed in subject 2 using the A1 approach might influence the HRV results as well, since the error in BPM is often higher than the one obtained with the ORS. Nonetheless, all results obtained for the A2 approach demonstrated generally a higher correlation in both neutral and fear scenarios, and therefore the HRV results can be more reliable.

Considering exclusively the results obtained for the A2 approach, the results of the same day during the fear condition test for subject 1 (see Figure 5.25a and Figure 5.26a), start with a high match with the ones provided by the ECG signal, but cannot keep that similarity over time, reaching values close to ORS or even higher. Likewise, the results obtained for a

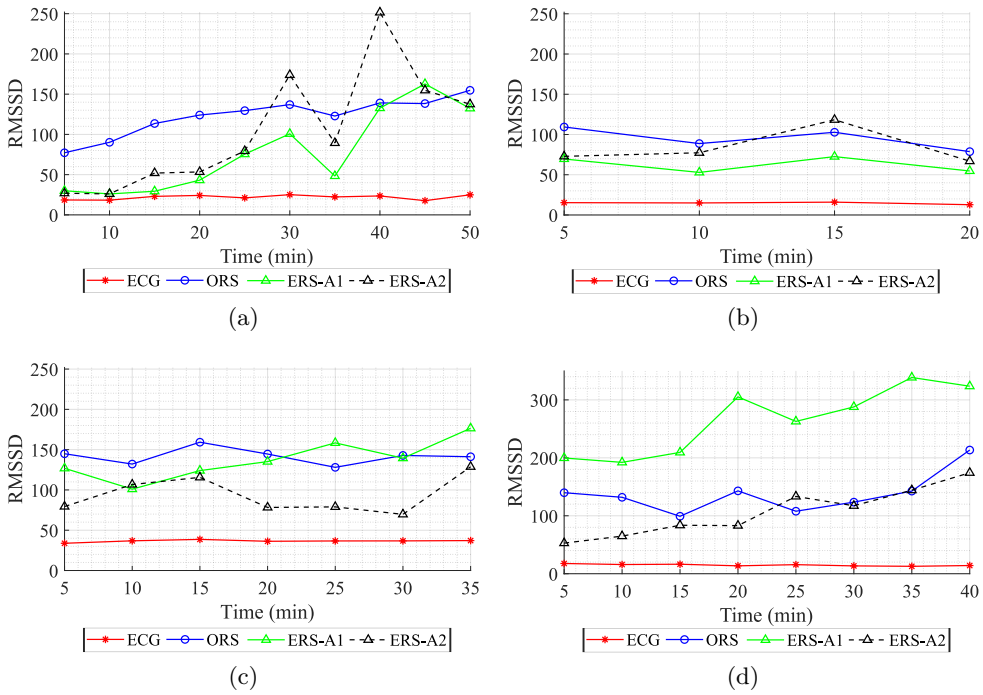

Figure 5.26: RMSSD [176]: (a) using a fear condition of subject 1, (b) Using a neutral condition of subject 1, (c) using a fear condition of subject 2, (d) Using a neutral condition of subject 2.

---

neutral condition on a different day are equally higher than the ones obtained with the ECG, specially on the RMSSD case.

In subject 2, although the A2 approach presented results closer to the ones obtained for ECG, they were still largely different. These results indicate that the mechanical motion caused by the heart bumping perceived on the chest, do not provide enough resolution to obtain accurate results for the HRV parameters. This conclusion was raised with the fact that the ERS is directly extracted from a ECG signal, which means that does not encompass radar problems, such as the subject random motion or the temporary misalignment with the front-end. In this way, it is assumed that the acquisition conditions are kept over time. Furthermore, it was also observed that radar signal models derived using a Wiener filter through the A2 approach presented a trustworthy behavior when signals are stable over time. Dynamic signals alter the correlation with the original radar signals, which can directly affect the cardiac parameters further computed, hence providing biased results.

One should note that these conclusions are valid for the radar setup herein used and for the algorithms described in Chapter 3 and in Section 5.2. Additionally, the cardiac models developed in this work mitigated external disruptive sources that might occurred in these specific scenarios. Therefore, if the surrounding conditions change or if the subjects present a more unstable behavior, a new model must be determined to conduct a similar analysis.

5.6 Windowed-based heart rate variability parameters

Despite not being possible to estimate the HRV parameters accurately as shown in the previous section, if the error of the radar HRV parameters is decreased, they still might have useful information that can be later leveraged by the machine learning to identify pertinent patterns and thus assess the subject's psychophysiological condition. This time, the usage of the IM-ANN approach might not be suitable, since there are a wide range of HRV parameters implying an extensive number of models and hence increasing the complexity of the process. Therefore, a different solution was developed to decrease the error.

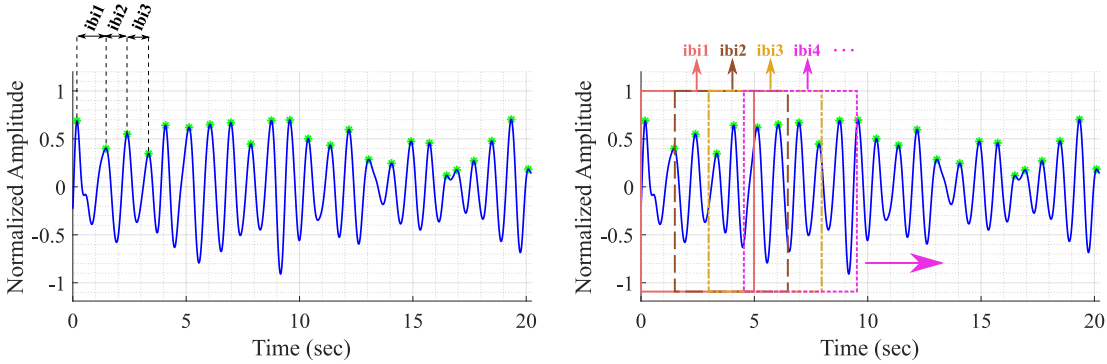

Figure 5.27: Illustration of the IBI computation: (a) Through conventional method, (b) Through sliding window.

Similarly to the previous section, only the time-domain HRV parameters are going to be considered henceforth. As mentioned previously, they are obtained through the analysis of the IBIs, which are computed through the difference between consecutive peaks, as depicted in Figure 5.27a. Due to the high variability on the radar cardiac peaks location, using all the IBI values generate a high error in the HRV parameters computation. This effect was already observed in the results presented in Figure 5.25 and Figure 5.26, more specifically for the ORS case.

The sliding window approach depicted in Figure 5.27b can reduce this error substantially. This approach consists on computing the IBIs inside a window of 5 seconds and compute its median value. The 5-seconds window duration was selected to guarantee at least 5 peaks and hence 4 IBIs, considering as reference the 60 BPM of as a healthy heart rate [157]. The median was used to neglect outliers [119]. The window moves forward only the enough to overlap the previous one 75% and a new median value is computed. In the end, the IBI vector is the result of these median values, rather than the difference of all consecutive peaks.

Using the 20-subjects dataset from Table 3.6, the time-domain HRV parameters were computed at every 5 minutes using the conventional and windowed methods, and the results for some subjects are shown in Figure 5.28.

First of all, and similarly to what was observed in Figure 5.25 and Figure 5.26, it is clear the discrepancy between the ECG and the conventional method applied to the radar. In average, the SDNN can vary between $105 - 145$ ms^2, the RMSSD $155 - 227$ ms^2 and the pNN50 $40\% - 75\%$. By applying the sliding window, this error decreases to the ranges of $30 - 72$ ms^2, $22 - 77$ ms^2 and $6\% - 40\%$ for the SDNN, RMSSD and pNN50 respectively. More specifically, for subject ID01 the mean value of the sliding window method approximates

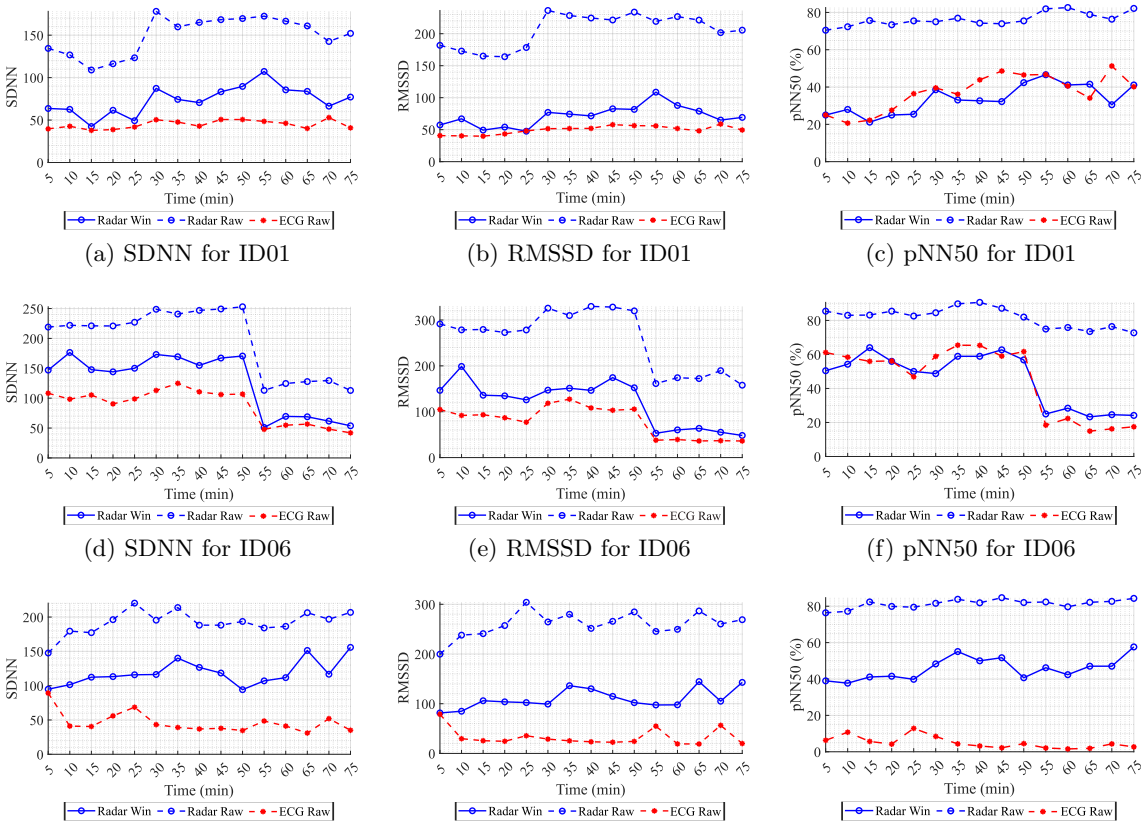

(a) SDNN for ID01 (b) RMSSD for ID01 (c) pNN50 for ID01

(d) SDNN for ID06 (e) RMSSD for ID06 (f) pNN50 for ID06

(g) SDNN for ID10 (h) RMSSD for ID10 (i) pNN50 for ID10

Figure 5.28: Comparison of the time-domain HRV parameters computed using the conventional method on radar signal, the sliding window method and the original ECG result.

highly of the mean value obtained for the ECG and for subject ID06 the sliding window results keeps track on the tendency of the ECG. On the other hand, subject ID10 still presented a considerable error in relation with the ECG, but it decreased considerably in relation to the conventional method. In sum, the median values of small size windows may remove outliers and still preserve useful information regarding the vagal tone of the subject.

5.7 Final considerations

This chapter was fully dedicated to the ability to recover the CS. First of all a comparative study for CS extraction was performed, considering real application scenarios. Six different methods were selected from literature, implemented and compared, considering two main issues: the inter-individual stature variability and non-controlled monitoring environments. The impact of the inter-individual variability in the signals amplitude was observed, but more research is required to understand if the lower amplitude is necessarily related with the subjects' gender or exclusively related with the body stature.

Regarding the performance of the cardiac extraction methods, standalone wavelet-based methods showed to be the more indicated for heart rate estimation, since it presented the smallest error and the fastest computational effort, regardless of the subject's body stature.

This was observed for both CWT and DWT, where DWT stand out as being the method with the best performance. However, a results degradation was verified in general, when subjects with lower amplitude motions were included in the dataset. The CS rate could be indeed improved by using machine learning algorithms, since they are able to learn individual patterns and generate individual models. At the end it was possible to estimate the signal rate of all subjects with an error inferior to 2 BPM.

Additional information can be extracted from the CS, such as the HRV. But the effectiveness of this procedure is directly related with the signal resolution. Radar biosignals contain the chest wall displacement due to the cardiopulmonary function, and the CS is specifically obtained by the tenuous mechanical motion that can be perceived on the chest surface. This cardiac micro motion lacks of resolution by itself, but it might be enough for radars operating with higher carriers. Additionally, long term monitoring periods encompass other damaging effects, such as the RBM or the misalignment with the antennas beams, which decreases the signal quality. Under these conditions, it is difficult to verify if lower carriers can provide accurate HRV parameters.

Taking into consideration the prototype limitations in terms of sensitivity due to the used carrier frequency, it was verified if the HRV assessment is possible in two stages. In the first stage, the radar peaks position consistency was evaluated. Although the DWT presented the best accuracy results for the cardiac rate computation, there is no guarantee that this method, or any other tested, can provide the peak location with enough precision for HRV parameters estimation, at least using the proposed system setup. The radar $\sigma_{\overline{\mathrm{IBI}}}$ varied largely from the one observed for ECG, as well as $\sigma_{\overline{\Delta_t}}$. This fact can contribute to an additional error in HRV parameters estimation. Therefore, other approaches should be explored to estimate HRV, since the DWT might not be used solely.

In a second stage, a radar cardiac model derived from ECG was developed to further verify if is it possible to compute HRV parameters using to proposed front-end. This model does not encompass the aforementioned external issues, hence it can be useful to fully validate the hypothesis. This signal model was obtained using a Wiener filter, which generate band pass coefficients to approximate the ECG signal to a given real radar signal, acquired at the exact same time. In order to simultaneously guarantee the system stability and the track of the subject behavior, the Wiener filter coefficients were either extracted considering a fully static system and also updated on every 5 minutes, respecting the signal duration required to compute HRV parameters. The results of both approaches were compared, showing that reliable results are only obtained if the ERS is similar to ORS, and this was not verified for the fully static system model.

Thus, the updated approach provided high correlation results and it showed that the computed HRV is deviated from the ECG results even in ideal circumstances. In sum, the proposed radar prototype is not indicated to be used in the HRV assessment, since the mechanical heart displacement do not provide enough resolution to accurately identify the cardiac peaks and their exact time location. Even though, an alternate solution was developed to take advantage of the existent HRV information to be later used in the subject's psychological assessment. The error of time-domain HRV parameters decreased if they are computed through the median of a moving window.

Chapter 6

Emotion Recognition

The content of this chapter was the result of a collaboration with the Department of Education and Psychology, of University of Aveiro, namely with the research team of the EmoSenses Lab. The developments report is divided in two work stages. The first stage was dedicated to evaluate the ability to use the bio-radar for emotion recognition, exclusively using the respiratory signal. The second stage aimed to verify if the results could improve if the cardiac signal is also included. It resulted in the following contributions:

- C. Gouveia, D. Albuquerque, F. Barros, S. C. Soares, P. Pinho, J. Vieira "Performance comparison of Emotion Recognition using Bio-Radar and Contact-Based Methods", *IEEE Transactions on Affective Computing*, submitted in July of 2022.
- C. Gouveia, A. Tomé, F. Barros, S. C. Soares, J. Vieira, P. Pinho, "Study on the usage feasibility of continuous-wave radar for emotion recognition", *Biomedical Signal Processing and Control*, **58**, January 2020, p. 101835.

6.1 Introduction

The bio-radar potential can be fully exploited by for instance, take advantage of information contained in the vital signs and identify patterns to assess the psychophysiological state of the subject. In order to verify this possibility, a specific case study was considered in the PhD work. Psychology and psychiatry are promising areas of application, considering both clinical and research settings, since a more objective assessment and monitoring of the psychophysiological response is not always available or possible to implement. The psychophysiological response may give critical objective information about the emotional response, and there are many scenarios where a non-invasive, effortless, and safe device would be especially critical for this assessment, such as with children [178], or people with sensory hypersensitivity, behavioral problems, and/or difficulties expressing emotions and feelings, (e.g. as observed in people with autism [179]).

Emotions are adaptive and multidimensional responses triggered by meaningful events and/or stimuli, that affect the way we think, feel, behave and interact with others in our daily life [180], [181]. These responses encompass changes in different systems including cognition, physiology, motivation, motor expression and subjective sensations, hence allowing for effective self-regulation processes and providing crucial resources to a successful adaptation to the environment [182], [183]. The biological system changes can then be expressed by

different means, such as via verbal communication, facial expressions and body motion [184], as well as by more subtle cues, including biological signs (increased heart rate and respiration) [5].

Although automatic emotion recognition represents a challenging process, it can provide useful information regarding the individuals' well-being and, generally speaking, contribute to systems' enhancement, according to the user's needs. For example, it can be useful to adjust medical and psychological treatments or even aid in detecting the veracity of information in forensic investigations. Additionally, emotion identification can be a crucial asset in the human-computer interaction field, once it enables the adjustment of the design and its functional features to the users' needs [184], [185].

Emotion recognition through physiological signs has already been reported, namely by using breathing rate, electrodermal activity, electromyogram, electroencephalogram, and ECG [5], [185], [186]. Among this wide range of vital signs there are some more informative than others. For instance, in [186] it was determined that a combination of multiple vital signs can provide a better accuracy to identify the fear, happiness and a neutral condition state, since all signals have different information that can be combined coherently. The authors also suggest that the ECG is the most effective signal for this scope.

Emotions can be identified using machine learning algorithms applied to vital signs with the goal to identify patterns. For instance, in [186] it was used the Random Forest (RFO) and ANN applied to ECG, electrodermal activity and electromyogram zygomatic and medial frontal signals. The most used algorithms for this purpose are the ANN (already explained in Section 5.4), the Support-Vector Machines (SVM), the K-Nearest Neighbour (KNN) and the RFO (see the references of Table 6.1). The SVM are learning algorithms, with the objective of finding a hyperplane with the widest margin possible, in a N-dimensional space (where N is defined as the number of classes one aims to distinguish), that separates the data points into well defined clusters [173]. In other words, the hyperplane is a unique threshold that allows the model to classify a cluster of data and it can be defined by looking to the position of "support vector", i.e. the nearest cluster points to the hyperplane. For instance, Figure 6.1 shows an example where the samples could be easily separated into two cluster using a linear kernel. However, more complex cases might require to use complex kernel functions, such as polynomial or Gaussian Kernels [187]. The KNN is characterized for being

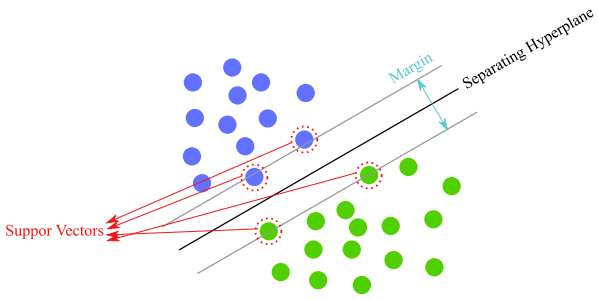

Figure 6.1: Illustration of the SVM algorithm (adapted from [187]).

a simple classification algorithm, since it is able to classify the data samples by evaluating the labels of their K neighbors as depicted in Figure 6.2. Thus, the data label is determined considering the majority vote of the K neighbors [173]. Finally, the RFO algorithm consists on an ensemble learning method based in several decision trees, which can be trained following

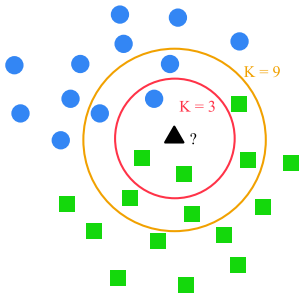

Figure 6.2: Illustration of the KNN algorithm (adapted from [188]).

different modes. For instance, with the bagging mode the decision trees are trained in parallel, in order to reach a classification decision based in the majority vote. Each decision tree uses a random data subset for training and the splits are made by evaluating one feature at the time [189].

Nowadays, most of these physiological-based systems still rely on the direct contact with sensors and it is recognized that the individual's awareness of the monitoring process may influence the results [5]. Moreover, the use in real life contexts, which is of great value to allow for the establishment of individualized profiles, can also interfere with the signal. Therefore, non-contact systems can be advantageous in these applications, as they can remotely monitor vital signs.

The emotion recognition using vital signs captured remotely with a radar system have already been reported, namely in [4], [52], [190]–[192]. Table 6.1 sums up the main characteristics of the identified works. Even though, these works are still scarce and a proper comparison with a certified equipment is lacking. In [52], the happiness, fear, sadness and neutral state were identified using a CW radar operating at 2.4 GHz combined with a RGB camera. The conducted procedure was monitored by psychologist professionals and their feedback served mostly to assist on data labeling. In this case, the obtained results were only compared with the ones obtained with the standalone camera or the standalone radar. The same emotions were identified in [191], but without performing any type of validation. On the other hand, a different set of emotions were distinguished in [190], namely the happiness, fear and disgust. The vital signs were acquired using a UWB radar and the performance of nine different classifiers was compared, but similarly to [191] no validation study was conducted. At last, happiness, sadness, anger and pleasure were identified in [4] using the respiratory and cardiac signals acquired by a FMCW radar.

All works used different radar front-ends. For instance, [52], [191] used CW radars operating with a lower carrier frequency. The carrier frequency influences the sensitivity of the system to detect micro-motions such as the ones related with the heart motion at the chest-surface [18]. In this sense, higher carrier frequencies are more sensitive and might be able to detect more easily the micro-motions caused by the heart. Nonetheless, such level of sensitivity turn signals prone to be highly affected by random body motion during the monitoring period and high carrier signals are also severely attenuated. The works [4], [190] used higher carriers but with different radar operation modes, namely FMCW and UWB, which have different implementation challenges in comparison with CW radars [20].

In general, all datasets are short varying between 5-35 subjects [190]. In this context, it is important to note that according to [193], 20 subjects is enough to detect large effects of

Work Reference		[52]	[4]	[190]	[191]
Set-up		CW radar @ 2.4 GHz + RGB camera	FMCW radar @ 5.46 - 7.25 GHz	UWB radar @ 7.29 - 8.79 GHz	CW @ 2.4 GHz
Population (Total/Female/Male)		18/7/11	12/6/6	35/21/14	5/4/1
Vital Signs		RS and CS	RS and CS	RR	RS
N^{o} observations		2010 (1 min)	400 (2 min)	315 (5 min)	48-80 (1 min)
Tested Classifiers		RFO	SVM	KNN, ETC, ADB, GBM, SV, HV, CNN, MLP	subspace KNN
Emotions		H, N, F, S	H, S, A, P	H, F, D	H, N, F, S
Emotional Trigger		30-min videos. All in the same day	music, photos and videos. All in the same day	5-min videos. In consecutive days.	3-5 minute videos mixed. In the same day.
N^{o} Features		63 $\rightarrow$ 23	27	3 $\rightarrow$ 1	11
Baseline Normalization		Yes	Yes	No	No
Feature Selection Method		Embedded	Embedded	Embedded	Manual
Performance Evaluation	CV	10-fold	-	10-fold	5-fold
	Test	Hold-out with 70:30 ratio over the dataset	Hold-out with 11/12 and 1/12 for test	Hold-out with various ratios over the dataset	-
Results	CV	89.6%	-	66%	67.6%
	Test	71%	72.3%	76% with 80:20 ratio	67.6%

CW - Continuous Wave, FMCW - Frequency-Modulated Continuous Wave, UWB - Ultra Wideband
CS - Cardiac signal, RS - Respiratory signal, RR - Respiratory rate, RFO - Random Forest, SVM - Support Vector Machines,
KNN - K-Nearest Neighbor, ETC - Extra tree classifier, ADB - AdaBoost classifier, GBM - gradient boost machine,
SV - soft voting, HV - hard voting, CNN - Convolutional neural networks, MLP - multi-layered perceptron,
H - Happiness, N - Neutral condition, F - Fear, S - Sadness, A - Anger, P - Pleasure, D - Disgust, CV - Cross-Validation

Table 6.1: Comparison of the results obtained in different works on emotion recognition using radar systems.

the HRV parameters and hence more robust results might be obtained with such population sizes. The emotions under study are different among all the considered studies. Some works were dedicated to distinguish three emotions and others four, and in general the considered emotions were: Fear, Happiness, Neutral condition, Sadness, Anger, Pleasure and Disgust.

It is also important to mention that the process of emotion elicitation, as well as the general methodological procedure, may have a strong influence in results. For instance, depending on the procedure used to elicit emotions and if this elicitation was or not successful, it may be more difficult to distinguish between different emotional conditions [194], [195]. Also, more authentic reactions may be obtained if the subject is not aware of the video's content, and if the emotional inductions are sufficiently spaced in time (which also helps do decrease emotional contagion from one session to another). The works [4], [52], [191] induced all the emotions on the same day and [190] on consecutive days. The emotion induction was performed using thematic videos with different duration in [52], [190], [191] and by showing music or photos in [4].

Thus, the induction protocol followed in [186] might be one that leads to more unbiased results. In [186] the goal was to identify the happiness, fear and a neutral condition. The experiment was conducted in three different days, spaced by at least one week. Each session was composed by a baseline lasting 5 minutes (where no emotion was induced) and an emotion

inducing period lasting between 25-30 minutes. Each day was dedicated to eliciting a different emotion, by showing a set of thematic videos already used in previous studies [186], [196]. More specifically, happiness was induced via comedy videos, whereas fear was induced using scary videos and documentaries were used on the baseline and also to induce the neutral condition. Each set of videos was organized according to an increasing order of emotional intensification, in order to allow for a continuous induction throughout the session. In order to avoid biased results, the subjects did not have prior knowledge of the videos content. Additionally, they were asked not to drink coffee in the previous hour and to avoid attending the session if they were feeling stressed out or if an emotionally intense situation had happened. As one could see throughout this PhD thesis, this consists on the *Emotional Protocol*, already used in different work stages.

Regarding the used vital signs, the works [4], [52], used the RS and CS to compute features, while [190], [191] only considered the RS. Different set of features were considered on each work. More specifically, in [190] the authors considered as features the age, gender and the respiratory rate being the latter the only feature considered. A group of 11 features was manually selected in [191], and they were mainly focused on the signal waveform and spectral content. Conversely, embedded methods might be preferential since it allows to learn which is the best feature set during the training phase [197]. Thus, in [198] a total of 63 features was computed over the RS and CS and a recursive feature elimination based on Gini gain was applied iteratively, to determine which features provide more information [199], reducing the dataset to 23 features. In [4] features were also selected with an embedded method, namely the l_1-SVM, which selects a subset of relevant features also during the training phase, leading to a 27-length subset.

In order to obtain authentic and unbiased results an additional step needs to be applied over the features. The physiological parameters differ between subjects, considering the same emotional scenario. Furthermore, and assuming a neutral condition, the same subject might present altered physiological parameters in different days and these differences are related to several factors, among them the coffee ingestion, the subject's mood or the lack of sleep [4]. In this context, for a fair analysis all subjects under study should be in a equivalent state, therefore the computed features should be normalized. For this purpose, the signals captured during the baseline are also used to compute the features and their mean value is subtracted from the features computed over the further experiment. This procedure was only carried out in [4], [52].

Finally, the results obtained in the literature cannot be compared directly, since different RF front-ends were used and each work was dedicated to a different set of emotions. Table 6.1 presents results exclusively for the multiclass strategy (i.e. the ability to distinguish all emotions) and for a person-independent scenario, where the dataset is relative to all subjects. Different machine learning algorithms were implemented with the goal to classify the emotions. The works [4], [52], [191] implemented a single classification algorithm, namely the RFO, the SVM and the subspace KNN, respectively. On the other hand, a total of 8 different classification algorithms were implemented and their performance compared in [190]. Their study included machine learning algorithms, the ensemble of their results through hard and soft voting and the exploitation of deep learning models.

In order to evaluate the classifiers performance, almost all works used the K-Fold as cross-validation method and then used a Hold-out strategy for testing. The Hold-out involves a random data partition in train and test subsets. For instance, [52] used a 70:30 ratio, where 70% of the dataset was used in training and the remain 30% was used to test the classifiers

performance. In [52] the data partition was repeated 10 times and the average and standard deviation were analyzed. The same principle was followed in [190], but the authors tested different ratios and selected the one providing the best accuracy results. Instead of using the Hold-out strategy, the authors in [4] opted for using 11/12 subjects for training and test in a single one. The obtained accuracy results varied between $67\% - 72\%$ to detect four emotions in [4], [52], [191] and an accuracy of 76% was obtained in [190] to distinguish three emotions using the 80:20 data partition (see Table 6.1).

Considering the state of the art presented above some loopholes were identified, among them the lack of validation of the obtained results with a proper certified equipment and the adopted emotion induction procedures which may have biased the results with emotional contamination. Thus, a study on the usage feasibility of the Bio-Radar prototype described in Chapter 2 for emotion recognition was carried out. This study included a complete validation of the developed prototype, using an unbiased emotional induction protocol developed in the Department of Education and Psychology of the University of Aveiro and previously described in [186]. The happiness, fear and a neutral condition were identified using the vital signs acquired by two systems simultaneously: the BRD and the BPC as the certified measuring equipment. While the BPC uses a chest-band attached to the subject's chest to acquire the respiratory signal and the ECG is measured using a three-derivation of skin-contact electrodes, the BRD system is able to capture both cardiac and respiratory signals concurrently and without requiring the direct contact with the subject.

The conducted study is divided in two stages. Section 6.2 describes the first stage, which was a preliminary study dedicated exclusively to the information encompassed in the RS and the RBM. This stage served as a proof of concept, so the signals were processed with the *Simplified DSP* algorithm presented in Section 3.1. The second stage presented in Section 6.3, aimed to improve the preliminary results and it was implemented after developing the dynamic algorithms for the CDC offsets removal, presented in Section 3.3. In this case, the CS was also included, the population under study was increased and a statistical study was carried out to evaluate which features are the most informative to distinguish between the elicited emotions.

6.2 Study on the usage feasibility of bio-radar for emotion recognition

The Bio-Radar signal is lowpass with a bandwidth equal to $0.2 - 2$ Hz, which comprises the respiratory bandwidth for a healthy adult ($0.2 - 0.4$ Hz) [121], the hyperpnea cases ($0.4 - 0.8$ Hz) and the cardiac signature along with other random motions from the body ($0.8 - 2$ Hz) [200]. Therefore, in this work stage along with the respiratory signal, one also aimed at capturing other types of body motion that occur naturally due to the individual's reaction to specific emotions. These body movements, that have been seen as a source of distortion in similar works, hold important information regarding human responsiveness to specific emotions. The goal of this work stage is to verify how much information these two elements are able to provide in the emotion recognition context.

6.2.1 Data collection and signal processing

The experiment was conducted with nine volunteers using the *Emotional Protocol*. The respiratory signal of all subjects was acquired using a preliminary version of the BRD prototype (namely the bio-radar prototype version 1 of Figure 2.6 which was developed in [2]) and the BPC as reference.

Figure 6.3 shows the setup disposition and the conditions of the monitoring scenario used in both work stages. The subject was seated with his/her arms laying on the table in front. This position helped the subjects to remain stable during the experiment. The radar antennas were located at a distance of half a meter, in front of the subject (under the computer monitor as depicted in Figure 6.3).

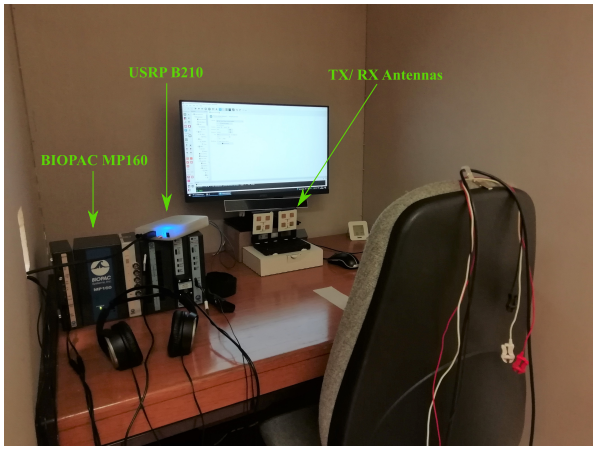

Figure 6.3: Setup disposition used in both work stages for emotion recognition with the BRD and the BPC acquiring simultaneously.

After acquisition BRD and BPC were processed offline in MATLAB. The *Simplified DSP* algorithm was used to process the BRD signal. The BRD signal was received with a sampling rate equal to 100 kHz and the BPC signal was acquired with a sampling rate equal to 1 kHz. Once we are dealing with lowpass signals, both BRD and BPC signals were downsampled to the new sampling rate equal to 100 Hz. Then BRD and BPC signals were synchronized and for this purpose the subjects were asked to perform the breathing pattern shown in Figure 3.27. The CDC offsets were removed in the BRD signal and the arc position was adjusted in relation to the complex origin. The respiratory signal was recovered by performing phase demodulation with the arctangent computation, resulting in the real signal $y(n)$. Later, the radar respiratory signal $y(n)$ as well as the one acquired by the BPC were divided in sub-segments with one minute duration for the feature extraction for classification.

6.2.2 Bio-radar signal viability for emotion recognition

Before implementing the machine learning algorithms for emotion recognition, a comparison between BRD and BPC signals was made, with the goal to identify informative signal patterns. Figure 6.4 shows two signal samples obtained during the *Fear* state test, acquired simultaneously with these two systems. It depicts how BRD and BPC might present similar information and it also depicts the additional information contained in the RBM captured by the BRD. In this sample, it is possible to observe that the subject was frightened twice and

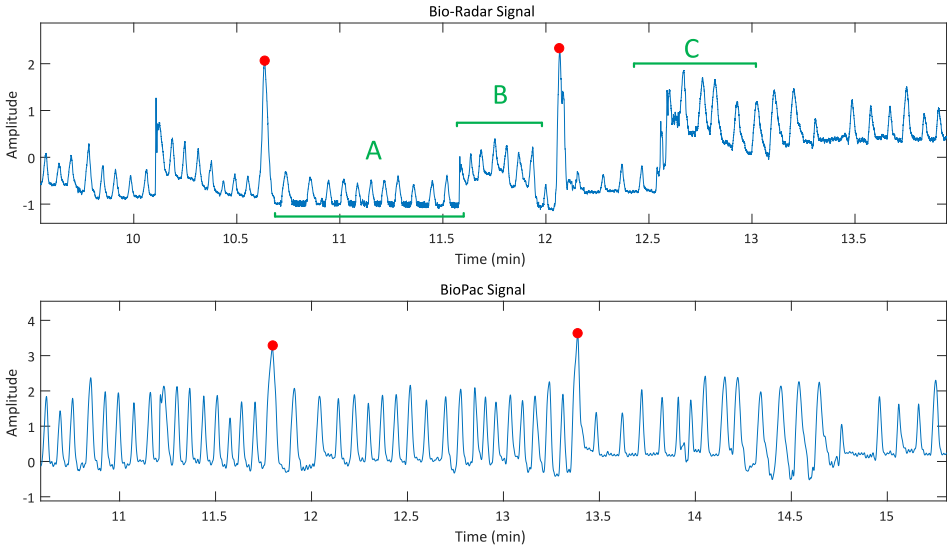

Figure 6.4: Respiratory signal acquired during the *Fear* state [192]: by the BRD system (on top) and by the BPC system (on bottom). Peaks with red dots were the moments where subject got frightened. Segment 'A' contains an increase of the heartbeat rate and the remain segments ('B' and 'C') sign the body motion of the subject.

---

these events are represented by two peaks with higher amplitudes, marked with a red point in the figure. Immediately after each moment of fright, it is possible to identify an increase in the heart rate during the exhale periods. This event is signed in green with the capital letter 'A'. The radar system can also detect the random motion of the subject, that occurs naturally due to the sudden reactions of videos (such as laugh or fright), or for comforting purposes. In fact, this random motion along with other signal signatures that arise from the emotional induction, serve as additional information for the proper emotion recognition. For example, the subject's discomfort can be observed in the BRD signal from Figure 6.4. If the he/she moves slightly his/her position the signal mean value change, as showed in the signal slots marked as 'B' and 'C'. On the other hand, this type of event is not evident in the BRD signal.

6.2.3 Classification procedure

Features extraction

After extracting the vital signals, appropriate features were manually selected and computed from one minute observations. Figure 6.5 represents the block diagram of the signal segmentation process, which was adapted according to the features categories that are going to be used. The signal at the *Segmentation block* input is the result of phase demodulation $y(n)$.

During the monitoring period, changes on the respiration pattern and other body motions are expected according to the natural reaction of the body due to emotions. Thus, statistical and waveform characteristics can be identified. In addition, the spectral evaluation is also carried out, not only for the respiratory bandwidth $0.2-0.4$ Hz, but also for higher frequencies that can reveal heartbeat detection or sudden motions from the subject.

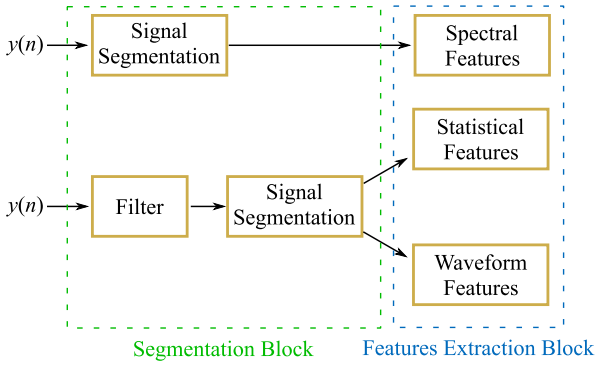

Figure 6.5: Specification of the segmentation process for the different feature categories [192].

For spectral features, the input data is only divided in 1 minute sub-segments, without any prior processing. On the other hand, for statistical and waveform features, a filter was applied in the full signal before the sub-segmentation process. The filter used was a 2^{nd} order Butterworth with a bandpass equal to $0.05 - 1.5$ Hz. The usage of this filter is important to center the respiratory signal in zero and to remove noise that might have impact in the features computation.

A total of 12 features were extracted from the segmented signals and they are shown in Table 6.2.

Category	**Feature Nº**	**Description**
Statistical	F1	Mean
	F2	Variance
Waveform	F3	Waveform width
	F4	IBI of respiratory peaks
	F5	Respiratory rate
Spectral	F6-F11	Power spectral density in different bands
	F12	Power spectral density ratio

Table 6.2: Features selected manually for the first stage of the emotion recognition [192].

More details are now provided over these features computation:

- F1-F2 corresponds to the mean value and variance of the one-minute segment;
- F3 is the mean value of all peak widths in that segment. The width is defined as the distance between the samples where the signal intercepts a reference line. In this case, the reference line is located beneath the peak, at half of the peak prominence;
- F4 corresponds to the mean value of the number of samples between consecutive peaks, over the segment;
- F6-F11 are the magnitudes of the spectral components in the different frequency bands (0 - 0.1 Hz, 0.1 - 0.2 Hz, 0.2 - 0.3 Hz, 0.3 - 0.4 Hz, 0.4 - 0.9 Hz, 0.9 - 1.5 Hz), obtained

through the Power Spectral Density (PSD), using the Welch method with a sliding Hamming window with 50% of overlap;

- F12 relates the spectral components within the low band ($0.1 - 0.5$ Hz) and the high band ($0.6 - 1.5$ Hz). It is expected that the low band expresses only the respiratory presence and the high band expresses a restless behavior together with the cardiac component.

Once again these features have different natures so they were standardized applying equation (5.1).

Classifiers

In this work, three different classifiers were implemented and their performance was compared. The same classification procedure was applied for both BPC and BRD signals, in order to validate the ability to use of the developed prototype for this scope.

The classification was performed considering a binary and multiclass problems, both using a dataset with 221 observations for each emotion. For the binary problem, only pairs of emotions were considered, therefore the dataset length had 442 observations. On the other hand, the multiclass case considered three elicited emotions, corresponding to a final dataset length equal to 663 observations.

Notice that the observations were chosen after visual inspection of the signal, where noisy segments were discarded. This resulted in an imbalanced dataset, since it was not possible to have the same number of observations per subject, at each emotion. Thus, in order to balance the dataset, the number of observations was limited to the minimum duration time of all emotional conditions.

Three classification algorithms were chosen - SVM, KNN and RFO, considering their good performance with short datasets [189]. Moreover, SVM and KNN were also used in literature for the same purpose (for instance in [4], [191]) and since the goal of this work is to reinforce the possibility to use radar systems in emotion recognition, that same algorithms should be used. These algorithms were implemented for both binary and multiclass problems. Their implementation used the following hyperparameters, selected manually by trial and error:

- SVM was applied with a radial basis function kernel [189], in both binary and multiclass problems.
  - Regarding the multiclass case, since SVM algorithms are based in binary classification only, a decision strategy based in voting was applied in order to reduce the multiclass problem in a set of binary problems. In this sense, a one-versus-one strategy selects the class through the major vote occurring within $C(C-1)/2$ binary classifiers, where C is the total number of classes [201].
- The KNN algorithm uses the Euclidean distance as measure of proximity and the closest neighbour (with $k = 1$) is considered as decision rule [202].
- Finally, the RFO algorithm consists in an ensemble of decision trees trained in parallel to give a contribute to the final decision. This ensemble classifier was implemented with the Bagging mode, i.e. each tree was trained with a bootstrap sample of the dataset [189]. In order to prevent the deep grow of trees, a minimum leaf size was assigned to

five observations. The out-of-bag score was then used to choose the number of trees (see Figure 6.6) and 70 trees were selected.

– Additionally, the feature impact can also be studied from the RFO classifier. For this purpose, the relevance of the feature selection on each node was analyzed and the six more relevant features were chosen to create a new dataset.

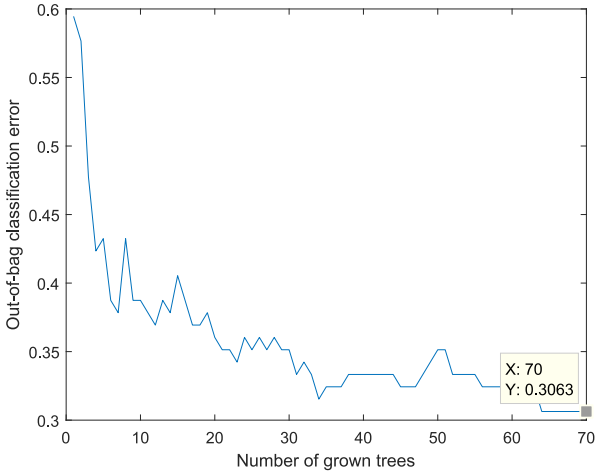

Figure 6.6: Out-of-bag error curve to choose the appropriate number of trees to be further used in RFO [192].

6.2.4 Results discussion

Since the dataset was small, the SVM and KNN classifiers were trained and tested using the Leave-one-out cross-validation strategy. Leave-One-Out is an extreme case of the K-fold cross-validation. Considering that the dataset has N observations, this strategy uses N-1 observations for training and leave one observation out for testing [189]. With this approach there are N combinations of training sets with different single instances for testing. The final result shows how many times the prediction was right on identifying the correct label. As for the RFO case, the out-of-bag observations (samples not included in the bootstrap sample) were used to estimate the performance of the classifier.

Table 6.3 present the results regarding the binary and multiclass problems for this first emotion recognition stage.

Binary problem

Starting with the binary problem analysis, similar accuracies were obtained using both BRD and BPC signals. Generally, the *Happy vs. Fear* case is the one that presents lower accuracy, with a difference of less than 10%, if we compare with the other binary cases. This can be explained by the similar responses for these two emotions, leading to an approximated feature result, which hinders the class identification. Since both positive and negative emotions serve motivational purposes (reward or withdrawal, respectively), similar autonomic nervous system responses favor environmental adaptation purposes, as to prepare the organism for appropriate behavioral responses [203]. Although this remains a controversial topic in the

	Binary problem			Multiclass problem		
	HN	FH	FN	HNF	HNF-F	
SVM	70.8%	68.8 %	72.2 %	58.1 %	63.3 %	**BRD**
	79.2 %	73.5 %	81.7 %	65.2 %	63.3%	**BPC**
KNN	72.6 %	72.4 %	72.4 %	58.2 %	66.2 %	**BRD**
	75.8 %	71.0 %	79.2 %	61.4 %	76.5 %	**BPC**
RFO	77.4 %	73.8 %	77.8 %	65.2 %	67.1 %	**BRD**
	83.9 %	73.3 %	83.0 %	69.1 %	75.1 %	**BPC**

HN - Happy vs. Neutral, FH - Fear vs. Happy, FN - Fear vs. Neutral

HNF - Happy vs. Neutral vs. Fear

HNF-F - HNF with reduced number of features

Table 6.3: Accuracy rate results for emotion recognition using the respiratory signal [192].

literature, several studies have corroborated this view, by showing an increased physiological arousal (e.g., increased heart rate) not only in negative emotional states (which trigger "fight or flight" responses) but also in positive emotional states [204]. The current results support such view for respiratory signals captured using the BRD, since the same behavior was observed with the BPC signals.

On the other hand, the algorithm with better performance was the RFO and the worst accuracy results were obtained with the SVM classifier, which also presented the biggest deviation between BRD and BPC signals, with a maximum drift of 10%, approximately.

Aside from these results and in order to properly validate the BRD system usage, the McNemar test was performed [189], with the mid-p-value test. This test helps to understand which type of signal could be used to identify more true labels accurately, or if the classifier accuracy is similar using both systems. It verifies if the null hypothesis is accepted or rejected. In this case, the null hypothesis stands as the classifier having the same accuracy of predicting correctly the provided class labels for both BRD and BPC systems.

The McNemar test was performed for every classification algorithm and for every binary case. To apply the test, the predicted values of the test set of the Leave-one-out strategy loop were stored for all classifiers. Then, the null hypothesis was tested and indeed verified, indicating that a BRD-based classifier have the same accuracy of predicting true labels as a BPC-based classifier, for a specific binary problem. The test was applied with 5% of significance level to compare the results of both classifiers.

Multiclass problem

Observing now the multiclass problem, the results were again similar within the different classifiers and the different acquisition systems. With a detailed analysis it is possible to verify that the results of the KNN and RFO classifiers were approximately the same for BRD and BPC signals, with only 3.2% and 3.9% of difference, respectively. The difference was slightly more evident for the SVM, with 7.1% of difference. Likewise the binary problem, the best classification algorithm was the RFO with 65.2% of accuracy for the BRD case and 69.1% for the BPC. Consistently with the previous results, the BPC signal resulted in better

accuracy results than the BRD. However, the McNemar test performed for every classification algorithm did not rejected the null hypothesis at the 5% significance level, which sustain that differences between accuracy results with BRD and BPC signals are not relevant.

An alternative way to evaluate the results is by computing the confidence interval of the accuracy results. For this purpose, the normal approximation of binomial confidence interval was computed through equation (6.1):

$$\hat{p} \pm z\sqrt{\frac{\hat{p}(1-\hat{p})}{N}} \tag{6.1}$$

where $\hat{p}$ is the probability of a correct decision, N is the total number of observations and z is equivalent to $1 - \frac{\alpha}{2}$ quartile of the standard deviation. In this case, $\alpha = 0.05$ was considered, which results in $z = 1.96$. In fact, $\hat{p}$ is also an estimate of accuracy, and it can be obtained through the relation $\frac{N_s}{N}$, where N_s is the number of correct decisions [205]. Figure 6.7 shows the performance of each classifier using the BRD and BPC signals, and their distribution through the computed intervals.

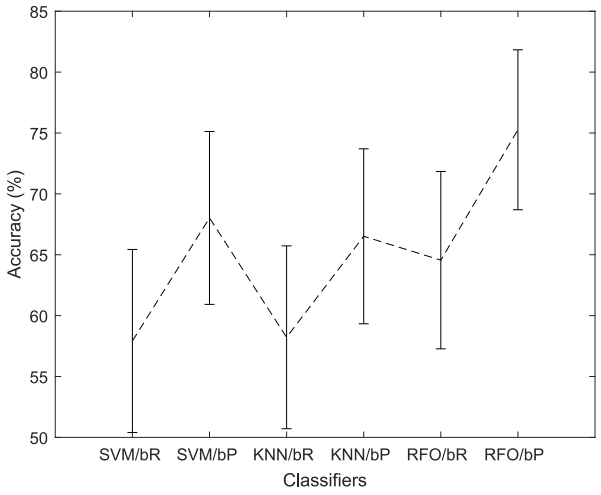

Figure 6.7: Comparison of the classification accuracy for different classifiers considering the BRD and BPC signals [192].

Results are disposed in consecutive pairs of 'name/signal', with the respective classifier name and signal type. By analyzing this graph it is possible to observe that the results under the same classifier deviate slightly between the different signals, by keeping an interval portion in common.

Finally, RFO classifier allowed the execution of a preliminary study regarding the feature importance. This study revealed which features had more influence on the achieved results and this information can be used to presumably increase the accuracy results, by decreasing the number of features used in dataset. The last column of Table 6.3 shows the accuracy results after training and testing the classifiers with the most relevant features. In the BRD case the selected features were F6, F7, F12, F4, F9 and F2 (disposed in decreasing order of importance). In the BPC case, the selected features were F9, F7, F2, F3, F10 and F8. There were some common features used by both systems, such as the variance (F2) and the power spectral density in the range of 0.1 - 0.2 Hz, (F7) and in the range of 0.3 - 0.4 Hz (F9). These features can depict modifications on the breathing signal characteristics, i.e. the

change of the waveform over time, which can occur due to random motions or to sudden change of emotional state (caused by laughs or frights) and also the dynamic range variation of the breathing rate on a healthy person. It should be also highlighted the features that were differently selected. For example, F4 which measures the time between peaks and F12 that represents the ratio between low frequency components and high frequency components, were only selected on the BRD based system. These features can encompass either the cardiac signal (mostly detected in apnea periods), but mostly the RBM that is not easily detected by the BPC, as seen previously.

With the limited number of features, the results increased in general (excepting SVM for the BPC case). This determines the importance of the selected features and proves their relation with the current emotional state of the subject. In conclusion, using exclusively the respiratory signal and RBM, the BRD system is able to differentiate between the three elicited emotions with an accuracy of 67.1%. In contrast, the BPC presented a better but yet similar performance namely 75.1%, which is less than 10% difference, when compared with the BRD.

6.3 Performance comparison of emotion recognition using bio-radar and contact-based methods

In the previous section, one could conclude that the differences between BRD and BPC systems are not relevant. The developed work was only focused on the respiratory signal and RBM, and despite the results showed that the respiratory signal is a highly informative element, the obtained results can be improved. As seen in Chapter 3, the DSP algorithms performance is greatly improved if the CDC offsets are removed dynamically. This dynamic implementation allows to account with environment changes as well as keep track of the subject RBM, without alter useful information.

This section describe the developments related with the second stage of emotion recognition using the BRD system. In order to step forward on this research, the BRD prototype was generally improved not only at a hardware level, but also in a software level. On the hardware side, the BRD prototype used to acquire the vital signs was the final selected in Chapter 2 and it is depicted in Figure 6.3. On the software side, the *Dynamic DSP* algorithm was implemented to pre-process and extract the vital signs before the features extraction, and the cardiac signal extracted using the wavelet-based algorithms described in Chapter 5 was included in the analysis. In this case, and considering the lack of signal resolution reported Chapter 5, windowing approaches were used to extract the cardiac features, in order to take advantage and to fully exploit the information contained in the cardiac signal without risking to obtain biased results.

Finally, the population under analysis was increased to 20 subjects (20-subject dataset from Table 3.6). The same classification procedure was adopted as previously, where the SVM, KNN and RFO classifiers were applied to the signals acquired by BRD and BPC systems. The features typically used in literature were surveyed and computed over BRD and BPC signals, to subsequently study statistically which are able to differentiate between emotions.

6.3.1 Considerations on vital signs extraction

Similarly to the procedure conducted in the first work stage, both BRD and BPC signals were pre-processed to obtain the RS and CS waveforms. Figure 6.8 presents the complete

block diagram of the DSP algorithm implemented at this stage for both BRD and BPC signals.

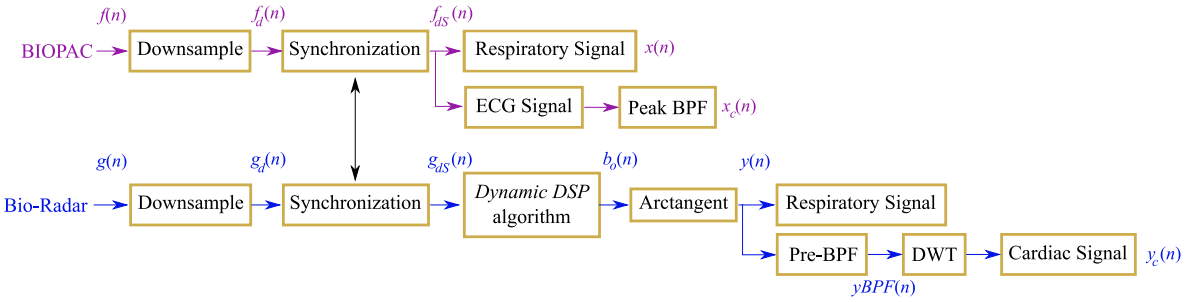

Figure 6.8: Block diagram of the BRD and BPC signals pre-processing before the classification considered in the second stage of emotion recognition.

In sum the BRD signals are pre-processed using the *Dynamic DSP* algorithm and then the arctangent was applied to recover the vital signs resulting in signal $y(n)$. Signal $y(n)$ contains both RS and CS mixed together, so in order to obtain the $y_c(n)$ exclusively the algorithm described in Chapter 5 was applied, starting by passing the $y(n)$ signal by a 100^{th} order FIR BPF, with a pass-band within 0.7-2 Hz and then apply a multi-resolution analysis through the DWT. On the BPC side, the only signal processing applied after synchronization was dedicated to the ECG signal. A 15^{th} order FIR BPF with a pass-band equal to 6-20 Hz was applied to highlight the R-peak and remove noise [166].

6.3.2 Features extraction

After processing the BRD and BPC signals, they were divided in one-minute segments, leading to a balanced dataset with size equal to 1626 minutes (542 minutes per emotion). The dataset was balanced using the same strategy adopted in Stage 1. Several features were computed over the one-minute segments, to further build the observation matrix which will be used by the classifiers. For starters, the works [4], [52], [186], [190], [191] were analyzed and almost all features were considered and extracted from the segments. Thereafter, a statistical study was conducted over all features, aiming to select the ones that provide significant information to differentiate between the different emotions. The features considered at this stage can be once again divided in four different categories - waveform features, statistical features, spectral features and HRV features - and they are compiled in Table 6.4.

Waveform, statistical and spectral features are computed directly over one minute segments, and more details are now provided:

- F1 for the BRD signal is computed using two different approaches - ANN result using the individual models and through ZC - to later study the differences on results. For the BPC case this feature corresponds to the inverse of the median of IBI;
- F2 is obtained through a zero-crossing approach fully introduced earlier in Chapter 3;
- F5-F10 correspond to the mean absolute value of the first and second derivative of CS, RS, normalized RS and the IBI of the CS;
- F11 represents the energy ratio between RS and CS;

Category	Feature No.	Description	Applied Signal
Waveform	F1-F2	Signal Rate	CS and RS
	F3-F4	AppEn	CS and RS
	F5-F7	First derivative	RS, RS-N, IBI-CS
	F8-F10	Second derivative	RS, RS-N, IBI-CS
	F11	Energy Ratio	RS
	F12	Kurtosis	RS
	F13	Peak Width	RS
	F14	Variance	RS
Statistical	F15-F18	Sk, Med, IQR, Av	IBI-CS
	F19-F22		IBI-RS
	F23-F26		CS
	F27-F30		RS
	F31-F34		Inhale (RS)
	F35-F38		Exhale (RS)
Spectral	F39-F44	PSD	RS
	F45	PSD ratio	RS
HRV parameters	F46-F47	SDNN	IBI-CS, IBI-RS
	F48-F49	RMSSD	IBI-CS, IBI-RS
	F50	pNN50	IBI-CS
	F51-F52	DFA2 α_1 and α_2	IBI-CS
	F53-F56	Poincaré plot for $m = 1$	IBI-CS
	F57-F60	Poincaré plot for $m = 10$	IBI-CS

CS - Cardiac signal, RS - Respiratory signal, RS-N - Normalized respirtory signal, IBI-CS - Interbeat Interval for CS
IBI-RS - Interbeat Interval for RS, AppEn - Approximate Entropy, Sk - Skewness, Med - Median,
IQR - Inter-Quartile Range, Av - Average, PSD - Power Spectral Density,
SDNN - Standard deviation of all IBI, RMSSD - root mean square of the successive differences of the IBI,
pNN50 - Percentage of successive normal sinus IBI taking more than 50 ms, DFA - Detrend Fluctuation Analysis

Table 6.4: Initial set of features considered in the second stage of emotion recognition.

- F13 is the mean value of the width of peaks and valleys;
- F39-F44 correspond to the PSD over separated frequency bands, namely 0 - 0.1 Hz, 0.1 - 0.2 Hz, 0.2 - 0.3 Hz, 0.3 - 0.4 Hz, 0.4 - 0.9 Hz and 0.9 - 1.5 Hz;
- F45 is the PSD ratio between a lower frequency range within 0.1-0.4 Hz and a high frequency range within 0.5 - 1.5 Hz;

F11 is being computed differently for BRD and BPC signals. For BRD, F11 corresponds to the ratio between the RS and the signal resulting from the BPF application prior the computation of the DWT coefficients, (i.e. the ratio between signals $yBPF(n)$ and $b(n)$ in Figure 6.8). This filtered signal was considered instead of the wavelets results, for containing all high frequency spectral components. For BPC, the F11 is the ratio between the signal coming from the chest-band and the ECG signal. Note that at this work stage, the statistical and waveform features did not require the application of any filter as it was necessary in the first work stage, since the filter could remove characteristics that might be more important for some of the features.

On the other hand, the HRV features needed to follow a different computation strategy. The observation matrix applied to all classifiers has a $N \times M$ dimension, where N is the number of features and M is the number of observations and each observation corresponds to the feature result computed over a one-minute signal. However, the Task Force in [158] recommended to use signals with at least 5 minutes of duration to compute the HRV parameters, as a gold standard. Therefore, we computed the HRV parameters using sliding windows

with 5 minutes length, moving forward at a 1 minute pace, as depicted in Figure 6.9. The observation number corresponds to the central minute of the 5-minute window.

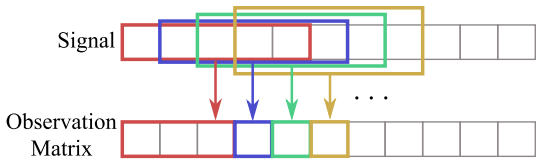

Figure 6.9: Illustration of how HRV features are computed and assigned to each observation.

More details can be also provided about the HRV parameters:

- F47 and F49 are related to the respiratory peaks, so they were computed in one minute segments;
- F46-F49 the results are presented in log transform to adjust for the unequal variance, since data presented a non-normal distribution [156];
- F51-F52 were computed using a quadratic fitting and considering a short range (α_1) between 20 and 60 beats and a long range (α_2) between 10 and 100 beats [206];
- F53-F60 correspond to the Poincaré plot features, namely the standard deviation in crosswise (SD1), the standard deviation in lengthwise (SD2), the ratio between SD1 and SD2 (SD12) and the SDRR. All the Poincaré plot parameters are computed without and with delay (i.e. $m = 1$ and $m = 10$, respectively).

Additionally, a features normalization was conducted at this work stage. Features were computed on baseline signals and on signals from the inducted conditions. In order to guarantee a user-independent and day-independent analysis, the mean value of the baseline features on a given day and for a specific subject was subtracted from the features computed for the emotional condition of that day [207].

6.3.3 Statistical study over the features information

After computing all features and normalize them, the most informative ones were selected through a statistical study. Before describing the conducted procedure, a note must be exposed. As previously discussed in Chapter 5, when the CS is measured through the mechanical motion of the heart at the chest surface, there is an interpersonal variation of the heartbeat morphologies related with the differences on body mass index, age, sex, among other health-related factors. This was in fact observed on the MAE differences presented in Table 5.4 and for this reason ANN were developed as an alternative to decrease the MAE. However, despite the error minimization, using ANN models increase the complexity of the process, therefore, it is required to evaluate if the final results justify such complexity. In this context, the impact of the heart rate accuracy was studied in this work stage, by performing a feature selection and also running the classifiers results using the F1 computed through both ANN (F1-ANN) and ZC (F1-ZC) approaches.

Figure 6.10 depicts the workflow being followed. First of all, the One-way analysis of variance (ANOVA) test was applied over all features in order to inspect if the resultant residuals have a normal distribution. In this case, it was considered the most voted answer

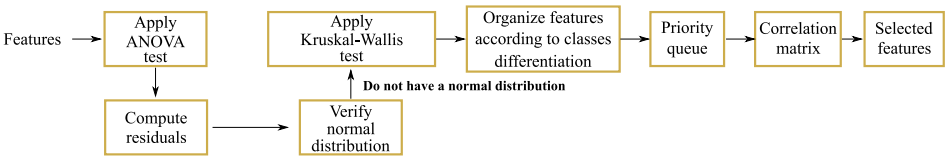

Figure 6.10: Workflow of the statistical study for features selection.

of three different tests - the Kolmogorov-Smirnov test, the Anderson-Darling test and the Lilliefors test. All features presented a non-normal distribution. Secondly, an hypothesis testing is performed to verify which features represent statistical differences between the classes being identified. Since all features have a non-normal distribution, the Kruskal-Wallis test was conducted, since it makes no normality assumption about the population distribution [208]. The Kruskal-Wallis test analyze the variance of ranks, in this case by inspecting the medians of the features. At this stage, one intend to find the features presenting different medians for distinctive classes. For each feature the resultant $p-$value was inspected and only the features with $p < 0.05$ were considered further. Subsequently, the Pairwise T-test with one-step Bonferroni correction was applied, to analyze which pair of classes each feature can differentiate.

The third step of this analysis is building a priority queue of features. For each binary classification namely Fear vs. Happy (FH), Fear vs. Neutral (FN) and Happy vs. Neutral (HN), features were settled in a column, in ascending order according to the $p-$values obtained in the Pairwise T-test. Thus, the first row of each column presents the features that better distinguishes the correspondent classes (with lower $p-$values) and the last row presents the less significant features (with higher $p-$values). From this point, the queue is build over the rows, prioritizing the elements with lower $p-$values and removing the repeated entries.

The final step of this study is creating a correlation matrix, in order to remove features with redundant information and simplify the classification models. If a given pair of features present high correlation, it indicates that the variation of one affects directly the other. In this case, one of them can be removed keeping always the one with more priority in the queue. Thus, the final selected features were the ones presenting correlation values inferior to 0.7, selected according to their position in the priority queue. For instance, Figures 6.11 and Figures 6.12 shows the correlation matrices before and after removing the redundant elements for both BRD and BPC signals respectively, where the BRD case was the one using F1-ANN. At the end, one could reduce an observation matrix with 60 features to 23 features for the BRD if using F1-ANN approach or 22 if using F1-ZC. For the BPC 19 features were selected. Table 6.5 presents the list of features for both systems and for both F1-approaches, in decreasing order of importance, according to their priority queues.

Feature selection discussion

Starting with features selected for the ANN approach, in total there are 11 features commonly selected by both systems, namely the F25, F55, F51, F34, F2, F45, F27, F3, F12, F43 and F9, which is approximately half of the set. This fact could indicate that both systems present a similar information content, despite the different particularities related to the signals nature. The body motion is highly accounted on the BRD case, since the first four features with more priority are dedicated to RS (and therefore indirectly related with RBM), while the first four ones on the BPC case are relative to the CS. Besides, in total 5 and 8

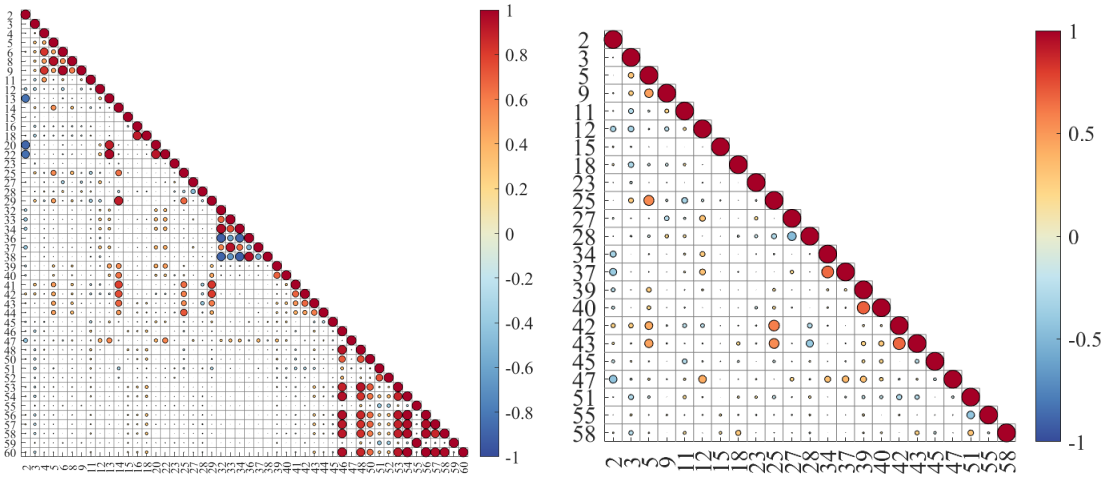

(a) (b)

Figure 6.11: Correlation matrix for feature selection considering F1-ANN approach for the BRD case: (a) after the Pairwise T-test, (b) after removing redundant features.

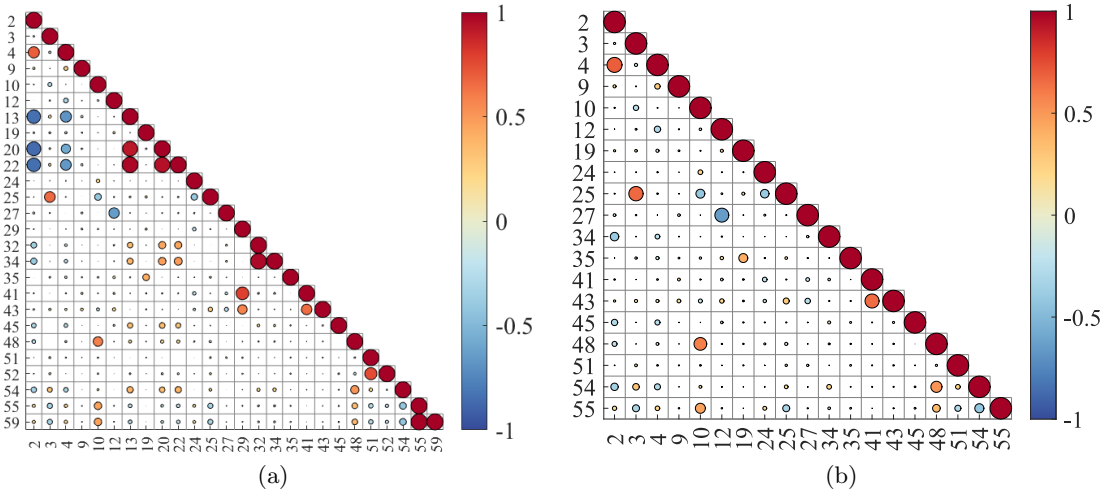

(a) (b)

Figure 6.12: Correlation matrix for feature selection for the BPC case: (a) after the Pairwise T-test, (b) after removing redundant features.

---

features were selected from the spectral and statistical categories on the BRD case, whereas only 3 and 5 features were selected for the BPC case on the same categories.

On the other hand, if the F1 was computed through ZC, only three features were selected differently. More specifically, the F1-ZC approach also selected F1, F52 and F50 and the F1-ANN selected F58, F51, F18 and F47 differently. Since the F1 was selected if computed with the ZC, one can conclude that the additional error contributed to distinguish between different classes, which might lead to biased results. Furthermore, the selection of F1 discarded other features correlated to it, that might have relevant information. Even though, both feature sets are highly similar, therefore it is not expected to obtain disparate classification results between these two cases.

Bio-Radar (F1-ANN)		Bio-Radar (F1-ZC)		BIOPAC	
Feature	Description	Feature	Description	Feature	Description
F28	Median of RS	F28	Median of RS	F25	IQR of CS
F34	Mean of inhale time	F34	Mean of inhale time	F55	SD12 for $m = 1$
F2	RS rate	F2	RS rate	F24	Median of CS
F43	PSD in 0.4 - 0.9 Hz	F43	PSD in 0.4 - 0.9 Hz	F51	DFA2 α_1
F23	Skewness of CS	F23	Skewness of CS	F34	Median of inhale time
F3	AppEn of CS	F3	AppEn of CS	F2	RS rate
F42	PSD in 0.3 - 0.4 Hz band	F42	PSD in 0.3 - 0.4 Hz band	F45	PSD ratio
F9	Second derivative of RS-N	F9	Second derivative of RS-N	F27	Skewness of RS
F27	Skewness of RS	F27	Skewness of RS	F41	PSD in 0.2 - 0.3 Hz
F25	IQR of CS	F25	IQR of CS	F3	AppEn of CS
F58	SD2 for $m = 10$	F45	PSD Ratio	F10	Second derivative of IBI-CS
F51	DFA2 α_1	F37	IQR of exhale time	F4	AppEn of RS
F37	IQR of exhale time	F1	CS Rate	F12	Kurtosis of RS
F40	PSD in 0.1 - 0.2 Hz band	F55	SD12 for $m = 1$	F35	Skewness of exhale time
F18	Mean of IBI-CS	F52	DFA α_2	F54	SD2 for $m = 1$
F45	PSD ratio	F5	First derivative of RS	F43	PSD in 0.4 - 0.9 Hz
F39	PSD in 0 - 0.1 Hz band	F40	PSD in 0.1 - 0.2 Hz	F19	Skewness of IBI-RS
F5	First derivative of RS	F39	PSD in 0 - 0.1 Hz band	F9	Second derivative of RS-N
F55	SD12 for $m = 1$	F11	Energy ratio	F48	RMSSD for IBI-CS
F11	Energy ratio	F12	Kurtosis of RS		
F12	Kurtosis of RS	F15	Skewness of IBI-CS		
F15	Skewness of IBI-CS	F50	pNN50		
F47	SDNN of IBI-RS				

Table 6.5: List of selected features for BRD and BPC systems in decreasing order of importance.

Additionally, one should note that the same features were computed over the BRD and BPC signals for a fair comparison. This work aims to verify if both systems have the same ability to detect emotions in the same conditions, rather than choosing the one with the best performance. Therefore, it should be stated that more appropriate features can be selected for the BPC system such as the frequency domain parameters of the HRV, and in that case the features selected for the BPC might be different, as well as the results obtained further.

6.3.4 Classification results

After selecting which are the features with pertinent information to differentiate between classes, three machine learning algorithms were implemented - SVM, KNN and RFO. The classifiers hyperparameters used were the same previously presented in the first work stage and the considered evaluation metrics were the following:

- Cross-Validation (CV) using the leave-one-out strategy;
- First testing stage (T_{30}) - using a hold-out strategy where 70% of the dataset of each condition was used to train the model and the remain 30% was used to test it. For this first testing stage, 19 subjects were considered and one was left out. The partition of data as well as the selection of the subject to be left out were performed randomly. The train-test procedure was repeated 20 times and the mean value and standard deviation of the accuracy and F1-score were verified.

- Second testing stage (T_{id}) - accuracy and F1-score were evaluated for the subject being left out in the T_{30} stage, serving as a new subject.

The performance results of the classification accuracy are again presented separately in the binary and multiclass problems. The classification results were evaluated for both F1-ANN and F1-ZC cases, and also for the BPC case, in order to compare performances.

Binary problem

The results obtained for the binary problem are presented in Table 6.6.

Classifiers	HN [$m \pm std$]			FH [$m \pm std$]			FN [$m \pm std$]			
	CV	T_{30}	T_{id}	CV	T_{30}	T_{id}	CV	T_{30}	T_{id}	
SVM	82.2 ± 3.1	83.6 ± 4.7	50.6 ± 9.1	83.6 ± 2.3	83.7 ± 3.9	48.0 ± 6.2	84.9 ± 2.3	86.1 ± 3.1	50.8 ± 1.9	BRD_1
	78.8 ± 1.4	79.2 ± 2.7	49.2 ± 3.5	81.9 ± 2.1	82.8 ± 2.7	50.3 ± 6.0	82.4 ± 3.5	86.0 ± 4.0	52.1 ± 10.5	BRD_2
	80.1 ± 1.5	80.3 ± 3.1	55.2 ± 11.0	81.7 ± 2.5	83.7 ± 2.5	48.8 ± 11.3	79.8 ± 1.3	79.6 ± 2.7	60.6 ± 11.9	BPC
KNN	97.2 ± 0.5	97.3 ± 0.7	61.0 ± 12.0	97.9 ± 0.4	97.5 ± 0.9	35.9 ± 21.1	97.4 ± 0.4	97.8 ± 0.8	63.6 ± 15.9	BRD_1
	95.7 ± 0.7	96.0 ± 0.9	58.0 ± 19.8	95.9 ± 0.5	95.9 ± 1.1	48.5 ± 14.9	96.3 ± 0.6	96.6 ± 1.1	58.9 ± 19.2	BRD_2
	91.8 ± 0.8	91.8 ± 1.4	46.5 ± 14.3	91.8 ± 0.8	91.8 ± 1.4	46.5 ± 14.3	91.4 ± 0.7	91.1 ± 2.3	65.6 ± 12.5	BPC
RFO	99.5 ± 0.2	99.6 ± 0.4	55.9 ± 15.0	99.2 ± 0.4	99.4 ± 0.5	38.3 ± 32.1	99.3 ± 0.3	99.6 ± 0.7	67.0 ± 23.6	BRD_1
	94.6 ± 0.6	95.6 ± 1.1	58.4 ± 21.8	94.2 ± 0.9	95.5 ± 1.1	39.5 ± 15.7	94.8 ± 0.6	96.2 ± 1.2	62.8 ± 22.7	BRD_2
	91.0 ± 1.0	91.9 ± 1.6	74.6 ± 20.2	90.2 ± 1.3	91.6 ± 2.2	54.9 ± 23.8	91.2 ± 0.7	91.2 ± 1.6	71.4 ± 19.3	BPC

BRD_1 - bio-radar results with F1 obtained through ANN, BRD_2 - bio-radar results with F1 obtained through ZC, BPC - BIOPAC results
HN - Happy vs. Neutral, FH - Fear vs. Happy, FN - Fear vs. Neutral, m - mean value, std - standard deviation

Table 6.6: Accuracy results in (%) for the binary problem relative to the second stage of the emotion recognition.

The first aspect that should be highlighted is that the accuracy increased in comparison to the first work stage. By comparing only the CV results presented in Table 6.3 with the ones in Table 6.6, one can conclude that by increasing the set of features, by removing the individual and daily dependency and by carefully selecting the most important ones, increase the performance for both BRD and BPC systems. The impact was more prominent in the BRD system, which increased approximately 20% for all binary conditions. An inferior rise was observed for the BPC, varying between 7% and 15%. Other important aspect is that, while in Table 6.3 the FN condition was the one obtaining the best results, in this case no condition stand out, presenting all equivalent performances. This effect was observed for both BRD and BPC cases.

Observing now the test performance using the remain 30% of the data not used for training (T_{30}), one can verify the robustness of the model, since the testing results do not differ largely from the CV ones. This was observed for all classifiers, whereas each presented similar but yet different performances. For instance, in the BRD_1 case, the SVM classifier presented an average performance of 84.5% for all binary cases, while the KNN and RFO performed better with an average of 97.5% and 99.5%, respectively. In general, the BRD case presented a better accuracy than the BPC case, for both CV and T_{30}, where the difference did not exceeded 8%.

The T_{id} testing case was the one presenting the worst results. The standard deviation increased abruptly indicating a large variance in results. This was somehow expected since the subject used in test was not considered in the training phase. If the subject being tested do

not have similarities with the data used to train the model, the model will not fit with his/her behavior and the accuracy decreases, which explains the increase observed in the standard deviation value. Hence, one can conclude that the data of 20 subjects may not be enough to generalize the models for the general population. As for the classifiers performance in the T_{id}, considering the BRD case, each classifier stand out as the best for a different binary case. This time the BPC case performed better than the BRD, and the best results were obtained with the RFO classifier, with 74.6% of accuracy for the HN case, 54.9% for the FH case and 71.4% for the FN case. Looking at the best results of the BRD, all binary cases presented an accuracy varying between $48\% - 67\%$.

The differences observed in T_{30} and T_{id} results obtained for BRD and BPC systems, can be justified with the occurrence of random body motions (usually treated as noise), which are easily captured by BRD but are less evident in BPC signals. Each emotional condition can provoke motions specific to the emotion and emotional intensity experienced by the individuals [209]. For instance, the fear induce frights that can be more subtle in some subjects or more evident in others. Concurrently, some subjects reported that they found some comedy videos funnier than others. Since BRD is more affected by external motions and BPC results are exclusively dedicated to patterns in vital signs, the motion patterns might have an increased individual variability rather than the vital signs solely [209].

Finally, the performance of the BRD classifiers was compared considering that F1 was computed using two different approaches: ANN individual models (BRD_1 results) and the ZC method (BRD_2 results). The ZC one was more traditional and less complex to implement, but implied a high MAE depending on the subject at hand. The ANN presented an average MAE of 1 BPM, but it requires a complex implementation. The results presented in Table 6.6 suggest that this complexity effort required to obtain the BRD_1 results might compensate, since an average of 99% of accuracy was obtained for all the binary cases, in CV and T_{30} cases. Nonetheless, it is worth to mention that the differences between BRD_1 and BRD_2 are not relevant, being less than 5%.

6.3.5 Multiclass problem

Table 6.7 presents the results of the multiclass problem. For this case, besides the accuracy, other metric was evaluated namely the F1-score. This metric establishes a balance between recall and precision, which is more appropriated for short datasets applied in a multiclass problem [186], [190].

The multiclass problem achieved similar performances compared with the binary one. The CV is again close to the T_{30}, indicating the robustness of the models. Better results were obtained for the BRD_1 on the T_{30}, which could differentiate the three emotions with 99.7% of accuracy and 99.9% of F1-score using the RFO classifier, while the BPC presented an accuracy almost 10% below with 87.8% and 92.7% of F1-score, also using the same classifier. Since the binary problem presented a high performance in all cases (also around 99%), the BRD_1 multiclass results were expected. As regard with the remain classifiers, for both BRD and BPC, the SVM classifier was the worse and KNN presented a performance similar to the RFO classifier.

The T_{id} results of the multiclass problem were presented the same order of magnitude as the binary case. Likewise Table 6.3, a high standard deviation was verified in the T_{id} test and the BPC performed better than the BRD most of the times.

	Accuracy $[m \pm std]$			F1-score $[m \pm std]$		
	CV	T_{30}	T_{id}	T_{30}	T_{id}	
SVM	76.8 ± 2.1	76.7 ± 3.5	34.6 ± 8.4	85.2 ± 3.9	60.4 ± 20.1	BRD_1
	73.3 ± 1.8	73.5 ± 3.5	33.8 ± 5.1	83.0 ± 2.5	65.5 ± 5.9	BRD_2
	72.9 ± 2.3	74.7 ± 2.5	39.4 ± 6.5	94.0 ± 4.7	37.2 ± 36.8	BPC
KNN	96.0 ± 0.4	96.4 ± 0.8	37.1 ± 9.0	98.0 ± 1.0	41.0 ± 28.4	BRD_1
	93.4 ± 0.7	93.8 ± 0.9	40.2 ± 13.3	96.5 ± 1.0	61.3 ± 15.9	BRD_2
	86.2 ± 1.0	86.6 ± 1.3	41.8 ± 7.4	92.8 ± 2.0	60.7 ± 19.6	BPC
RFO	99.2 ± 0.3	99.7 ± 0.3	35.3 ± 21.7	99.9 ± 0.2	40.8 ± 39.4	BRD_1
	92.7 ± 0.7	94.3 ± 1.2	38.4 ± 16.4	96.9 ± 0.9	50.3 ± 30.4	BRD_2
	86.5 ± 1.0	87.8 ± 1.4	51.5 ± 20.1	92.7 ± 1.9	59.1 ± 37.2	BPC

BRD_1 - bio-radar results with F1 obtained through ANN

BRD_2 - bio-radar results with F1 obtained through ZC, BPC - BIOPAC results

m - mean value, std - standard deviation

Table 6.7: Performance results in (%) for the multiclass problem relative to the second stage of the emotion recognition.

6.4 Final considerations

This chapter was dedicated to perform a complete validation of the bio-radar prototype to be used in emotion recognition. This validation was supported by comparing the classification results with the ones obtained using the BPC as a certified measuring equipment. The work was divided in two stages. The first stage was presented in Section 6.2, and it used only the RS signal to distinguish the happiness, fear and a neutral condition. The second stage was presented in Section 6.3, and it included the CS on the analysis. Furthermore, a total of 60 features were computed and a statistical study was implemented to identify the most informative ones. The individual and daily dependency contained in the baseline were also canceled. In sum, the results accuracy increased more than 20% in comparison to the first work stage.

In general, the latter results demonstrated that if classifiers include the population under study in the training process, the BRD outperforms the BPC in the emotion recognition, considering the same set of 60 features as starting point. More specifically, according to the F1-score obtained in the multiclass problem, we were able to recognize $\approx 100\%$ of the cases.

The statistical study implemented for both systems provided a reduced set of features, where half of them were common in BRD and BPC, indicating that signals acquired by radar contain equivalent information. Additionally, the body motion captured by BRD could possibly explain its superior performance. For instance, frights have an inherent motion pattern as well as chuckles, which are captured more easily by the BRD than the chest-band of the BPC. Nonetheless, if new data is being tested in the classifiers, BPC stand out with a better performance most of the times. This might also be related with the body motion due to the increased individual reaction variability.

Regarding the results presented in the literature so far, a direct comparison cannot be performed fairly. All works used different radar front-ends and the emotions under study

were different. The works [4], [52], used both RS and CS to compute features, while [190], [191] only considered the RS. The features normalization using the baseline information was only implemented in [4], [52]. The works [4], [52], [191] presented an accuracy varying between $67\% - 72\%$ to detect four emotions, where [52], [191] were dedicated to the same emotion set and [4] was focused on a different set. On the other hand, our work and [190] were dedicated to three emotions, where [190] achieved 76%. Despite we obtained a better accuracy of 99%, [190] was not focused on the same emotional set and used a completely different radar setup. Therefore, one can only conclude that the results obtained in our work are in line with the ones presented in the countable works of literature.

Additionally to the works presented on Table 6.1, the work presented in [186] can also be included in the literature analysis, since they conducted a study on emotion recognition focused on the same emotional set and following the same emotion induction protocol. Their dataset was composed by the ECG, the electrodermal activity and the electromyogram of 55 subjects, acquired with BPC. They also conducted a classifier performance analysis similar to the one herein presented, where one can stand out two of their testing cases. In their (a) testing case, 12 subjects were left out of the training process and tested separately, and in the (c) case, 30% of each emotional condition of the test data was included in the training process. Their (a) case was similar to ours T_{id}, but we only used one subject to test separately and their (c) case was similar to our T_{30}, but we used 70% for training instead of only 30%. Comparing now the F1-score results, in [186] 42% was obtained for the RFO classifier on the (a) case, and we were able to obtain 40.8% testing in only one subject. For the (c) case, also using the RFO classifier, a F1-score of 73% was obtained in [186], while we were able to accomplish 99.9%. Our results are thus also in line with the ones obtained in [186] and the observed differences might be mostly justified with the sample size, the number of observations used for training and testing, and the different vital signs used in both works.

Chapter 7

Conclusion

The main goal of this PhD was to verify the viability of using bio-radar systems in real applications. In order to accomplish such purpose, it should be possible to integrate the system in specific objects to confer a low profile appearance and streamline the manufacturing process of the product at hand. Concurrently, the prototype performance must be assured for long-time periods and deal successfully with low quality signals, retrieving important information regardless the subject's physical characteristics. For this purpose, a bio-radar prototype was developed and applied in specific case study scenarios, limitations and potentials were identified and appropriate solutions were designed to overcome the implementation issues and enhance the system robustness.

The main prototype operation characteristics were firstly studied and selected considering the purpose of the PhD. In this sense, a flexible front-end was opted which consisted on an SDR operating in CW mode at 5.8 GHz. CW radars are narrow band and the vital signs are extracted using accurate phase measurements. The carrier frequency respects a balanced trade-off between sensitivity and system design simplicity. The SDR was selected to be used as RF front-end for being compact and flexible to configure. A set of antenna design guidelines were also provided, based on a state of the art review. Throughout the different work stages, one could conclude that the appropriate antenna design could be different depending on the application at hand. For instance, in acquisitions performed in front of the subject, directive antennas might be more indicated to improve the SNR, but the same might not be applied for alternate chest areas (e.g. sideways). Nonetheless, characteristics such as high gain and crossed circular polarization should be kept commonly.

In order to study the prototype performance under the different perspectives, two specific case studies were considered. The first case study was mostly dedicated to the system appearance. Therefore, in this framework, low profile solutions were developed to fully integrate a bio-radar system in a car seat upholstery. For this purpose, textile materials were used to manufacture antennas and they were embedded in the side lumbar support upholstery, aiming to monitor the respiratory signal from the subject's sideways. The system performance was tested and the results showed that it is possible to acquire the respiratory signal from sideways using textile antennas, with a similar precision as conventional substrate antennas. For this specific application, the appropriate antenna design was selected and it was concluded that single patch antennas might be more indicated, due to their wider beam in the radiation pattern, that allows an easier alignment with the subject considering the limited RCS. In sum, the results obtained in this case study demonstrated that it is possible to fully

integrate a bio-radar in a specific application, by adapting the antennas design, since they are the system element which is in the line-of-sight with the subject. A complete validation was also performed by comparing the bio-radar performance to capture the respiratory signal from sideways, with a certified measuring equipment, which measures the full chest wall expansion.

On the other hand, real application scenarios imply the bio-radar operation during long term periods. With this fact, several challenges arise since the subject cannot stay entirely stable, neither the monitoring environment. Hence, the DSP algorithm implemented to extract vital signs must adapt to eventual monitoring conditions changes. In real context scenarios, the RBM generates high amplitude signals which overshadow the vital signs information, compromising the DSP algorithms effectiveness. Besides, the vital signals amplitude can severely decrease, not only due to the subject physical characteristics, but also due to an eventual misalignment with the antennas beam. In this sense, an algorithm was developed to extract the vital signs considering long term acquisition periods. The developed algorithm determines the CDC offsets related with the parasitic reflections occurring in the environment, using a novel arc fitting method, which forces the arc center estimation to be outside the radar samples. This method revealed being highly effective when applied to weak signals, and robust to sporadic body motions. The CDC offsets removal was implemented dynamically through a windowing approach, to contemplate time changes in the acquired signal. The DSP algorithm was also developed having in mind a real time implementation, by altering the average signal angle in order to oscillate around 0°.

The ability to extract the cardiac signal under the same circumstances was verified. For this case, the impact of the subject's inter-individual variability was more evident, since only in half of the tested subjects the heart rate error was inferior to 3 BPM. The inter-individual variability might be related to several factors, such as the body posture under test, the individual chest wall motion, the physical body characteristics or even the psychological state. Solutions such as machine learning algorithms might be used to decrease this error, where individually trained models were the most effective. Additionally, it was inspected if it would be possible to assess pertinent cardiac characteristics, considering the used prototype and carrier frequency. One could conclude that due to the lack of signal resolution it is not possible to estimate HRV parameters accurately, but even though it is possible to extract useful information from these parameters, through windowing approaches.

Finally, the bio-radar vital signs usage was exploited by verifying if it is possible to estimate the emotional state of a subject in a given moment. For this purpose, three different emotions where induced by a video visualization, and the vital signs were acquired using the bio-radar and a certified measuring equipment for comparison purposes. On a preliminary study, where only the respiratory signal was used, similar accuracies were obtained by both acquisition systems, demonstrating that the bio-radar signals can be used for psychophysiological assessment. Later, the results were indeed improved by adding also the cardiac signal as information and improving the prototype in general. In this case, the bio-radar system outperformed the certified measuring equipment used as reference, achieving 99% of accuracy on the emotion identification. It was concluded that this final result was obtained mostly due to RBM that occurred according to the subject's reaction to specific emotions. Therefore, despite having impact in the vital signs extraction and even compromising the system's accuracy, the RBM have also useful information regarding the subject's state, that should be equally preserved.

7.1 Future Work

The work developed in the PhD demonstrated that the bio-radar potential can be optimized if it is integrated in specific applications. Only two case studies were evaluated, hence, as the future work more applications should be considered and explored in order to step forward in a future system quality certification.

In Chapter 4, it was studied how to integrate the bio-radar in a specific object considering the vehicular scope. However, all tests were conducted in a laboratory environment using a car seat model. More research is still required for automobile applications, to verify the ability to operate the bio-radar inside a vehicle, considering the high multipath environment and also the car trepidation during its mobility. To solve the multipath issue, alternate antenna designs can be explored aiming to decrease the antenna beam and its side lobes. One possible solution is the usage of dielectric lens in front of the antenna, or the usage of MIMO (Multi-Input Multi-Output), to redirect a narrow beam to a pertinent location and fully eliminate the acquisition of parasitic reflections. Although these two solutions imply bulky antennas or larger antenna arrays, they might be suitable if the radar is incorporated in alternate positions, such as in the ambulance ceiling to remotely monitor critical patients.

The impact of the inter-individual variability in the signs accuracy should be further studied, as well as the impact of the body structure in the propagation channel. During the work stages conducted in this PhD, signals with different SNR were received by different subjects, under the same acquisition conditions. Since an electromagnetic signal is reflected in the subject's chest wall, the body is indirectly a radiating element and might have a different impact in the signal received by the radar. It is important to understand the causes of such variability, if they are relative to the gender or exclusively to the subject body. This information is important to correctly calibrate the overall system.

On the other hand, one could verify that the RBM can be either a disruptive source for the extracted signals, but also an informative element to assess the psychological condition of the subject. Aiming to develop a system fully robust in long-term applications, it is important to classify the types of RBM and identify which must be compensated and when. Then, the RBM can be either compensated using DSP algorithms or using hardware solutions, such as MIMO systems, by coherently combine signals acquired by different antenna elements and thus recover signals in case of path loss.

Additionally, the ability to identify emotions with the bio-radar system demonstrated that by using appropriate machine learning algorithms, informative patterns are indeed present in the vital signs, and they can be captured more easily with the radar when compared with conventional contact equipment. This conclusion open doors to multiple applications worth to be explored, such as in the forensic research by implementing a remote and hidden polygraph. Under these circumstances more authentic reactions can be assessed, since the subject is not directly aware of being monitored. The prototype proposed in this PhD is suitable for that purpose, since it can be hidden in objects keeping simultaneously its accuracy at a superior level.

Finally, it is also worth to explore the ability to use the remotely captured vital signs to assist in diseases diagnosis, either pulmonary or cardiac, such as dysfunctional breathing, chronic obstructive pulmonary disease, arrhythmia or other pertinent conditions that could be detected through the motion at the chest wall surface. In this case, the current bio-radar front-end could be either explored using the proposed windowed-based approaches or it can also be adjusted in order to increase its sensitivity, by using higher frequency carriers.

Bibliography

[1] O. B-.Lubecke, V. Lubecke, A. Droitcour, B. Park, and A. Singh, *Doppler Radar Physiological Sensing*. NJ, USA: Wiley - Hoboken, 2015.

[2] C. Gouveia, "Bio-radar", Master's thesis, Universidade de Aveiro, Aveiro, Portugal, Dec. 2017.

[3] L. Anishchenko, "Challenges and potential solutions of psychophysiological state monitoring with bioradar technology", *Diagnostics*, vol. 8, no. 4, p. 73, 2018.

[4] M. Zhao, F. Adib, and D. Katabi, "Emotion recognition using wireless signals", in *Proceedings of the 22nd Annual International Conference on Mobile Computing and Networking*, 2016, pp. 95–108.

[5] M. Raja and S. Sigg, "Applicability of RF-based methods for emotion recognition: A survey", in *IEEE International Conference on Pervasive Computing and Communication Workshops*, 2016, pp. 1–6.

[6] J. Lin, "Non-invasive microwave measurement of respiration", in *Proceedings of the IEEE*, vol. 63, 1975.

[7] J. Lin, E. Dawe, and J. Majcherek, "A non-invasive microwave apnea detector", in *In Proceedings of the San Diego Biomedical Symposium*, vol. 16, 1977, p. 441.

[8] J. Lin, J. Kiernicki, M. Kiernicki, and P. Wollschlaeger, "Microwave apexcardiography", in *IEEE Transactions on Microwave Theory and Techniques*, vol. 27, 1979, pp. 618–620.

[9] K. Chan and J. Lin, "Microprocessor-based cardiopulmonary rate monitor", in *Medical and Biological Engineering and Computing*, vol. 25, 1987, pp. 41–44.

[10] C. Li, X. Yu, C.-M. Lee, D. Li, L. Ran, and J. Lin, "High-sensitivity software-configurable 5.8-GHz radar sensor receiver chip in 0.13-um CMOS for noncontact vital sign detection", *IEEE Transactions on Microwave Theory and Techniques*, vol. 58, no. 5, pp. 1410–1419, 2010.

[11] D. Malafaia, J. Vieira, and A. Tomé, "Improving performance of bio-radars for remote heartbeat and breathing detection by using cyclostationary features", in *In Proceedings of the International Joint Conference on Biomedical Engineering Systems and Technologies, SCITEPRESS—Science and Technology Publications*, vol. 4, 2015, pp. 344–349.

[12] Texas Instruments, *AWR1642 single-chip 76-GHz to 81-GHz automotive radar sensor evaluation module*, [Online; accessed in september-2022]. [Online]. Available: `https://training.ti.com/mmwave-vital-signs-lab`.

[13] SensorLogic, *SLMX4*, [Online; accessed in september-2022]. [Online]. Available: `https://sensorlogic.ai/applications`.

[14] NOVELIC, *NOVELIC radars*, [Online; accessed in september-2022]. [Online]. Available: `https://www.novelic.com/radar-solutions/`.

[15] R. Mpanda, Q. Liang, L. Xu, Q. Lin, and J. Shi, "Investigation on various antenna design techniques for vital signs monitoring", in *In Proceedings of the Cross Strait Quad-Regional Radio Science and Wireless Technology Conference (CSQRWC), Xuzhou, China*, July 2018, pp. 1–3.

[16] V. Das, A. Boothby, R. Hwang, T. Nguyen, J. Lopez, and D. Y. C. Lie, "Antenna evaluation of a non-contact vital signs sensor for continuous heart and respiration rate monitoring", in *2012 IEEE Topical Conference on Biomedical Wireless Technologies, Networks, and Sensing Systems (BioWireleSS)*, 2012, pp. 13–16.

[17] M. Nosrati and N. Tavassolian, "Effects of antenna characteristics on the performance of heart rate monitoring radar systems", vol. 65, no. 6, pp. 3296–3301, 2017.

[18] C. Li, Y. Xiao, and J. Lin, "Design guidelines for radio frequency non-contact vital sign detection", in *29th Annual International Conference of the IEEE Engineering in Medicine and Biology Society*, IEEE, 2007, pp. 1651–1654.

[19] Y.-J. An, Y.-P. Hong, B.-J. Jang, and J.-G. Yook, "Comparative study of 2.4 GHz and 10 GHz vital signal sensing Doppler radars", in *40th European Microwave Conference*, IEEE, 2010, pp. 501–504.

[20] S. Pisa, E. Pittella, and E. Piuzzi, "A survey of radar systems for medical applications", *IEEE Aerospace and Electronic Systems Magazine*, vol. 31, no. 11, pp. 64–81, 2016.

[21] B.-K. Park, O. Boric-Lubecke, and V. M. Lubecke, "Arctangent demodulation with DC offset compensation in quadrature Doppler radar receiver systems", *IEEE Transactions on Microwave Theory and Techniques*, vol. 55, no. 5, pp. 1073–1079, 2007.

[22] J. Wang, X. Wang, L. Chen, J. Huangfu, C. Li, and L. Ran, "Noncontact distance and amplitude-independent vibration measurement based on an extended DACM algorithm", *IEEE Transactions on Instrumentation and Measurement*, vol. 63, no. 1, pp. 145–153, 2013.

[23] B.-K. Park, V. Lubecke, O. Boric-Lubecke, and A. Host-Madsen, "Center tracking quadrature demodulation for a Doppler radar motion detector", in *IEEE/MTT-S International Microwave Symposium*, 2007, pp. 1323–1326.

[24] Q. Lv, D. Ye, S. Qiao, Y. Salamin, J. Huangfu, C. Li, and L. Ran, "High dynamic-range motion imaging based on linearized Doppler radar sensor", *IEEE Transactions on Microwave Theory and Techniques*, vol. 62, no. 9, pp. 1837–1846, 2014.

[25] W. Hu, Z. Zhao, Y. Wang, H. Zhang, and F. Lin, "Noncontact accurate measurement of cardiopulmonary activity using a compact quadrature Doppler radar sensor", *IEEE Transactions on Biomedical Engineering*, vol. 61, no. 3, pp. 725–735, 2014.

[26] M. Li and J. Lin, "Wavelet-transform-based data-length-variation technique for fast heart rate detection using 5.8-GHz CW Doppler radar", *IEEE Transactions on Microwave Theory and Techniques*, vol. 66, no. 1, pp. 568–576, 2017.

[27] J. Tu, T. Hwang, and J. Lin, "Respiration rate measurement under 1-D body motion using single continuous-wave Doppler radar vital sign detection system", *IEEE Transactions on Microwave Theory and Techniques*, vol. 64, no. 6, pp. 1937–1946, June 2016.

[28] J.-M. Muñoz-Ferreras, Z. Peng, R. Gómez-García, and C. Li, "Random body movement mitigation for FMCW-radar-based vital-sign monitoring", in *IEEE Topical Conference on Biomedical Wireless Technologies, Networks, and Sensing Systems (BioWireleSS)*, IEEE, 2016, pp. 22–24.

[29] S. Batchu, H. Narasimhachar, J. Mayeda, T. Hall, J. Lopez, T. Nguyen, R. Banister, and D. Lie, "A phased array non-contact vital signs sensor with automatic beam steering", in *39th Annual International Conference of the IEEE Engineering in Medicine and Biology Society (EMBC), Seogwipo, Korea*, July 2017, pp. 763–766.

[30] C.-M. Nieh and J. Lin, "Adaptive beam-steering antenna for improved coverage of non-contact vital sign radar detection", in *IEEE MTT-S International Microwave Symposium (IMS2014), Tampa, FL*, 2014, pp. 1–3.

[31] C. Li and J. Lin, "Complex signal demodulation and random body movement cancellation techniques for non-contact vital sign detection", in *2008 IEEE MTT-S International Microwave Symposium Digest*, IEEE, 2008, pp. 567–570.

[32] M. Kaisti, M. J. Tadi, O. Lahdenoja, T. Hurnanen, A. Saraste, M. Pänkäälä, and T. Koivisto, "Standalone heartbeat detection in multidimensional mechanocardiograms", *IEEE Sensors Journal*, vol. 19, no. 1, pp. 234–242, 2018.

[33] Y. I. Jang, J. Y. Sim, J.-R. Yang, and N. K. Kwon, "The optimal selection of mother wavelet function and decomposition level for denoising of DCG signal", *Sensors*, vol. 21, no. 5, p. 1851, 2021.

[34] G. Benchetrit, "Breathing pattern in humans: Diversity and individuality", *Respiration physiology*, vol. 122, no. 2-3, pp. 123–129, 2000.

[35] A. Ahmad, J. C. Roh, D. Wang, and A. Dubey, "Vital signs monitoring of multiple people using a FMCW millimeter-wave sensor", in *2018 IEEE Radar Conference (RadarConf18)*, IEEE, 2018, pp. 1450–1455.

[36] A. LoMauro and A. Aliverti, "Sex differences in respiratory function", *Breathe*, vol. 14, no. 2, pp. 131–140, 2018.

[37] J. Fernandez and L. Anishchencko, "Mental stress detection using bioradar respiratory signals", *Biomedical Signal Processing and Control, Elsevier*, vol. 43, pp. 244–249, 2018.

[38] C. Li, V. M. Lubecke, O. Boric-Lubecke, and J. Lin, "A review on recent advances in Doppler radar sensors for noncontact healthcare monitoring", *IEEE Transactions on Microwave Theory and Techniques*, vol. 61, no. 5, pp. 2046–2060, 2013.

[39] C. Li, Y. Xiao, and J. Lin, "Experiment and spectral analysis of a low-power Ka-band heartbeat detector measuring from four sides of a human body", *IEEE Transactions on Microwave Theory and Techniques*, vol. 54, no. 12, pp. 4464–4471, 2006.

[40] F. Wang, T. Horng, K. Peng, J. Jau, J. Li, and C. Chen, "Mutual injection-locked SIL sensor array for vital sign detection with random body movement cancellation", in *IEEE MTT-S International Microwave Symposiuml*, IEEE, 2011, pp. 1–4.

[41] I. Mostafanezhad, O. Boric-Lubecke, V. Lubecke, and A. Host-Madsen, "Cancellation of unwanted motion in a handheld Doppler radar used for non-contact life sign monitoring", in *IEEE MTT-S International Microwave Symposium Digest, Atlanta, GA, USA*, IEEE, 2008, pp. 1171–1174.

[42] M. Nosrati, S. Shahsavari, S. Lee, H. Wang, and N. Tavassolian, "A concurrent dual-beam phased-array Doppler radar using MIMO beamforming techniques for short-range vital-signs monitoring", *IEEE Transactions on Antennas and Propagation*, vol. 67, no. 4, pp. 2390–2404, 2019.

[43] J. Oum, D. Kim, and S. Hong, "Two frequency radar sensor for non-contact vital signal monitor", in *IEEE MTT-S International Microwave Symposium Digest, Atlanta, GA, USA*, IEEE, June 2008, pp. 919–922.

[44] I. Mostafanezhad, E. Yavari, O. Boric-Lubecke, V. Lubecke, and D. Mandiac, "Cancellation of unwanted Doppler radar sensor motion using empirical mode decomposition", *IEEE Sensors Journal*, vol. 13, no. 5, pp. 1897–1904, May 2013.

[45] Ettus Research, *USRP hardware driver and USRP manual*, [Online; accessed september-2022]. [Online]. Available: `https://files.ettus.com/manual/page_usrp_b200.html`.

[46] T. Varum, J. N. Matos, P. Pinho, and R. Abreu, "Nonuniform broadband circularly polarized antenna array for vehicular communications", *IEEE Transactions on Vehicular Technology*, vol. 65, no. 9, pp. 7219–7227, 2015.

[47] C. Gouveia, D. Malafaia, J. Vieira, and P. Pinho, "Bio-radar performance evaluation for different antenna design", in *URSI Radio Science Bulletin*, vol. 364, 2018, pp. 30–38.

[48] M. I. Skolnik, *Radar handbook*. McGraw-Hill Education, 2008.

[49] I. Oppermann, M. Hämäläinen, and J. Iinatti, *UWB: theory and applications*. John Wiley & Sons, 2004.

[50] J. D. Taylor, *Ultra-wideband radar technology*. CRC press, 2000.

[51] Y. Zhang, F. Qi, H. Lv, F. Liang, and J. Wang, "Bioradar technology: Recent research and advancements", *IEEE Microwave Magazine*, vol. 20, no. 8, pp. 58–73, 2019.

[52] L. Zhang, C.-H. Fu, H. Hong, B. Xue, X. Gu, X. Zhu, and C. Li, "Non-contact dual-modality emotion recognition system by CW radar and RGB camera", *IEEE Sensors Journal*, vol. 21, no. 20, pp. 23 198–23 212, 2021.

[53] M. Alizadeh, G. Shaker, J. C. M. De Almeida, P. P. Morita, and S. Safavi-Naeini, "Remote monitoring of human vital signs using mm-wave FMCW radar", *IEEE Access*, vol. 7, pp. 54 958–54 968, 2019.

[54] H. Lee, B.-H. Kim, J.-K. Park, and J.-G. Yook, "A novel vital-sign sensing algorithm for multiple subjects based on 24-GHz FMCW Doppler radar", *Remote Sensing*, vol. 11, no. 10, p. 1237, 2019.

[55] F. Wang, X. Zeng, C. Wu, B. Wang, and K. J. R. Liu, "mmHRV: Contactless heart rate variability monitoring using millimeter-wave radio", *IEEE Internet of Things Journal*, vol. 8, no. 22, pp. 16 623–16 636, 2021.

[56] T. K. Vodai, K. Oleksak, T. Kvelashvili, F. Foroughian, C. Bauder, P. Theilmann, A. Fathy, and O. Kilic, "Enhancement of remote vital sign monitoring detection accuracy using multiple-input multiple-output 77 GHz FMCW radar", *IEEE Journal of Electromagnetics, RF and Microwaves in Medicine and Biology*, 2021.

[57] E. M. Staderini, "UWB radars in medicine", *IEEE Aerospace and Electronic Systems Magazine*, vol. 17, no. 1, pp. 13–18, 2002.

[58] J. Shin, J. Moon, B. Kim, J. Eom, N. Park, and K. Lee, "Attention-based stress detection exploiting non-contact monitoring of movement patterns with IR-UWB radar", in *Proceedings of the 36th Annual ACM Symposium on Applied Computing*, 2021, pp. 637–640.

[59] E. Schires, P. Georgiou, and T. S. Lande, "Vital sign monitoring through the back using an UWB impulse radar with body coupled antennas", *IEEE Transactions on Biomedical Circuits and Systems*, vol. 12, no. 2, pp. 292–302, 2018.

[60] T. Sakamoto, "Noncontact measurement of human vital signs during sleep using low-power millimeter-wave ultrawideband MIMO array radar", in *2019 IEEE MTT-S International Microwave Biomedical Conference (IMBioC)*, IEEE, vol. 1, 2019, pp. 1–4.

[61] C. Gouveia, C. Loss, P. Pinho, and J. Vieira, "Different antenna designs for non-contact vital signs measurement: A review", *Electronics*, vol. 8, no. 11, p. 1294, 2019.

[62] R. Fletcher and J. Han, "Low-cost differential front-end for Doppler radar vital sign monitoring", in *2009 IEEE MTT-S International Microwave Symposium Digest*, IEEE, 2009, pp. 1325–1328.

[63] A. Boothby, R. Hwang, V. Das, J. Lopez, and D. Y. C. Lie, "Design of axial-mode helical antennas for Doppler-based continuous non-contact vital signs monitoring sensors", in *2012 IEEE Radio and Wireless Symposium*, IEEE, 2012, pp. 87–90.

[64] Q. Liang, R. S. Mpanda, X. Wang, J. Shi, and L. Xu, "A printed dipole array antenna for non-contact monitoring system", in *2018 Cross Strait Quad-Regional Radio Science and Wireless Technology Conference (CSQRWC)*, IEEE, 2018, pp. 1–3.

[65] C.-H. Tseng and C.-H. Chao, "Noncontact vital-sign radar sensor using metamaterial-based scanning leaky-wave antenna", in *2016 IEEE MTT-S International Microwave Symposium (IMS)*, IEEE, 2016, pp. 1–3.

[66] T.-M. Shen, T.-Y. J. Kao, T.-Y. Huang, J. Tu, J. Lin, and R.-B. Wu, "Antenna design of 60-GHz micro-radar system-in-package for noncontact vital sign detection", *IEEE Antennas and Wireless Propagation Letters*, vol. 11, pp. 1702–1705, 2012.

[67] S. Lan, Y. Xu, H. Chu, J. Qiu, Z. He, and A. Denisov, "A novel 24 GHz microstrip array module design for bioradars", in *2015 International Symposium on Antennas and Propagation (ISAP)*, IEEE, 2015, pp. 1–3.

[68] S. Lan, L. Duan, Z. He, C. Yang, A. Denisov, S. Ivashov, and L. Anishchenko, "A 77 GHz bioradar antenna module design using microstrip arrays", in *2016 IEEE International Symposium on Antennas and Propagation (APSURSI)*, IEEE, 2016, pp. 1177–1178.

[69] L. Chioukh, H. Boutayeb, D. Deslandes, and K. Wu, "Noise and sensitivity analysis of harmonic radar system for vital sign detection", in *2013 IEEE MTT-S International Microwave Workshop Series on RF and Wireless Technologies for Biomedical and Healthcare Applications (IMWS-BIO)*, IEEE, 2013, pp. 1–3.

[70] S.-S. Myoung, Y.-J. An, J.-G. Yook, B.-J. Jang, and J.-H. Moon, "A novel 10 GHz super-heterodyne bio-radar system based on a frequency multiplier and phase-locked loop", *Progress In Electromagnetics Research C*, vol. 19, pp. 149–162, 2011.

[71] J.-H. Park, Y.-J. Jeong, G.-E. Lee, J.-T. Oh, and J.-R. Yang, "915-MHz continuous-wave Doppler radar sensor for detection of vital signs", *Electronics*, vol. 8, no. 5, p. 561, 2019.

[72] J.-G. Kim, S.-H. Sim, S. Cheon, and S. Hong, "24 GHz circularly polarized Doppler radar with a single antenna", in *2005 European Microwave Conference*, IEEE, vol. 2, 2005, p. 4.

[73] C. Gu, Y. He, and J. Zhu, "Noncontact vital sensing with a miniaturized 2.4 GHz circularly polarized Doppler radar", *IEEE Sensors Letters*, vol. 3, no. 7, pp. 1–4, 2019.

[74] K. K.-M. Chan, A. E.-C. Tan, and K. Rambabu, "Circularly polarized ultra-wideband radar system for vital signs monitoring", *IEEE Transactions on Microwave Theory and Techniques*, vol. 61, no. 5, pp. 2069–2075, 2013.

[75] M. Nosrati and N. Tavassolian, "Experimental study of antenna characteristic effects on Doppler radar performance", in *In Proceedings of the IEEE International Symposium on Antennas and Propagation & USNC/URSI National Radio Science Meeting, San Diego, CA, USA*, 2017, pp. 209–211.

[76] R. Salvado, C. Loss, R. Gonçalves, and P. Pinho, "Textile materials for the design of wearable antennas: A survey", *Sensors*, vol. 12, no. 11, pp. 15 841–15 857, 2012.

[77] S Sankaralingam and B. Gupta, "Determination of dielectric constant of fabric materials and their use as substrates for design and development of antennas for wearable applications", *IEEE Transactions on Instrumentation and Measurement*, vol. 59, no. 12, pp. 3122–3130, 2010.

[78] L. Zhang, Z. Wang, and J. L. Volakis, "Textile antennas and sensors for body-worn applications", *IEEE Antennas and Wireless Propagation Letters*, vol. 11, pp. 1690–1693, 2012.

[79] C. Loss, R. Salvado, R. Gonçalves, and P. Pinho, "Influence of the laminating manufacturing technique on the SN parameter of printed textile antennas", in *2017 IEEE MTT-S International Microwave Workshop Series on Advanced Materials and Processes for RF and THz Applications (IMWS-AMP)*, IEEE, 2017, pp. 1–3.

[80] M. L. Scarpello, I. Kazani, C. Hertleer, H. Rogier, and D. V. Ginste, "Stability and efficiency of screen-printed wearable and washable antennas", *IEEE Antennas and Wireless Propagation Letters*, vol. 11, pp. 838–841, 2012.

[81] J. Spurek, J. Velim, M. Cupal, Z. Raida, J. Prasek, and J. Hubalek, "Slot loop antennas printed on 3D textile substrate", in *2016 21st International Conference on Microwave, Radar and Wireless Communications (MIKON)*, IEEE, 2016, pp. 1–3.

[82] A. Tsolis, W. G. Whittow, A. A. Alexandridis, and J. C. Vardaxoglou, "Embroidery and related manufacturing techniques for wearable antennas: Challenges and opportunities", *Electronics*, vol. 3, no. 2, pp. 314–338, 2014.

[83] G. Ginestet, N. Brechet, J. Torres, E. Moradi, L. Ukkonen, T. Björninen, and J. Virkki, "Embroidered antenna-microchip interconnections and contour antennas in passive UHF RFID textile tags", *IEEE Antennas and Wireless Propagation Letters*, vol. 16, pp. 1205–1208, 2016.

[84] S. Agneessens, P. Van Torre, F. Declercq, B. Spinnewyn, G.-J. Stockman, H. Rogier, and D. V. Ginste, "A through wall Doppler radar system: Active textile antenna design, prototyping and experiment", in *2013 IEEE Topical Conference on Wireless Sensors and Sensor Networks (WiSNet)*, IEEE, 2013, pp. 16–18.

[85] L. Alonso, S. Ver Hoeye, M. Fernández, C. Vázquez, R. Camblor, G. Hotopan, A. Hadarig, and F. Las-Heras, "Millimetre wave textile integrated waveguide beamforming antenna for radar applications", in *Global Symposium on Millimeter-Waves (GSMM)*, IEEE, 2015, pp. 1–3.

[86] M. Roudjane, M. Khalil, A. Miled, and Y. Messaddeq, "New generation wearable antenna based on multimaterial fiber for wireless communication and real-time breath detection", *Photonics*, vol. 5, no. 4, p. 33, 2018.

[87] R. R. Perron, G. C. Huang, and M. F. Iskander, "Textile electromagnetic coupler for monitoring vital signs and changes in lung water content", *IEEE Antennas and Wireless Propagation Letters*, vol. 14, pp. 151–154, 2014.

[88] H. Bo, Q. Fu, L. Xu, F. Lure, and Y. Dou, "Design and implementation of a 2.45 GHz RF sensor for non-contacting monitoring vital signs", in *2016 Computing in Cardiology Conference (CinC)*, IEEE, 2016, pp. 1113–1116.

[89] H.-R. Chuang, H.-C. Kuo, F.-L. Lin, T.-H. Huang, C.-S. Kuo, and Y.-W. Ou, "60-GHz millimeter-wave life detection system (MLDS) for noncontact human vital-signal monitoring", *IEEE Sensors Journal*, vol. 12, no. 3, pp. 602–609, 2011.

[90] S.-S. Myoung, J.-H. Park, J.-G. Yook, and B.-J. Jang, "2.4 GHz bio-radar system with improved performance by using phase-locked loop", *Microwave and Optical Technology Letters*, vol. 52, no. 9, pp. 2074–2076, 2010.

[91] M. S. Rabbani and H. Ghafouri-Shiraz, "Ultra-wide patch antenna array design at 60 GHz band for remote vital sign monitoring with Doppler radar principle", *Journal of Infrared, Millimeter, and Terahertz Waves*, vol. 38, no. 5, pp. 548–566, 2017.

[92] T. W. Hsu and A. C. H. Tseng, "Compact 24 GHz Doppler radar module for non-contact human vital sign detection", in *In Proceedings of the International Symposium on Antennas and Propagation, Okinawa, Japan*, 2016, pp. 994–995.

[93] Y. Xiao, C. Li, and J. Lin, "A portable noncontact heartbeat and respiration monitoring system using 5-GHz radar", *IEEE Sensors Journal*, vol. 7, no. 7, pp. 1042–1043, 2007.

[94] J.-K. Huang and C.-H. Tseng, "A 5.8-GHz radar sensor chip in 0.18-um CMOS for non-contact vital sign detection", in *2016 IEEE International Symposium on Radio-Frequency Integration Technology (RFIT)*, IEEE, 2016, pp. 1–3.

[95] International Commission on Non-Ionizing Radiation Protection, "Guidelines for limiting exposure to time-varying electric, magnetic, and electromagnetic fields (up to 300 GHz)", *Health physics*, vol. 74, no. 4, pp. 494–522, 1998.

[96] R. Duarte, C. Gouveia, P. Pinho, and D. Albuquerque, "Limits of WPT through the human body using radio frequency", in *16th European Conference on Antennas and Propagation (EuCAP)*, IEEE, 2022, pp. 1–5.

[97] G. Wang, J.-M. Munoz-Ferreras, C. Gu, C. Li, and R. Gomez-Garcia, "Application of linear-frequency-modulated continuous-wave (LFMCW) radars for tracking of vital signs", *IEEE Transactions on Microwave Theory and Techniques*, vol. 62, no. 6, pp. 1387–1399, 2014.

[98] A. D. Droitcour, "Non-contact measurement of heart and respiration rates with a single-chip microwave Doppler radar", PhD thesis, Citeseer, 2006.

[99] A. Kumar, Z. Li, Q. Liang, B. Zhang, and X. Wu, "Experimental study of through-wall human detection using ultra wideband radar sensors", *Measurement*, vol. 47, pp. 869–879, 2014.

[100] D. R. Morgan and M. G. Zierdt, "Novel signal processing techniques for Doppler radar cardiopulmonary sensing", *Signal Processing*, vol. 89, no. 1, pp. 45–66, 2009.

[101] M. Zakrzewski, H. Raittinen, and J. Vanhala, "Comparison of center estimation algorithms for heart and respiration monitoring with microwave Doppler radar", *IEEE Sensors Journal*, vol. 12, no. 3, pp. 627–634, 2011.

[102] C. Gouveia, D. Albuquerque, J. Vieira, and P. Pinho, "Dynamic digital signal processing algorithm for vital signs extraction in continuous-wave radars", *Remote Sensing*, vol. 13, no. 20, p. 4079, 2021.

[103] F. E. Churchill, G. W. Ogar, and B. J. Thompson, "The correction of I and Q errors in a coherent processor", *IEEE Transactions on Aerospace and Electronic Systems*, no. 1, pp. 131–137, 1981.

[104] C. A. Balanis, *Antenna theory: analysis and design*. John wiley & sons, 2016, pp. 474–953.

[105] C. Gouveia, B. Cruz, P. Pinho, and D. Albuquerque, "Signal power variation for bio-radar applications", in *XIV Iberian Meeting on Computational Electromagnetics EIEC (2022)*, Universitat Politècnica de Catalunya. Remote Sensing, Antennas, Microwaves and Superconductivity Group (CommSensLab), 2022.

[106] X. Hui and E. C. Kan, "Seat integration of RF vital-sign monitoring", in *2019 IEEE MTT-S International Microwave Biomedical Conference (IMBioC)*, IEEE, vol. 1, 2019, pp. 1–3.

[107] A. D. Droitcour, O. Boric-Lubecke, V. M. Lubecke, J. Lin, and G. T. Kovacs, "Range correlation and I/Q performance benefits in single-chip silicon Doppler radars for noncontact cardiopulmonary monitoring", *IEEE Transactions on Microwave Theory and Techniques*, vol. 52, no. 3, pp. 838–848, 2004.

[108] S. S. Gao, Q. Luo, and F. Zhu, *Circularly polarized antennas*. John Wiley & Sons, 2013.

[109] P. Vecchia, R. Matthes, G. Ziegelberger, J. Lin, R. Saunders, and A. Swerdlow, "Exposure to high frequency electromagnetic fields, biological effects and health consequences (100 kHz-300 GHz)", *International Commission on Non-Ionizing Radiation Protection*, vol. 378, 2009.

[110] A. Alemaryeen, S. Noghanian, and R. Fazel-Rezai, "Antenna effects on respiratory rate measurement using a UWB radar system", *IEEE Journal of Electromagnetics, RF and Microwaves in Medicine and Biology*, vol. 2, no. 2, pp. 87–93, 2018.

[111] J.-Y. Kim, J.-H. Park, S.-Y. Jang, and J.-R. Yang, "Peak detection algorithm for vital sign detection using Doppler radar sensors", *Sensors*, vol. 19, no. 7, p. 1575, 2019.

[112] X. Gao, A. Singh, E. Yavari, V. Lubecke, and O. Boric-Lubecke, "Non-contact displacement estimation using Doppler radar", in *Engineering in Medicine and Biology Society (EMBC), 2012 Annual International Conference of the IEEE*, IEEE, 2012, pp. 1602–1605.

[113] X. Gao, J. Xu, A. Rahman, V. Lubecke, and O. Boric-Lubecke, "Arc shifting method for small displacement measurement with quadrature CW Doppler radar", in *IEEE MTT-S International Microwave Symposium (IMS)*, IEEE, 2017, pp. 1003–1006.

[114] J.-H. Park and J.-R. Yang, "Multiphase continuous-wave Doppler radar with multiarc circle fitting algorithm for small periodic displacement measurement", *IEEE Transactions on Microwave Theory and Techniques*, vol. 69, no. 11, pp. 5135–5144, 2020.

[115] I. Kåsa, "A circle fitting procedure and its error analysis", *IEEE Transactions on Instrumentation and Measurement*, no. 1, pp. 8–14, 1976.

[116] C. Gouveia, J. Vieira, and P. Pinho, "Motion detection method for clutter rejection in the bio-radar signal processing", *International Journal of Electronics and Communication Engineering*, vol. 12, no. 8, pp. 518–526, 2018.

[117] O. Gal, *Ellipse fit using least squares criterion*, [Online; accessed september 2022]. [Online]. Available: `http://it.mathworks.com/matlabcentral/fileexchange/3215-fit-ellipse`.

[118] N. Chernov and C. Lesort, "Least squares fitting of circles", *Journal of Mathematical Imaging and Vision*, vol. 23, no. 3, pp. 239–252, 2005.

[119] I. L. De Guevara, J Muñoz, O. De Cózar, and E. B. Blázquez, "Robust fitting of circle arcs", *Journal of Mathematical Imaging and Vision*, vol. 40, no. 2, pp. 147–161, 2011.

[120] J. C. Lagarias, J. A. Reeds, M. H. Wright, and P. E. Wright, "Convergence properties of the nelder–mead simplex method in low dimensions", *SIAM Journal on Optimization*, vol. 9, no. 1, pp. 112–147, 1998.

[121] G. Yuan, N. A. Drost, and R. A. McIvor, "Respiratory rate and breathing pattern", *McMaster University Medical Journal*, vol. 10, no. 1, pp. 23–25, 2013.

[122] I. Van Diest, K. Verstappen, A. E. Aubert, D. Widjaja, D. Vansteenwegen, and E. Vlemincx, "Inhalation/exhalation ratio modulates the effect of slow breathing on heart rate variability and relaxation", *Applied Psychophysiology and Biofeedback*, vol. 39, no. 3-4, pp. 171–180, 2014.

[123] H. Akima, "A new method of interpolation and smooth curve fitting based on local procedures", *Journal of the ACM (JACM)*, vol. 17, no. 4, pp. 589–602, 1970.

[124] N. Chernov, *MATLAB code for circle fitting algorithms*, [Online; accessed september 2022]. [Online]. Available: `https://people.cas.uab.edu/~mosya/cl/MATLABcircle.html`.

[125] G. Taubin, "Estimation of planar curves, surfaces, and nonplanar space curves defined by implicit equations with applications to edge and range image segmentation", *IEEE Computer Architecture Letters*, vol. 13, no. 11, pp. 1115–1138, 1991.

[126] W. Zeng, L. Shu, Q. Li, S. Chen, F. Wang, and X.-M. Tao, "Fiber-based wearable electronics: A review of materials, fabrication, devices, and applications", *Advanced Materials*, vol. 26, no. 31, pp. 5310–5336, 2014.

[127] C. Loss, R. Gonçalves, P. Pinho, and R. Salvado, "Influence of some structural parameters on the dielectric behavior of materials for textile antennas", *Textile Research Journal*, vol. 89, no. 7, pp. 1131–1143, 2019.

[128] C. Loss, "Study of the electromagnetic properties of textiles: Development of textile antennas for energy harvesting", PhD thesis, Universidade da Beira Interior (Portugal), 2017.

[129] S. Kawabata, "Measurement of the mechanical properties of fabrics", *The Standardization and Analysis of Hand Evaluation*, pp. 36–37, 1980.

[130] M. Rossi, S. Agneessens, H. Rogier, and D. V. Ginste, "Stochastic analysis of the impact of substrate compression on the performance of textile antennas", *IEEE Transactions on Antennas and Propagation*, vol. 64, no. 6, pp. 2507–2512, 2016.

[131] M. Yang, X. Yang, L. Li, and L. Zhang, "In-car multiple targets vital sign monitoring using location-based VMD algorithm", in *10th International Conference on Wireless Communications and Signal Processing (WCSP)*, IEEE, 2018, pp. 1–6.

[132] A. R. Diewald, J. Landwehr, D. Tatarinov, P. D. M. Cola, C. Watgen, C. Mica, M. Lu-Dac, P. Larsen, O. Gomez, and T. Goniva, "RF-based child occupation detection in the vehicle interior", in *7th International Radar Symposium (IRS)*, IEEE, 2016, pp. 1–4.

[133] Z. Yang, M. Bocca, V. Jain, and P. Mohapatra, "Contactless breathing rate monitoring in vehicle using UWB radar", in *Proceedings of the 7th International Workshop on Real-World Embedded Wireless Systems and Networks*, 2018, pp. 13–18.

[134] K. Evteeva, A. Turetskaya, and L. Anishchenko, "Sensing of human breathing and heart beating at different orientation angles by CW doppler radar", in *2019 Ural Symposium on Biomedical Engineering, Radioelectronics and Information Technology (USBEREIT)*, IEEE, 2019, pp. 36–39.

[135] T. Varum, J. N. Matos, and P. Pinho, "Non-uniform microstrip antenna array for DSRC in single-lane structures", *Sensors*, vol. 16, no. 12, p. 2101, 2016.

[136] C. Loss, C. Gouveia, R. Salvado, P. Pinho, and J. Vieira, "Textile antenna for bio-radar embedded in a car seat", *Materials*, vol. 14, no. 1, p. 213, 2021.

[137] A. M. Shepherd, "Weft knitted spacer fabrics", pat. US6779369B2,GB0220181D0.

[138] C. Gouveia, C. Loss, Z. Raida, J. Lacik, P. Pinho, and J. Vieira, "Textile antenna array for bio-radar applications", in *23rd International Microwave and Radar Conference (MIKON)*, IEEE, 2020, pp. 315–319.

[139] C. Hertleer, A. Van Laere, H. Rogier, and L. L. Van, "Influence of relative humidity on textile antenna performance", *Textile Research Journal*, vol. 80, pp. 177–183, 2010.

[140] R. Silva, M. Midão, D. Esteves, A. Leite, P. Peixoto, C. Gouveia, P. Pinho, J. Vieira, D. Pires, T. Silveira, C. Loss, and R. Salvado, "Vehicle seat cover with a monitoring system", Patent Pending WO/2022/070137, PCT/IB2021/059011.

[141] A. E. Aubert, L. Welkenhuysen, J. Montald, L. de Wolf, H. Geivers, J. Minten, H. Kesteloot, and H. Geest, "Laser method for recording displacement of the heart and chest wall", *Journal of Biomedical Engineering*, vol. 6, no. 2, pp. 134–140, 1984.

[142] G. Ramachandran and M. Singh, "Three-dimensional reconstruction of cardiac displacement patterns on the chest wall during the P, QRS and T-segments of the ECG by laser speckle inteferometry", *Medical and Biological Engineering and Computing*, vol. 27, no. 5, pp. 525–530, 1989.

[143] J. Jaakkola, S. Jaakkola, O. Lahdenoja, T. Hurnanen, T. Koivisto, M. Pänkäälä, T. Knuutila, T. O. Kiviniemi, T. Vasankari, and K. J. Airaksinen, "Mobile phone detection of atrial fibrillation with mechanocardiography: The mode-af study (mobile phone detection of atrial fibrillation)", *Circulation*, vol. 137, no. 14, pp. 1524–1527, 2018.

[144] V. L. Petrović, M. M. Janković, A. V. Lupšić, V. R. Mihajlović, and J. S. Popović-Božović, "High-accuracy real-time monitoring of heart rate variability using 24 GHz continuous-wave Doppler radar", *IEEE Access*, vol. 7, pp. 74 721–74 733, 2019.

[145] J. Wang, X. Wang, Z. Zhu, J. Huangfu, C. Li, and L. Ran, "1-D microwave imaging of human cardiac motion: An ab-initio investigation", *IEEE Transactions on Microwave Theory and Techniques*, vol. 61, no. 5, pp. 2101–2107, 2013.

[146] F. Weishaupt, I. Walterscheid, O. Biallawons, and J. Klare, "Vital sign localization and measurement using an LFMCW MIMO radar", in *19th International Radar Symposium (IRS), Bonn*, 2018, pp. 1–8.

[147] S. Tomii and T. Ohtsuki, "Heartbeat detection by using Doppler radar with wavelet transform based on scale factor learning", in *IEEE International Conference on Communications*, 2015, pp. 483–488.

[148] X. Li, B. Liu, Y. Liu, J. Li, J. Lai, and Z. Zheng, "A novel signal separation and de-noising technique for Doppler radar vital signal detection", *Sensors*, vol. 19, no. 21, p. 4751, 2019.

[149] L. Liu, W. Xiao, J. Wu, and S. Xiao, "Wavelet analysis based noncontact vital signal measurements using mm-wave radar", in *International Conference on Green, Pervasive, and Cloud Computing*, Springer, 2020, pp. 3–14.

[150] A. Graps, "An introduction to wavelets", *IEEE Computational Science and Engineering*, vol. 2, no. 2, pp. 50–61, 1995.

[151] C. Gargour, M. Gabrea, V. Ramachandran, and J.-M. Lina, "A short introduction to wavelets and their applications", *IEEE Circuits and Systems Magazine*, vol. 9, no. 2, pp. 57–68, 2009.

[152] J. Kevric and A. Subasi, "Comparison of signal decomposition methods in classification of EEG signals for motor-imagery BCI system", *Biomedical Signal Processing and Control*, vol. 31, pp. 398–406, 2017.

[153] N. E. Huang, Z. Shen, S. R. Long, M. C. Wu, H. H. Shih, Q. Zheng, N.-C. Yen, C. C. Tung, and H. H. Liu, "The empirical mode decomposition and the Hilbert spectrum for nonlinear and non-stationary time series analysis", *Proceedings of the Royal Society of London. Series A: mathematical, physical and engineering sciences*, vol. 454, no. 1971, pp. 903–995, 1998.

[154] G. Wang, X. Y. Chen, F. L. Qiao, Z. Wu, and N. E. Huang, "On intrinsic mode function", *Advances in Adaptive Data Analysis*, vol. 2, no. 03, pp. 277–293, 2010.

[155] Z. Wu and N. E. Huang, "Ensemble empirical mode decomposition: A noise-assisted data analysis method", *Advances in Adaptive Data Analysis*, vol. 1, no. 01, pp. 1–41, 2009.

[156] S. Laborde, E. Mosley, and J. Thayer, "Heart rate variability and cardiac vagal tone in psychophysiological research – recommendations for experiment planning, data analysis, and data reporting", *Frontiers in Psychology*, vol. 8, p. 213, 2017.

[157] F. Shaffer and J. P. Ginsberg, "An overview of heart rate variability metrics and norms", *Frontiers in Public Health*, p. 258, 2017.

[158] Electrophysiology Task Force of the European Society of Cardiology the North American Society of Pacing, "Heart rate variability: Standards of measurement, physiological interpretation, and clinical use", *Circulation*, vol. 93, no. 5, pp. 1043–1065, 1996.

[159] W. Massagram, V. M. Lubecke, A. HØst-Madsen, and O. Boric-Lubecke, "Assessment of heart rate variability and respiratory sinus arrhythmia via Doppler radar", *IEEE Transactions on Microwave Theory and Techniques*, vol. 57, no. 10, pp. 2542–2549, 2009.

[160] N. T. P. Nguyen, P.-Y. Lyu, M. H. Lin, C.-C. Chang, and S.-F. Chang, "A short-time autocorrelation method for noncontact detection of heart rate variability using CW doppler radar", in *IEEE MTT-S International Microwave Biomedical Conference (IMBioC)*, IEEE, vol. 1, 2019, pp. 1–4.

[161] E. Turppa, J. M. Kortelainen, O. Antropov, and T. Kiuru, "Vital sign monitoring using FMCW radar in various sleeping scenarios", *Sensors*, vol. 20, no. 22, 2020.

[162] S. Suzuki, T. Matsui, S. Gotoh, Y. Mori, B. Takase, and M. Ishihara, "Development of non-contact monitoring system of heart rate variability (HRV) - an approach of remote sensing for ubiquitous technology", in *International Conference on Ergonomics and Health Aspects of Work with Computers*, Springer, 2009, pp. 195–203.

[163] W. Xia, Y. Li, and S. Dong, "Radar-based high-accuracy cardiac activity sensing", *IEEE Transactions on Instrumentation and Measurement*, vol. 70, pp. 1–13, 2021.

[164] C. Gouveia, D. Albuquerque, P. Pinho, and J. Vieira, "Evaluation of heartbeat signal extraction methods using a 5.8 GHz Doppler radar system in a real application scenario", *IEEE Sensors Journal*, vol. 22, no. 8, pp. 7979–7989, 2022.

[165] D. Batista, H. P. da Silva, A. Fred, C. Moreira, M. Reis, and H. A. Ferreira, "Benchmarking of the BITalino biomedical toolkit against an established gold standard", *Healthcare Technology Letters*, vol. 6, no. 2, pp. 32–36, 2019.

[166] P. Kathirvel, M. S. Manikandan, S. R. M. Prasanna, and K. P. Soman, "An efficient R-peak detection based on new nonlinear transformation and first-order Gaussian differentiator", *Cardiovascular Engineering and Technology*, vol. 2, no. 4, pp. 408–425, 2011.

[167] D. Giavarina, "Understanding bland altman analysis", *Biochemia Medica*, vol. 25, no. 2, pp. 141–151, 2015.

[168] R. Klein, *Bland-Altman and correlation plot*, [MATLAB Central File Exchange; Online; accessed september 2022]. [Online]. Available: `https://www.mathworks.com/matlabcentral/fileexchange/45049-bland-altman-and-correlation-plot`.

[169] D. Toda, R. Anzai, K. Ichige, R. Saito, and D. Ueki, "ECG signal reconstruction using FMCW radar and convolutional neural network", in *20th International Symposium on Communications and Information Technologies (ISCIT)*, IEEE, 2021, pp. 176–181.

[170] S. Wu, T. Sakamoto, K. Oishi, T. Sato, K. Inoue, T. Fukuda, K. Mizutani, and H. Sakai, "Person-specific heart rate estimation with ultra-wideband radar using convolutional neural networks", *IEEE Access*, vol. 7, pp. 168 484–168 494, 2019.

[171] Y.-C. Tsai, S.-H. Lai, C.-J. Ho, F.-M. Wu, L. Henrickson, C.-C. Wei, I. Chen, V. Wu, and J. Chen, "High accuracy respiration and heart rate detection based on artificial neural network regression", in *2020 42nd Annual International Conference of the IEEE Engineering in Medicine & Biology Society (EMBC)*, IEEE, 2020, pp. 232–235.

[172] N. Malešević, V. Petrović, M. Belić, C. Antfolk, V. Mihajlović, and M. Janković, "Contactless real-time heartbeat detection via 24 GHz continuous-wave Doppler radar using artificial neural networks", *Sensors*, vol. 20, no. 8, p. 2351, 2020.

[173] S. L. Brunton and J. N. Kutz, *Data-driven science and engineering: Machine learning, dynamical systems, and control*. Cambridge University Press, 2019.

[174] Y. LeCun, Y. Bengio, *et al.*, "Convolutional networks for images, speech, and time series", *The handbook of brain theory and neural networks*, vol. 3361, no. 10, p. 1995, 1995.

[175] S. Vaseghi, *Wiener Filters. In: Advanced Signal Processing and Digital Noise Reduction*. Switzerland AG: Vieweg+Teubner Verlag, 1996, pp. 140–163.

[176] C. Gouveia, D. F. Albuquerque, P. Pinho, and J. Vieira, "Bio-radar cardiac signal model used for HRV assessment and evaluation using adaptive filtering", *IEEE Transactions on Instrumentation and Measurement*, vol. 71, pp. 1–10, 2022.

[177] F. Shaffer, R. McCraty, and C. L. Zerr, "A healthy heart is not a metronome: An integrative review of the heart's anatomy and heart rate variability", *Frontiers in Psychology*, vol. 5, p. 1040, 2014.

[178] M. A. Connelly, J. T. Brown, G. L. Kearns, R. A. Anderson, S. D. St Peter, and K. A. Neville, "Pupillometry: A non-invasive technique for pain assessment in paediatric patients", *Archives of Disease in Childhood*, vol. 99, no. 12, pp. 1125–1131, 2014.

[179] R. A. Vasa, A. Keefer, J. Reaven, M. South, and S. W. White, "Priorities for advancing research on youth with autism spectrum disorder and co-occurring anxiety", *Journal of Autism and Developmental Disorders*, vol. 48, no. 3, pp. 925–934, 2018.

[180] N. H. Frijda, "Emotion experience and its varieties", *Emotion Review*, vol. 1, no. 3, pp. 264–271, 2009.

[181] K. R. Scherer, "What are emotions? and how can they be measured?", *Social Science Information*, vol. 44, no. 4, pp. 695–729, 2005.

[182] L. F. Barret, "Emotions are real", *Emotion (Washington, D.C.)*, vol. 12, pp. 413–29, Jun. 2012.

[183] A. H. Fischer and A. S. R Manstead, "Social functions of emotion", *Handbook of emotions (New York Guilford Press)*, vol. 3, pp. 456–465, 2008.

[184] S. Koelstra, C. Muhl, M. Soleymani, J.-S. Lee, A. Yazdani, T. Ebrahimi, T. Pun, A. Nijholt, and I. Patras, "DEAP: A database for emotion analysis using physiological signals", *IEEE Transactions on Affective Computing*, vol. 3, no. 1, pp. 18–31, 2012.

[185] S. Katsigiannis and N. Ramzan, "DREAMER: A database for emotion recognition through EEG and ECG signals from wireless low-cost off-the-shelf devices", *IEEE Journal of Biomedical and Health Informatics*, vol. 22, no. 1, pp. 98–107, 2018.

[186] G. Pinto, J. M. Carvalho, F. Barros, S. C. Soares, A. J. Pinho, and S. Brás, "Multimodal emotion evaluation: A physiological model for cost-effective emotion classification", *Sensors*, vol. 20, no. 12, p. 3510, 2020.

[187] N. Cristianini and J. Shawe-Taylor, *An introduction to support vector machines and other kernel-based learning methods*. Cambridge university press, 2000.

[188] D. Bzdok, M. Krzywinski, and N. Altman, "Machine learning: Supervised methods", *Nature Methods*, vol. 15, no. 1, p. 5, 2018.

[189] E. Alpaydin, *Introduction to Machine Learning*. Massachusetts Institute of Technology, Cambridge, Massachusetts: The MIT Press, 2004, pp. 173–342.

[190] H. U. R. Siddiqui, H. F. Shahzad, A. A. Saleem, A. B. Khan Khakwani, F. Rustam, E. Lee, I. Ashraf, and S. Dudley, "Respiration based non-invasive approach for emotion recognition using impulse radio ultra wide band radar and machine learning", *Sensors*, vol. 21, no. 24, p. 8336, 2021.

[191] Q. Gao, L. Zhang, J. Yan, H. Zhao, C. Ding, H. Hong, and X. Zhu, "Non-contact emotion recognition via CW doppler radar", in *2018 Asia-Pacific Microwave Conference (APMC)*, IEEE, 2018, pp. 1468–1470.

[192] C. Gouveia, A. Tomé, F. Barros, S. C. Soares, J. Vieira, and P. Pinho, "Study on the usage feasibility of continuous-wave radar for emotion recognition", *Biomedical Signal Processing and Control*, vol. 58, p. 101 835, 2020.

[193] D. S. Quintana, "Statistical considerations for reporting and planning heart rate variability case-control studies", *Psychophysiology*, vol. 54, no. 3, pp. 344–349, 2017.

[194] J. J. McGinley and B. H. Friedman, "Autonomic specificity in emotion: The induction method matters", *International Journal of Psychophysiology*, vol. 118, pp. 48–57, 2017.

[195] P. Rainville, A. Bechara, N. Naqvi, and A. R. Damasio, "Basic emotions are associated with distinct patterns of cardiorespiratory activity", *International journal of psychophysiology*, vol. 61, no. 1, pp. 5–18, 2006.

[196] F. Barros, C. Figueiredo, S. Brás, J. M. Carvalho, and S. C. Soares, "Multidimensional assessment of anxiety through the state-trait inventory for cognitive and somatic anxiety (STICSA): From dimensionality to response prediction across emotional contexts", *PloS one*, vol. 17, no. 1, e0262960, 2022.

[197] I. Guyon and A. Elisseeff, "An introduction to variable and feature selection", *Journal of Machine Learning Research*, vol. 3, no. Mar, pp. 1157–1182, 2003.

[198] H. Zhang, S. Li, X. Jing, P. Zhang, Y. Zhang, T. Jiao, G. Lu, and J. Wang, "The separation of the heartbeat and respiratory signal of a Doppler radar based on the LMS adaptive harmonic cancellation algorithm", in 6^{th} *International Symposium on Computational Intelligence and Design, Hangzhou*, 2013, pp. 362–364.

[199] P. M. Granitto, C. Furlanello, F. Biasioli, and F. Gasperi, "Recursive feature elimination with random forest for ptr-ms analysis of agroindustrial products", *Chemometrics and Intelligent Laboratory Systems*, vol. 83, no. 2, pp. 83–90, 2006.

[200] V. L. Clark and J. A. Kruse, "Clinical methods: The history, physical, and laboratory examinations", *Jama*, vol. 264, no. 21, 1990.

[201] E. L. Allwein, R. E. Schapire, and Y. Singer, "Reducing multiclass to binary: A unifying approach for margin classifiers", *Journal of machine learning research*, vol. 1, no. Dec, pp. 113–141, 2000.

[202] P.-N. Tan, M. Steinbach, A. Karpatne, and V. Kumar, *Introduction to Data Mining*, 2nd ed. Pearson, 2018, pp. 208–212.

[203] J. Panksepp, "Affective neuroscience: The foundations of human and animal emotions", *New York Oxford University Press*, 1998.

[204] N. R. Giuliani, K. McRae, and J. J. Gross, "The up-and down-regulation of amusement: Experiential, behavioral, and autonomic consequences", *Emotion, American Psychological Association*, vol. 8, no. 5, p. 714, 2008.

[205] T. M. Mitchell, *Machine Learning*. McGraw Hill, 1997, pp. 128–152.

[206] J. L. Rojo-Álvarez, A. Sanchez-Sanchez, O. Barquero-Perez, R. Goya-Esteban, E. Everss, I. Mora-Jimenez, and A. Garcia-Alberola, "Analysis of physiological meaning of detrended fluctuation analysis in heart rate variability using a lumped parameter model", in *2007 Computers in Cardiology*, IEEE, 2007, pp. 25–28.

[207] R. W. Picard, E. Vyzas, and J. Healey, "Toward machine emotional intelligence: Analysis of affective physiological state", *IEEE Transactions on Pattern Analysis and Machine Intelligence*, vol. 23, no. 10, pp. 1175–1191, 2001.

[208] D. L. Hahs-Vaughn and R. G. Lomax, *Statistical Concepts - A Second Course - Fifth edition*. Routledge, 2020.

[209] J. Ferreira, S. Brás, C. F. Silva, and S. C. Soares, "An automatic classifier of emotions built from entropy of noise", *Psychophysiology*, vol. 54, no. 4, pp. 620–627, 2017.